NTNU

Norwegian University of
Science and Technology

The Braking Effect of Trees on Snow Avalanches

An Experimental Study

Katharina Kahrs

Civil and Environmental Engineering
Submission date: June 2016
Supervisor: Steinar Nordal, BAT
Co-supervisor: Dieter Issler, NGI
Harald Norem, Statens vegvesen

Norwegian University of Science and Technology
Department of Civil and Transport Engineering

Preface

This is a master thesis in geotechnics written in the spring semester of 2016 as part of the MSc in Civil and Environmental Engineering at the Norwegian University of Science and Technology (NTNU). The thesis was carried out in cooperation with the Norwegian Geotechnical Institute (NGI). The master thesis is a sequel to a project thesis written in the autumn semester of 2015 (Kahrs, 2015). The project was proposed by Dieter Issler, NGI, and published in NTNU's database of project proposals.

Trondheim, 2016-06-28

Katharina Kahrs

Acknowledgements

First of all, I would like to thank my three supervisors Steinar Nordal, Dieter Issler, and Harald Norem. Dieter proposed the topic for this master thesis and supervised my project thesis in the autumn semester of 2015. He took time out of his busy schedule for a visit at NTNU, and gave me detailed feedback via e-mail. Harald stepped in as a local supervisor. His practical experience with chute experiments was invaluable in designing the chute and the program for the experiments. Harald was always available via phone and e-mail and frequently visited me at the laboratory. Steinar stepped in for Arnfinn Emdal as NTNU's official supervisor. His role was mainly administrative, and I would like to thank him for establishing contact with Harald and with NTNU's lab and workshop personnel to kick off the construction of the chute and its components.

Many of the staff at the Department of Civil and Transport Engineering, academic, engineering, and administrative, should be thanked for their help. In particular, I would like to thank the following people without whom this thesis could not have been written: Einar Husby, engineer at the Group for Geotechnics, drew the final design of the chute and oversaw its construction. He designed an easy-to-work-with chute that can be used for a wide range of experiments, both mine and that of future master- and PhD-students. He also made sure that the chute was safe to work with. The components of the chute were built by NTNU's carpenters. Thanks to them, the chute was built according to design and with professional quality. A big thank you to Frank Stæhli and Tage Westrum at Fellesverkstedet, the department's workshop. Frank drilled 1584 holes into aluminium plates and cut 1584 metal pins from filler rod for me, and both he and Tage were always helpful whenever I needed practical advice, tools, or a hand with lifting heavy equipment. Kenneth Sundli, senior engineer at the department, ordered different types of cameras for me and set up a laptop with the corresponding software.

I would like to thank NTNU for financing the equipment for the experiments and for employing Harald Norem in a part-time position. Finally, I would like to thank the Norwegian Geotechnical Institute (NGI) for supporting both my project thesis and this master thesis with a budget covering two trips to Trondheim for Dieter Issler.

K.K.

Summary and conclusions

Mountain forests can protect people and infrastructure from snow avalanches in a cost-effective way. In this thesis, we have carried out a series of small-scale chute experiments to study the braking effect of trees on snow avalanches. We assume that the avalanche releases above the forest and that the trees are not broken or bent upon impact of the avalanche.

The chute consists of three straight sections: an upper or "acceleration" section 0.2 m wide and 1.5 m long, a middle or "forest" section 1.0 m wide and 2.0 m long consisting of three aluminium plates with a rectangular grid of pre-drilled holes, and a lower or "runout" zone 1.0 m wide and 2.0 m long. The inclination of both the upper and the middle section is 35°, while the lower section is inclined at 10°. The avalanche is released from a container at the top of the upper section. The snow is modelled by glass beads (ballotini) with a diameter of 0.1 mm. The trees are modelled by metal pins that are inserted into the aluminium plates in computer-generated random patterns. The experiments were filmed from above and from the side with a frame rate of 60 fps.

A total of 54 experiments have been carried out: twelve reference experiments without a forest, of which six were carried out at the beginning and six at the end of the study, and 42 experiments with a forest. We have varied the following three parameters: the velocity at which the avalanche hits the forest (incident front velocity), the stem diameter of the trees, and the forest density. The incident front velocity was varied by varying the mass of the avalanche. Three different masses of ballotini were used: 2 kg, 4 kg, and 6 kg. We used two different stem diameters. The metal pins with a diameter of 3.2 mm were used as the thinner trees. For the thicker trees, plastic tubes with an outer diameter of 6 mm were threaded onto the metal pins. The forest density was varied by varying the number of metal pins inserted into the aluminium plates. The forest density is 100% if there is a metal pin inserted into every pre-drilled hole. Four different densities were used: 10%, 25%, 50%, and 90%. We have measured the front velocity and the flow depth of the avalanche along the forest section of the chute by analyzing the films manually frame-by-frame. Further, the runout distance was measured with a ruler straight after each experiment.

We have given a detailed phenomenological description of the flow of the avalanche through

the forest. We have observed two main phenomena that have a braking effect on the avalanche: (1) the creation of large fans in the first row of trees that slow down a large amount of the ballotini and (2) the creation of smaller fans further down the chute that spread the ballotini sideways. The larger the mass of ballotini, the larger the fans. The relative effect of each phenomenon depends on the density of the forest. As the forest density increases from 0% to 100%, the amount of ballotini that are slowed down upon entering the forest increases, while the degree of lateral spreading decreases. The optimal combination of the two phenomena occurs around a forest density of 50%. For a stem diameter of 6 mm, the fans in the first row are larger than for 3.2 mm, while the fans further down the chute are of about the same size as for 3.2 mm. Therefore, the amount of ballotini that are slowed down upon entering the forest is greater for 6 mm than for 3.2 mm, while the degree of lateral spreading is the same for both stem diameters.

We have plotted profiles of the front velocity of the avalanche for both the reference experiments and the forest experiments. The front velocity does not differ significantly between the reference experiments and the forest experiments. Further, we have plotted profiles of the flow depth of the avalanche and compared the flow depth for the different masses, the different stem diameters, and the different forest densities. The flow depth is greatest for a mass of 6 kg, followed by 4 kg and 2 kg, and is greater for a stem diameter of 6 mm than for 3.2 mm. The flow depth increases from the front of the avalanche, attains a maximum, and decreases again towards the tail. For a forest density of 10%, the flow depth both increases and decreases most rapidly. The flow depth is greatest for 10% at first, but after some time, the flow depths for 25% and 50% become greater. For 90%, the flow depth is smallest at all times. We have plotted the runout distance for each experiment as a function of the forest density and fitted quadratic trendlines for each mass and each stem diameter. The runout distance decreases from 0% through to 50%, but increases again slightly from 50% to 90%.

In summary, a forest has a maximum braking effect for forest densities around 50% where trees grow quite densely high up in the avalanche path, slowing down the bulk of the snow, and more openly further down the chute so that the snow can be spread sideways. The braking effect is greatest for mature forests where the trees have larger stem diameters than in younger forests. The larger the avalanche, the greater the braking effect of the forest.

Contents

List of Figures

List of Tables

Chapter 1

Introduction

1.1 Background

Problem formulation

Snow avalanches cause the closure of roads and railways and damage and destroy infrastructure and buildings. Between 2005 and 2015, four people in Norway were killed as houses were hit by snow avalanches. Every year, the Norwegian road authorities (Statens vegvesen) have to close roads either due to avalanching or due to a high risk of avalanching. Most snow avalanches that hit a road will block the road in both directions, isolating entire communities until it is safe to clear the road (Figure 1.1). In 2011, the driver of a snow clearing vehicle was killed by a snow avalanche in the county of Rogaland (NGI).

Figure 1.1: Snow avalanche blocking a road in the county of Troms, March 2014. From: http://www.nordlys.no/nyheter/stort-snoskred-blokkerer-e6/s/1-79-7218872.

Seasonal road closures are an example of passive protection measures, which regulate the presence of people and property in avalanche-prone areas. Other examples are seasonal occupation of houses, warning signs, avalanche forecasting, hazard mapping, and land-use planning. Active protection measures include avalanche control by explosives, snow fences, deviation, retarding, and catching dams, retarding earth mounds, splitting wedges, snow sheds, and tunnels (Figure 1.2). The most expensive measures – snow sheds and tunnels – give the best protection, especially along mountain roads where the largest avalanches occur. Along the coast and in the lowlands, dams, mounds, and wedges can be effective at a cost of only 10-20 %. For details on the different active protection measures and their application in road engineering, see Norem (2014).

(a) Retarding mounds. (b) Snow fences. (c) Snow shed.

Figure 1.2: Examples of active protection measures. From: http://avalancheservices.ca/images/ (1.2a and 1.2b) and http://www.fhwa.dot.gov/publications/publicroads/09julaug/03.cfm (1.2c).

Protection forests are another example of an active protection measure. According to the Protocol for the implementation of the Alpine Convention in the field of mountain forests (1996), "mountain forests [...] provide the most effective, the least expensive, and the most aesthetic protection against natural hazards". In Norway, it has been suggested to use existing mountain forests as protection forests at several locations in the country (Høydal et al., 2013). In this context, it is important to be able to quantify the braking effect trees have on snow avalanches.

The braking effect of trees on snow avalanches can be studied by observing natural avalanches and forested terrain in avalanche-prone areas, by developing theoretical models for snow avalanche dynamics that account for the braking effect of trees, by full-scale experiments with artificial avalanches released by explosives, by medium-scale experiments with large chutes and natural snow, or by small-scale experiments with medium to small chutes and a granular or powder ma-

terial instead of snow. In this master thesis, small-scale experiments will be carried out to study how the presence of a forest affects the flow of the avalanche. The goal of the thesis is to describe the flow phenomenologically and to quantify the front velocity, the flow height, and the runout distance as a function of three key parameters: the incident front velocity of the avalanche, the stem diameter, and the forest density.

Literature survey

Protection forests

Brang et al. (2001) define a protection forest to be "a forest that has as its primary function the protection of people or assets against the impacts of natural hazards or adverse climate". The protective capacity of a forest depends on the type, intensity, and frequency of the natural hazards involved as well as on the tree type, age, and forest structure. Forests can act as a means of protection in different ways depending on their position along the avalanche path. A forest in the starting zone may inhibit avalanche formation, while a forest in the transit or runout zone may decelerate or stop avalanches. In a field campaign in northern Sweden, Breien and Høydal (2014) study how birch forests stabilize the snow pack in avalanche starting zones. They find that in the forested area, there are no persistent weak layers, homogeneous layers are undulating, bent, or broken, and the surrounding snow is anchored to tree stems and low-lying branches by ice (Figure 1.3).

Figure 1.3: Low-lying branches of a birch acting as an anchor on the surrounding snow. From: Breien and Høydal (2014).

As part of the project "Evaluation of landslide hazards in forested terrain" ("Vurdering av skredfare i skogsbestander"), a collaboration between the Norwegian Geotechnical Institute (NGI) and the Norwegian Water Resources and Energy Directorate (NVE), Høydal et al. (2013) have published criteria for coniferous forests in the starting zone (Table 1.1). Most coniferous forest stands in Norway fulfill those criteria. Berger et al. (2013) have published criteria for protection forests in the European Alps (Table 1.2).

Table 1.1: Threshold values for protection forests, as given by Høydal et al. (2013) (starting zone only, coniferous forests).

Parameter	Threshold value
Gap size in the direction of the slope:	30°: < 50 m
	35-40°: < 40 m
	40-45°: < 30 m
Canopy cover	50%
Diameter at breast height (DBH)	> 12 cm
Tree height	> 5 m

Table 1.2: Threshold values for protection forests, as given by Berger et al. (2013). The acronyms H and DBH refer to the height and diameter at breast height of the trees, respectively.

Parameter	Threshold value
Proportion of deciduous trees and larch	
- in the starting zone:	< 30%
- in the transit and runout zones:	> 70% along corridor edges
	> 30% otherwise
Gap size	
- in the direction of the slope:	< 1.5 times the average tree height
- perpendicular to the slope:	< 15 m
Canopy cover	30°: > 30%
	35°: > 50%
	> 40°: > 70%
Coefficient of stability (H/DBH)	Coniferous forests: H/DBH < 65
	Broad-leaves: H/DBH < 80
Tree height	> twice the height of the snow cover
Crown height on the edges of gaps	> 2/3 H

Theoretical models for the braking effect of trees on snow avalanches

Different approaches have been used to model snow avalanche flow. The Voellmy-Salm model (Voellmy, 1955; Salm et al., 1990) is one of the oldest dynamical models. The motion of the avalanche is assumed to be governed by gravitational forces and two types of frictional forces: a Coulomb, or bed, friction, and a velocity dependent friction. Assuming that the mass of the avalanche is constant, the acceleration of an avalanche along its path is given by $a_{VS} = g\sin\alpha - \left(\mu g\cos\alpha + \frac{g}{\xi h}u^2\right)$, where μ and ξ are constants, α is the slope angle, and h and u are the flow height and velocity of the avalanche, respectively. Many 1D and 2D models based on the Voellmy-Salm approach have been implemented, for example AVAL-1D (Christen et al., 2002) and RAMMS (Christen et al., 2010).

Forests may act as a brake to avalanche flow in two different ways: either the avalanche may lose energy in breaking tree trunks and branches, overturning trees, and entraining woody debris and root plates, or the trees may act as rigid obstacles to the flow. The processes in the former case have been modelled by Bartelt and Stöckli (2001) and Feistl et al. (2015) ("friction approach"). A model for the latter case is presented in Feistl et al. (2014) and Teich et al. (2013) ("detrainment approach").

Bartelt and Stöckli (2001) derive formulae for the deceleration of an avalanche with mean flow density ρ_a, height h, and length l due to fracturing of trunks and branches (a_{ft} and a_{fb}), overturning (a_o), and entrainment of trees (a_{et}). Accounting for trunk fracturing and entrainment of trees, the acceleration of the avalanche is given by

$$\begin{aligned} a &= a_{VS} + a_{ft} + a_{et} \\ &= g\sin\alpha - \left(\mu + \underbrace{\frac{u_f \pi r_t^2}{\rho_a h l d_w d_l}\frac{1}{g\cos\alpha}}_{\Delta\mu}\right) g\cos\alpha - \left(\frac{g}{\xi h} + \underbrace{\frac{m_t}{\rho_a h l d_w d_l}}_{\Delta\frac{g}{\xi h}}\right) u^2, \end{aligned} \tag{1.1}$$

where u_f is the bending fracture energy per cross-sectional area, r_t is the radius of a tree trunk, m_t is the mass of a tree, and d_l and d_w are the mean tree spacing respectively in the direction of flow and perpendicular to the flow.

Feistl et al. (2014) derive formulae for the volume of snow deposited behind trees or groups

of trees and an average deposition height that depends on the forest structure. The momentum of the detrained mass per unit area is instantaneously subtracted from the total momentum of the avalanche flow: $\rho_a \frac{dh_d}{dt} \|\mathbf{u}\| = K$, where $\mathbf{u}$ is the velocity of the avalanche. The parameter K is calibrated by linking observed mean deposition heights to forest characteristics. Typical values for K are 10-100 Pa (Teich et al., 2013).

The Norwegian model (Bakkehøi et al., 1983) is a statistical method based on a data set of 206 registered snow avalanches where the runout distance of an avalanche is expressed in terms of an angle $\alpha = 0.96\beta - 1.4°$, with α and β as in Figure 1.4. Anderson and McClung (2012) present a probabilistic model for avalanches that start in timber-harvested terrain. For a non-exceedance probability P, the angle α is given by $\alpha(P) = \left(\mu - \frac{\sigma}{k}\right) + \frac{\sigma}{k}\left(\frac{P}{1-P}\right)^k$, where $\mu = 30.5°$, $\sigma = 1.78°$, and $k = -0.06$.

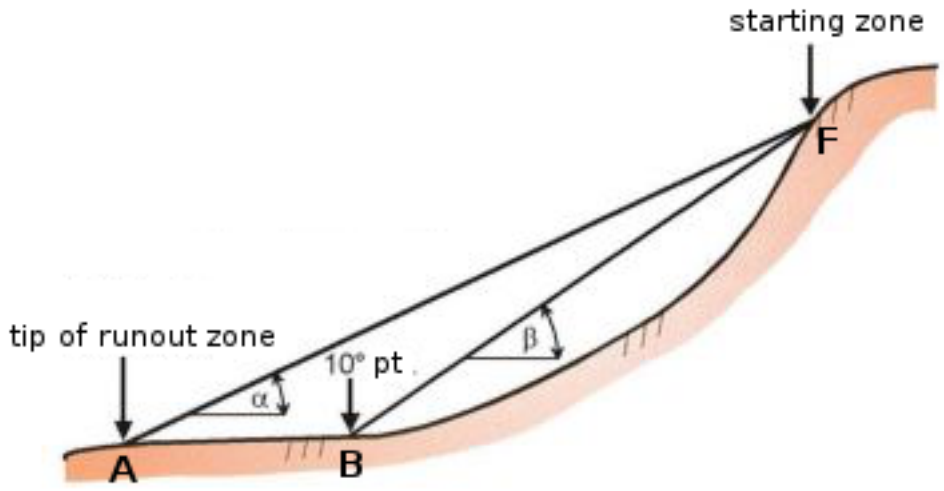

Figure 1.4: Definition of the angles α and β in the Norwegian model. Adapted from: Lied and Kristensen (2003).

A case study of an avalanche that partly ran through forested and partly through unforested terrain is presented in Takeuchi et al. (2011). The trees had an average height of H = 15.5 m and a stem diameter at breast height of DBH = 0.38 m. 9.2% of the trees were uninjured, 36.9% were upright with only the branches broken, 8.5% were leaning, 10% were broken and fallen, and 35.4% were stumps without fallen trunks or fallen trunks without stumps. The speed of the avalanche flowing into the forest was estimated to be 26-31 ms^{-1}. In a presentation at DACA-

13 in Davos, Switzerland, Y. Takeuchi quantifies the braking effect of the forest by simulating the avalanche for a large range of Coulomb bed friction angles ϕ_{bed} and comparing the output velocity profiles to the observed velocity profiles. The best fits for respectively the forested and the unforested part of the terrain were given by $\phi_{\text{bed}} = 13 - 14°$ and $\phi_{\text{bed}} = 24 - 26°$. The Swiss guidelines recommend that the velocity dependent friction coefficient ξ should be halved while the Coulomb friction coefficient μ is not changed.

Physical modelling of snow avalanche flow around obstacles

A large number of small-scale experimental studies on snow avalanche flow have been published. Powder snow avalanches have been modelled by for example Bozhinskiy and Sukhanov (1998), while Hutter and Koch (1991), Hutter et al. (1995), Greve and Hutter (1993), Wieland et al. (1999), Pouliquen (1999), Pouliquen and Forterre (2002), and Iverson et al. (2004), for example, have modelled granular snow avalanches. In particular, Gray et al. (2003), Hákonardóttir et al. (2001), Faug et al. (2003), Brateng (2005), and Hauksson et al. (2007) have studied the flow of granular snow avalanches around obstacles: a pyramid (Gray et al., 2003), braking mounds and a dam (Hákonardóttir et al., 2001), a dam (Faug et al., 2003), braking mounds, collecting dams, and diverting dams (Brateng, 2005), and cylinders and rectangular blocks (Hauksson et al., 2007).

For the granular material, Gray et al. (2003) use plastic pellets 2-3 mm in size, while Hákonardóttir et al. (2001), Faug et al. (2003), Brateng (2005), and Hauksson et al. (2007) use spherical glass beads (ballotini) 0.1 mm in size.

Gray et al. (2003) carry out two series of experiments using a plane chute inclined at respectively 42° and 34°. In the first series, the pyramid is placed with one of its corners pointing upslope, and in the second with one of its corners pointing downslope. With the pyramid pointing upslope (inflow Froude number: 5.79), oblique shocks are observed on the lateral sides of the pyramid. Two expansion waves form on the lee side, and a grain-free region opens up. With the pyramid pointing downslope (inflow Froude number: 3.82), the grain-free region is narrower. A normal shock propagates upslope from the blunt face of the pyramid, creating a dead zone that diverts the flow around the pyramid. The steady state for both experiments is shown in Figure 1.5. Gray et al. (2003) simulate their experiments using a hydraulic model.

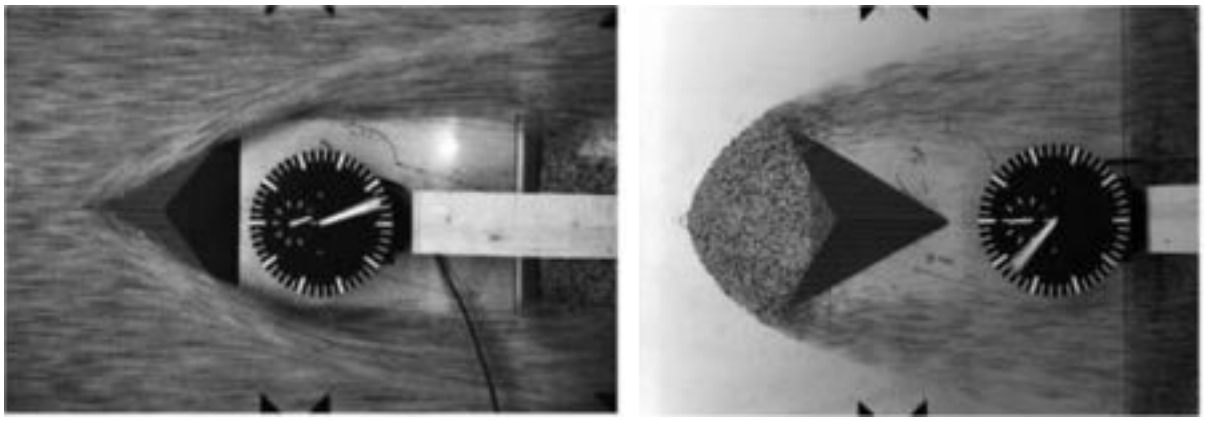

Figure 1.5: Steady state of the granular flow around a pyramid with the pyramid pointing upslope (left) and downslope (right). From: Gray et al. (2003).

Hákonardóttir et al. (2001), Faug et al. (2003), and Brateng (2005) use a chute consisting of two plane sections: an upper section with an inclination of up to 45° where the granular material is accelerated to a constant speed, and a lower section, or runout zone, with a smaller slope. Hákonardóttir et al. (2001) and Faug et al. (2003) place the obstacles at the top of the lower section, while Brateng (2005) places them at different locations on the lower section and at different angles. The setup used by Hákonardóttir et al. (2001) is shown in Figure 1.6.

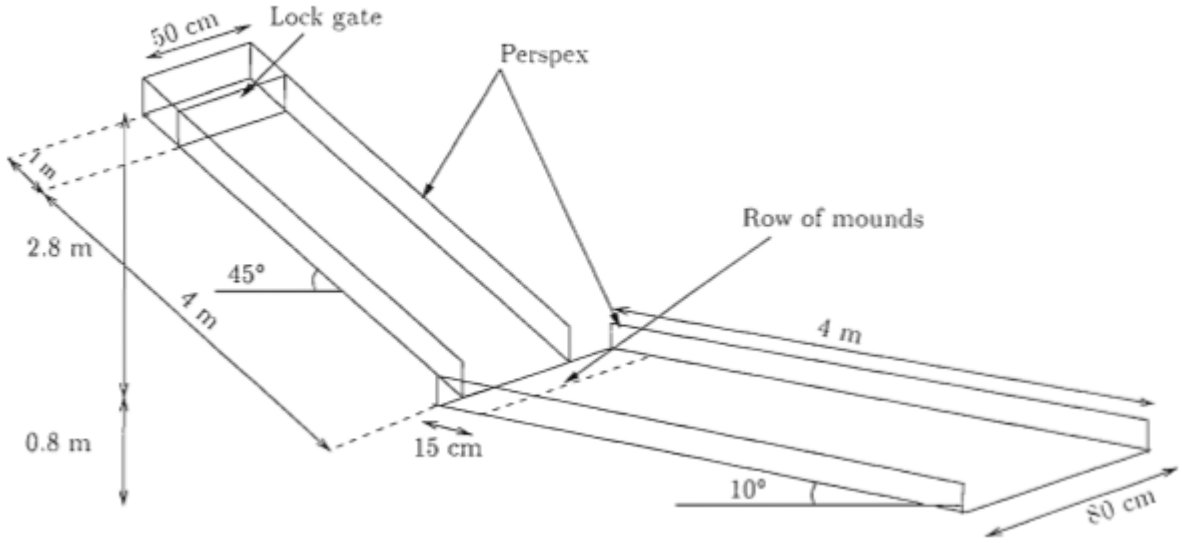

Figure 1.6: Setup for an experimental series with a plane chute with two sections. From: Hákonardóttir et al. (2001).

Faug et al. (2003) observe two types of local effects of the dam: the formation of a dead zone upstreams of the obstacle and a jet whereby a stream of particles is launched from the top of the obstacle and lands back on the chute further downstreams. Faug et al. (2003) plot the lengths of respectively the dead zone and the jet as a function of the dam Froude number $\mathrm{Fr}_{obs} = \frac{u}{\sqrt{g h_{obs}}}$ and find that the lower the Froude number, the longer the dead zone, and the higher the Froude number, the longer the jet. Three flow regimes are defined: one that is dominated by the detrainment of material in the dead zone, one that is dominated by local energy dissipation linked to the jet formation, and an intermediate regime. For each of the three regimes, Faug et al. (2003) derive formulas for the normalized runout length x/x_0 as a function of the normalized obstacle height h_{obs}/h, where x and x_0 are the runout lengths for respectively the experiment in question and a control experiment with no obstacles and h_{obs} and h are respectively the obstacle height and the maximum flow depth at the location of the obstacle for the control experiment.

Like Faug et al. (2003), Hákonardóttir et al. (2001) observe the formation of a jet, and derive an equation for the trajectory of a jet as a function of the throw angle and the throw velocity. In order to estimate the energy dissipated upon impact with the obstacle, the ratio $\frac{u_1}{\sqrt{u_0^2 - 2gh_{obs}}}$, where u_0 and u_1 are the flow velocity before and immediately after impact, is plotted against the normalized obstacle height. Plotting x/x_0 against h_{obs}/h, Hákonardóttir et al. (2001) find that obstacle heights greater than twice the flow depth do not further reduce the runout length. Hákonardóttir et al. (2001) also find that many narrow obstacles lead to a greater reduction in runout length than fewer, wider obstacles with the same cross-sectional area.

Brateng (2005) plots profiles of the specific energy $z + \frac{u^2}{2g}$ in order to estimate how much energy is dissipated upon impact with the obstacles. The slope of the energy line is assumed to be the sum of a Coulomb friction term, a velocity dependent term, and singular losses, for example due to the impact with an obstacle. Without obstacles, the energy line is found to be fairly straight, indicating that Coulomb friction is dominant. Brateng (2005) finds that braking mounds are most efficient further up, while dams are most efficient further down the runout zone. The mounds' efficiency increases with increasing height of the mounds up to three times the flow depth.

Hauksson et al. (2007) use a plane chute inclined at an angle of 34°. A single obstacle, a slender rectangular block or a cylinder of different dimensions, is placed close to the bottom

of the chute. Hauksson et al. (2007) measure the impact force F of rapid granular flow (Froude number: 13) and compute the dynamic drag coefficient $C_D = \frac{F}{\frac{1}{2}\rho_a A \bar{u}^2}$, where A is the projected area of impact and $\bar{u}$ is the depth-averaged steady state flow velocity. It is found that C_D is in the range 0.7-0.85 for rectangular blocks and in the range 0.5-0.55 for cylinders for obstacle heights greater than about three times the flow depth.

Figure 1.7 shows the granular material being thrown upwards and to the sides in a fan-shaped pattern upon impact.

Figure 1.7: Fan-shaped stream of granular material around a slender cylindrical obstacle. From: Hauksson et al. (2007).

What remains to be done?

To the author's knowledge, no experimental studies on the braking effect of a group of cylindrical obstacles exist. Neither the model for breaking and entrainment of trees by Bartelt and Stöckli (2001) nor the model for detrainment of snow behind trees by Feistl et al. (2014) has been verified by laboratory experiments. The probabilistic model by Anderson and McClung (2012) has not previously been applied to laboratory studies. The existing models have been developed on the basis of field data. An experimental study will shed light on the physical processes involved under controlled circumstances, and the data may be used to calibrate existing and develop new models.

1.2 Objectives

The main objective of this master thesis is to carry out an experimental laboratory study on the braking effect of trees on snow avalanches and to analyze the results. The objectives are to

1. carry out a series of small-scale chute experiments where the incident front velocity, the stem diameter of the trees, and the forest density are varied and the front velocity, the flow height, and the runout distance are measured

2. give a phenomenological description of the flow of the avalanche through the forest

3. quantify the front velocity, the flow height, and the runout distance as functions of the incident front velocity of the avalanche, the stem diameter, and the forest density

1.3 Approach

The chute experiments will be carried out at the pile laboratory at NTNU's Department of Civil and Transport Engineering. The design of the chute was originally proposed in Kahrs (2015) and adapted according to the dimensions of existing and commercially available components as well as to allow a greater range of experiments. The experiments will be filmed by two cameras set to 60 frames per second from the top and from one side, and the resulting videos will be analyzed manually frame-by-frame to determine the front velocity and the flow height of the avalanche with the help of a distance scale drawn onto respectively the bottom of the chute and onto a number of trees. The runout distance will be measured straight after each experiment using a ruler (Objective 1). Objective 2 will be met by observing the flow of the avalanche frame-by-frame as it passes through the forest. Profiles of the front velocity and the flow height will be plotted, and the runout distance will be plotted as a function of the key parameters incident front velocity, stem diameter, and forest density (Objective 3).

1.4 Limitations

The conditions at NTNU's pile laboratory are out of the author's control. As the laboratory is normally used for experimental studies on piles, the chute is set up on top of a large container of dry sand. The surfaces in the laboratory are covered with dust and grains of dry sand. The air at the laboratory is very dry, while the temperature is around 20°C. Both the relative humidity and the temperature vary within one day and from day to day. This limits the repeatability of the

experiments. All measurements are done manually, limiting their accuracy. The front velocity is computed based on distance measurements with a precision of 1 cm, the flow depth is read off from a scale with a precision of 1 mm and 5 mm, and the runout distance is measured with a precision of 5 mm. This limits the precision of the measurements.

1.5 Structure of the thesis

The rest of the thesis is structured as follows. Chapter 2 gives an overview of snow avalanche terminology, characteristics, and formation. In Chapter 3, a dynamical model for snow avalanche flow is presented. In analogy with hydrodynamics, laws governing open channel flow and the flow around cylindrical obstacles are given. In Chapter 4, we present the setup of the model including the filming equipment, the technique to measure raw data, and the experiments to be carried out. In Chapter 5, the raw data from the experiments is analyzed.

Chapter 2

Phenomenological background of snow avalanches

With minor changes, this chapter is taken from (Kahrs, 2015). In this chapter, we give an overview of snow avalanche terminology, types of snow avalanches, snow avalanche formation, and avalanche-prone terrain in general and in Norway in particular. Unless otherwise cited, the contents of this chapter are based on McClung and Schaerer (2006).

2.1 Terminology

By definition, a *snow avalanche* is a mass of snow that slides, tumbles, or flows down an inclined slope. Avalanche movement occurs along an *avalanche path* (Figure 2.1). The *starting zone* or *release zone* is the point or area where an avalanche releases. Upon release, the avalanche accelerates and moves through the *transit zone* or *track*, where it attains its maximum speed. The track is characterized by minimal deposition of snow. On the contrary, an avalanche can entrain snow mass up to ten times its initial mass. Initial masses range from 10 to 100000 t. In the *runout zone*, the avalanche quickly decelerates and stops, depositing debris. The *runout distance* is the horizontal distance from the top of the release zone to the tip of the runout zone.

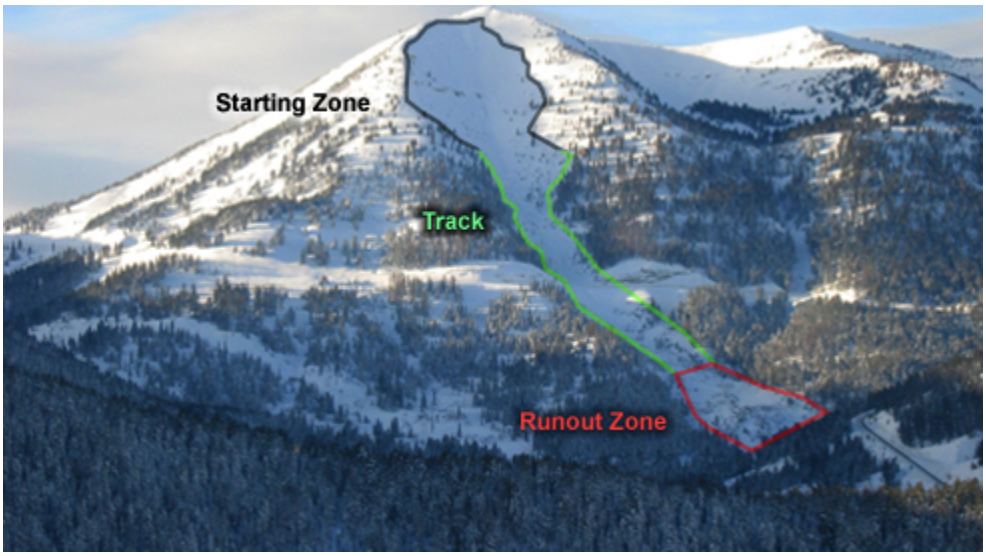

Figure 2.1: An avalanche path with a starting zone, a transit zone, and a runout zone. From: www.meted.ucar.edu/afwa/avalanche/.

An avalanche path can have multiple starting zones, transit zones, and runout zones. Figure 2.1 shows the definition of the starting, transit, and runout zones for the largest avalanche possible in a particular avalanche path.

2.2 Classification of snow avalanches

Snow avalanches may be classified into *loose-snow avalanches* and *slab avalanches* (Figure 2.2). Loose-snow avalanches start from a single point and consist of cohesionless surface or near-surface snow. They sweep out more surface snow as they move down the slope and have a triangular shape. Most slab avalanches form as a weak layer in the snowpack fails. The snowpack fractures at the top of the starting zone (crown), and a rectangular slab consisting of a cohesive layer of snow begins to slide down the slope along the bed surface as the fractures propagate along the left and right sides of the slab (flanks). At the lower end of the slab, a wedge-like fracture surface forms (stauchwall). The bed surface may coincide with the weak layer along which the original failure occurred, or the avalanche may sweep out a deeper slab as it moves down the slope. The initial height of the slab is usually between 0.5 and 2.0 m. Usually, the volume of slab avalanches is between 100 and 100000 m^3, but may be up to 1000000 m^3 and more (Norem, 2014).

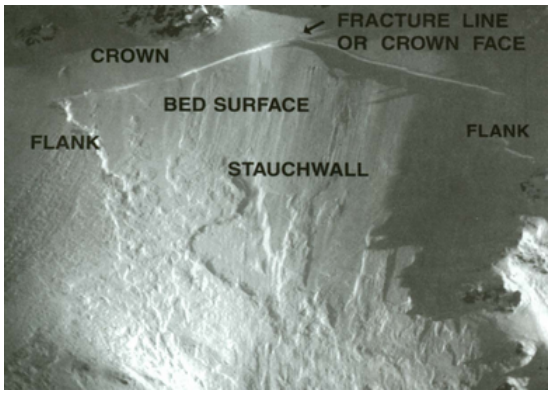

Figure 2.2: A slab avalanche with crown, flanks, and stauchwall. From: http://ffden-2.phys.uaf.edu/311_fall2004.web.dir/Jennifer_March/avybasics.htm.

Another way of classifying snow avalanches is by the water content of the snow, measured in % per volume. Dry, moist, wet, and very wet snow avalanches have water contents of respectively 0%, 0-3%, 3-8%, and 8-15%. Slush has a water content of more than 15%.

In general, a slab avalanche consists of three main components: a *dense core* of rounded particles with a diameter of the order of centimetres to metres, a *saltation layer* or *fluidized layer* of particles up to 50 cm in diameter, and a *suspension layer* or *powder cloud* of particles 0.1 mm to 1-2 mm in diameter (Figure 2.3). As a rule of thumb, the densities of the three layers are about 300 kg/m^3, 30 kg/m^3, and 3 kg/m^3 (Issler, 2004). A wet slab avalanche may consist of only a dense core. The destructive potential of a snow avalanche depends on its density and its speed. Wet slab avalanches have a high density, but generally move at speeds lower than 40 ms^{-1}. Dry slab avalanches, with a speed of up to 60-70 ms^{-1}, cause most damage and fatalities.

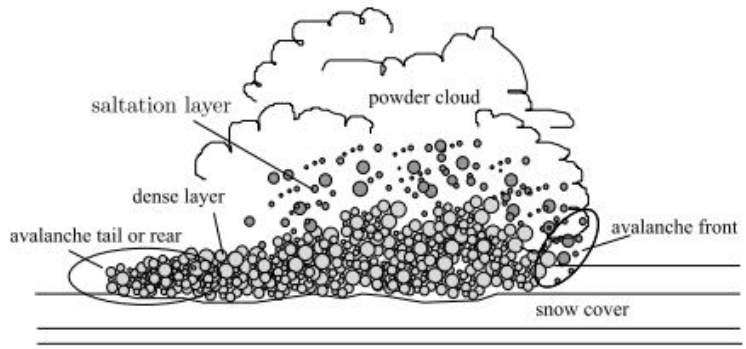

Figure 2.3: A mixed avalanche has three main components: the dense core, the saltation layer and the powder cloud. From: Sovilla (2004).

2.3 Avalanche formation

For both loose-snow and slab avalanches, initial failure is in shear. The shear strength of a snowpack depends on its cohesion and its internal friction.

Bond formation

Cohesion is a measure of how well snow grains and individual layers are bonded to each other. The rate of bond formation increases rapidly with increasing snow temperature. In maritime snow climates, which are characterized by heavy snowfall and relatively high temperatures, avalanches occur during or immediately after snow storms as the fresh snow quickly stabilizes. Rain, however, can melt bonds, lubricate the bed surface, and cause major avalanching. The meltwater can refreeze to ice, forming future sliding surfaces. Continental climates are characterized by relatively low snowfall and low temperatures. In such climates, bond formation is slow, and weak layers persist.

Persistent forms

Those weak layers may consist of depth hoar, surface hoar, or facets, so-called persistent forms. The persistent forms in layers form due to high temperature gradients (10°C/m) between the surface of the snow and the surrounding air (surface hoar), the bottom of the snowpack and the ground (depth hoar), or across near-surface layers. Surface hoar forms when moist air above a cold snow surface becomes oversaturated with water vapour. The vapour condenses on the snow surface, leading to the growth of feathery crystals. Depth hoar consists of large cup crystals that form as water vapour migrates from the warm ground upwards through the cold snowpack and condenses. Orientation to the sun is important as it influences incoming radiation. The balance between short- and longwave radiation can cause rapid temperature changes near the surface and large temperature gradients across the top few centimetres of the snowpack. This leads to so-called radiation crystallization at the surface. Several centimetres below the surface, the snow may melt and later refreeze to form an ice crust. Being impermeable to water vapour, this ice crust allows faceted crystals to grow immediately below the crust. Figure 2.4 shows an ice crust with a layer of faceted crystals above and below.

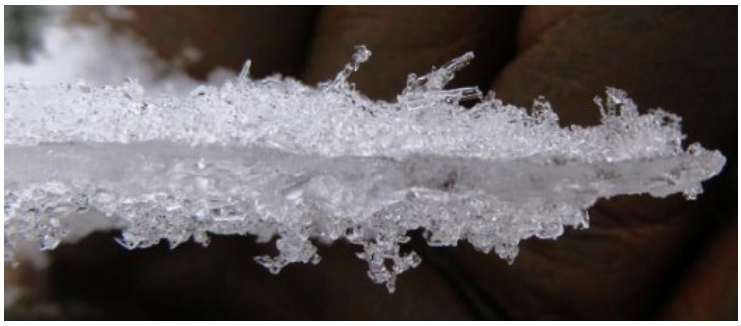

Figure 2.4: An ice crust with a layer of faceted crystals above and below. From: http://www.cnfaic.org/observations/fotogallery.php?id=p2640.

Persistent forms have low shear strength, but can remain unstable over long periods of time because they are resistant to vertical deformation.

Deformation and fracture mechanism

In general, deformation in the snowpack occurs in tension, in compression, and in shear. Figure 2.5 shows how deformation of the snowpack decomposes into a component of compression and a component of shear deformation. The steeper the slope, the larger the component of shear deformation.

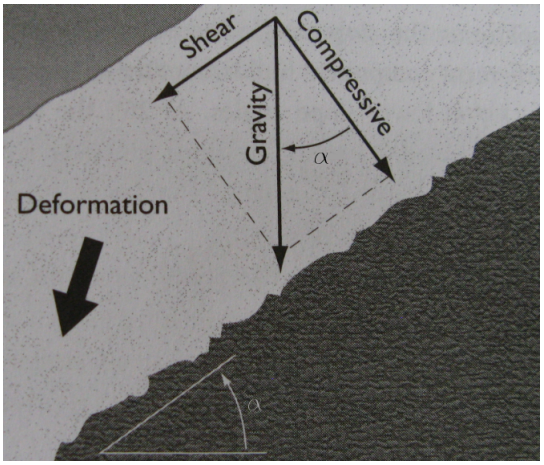

Figure 2.5: Decomposition of snowpack deformation into a component of compression and a component of shear deformation. From: McClung and Schaerer (2006).

Snow deforms readily under its own weight as it often is within more than 95% of its melting temperature (in K). It creeps like a viscous fluid, and the higher the temperature, the more

important viscous effects become. Brittle fractures cannot occur in snow unless the deformation rate exceeds 100 times the deformation rate under ordinary creep. Persistent forms are extremely prone to propagating shear fractures. In wet snow, the energy required to propagate brittle shear fractures is extremely high. With slush in the failure layer, the slab avalanche release mechanism changes from brittle shear fracture propagation to glide-induced tensile fracture. Loose-snow avalanches release when the slope angle is greater than the snow's angle of repose, which depends on the type of snow as shown in Figure 2.6.

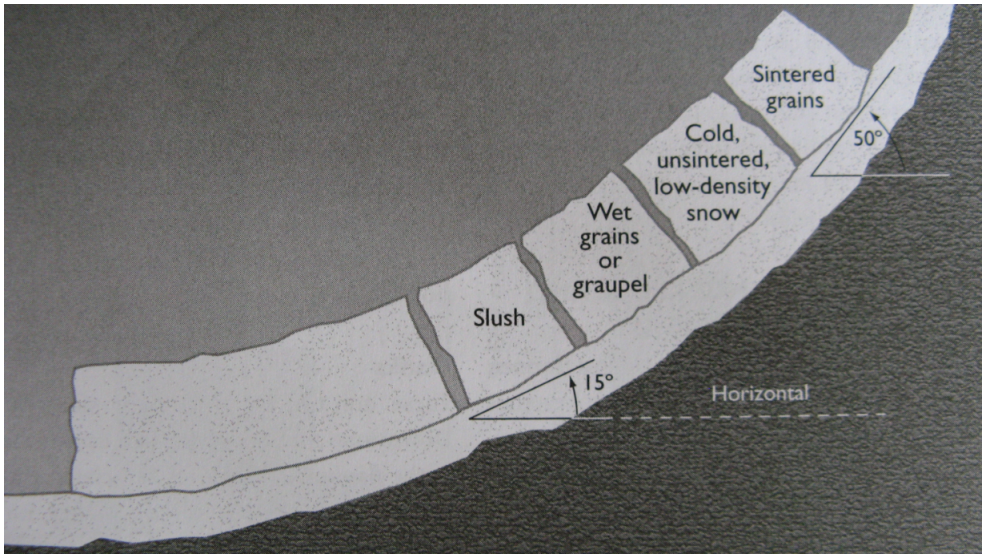

Figure 2.6: The snow's angle of repose depends on the type of snow. From: McClung and Schaerer (2006).

McClung and Schaerer (2006) give the following guidelines for starting zone inclines:

60-90°: frequent snow sluffs

30-60°: dry loose-snow avalanches

45-55°: frequent small slab avalanches

35-45°: slab avalanches of all sizes

25-35°: infrequent large slab avalanches, wet loose-snow avalanches

10-25°: infrequent wet slab avalanches, slush flows

Redistribution of snow

Often, an avalanche is triggered by the addition of snow load to the top of the snowpack. Snow can either be added to the snowpack directly from precipitation or as drifting snow. Redistribution of snow by wind is a major feature of mountain snowpacks. The redistribution of snow depends strongly on the local topography and the exposure to wind. In general, snow is picked up on the windward side of ridges and deposited on the lee side of ridges, in gullies, and in notches. Figure 2.7 shows a pattern of cross-loading, gully, and notch deposition depending on the prevailing wind direction. Wind speeds of 5 m/s are sufficient to pick up loose, unbonded snow, but may exceed 25 m/s for dense, bonded snow.

Figure 2.7: Redistribution of snow depending on the prevailing wind direction. From: McClung and Schaerer (2006).

2.4 Avalanche-prone terrain

When assessing whether or not a location is a potential release zone for snow avalanches, what type of snow avalanches may occur, and how large those avalanches may be, the following factors are important (Norem, 2014):

- slope inclination
- wind exposure and amount of precipitation
- topography

– ground roughness and vegetation cover

– orientation to the sun

In Norway, the counties of Møre og Romsdal, Sogn og Fjordane, and Hordaland along the western coast, Nordland, Troms, and Finnmark along the northern coast, and Telemark in the central part of the country are particularly prone to snow avalanching. Figure 2.8 shows a map of Norway with potential release and runout zones of snow avalanches.

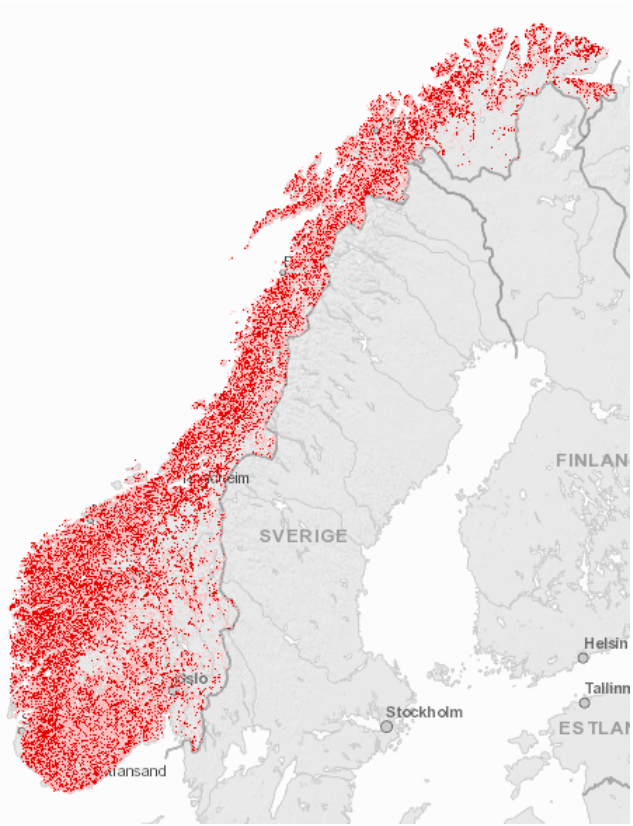

Figure 2.8: Potential release and runout zones of snow avalanches in Norway. From: atlas.nve.no.

Chapter 3

Theoretical background

The large-scale behaviour of a snow avalanche is commonly approximated by the flow of a continuous homogeneous fluid. In this chapter, we introduce concepts from fluid dynamics and apply those to snow avalanches. In Section 3.1, a dynamical model for snow avalanche flow is derived. This section is based on lecture notes by Issler (2004) and on Norem (2014) and is partly taken from Kahrs (2015). As the avalanche moves down the avalanche path, potential energy is converted to kinetic energy. Energy may be lost due to friction and in collision with obstacles. This may be visualized by means of an energy line, a concept introduced in Section 3.2. This section is based on Olsen (2015). In Section 3.3, two numbers that govern the behaviour of fluid flow, the Froude number and the Reynolds number, are introduced. This section is based on lecture notes by Øivind Arntsen for the course TVM4116 Fluid mechanics, taught at NTNU in the autumn semester of 2014. The flow of a snow avalanche through a forest may be viewed as the flow of a fluid around cylindrical obstacles. The basic case, one isolated cylinder, is based on Moe (2014). A review on fluid flow around a pair of circular cylinders has been published by Sumner (2010). Fluid flow around groups of three and four cylinders has been studied by for example Tatsuno et al. (1998) (three cylinders) and Lam et al. (2003a), Lam et al. (2003b), Lam and Zou (2007), and Lam et al. (2008) (four cylinders). Nicolle and Eames (2011) study fluid flow through and around a circular array of cylinders. The case of multiple cylinders is based on the latter. In Section 3.4, possible flow regimes are described. Finally, in Section 3.5, we derive a formula for the longitudinal force on cylindrical obstacles.

3.1 The Voellmy-Salm model

In this section, we derive a generic point-mass model for snow avalanche dynamics and its extension to one dimension. The Voellmy-Salm model is given as an example.

3.1.1 The Voellmy-Salm model as a point-mass model

One should note that point mass models indicate the runout distance for the avalanche's centre of mass, not the front of the avalanche. Point-mass models assume that the length of the avalanche is small compared to the length of the avalanche path. The avalanche is represented by a point mass m moving along the avalanche path.

By Newton's Second Law, the rate of change of momentum of m is equal to the sum of the forces acting on m:

$$ma + u\frac{dm}{dt} = \frac{d(mu)}{dt} = F_g - F_r, \tag{3.1}$$

or

$$a = \frac{1}{m}\left(F_g - F_r - u\frac{dm}{dt}\right), \tag{3.2}$$

where u and $a = \frac{du}{dt}$ are the velocity and acceleration of m averaged over the avalanche, and F_g and F_r are the gravitational and the resistive forces acting on m along the avalanche path (Figure 3.1). The term $u\frac{dm}{dt} = uq$ represents the change of momentum due to snow mass entrainment or detrainment. Here, we assume that $q = 0$.

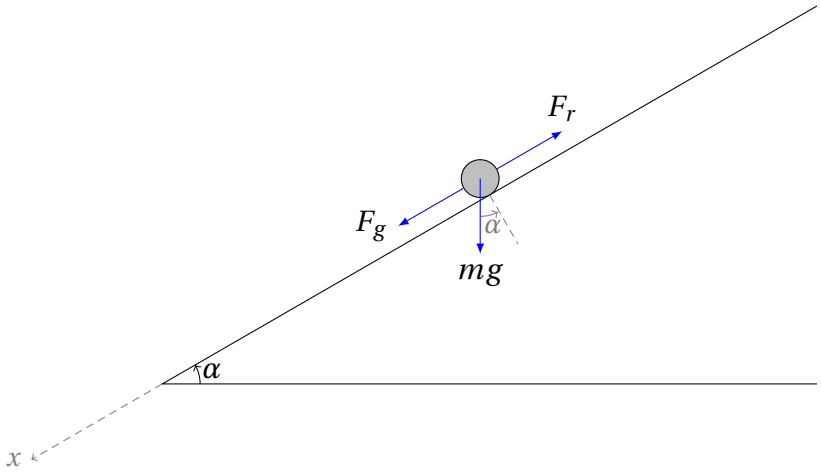

Figure 3.1: Setup of the point mass model.

The gravitational force is given by $F_g = mg\sin\alpha$, where α is the slope of the avalanche path. The resistive force F_r is usually expressed as the sum of a Coulomb friction term $F_c = mg\left(c + \mu\cos\alpha\right)$, where it is assumed that the snow behaves like a Mohr-Coulomb granular material with cohesion $c = 0$ and a bed friction coefficient μ between 0.25 (dry snow) and 0.6 (moist or wet snow), and a velocity-dependent term F_d. For F_d, different models exist. Often, those models are based on hydrodynamics. The Voellmy-Salm model (Voellmy, 1955; Salm et al., 1990), which assumes that a snow avalanche behaves like fluid flow in an open channel, is one of them:

$$F_r = F_c + F_d = mg\left(\mu\cos\alpha + \frac{u^2}{\xi h}\right), \tag{3.3}$$

where ξ is a constant with units ms^{-2}, and $h = h(x)$ is the height of the avalanche at position x. Assuming that the avalanche path is sufficiently long, m will reach a terminal velocity u_∞ and a corresponding runout distance x_∞ given by

$$u_\infty = \sqrt{\xi h_\infty\left(\sin\alpha - \mu\cos\alpha\right)} \tag{3.4}$$

and

$$x_\infty = \frac{\xi h_\infty}{2\mu g}\cos\alpha\left(\tan\alpha - \mu\right). \tag{3.5}$$

At the point where $u = u_\infty$, $F_r = F_g$ and

$$\frac{u}{\sqrt{gh\cos\alpha}} = \sqrt{\frac{\xi}{g}\left(\tan\alpha - \mu\right)}, \tag{3.6}$$

where $\mathrm{Fr} = \frac{u}{\sqrt{gh\cos\alpha}}$ is the Froude number (see Section 3.3).

As the terminal height h_∞ of the avalanche depends on the initial height h_0, a good estimate of h_0 is essential for this model. The Voellmy-Salm model is sensitive to the choice of parameters μ and ξ, and widely different combinations of parameters can result in the same runout distance computed. According to Norem (2014), the value for the runout distance x_∞ is most sensitive to the choice of μ, while the value of the terminal velocity u_∞ is most sensitive to the choice of ξ. Due to very limited data on avalanche speed and runout distances, the choice of parameters remains uncertain (Issler, 2004). Buser and Frutiger (1980) propose $\mu = 0.157$ and $\xi = 1067\ \mathrm{ms}^{-2}$

based on the back-calculation of ten extreme avalanche events.

3.1.2 The Voellmy-Salm model as a 1D model

For 1D models, the length of the avalanche is no longer considered negligible. Instead, the avalanche is divided into a number N of blocks (Figure 3.2).

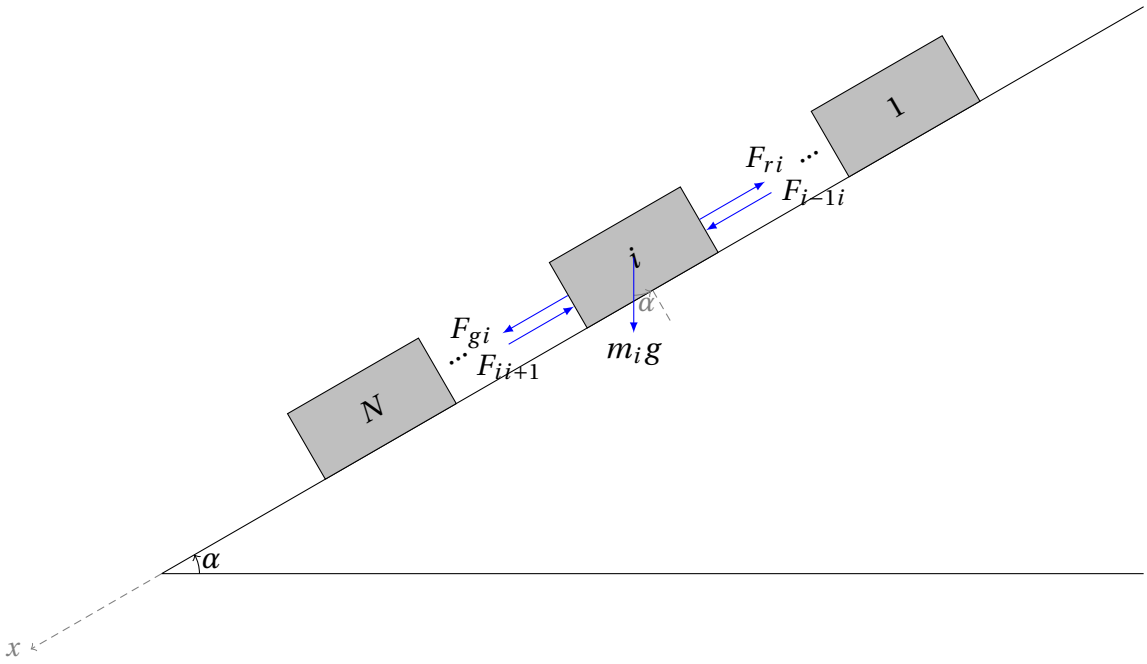

Figure 3.2: Setup of the 1D model.

The acceleration of block i is given by

$$a_i = \frac{1}{m_i}\left(F_{gi} - F_{ri} - v_i q_i + F_{i-1i} - F_{ii+1}\right), \tag{3.7}$$

where F_{i-1i} is the force exerted by block $i-1$ on block i and the other terms are as defined for the point mass model in Section 3.1.1. The force F_{i-1i} is modelled as the resultant of a hydrostatic pressure at the interface between blocks $i-1$ and i, adjusted by a factor λ_i to account for the fact that snow is not a perfect fluid:

$$F_{i-1i} = \rho_i \lambda_i \frac{h_{i-1/2}^2}{2} w_i g \cos\alpha, \tag{3.8}$$

where $h_{i-1/2}$ is the height at the interface, h_i and w_i are the height and the width of block i, and

ρ_i is the density of the snow in block i. In the following, it is assumed that $w_i = w$ and $\rho_i = \rho$ are constant. By considering conservation of mass and momentum for each block, two differential equations are derived:

$$\begin{aligned} \frac{\partial h}{\partial t} + \frac{\partial (hu)}{\partial x} &= q \\ \frac{\partial (hu)}{\partial t} + \frac{\partial \left(hu^2\right)}{\partial x} &= -g\frac{\partial}{\partial x}\left(\lambda \frac{h^2}{2}\cos\alpha\right) \\ &\quad + gh\left(\sin\alpha - \mu\cos\alpha\right) - \frac{g}{\xi}u^2 \end{aligned} \tag{3.9}$$

The model assumes that the entrained or detrained snow mass has zero velocity.

The 1D model can be extended to two dimensions. There are many implementations of both 1D and 2D models. Two of those are the packages AVAL-1D (1D, Christen et al. (2002)) and RAMMS (2D, Christen et al. (2010)).

3.2 The energy line

Since the height of a snow avalanche is small compared to its length and width, many dynamical models for snow avalanche flow use a depth-averaged velocity profile. This justifies the application of Bernoulli's equation for uniform fluid flow:

$$\frac{u_1^2}{2g} + \frac{p_1}{\rho g} + z_1 = \frac{u_2^2}{2g} + \frac{p_2}{\rho g} + z_2 + h_L, \tag{3.10}$$

where u_1, p_1, z_1 and u_2, p_2, z_2 are the flow velocity, the fluid pressure, and the elevation above an arbitrary reference level at points 1 and 2, respectively. The terms $\frac{u^2}{2g}$, $\frac{p}{\rho g}$ and z are called the velocity head, the pressure head, and the elevation head, respectively. The difference in total head at points 1 and 2 is equal to the head loss h_L, which consists of frictional losses h_f and singular losses h_s. Considering snow avalanches, $h_f = \mu\cos\alpha + \frac{u^2}{\xi h}$ per unit length of the avalanche path with the Voellmy-Salm approach. A singular loss h_s of the form $K\frac{u^2}{2g}$, where K is a constant, may occur as the avalanche hits an obstacle in the avalanche path. The effect of multiple obstacles is not generally equal to the sum of the effects of each single obstacle as obstacles may interact. In a forest, one would expect there to be a singular loss at each tree due

to the avalanche hitting the tree, but one would also expect there to be singular losses as the snow masses contract and expand between the trees.

For open channel flow, the fluid pressure p is equal to the hydrostatic pressure $\rho g h$ at that point, where h is the flow depth. Assuming that the flow depth is constant,

$$\frac{u_1^2}{2g} + z_1 = \frac{u_2^2}{2g} + z_2 + h_L. \tag{3.11}$$

An energy line is a diagram of the total head $\frac{u^2}{2g} + z$ plotted against the channel profile. The term $\frac{u^2}{2g}$ may be considered as the kinetic energy of the flow, and the term z as the potential energy. An example of an energy line for a snow avalanche is given in Figure 3.3. From the definition of h_L according to the Voellmy-Salm approach, we see that if Coulomb friction is dominant, the energy line will be straight with a slope equal to μ. For a number of back-calculated snow avalanches, an average slope of 0.4 : 1 was found (Norem, 2014).

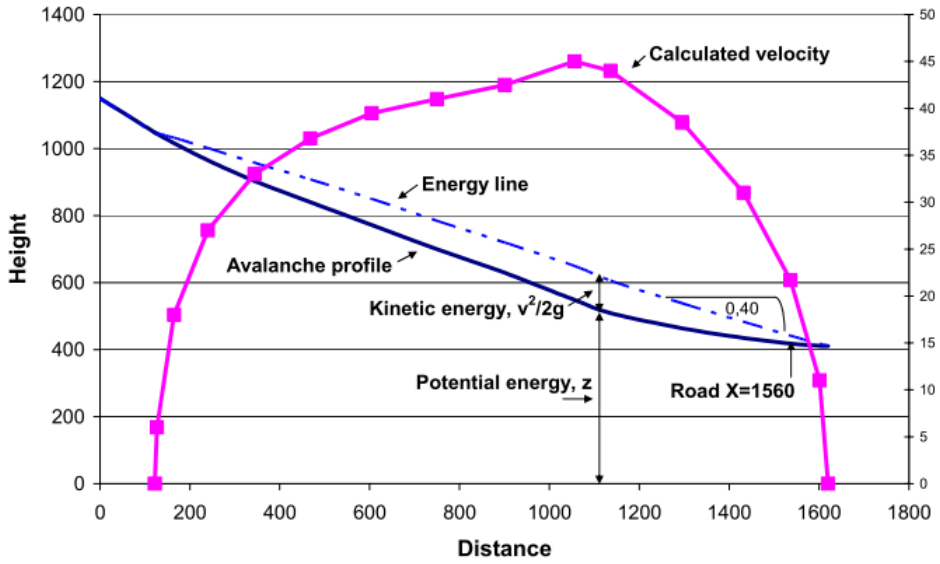

Figure 3.3: Profile of Nakkefonna, Norway, with back-calculated energy line and velocity profile. From: Norem et al. (2006).

3.3 The Froude and Reynolds numbers

The flow of a fluid is governed by three types of forces: an inertial force $F_i = \rho u^2 L^2$ related to the rate of change of flow velocity, a viscous force $F_v = \mu u L = \rho \nu u L$ related to the fluid's resistance

to shearing, and a gravitational force $F_g = \rho L^3 g$, where ρ, μ, and ν are the fluid's density and dynamic and kinematic viscosity, respectively, u is the flow velocity, and L is a characteristic length. For a snow avalanche, L may be the flow depth or the width of an obstacle.

The Froude number Fr, the square root of the ratio between the inertial forces and the gravitational forces, $\frac{F_i}{F_g} = \frac{u^2}{gL}$, determines whether a fluid flow is fluvial (subcritical, Fr < 1) or torrential (supercritical, Fr > 1). For dense avalanches, generally $5 \leq \text{Fr} \leq 10$ (Issler, 2004).

The ratio between the inertial forces and the viscous forces, $\frac{F_i}{F_v} = \frac{uL}{\nu}$ is called the Reynolds number, Re. It determines how turbulent a flow is. For sufficiently large velocity gradients in the flow (Re > 2500), vortices will occur and in turn induce new velocity gradients. Smaller and smaller vortices are created until the viscous forces are relatively large enough to dampen out new vortices. If the viscosity is very large (Re < 2000), no vortices will occur, and the flow is said to be laminar. Following the Voellmy-Salm approach, for a snow avalanche the shear force $F_v = \rho L^3 g(\mu \cos\alpha + \frac{u^2}{\xi L})$. Substituting this into the definition of the Reynolds number, $\text{Re}_{\text{Voellmy}} = \frac{u^2}{\mu g L \cos\alpha + \frac{u^2}{\xi/g}} \rightarrow \frac{\xi}{g}$ as $u \rightarrow \infty$. This means that with $\xi = 1067$ ms^{-2} as proposed by Buser and Frutiger (1980), $\text{Re}_{\text{Voellmy, max}} \approx 100$, and snow avalanche flow should be laminar. Note that $\text{Re}_{\text{Voellmy}} = \frac{1}{\mu \cos\alpha + \frac{u^2}{\xi L}} \text{Fr}^2$. A plot of $\text{Re}_{\text{Voellmy}}$ as a function of u with $\mu = 0.157$, $\xi = 1067$ ms^{-2}, a slope angle $\alpha = 35°$, and $L = 0.5$, 1, and 2 m is shown in Figure 3.4.

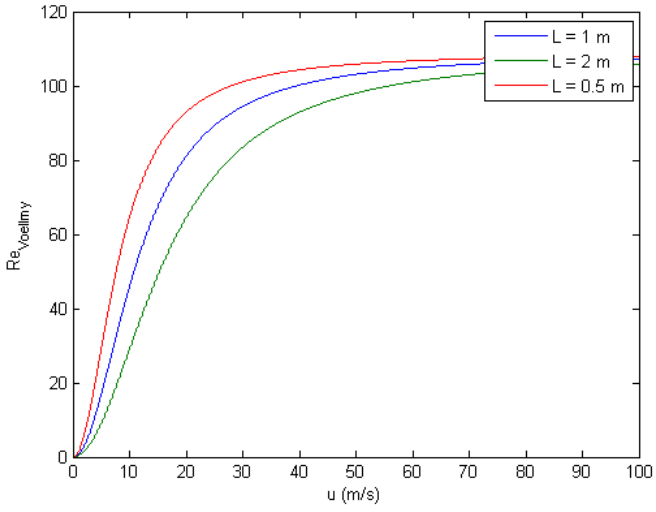

Figure 3.4: The Reynolds number according to the Voellmy-Salm approach as a function of the flow velocity u of the avalanche, with $\mu = 0.157$, $\xi = 1067$ ms^{-2}, a slope angle $\alpha = 35°$ and a characteristic length L of 0.5, 1, and 2 m.

3.4 Flow around cylindrical obstacles: flow regimes

It is important to bear in mind that while a tree is not surrounded by snow prior to being hit by an avalanche, fluid dynamics considers a cylinder that is immersed in a uniform fluid flow. Further, if the fluid is initially at rest, the final flow pattern does not develop until some time. The fully developed flow pattern depends on the ratio between the inertial forces and the viscous forces, the Reynolds number, as shown in Figure 3.5.

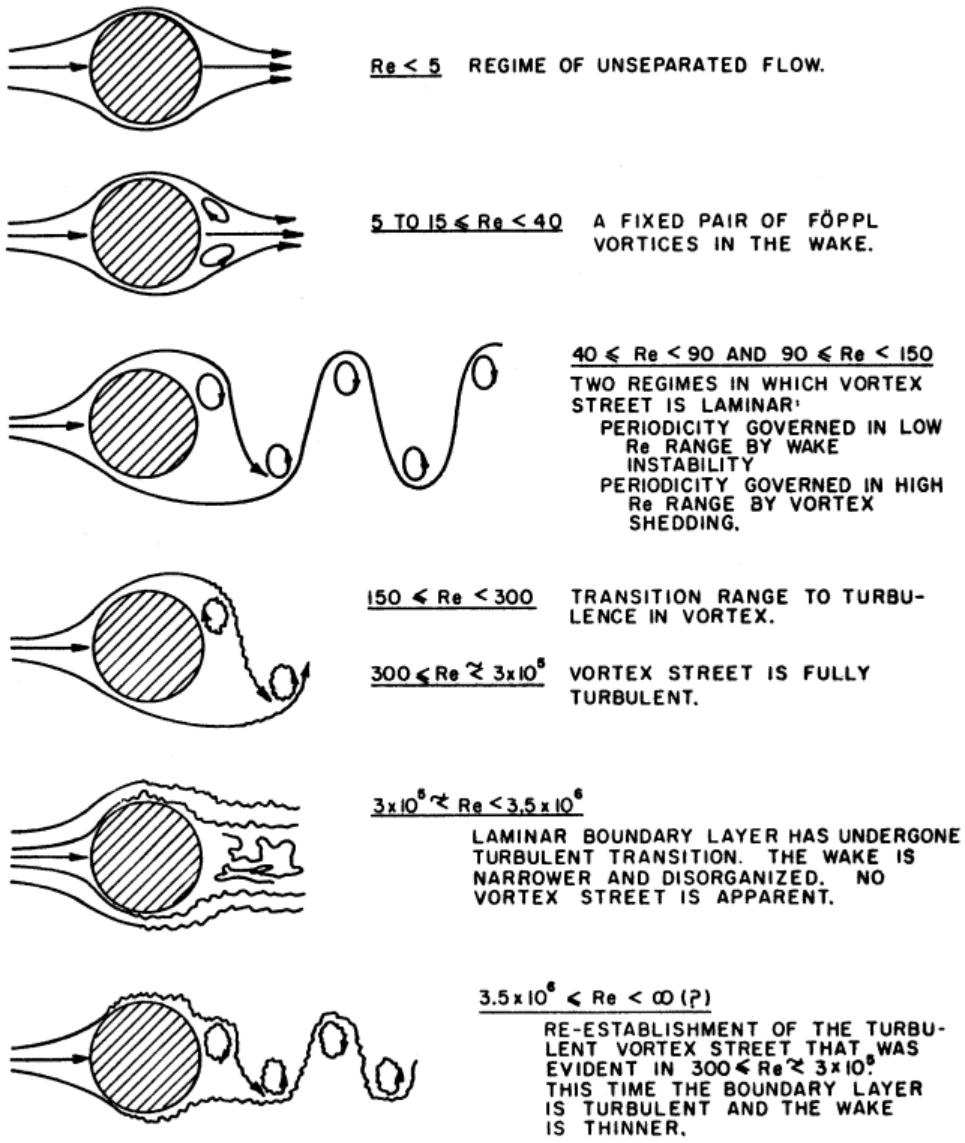

Figure 3.5: Regimes of fluid flow across a circular cylinder. From: Lienhard (1966).

For a snow avalanche with a Reynolds number between 40 and 100, one would expect a flow regime with a laminar vortex street. In this regime, the inertial forces are so much larger than the viscous forces that the flow along the surface of the cylinder separates at the so-called point of separation. In the wake on the downstream side of the cylinder, vortices are shed alternately from the left and the right side of the cylinder with a frequency $f_0 = \frac{u_\infty}{D}\mathrm{St}$, where u_∞ is the upstream flow velocity, D is the diameter of the cylinder, and $\mathrm{St} \approx 0.2$ is the Strouhal number. With an avalanche speed of the order of 10 ms^{-1} and a tree diameter of the order of 0.1 m, the vortex shedding frequency will be of the order of 10 Hz. As the avalanche is slowed down by the forest, one would expect a transition to a flow regime with a fixed pair of vortices in the wake and finally, to a regime of unseparated flow.

Nicolle and Eames (2011) simulate the flow through and around a circular array of cylinders for a range of void ratios $\phi = N_C\left(\frac{D}{D_G}\right)^2$, where N_C is the number of cylinders, D is the cylinder diameter, and D_G is the diameter of the array. The Reynolds number of the array is 2100. Three different flow regimes are observed (Figure 3.6). For low void ratios ($\phi < 0.05$) (Figure 3.6a), the cylinders have uncoupled individual wakes where vortex shedding occurs. For intermediate void ratios ($0.05 < \phi < 0.15$) (Figure 3.6b), a stable wake is generated behind the array. The individual wakes interact to quickly eliminate any vortices. For high void ratios ($\phi > 0.15$) (Figure 3.6c), the array generates a wake that is similar to that of a solid cylinder of the same scale.

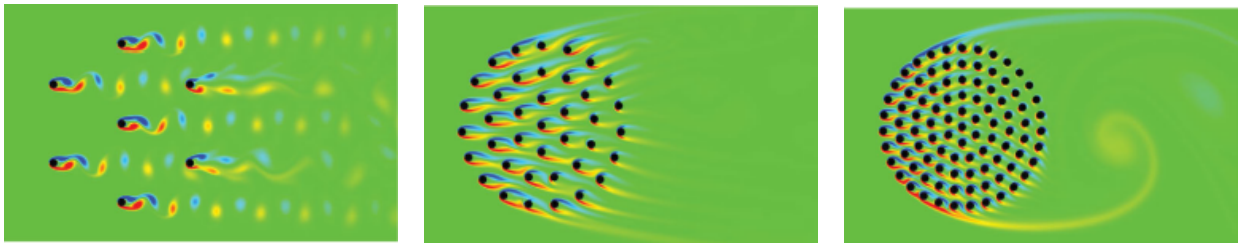

(a) (b) (c)

Figure 3.6: Vorticity fields for circular arrays with seven (3.6a), 39 (3.6b), and 95 (3.6c) cylinders. From: Nicolle and Eames (2011).

3.5 Flow around cylindrical obstacles: forces

Under the assumption that a fluid is incompressible, irrotational, and inviscid (ideal), the velocity and pressure distributions of a uniform flow with upstream velocity u_∞ and pressure p_∞ about a cylinder with radius R are given by potential theory:

$$\begin{aligned} u_r &= u_\infty \cos\theta \left(1 - \frac{R^2}{r^2}\right) \\ u_\theta &= -u_\infty \sin\theta \left(1 + \frac{R^2}{r^2}\right) \\ p &= p_\infty + \frac{\rho u_\infty^2}{2} \frac{R^2}{r^2} \left(2\cos 2\theta - \frac{R^2}{r^2}\right) \end{aligned} \tag{3.12}$$

Here, r and θ are polar coordinates with the origin at the centre of the cylinder. The resulting velocity and pressure fields are shown in Figure 3.7, where $x = r\sin\theta$ and $y = r\cos\theta$.

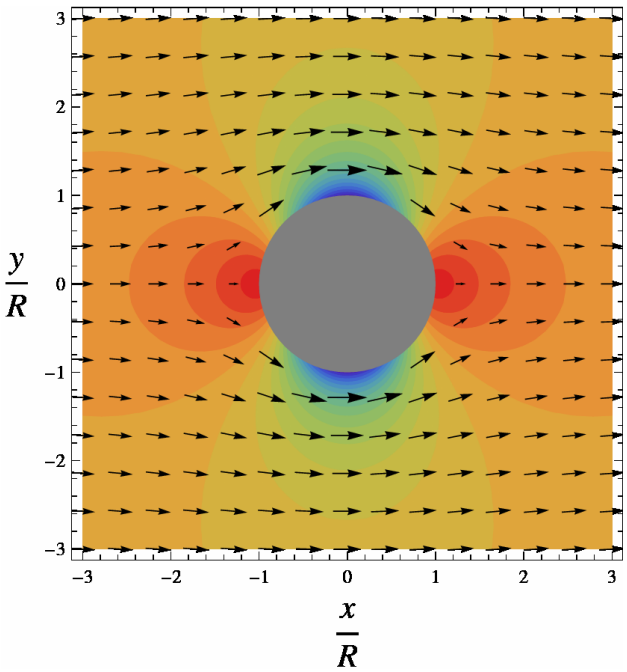

Figure 3.7: Velocity and pressure fields for uniform flow of an ideal fluid about a cylinder with radius R. From: https://en.wikipedia.org/wiki/Potential_flow_around_a_circular_cylinder.

Note that the pressure field is symmetric. In particular, the pressure at the surface of the cylinder is given by $p(r = R, \theta) = p_\infty + \frac{\rho u^2}{2}(2\cos 2\theta - 1)$ with a maximum of $p(R, 0) = p_\infty + \frac{\rho u^2}{2}$, the stagnation pressure. The components p_∞ and $\frac{\rho u^2}{2}$ are called the free-stream static and free-

stream dynamic pressure, respectively. Integrating over the surface of the cylinder, the total force on the cylinder is zero. This is known as d'Alembert's paradox. In reality, no fluid is completely inviscid. A common solution is to consider a boundary layer close to the surface of the cylinder where viscous forces are significant. Outside of this boundary layer, potential theory is applied.

Commonly, two types of forces acting on a cylinder are considered: a drag force F_d acting in the direction of the flow and a lift force F_l acting in a transversal direction. The drag force consists of two components, a friction drag due to the frictional forces acting along the sides of the cylinder and a form drag due to pressure differences across the cylinder in the direction of the flow. For circular cylinders, usually only the form drag is considered. Two snapshots of the pressure distribution around a cylinder for a flow with Re = 100 are shown in Figure 3.8. On the upstream side of the cylinder, the pressure is high, with its maximum at the stagnation point. All around the downstream side of the cylinder, the pressure is low. The resultant force is the form drag. The lift force, the resultant of pressure differences in the transversal direction, alternates in direction depending on whether a vortex is shed on the left or right side of the cylinder.

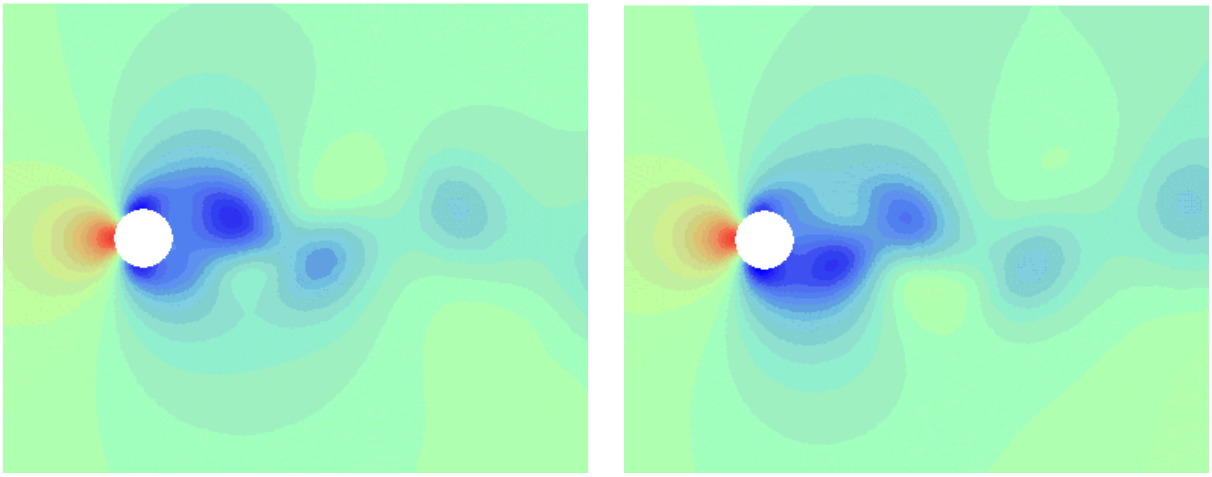

Figure 3.8: Two snapshots of the pressure distribution of fluid flow with Re = 100 across a circular cylinder. From: http://xoptimum.narod.ru/eng/results/incompressible/cylinder/cylinder.htm.

The drag force is expressed as a multiple of the free-stream dynamic pressure:

$$F_d = \frac{1}{2}\rho C_d A u^2, \tag{3.13}$$

where A is the projected area of the cylinder normal to the flow direction. The dimensionless drag coefficient C_d is a function of the Reynolds number and the relative roughness of the cylinder. A plot of C_d against the Reynolds number is shown in Figure 3.9 for a rough and for a smooth cylinder. For a Reynolds number of the order of 10-100, $C_d \approx 2$.

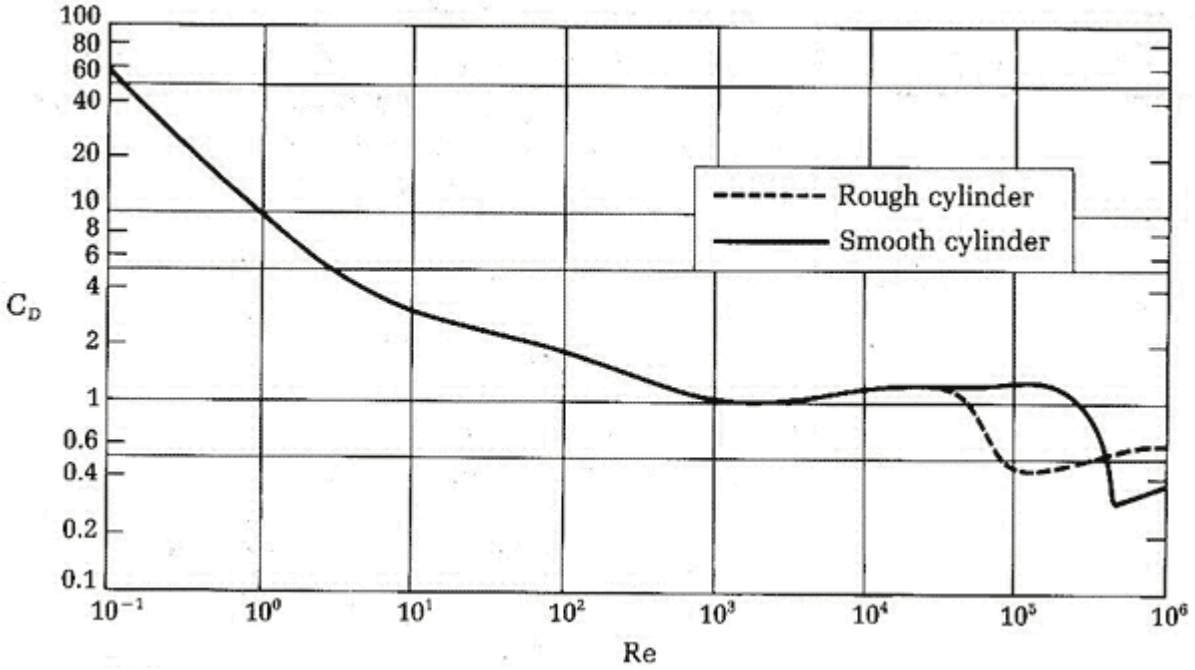

Figure 3.9: The drag coefficient C_d as a function of the Reynolds number. From: http://www.propellersafety.com/propeller-guard-reduced-drag/.

Holzinger and Hübl (2004) empirically find that the drag coefficient for snow avalanches is a decreasing function of the Froude number for Froude numbers in the range $1 < \mathrm{Fr} < 15$: $C_d = 9\mathrm{Fr}^{-1.2}$. According to this formula, the drag coefficient for snow avalanches with $5 \leq \mathrm{Fr} \leq 10$ will be in the range 0.6-1.3.

For a circular array of cylinders, force scatter plots are shown in Figure 3.10 for the same void ratios as in Figure 3.6. For low void ratios (Figure 3.10a), the drag force acting on an upstream cylinder is similar to that acting on an isolated cylinder while the lift force is slightly larger. For cylinders further downstream, both the drag force and the lift force are larger as the flow is ac-

celerated between the upstream cylinders. For intermediate void ratios (Figure 3.10b), the drag force acting on the individual cylinders is steady, with the force on the upstream cylinders dominating the total force on the array. The total lift force on the array is negligible. For large void rations (Figure 3.10c), the lift forces are significant.

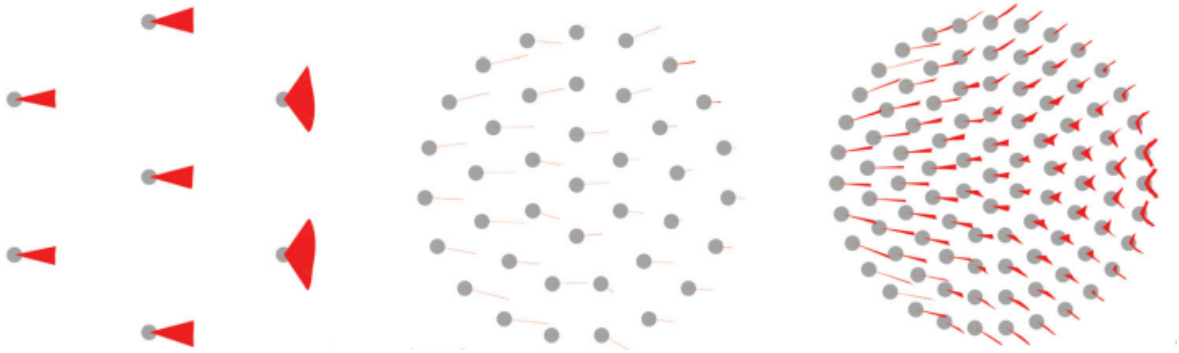

(a) (b) (c)

Figure 3.10: Force scatter plots for circular arrays with seven (3.10a), 39 (3.10b), and 95 (3.10c) cylinders. From: Nicolle and Eames (2011).

Chapter 4

Experiments

In this chapter, a series of chute experiments with a granular material is described. In particular, we describe the materials used for the chute and for the granular material, the design of the chute, and the equipment used for measuring and recording data. Further, the parameters to be varied and the parameters to be measured are given, along with a detailed description of the experimental program and procedure.

4.1 Objectives

In this thesis, we model the dense core of a dry snow avalanche released above and flowing into a forest in order to study the braking effect the tree stems have on the moving avalanche. The effect a forest in the release zone may have in inhibiting avalanche formation is not considered. The powder cloud of dry snow avalanches may cause significant damage in a forest by stripping the branches off trees and cutting off the tree tops in entire forest stands (Steinar Nordal, pers. comm.). We model only the tree stems, not the branches and crowns.

Four phenomena that may be considered when studying the flow of a snow avalanche through a forest are: (1) the hydrodynamic effect of a group of rigid obstacles in the flow path (normal and oblique shocks, interaction of shock waves, dead zones in front of the obstacles, jets, contraction and expansion of the flow), (2) reinforcement of the snow by broken trees, (3) energy loss due to entrainment of broken trees in the flow, and (4) energy loss due to breaking and overturning of trees. This study will focus on phenomenon (1) with the objective of answering

the following key questions:

1. Which hydrodynamic effects do we observe as the avalanche moves through the forest?
2. How do key parameters of the flow (flow depth, front velocity, runout distance) change as compared to a reference experiment?

4.2 Scaling

In order to be able to predict the behaviour of full-scale snow avalanches based on the results from small-scale laboratory studies with powder or granular materials, the experimental parameters need to be scaled correctly. Iverson et al. (2004) derive four similarity criteria assuming that the dynamic response of the avalanche (u, τ) is a function of its physical properties as a granular material and the slope angle α:

$$\left(\frac{u}{\sqrt{gl}}, \frac{\tau}{\rho g h}\right) = f\left(N_P, N_R, c^\star, E^\star\right), \tag{4.1}$$

where $N_P = \frac{\sqrt{l/g}}{\mu h^2/kE}$, where k is the hydraulic permeability of the granular mixture, is a timescale ratio between the timescale for avalanche motion and the timescale for the diffusion of excess pore pressure, $N_R = \frac{\rho h\sqrt{gl}}{\mu}$ is a Reynolds number with $\sqrt{gl}$ as the characteristic velocity, and $c^\star$ and $E^\star$ are the cohesion and the bulk stiffness normalized by the characteristic stress $\rho g h$. In an ideal granular avalanche, the effects of fluid pressure, viscosity, intergranular collisions, and bulk compression on the motion of the avalanche are negligible, that is, where $N_P, N_R, E^\star \to \infty$ and $c^\star \to 0$. However, if the pore fluid is at least as viscous as water, the motion of large avalanches containing water will be affected by the pore pressure, while the motion of small, laboratory scale avalanches will be affected by viscosity. The bulk stiffness $E^\star \gg 1$ for both small-scale and large-scale avalanches, while the cohesion $c^\star$ can have a much larger effect on small-scale than on large-scale avalanches. One example of cohesive forces is the electrostatic attraction of grains to surfaces of the experimental apparatus. In order to limit electrostatic effects, Iverson et al. (2004) carry out their experiments under an ion emission hood and apply an antistatic aerosol. Further, the relative humidity is limited to 30-70 %.

In this study, we apply a geometric similarity criterion given by a length scaling r and a kinetic similarity criterion. Assuming that the flow of a dry snow avalanche is dominated by gravity rather than viscosity, the Froude number is chosen as a kinematic similarity criterion. From Chapter 3, we know that $\mathrm{Re} = \frac{1}{\mu\cos\alpha + \frac{u^2}{\xi L}}\mathrm{Fr}^2$ with the Voellmy-Salm approach. If Coulomb friction is dominant and the friction coefficient μ and the slope angle α are the same in nature and in the model, kinematic similarity is also given for the Reynolds number. The two similarity criteria give the following scalings:

Length:	r
Volume:	r^3
Velocity:	$\sqrt{r}$
Time:	$\sqrt{r}$

Although the braking effect of trees on snow avalanches is the subject of this study, we did not measure the impact force exerted by the flow on the obstacles. It is, however, important that the force scales correctly so that the braking effect is not overestimated. From Chapter 3, we know that the dynamic drag coefficient C_D is a function of the Froude number for $1 < \mathrm{Fr} < 15$. With the similarity criterion on the Froude number, the impact forces should therefore scale correctly.

4.3 Experimental setup

4.3.1 Granular material

In previous small-scale laboratory studies on the flow of dry snow avalanches, the snow has been modelled by either powder or granular materials. Powder materials have been used to model dry snow avalanches with an aerosol cloud (Bozhinskiy and Sukhanov, 1998). A wide range of granular materials have been used: spherical glass beads with a diameter of 3 and 5 mm, plastic lens-shaped beads, and quartz and marmor granulates (Hutter and Koch, 1991; Greve and Hutter, 1993; Hutter et al., 1995; Wieland et al., 1999), sugar sprinkles (Gray et al., 2003), sand (Hákonardóttir et al., 2001), and spherical glass beads (ballotini) with a diameter of 0.1 mm (Hákonardóttir et al., 2001; Brateng, 2005; Hauksson et al., 2007). We used spherical

glass beads (Ballotini Solid Soda Glass Balls, SiLibeads, Sigmund Lindner GmbH, ordered from VWR) with a diameter of 0.090-0.15 mm. The bulk density, the internal friction angle (assumed to be equal to the angle of repose), and the static and dynamic bed friction angles (relative to the bed surface described in Section 4.3.2) are given in Table 4.1.[1]

Table 4.1: Bulk density ρ, internal friction angle ϕ_{int} , and static and dynamic bed friction angles $\phi_{\text{bed, stat}}$ and $\phi_{\text{bed, dyn}}$ of the ballotini.

ρ (kg/m^3)	ϕ_{int} (°)	$\phi_{\text{bed, stat}}$ (°)	$\phi_{\text{bed, dyn}}$(°)
1583	23-26	37-41	27-28

4.3.2 Chute

The chute has a wooden frame and consists of three sections: an upper, or "starting", section 200 mm wide and 1500 mm long, a middle, or "forest", section 1020 mm wide and 2000 mm long, and a lower, or "runout", section 1040 mm wide and 2000 mm long. The upper and lower sections as well as the top and bottom of the middle section are made of plywood with a thickness of 10 mm. The middle section consists of three aluminium plates with a thickness of 10 mm and a width and length of respectively 1000 and 480 mm. The lower section is fixed with an inclination of 10°. The three sections are hinged together so that the inclination of the middle and upper sections can be varied. For this study, both the upper and the middle sections were inclined at an angle of 35°. The setup of the chute is shown in Figure 4.1.

[1]The values given in Table 4.1 should be considered crude estimates. The internal friction angle was determined by pouring about 100 ml of ballotini onto a piece of aluminium foil and measuring the height and diameter of the resulting cone-shaped deposit. The static and dynamic bed friction angles were determined using a wooden board with the same bed surface as the chute. A rectangular area of 6 by 12 cm on the board was covered with a thin layer of ballotini, and the board was inclined until the ballotini began to move. The height was read off from a scale, and the board was quickly lowered again until the ballotini stopped. Again, the height was read off.

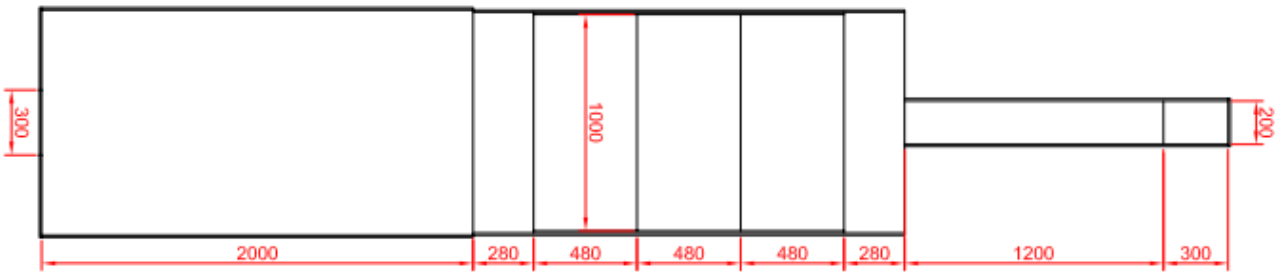

(a) Drawing of the chute viewed from above.

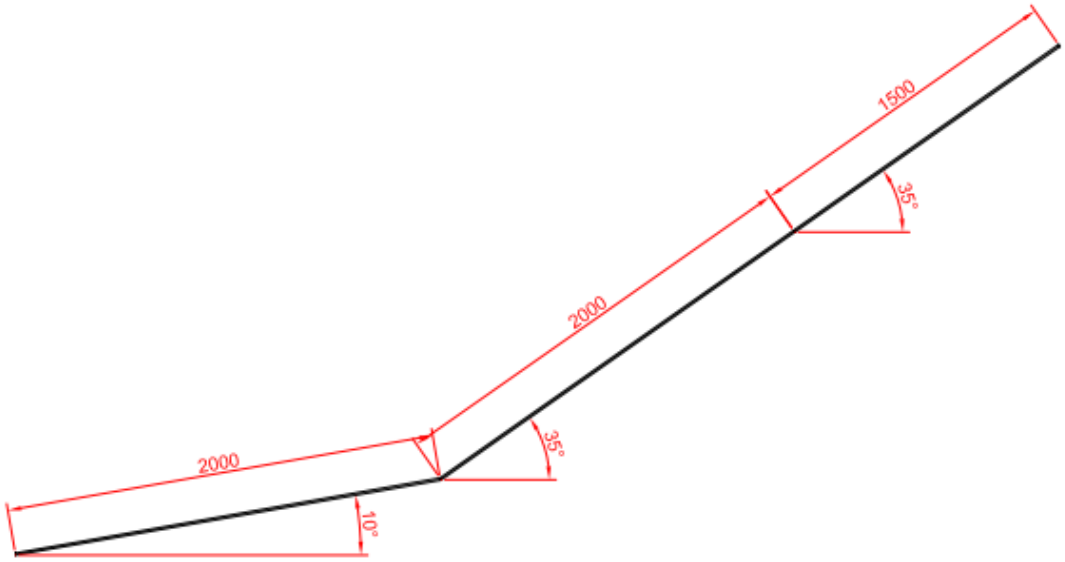

(b) Drawing of the chute viewed from the side.

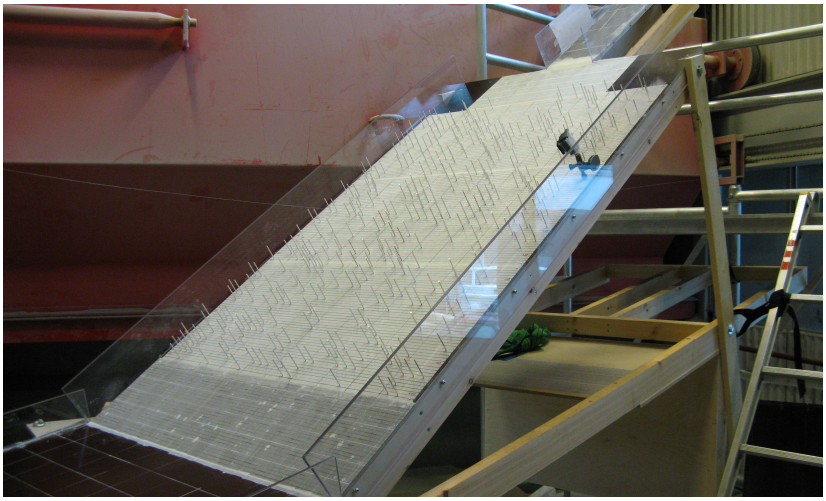

(c) Photo of the chute.

Figure 4.1: Setup of the chute.

Forest

Each aluminium plate has a rectangular grid of 33 by 16 pre-drilled holes with a diameter of 3.3 mm and a spacing of 30 mm, where each grid point represents a position where a tree may grow. The trees were modelled using metal pins cut from filler rod with a diameter of 3.2 mm. The metal pins have a length of 60 mm and were inserted into the holes to a depth of 10 mm.

Release mechanism

The top 30 cm of the upper section are used as a container from which the granular material is released by rapidly pulling up a wooden plate. The plate can either be pulled out, opening the container completely, or pulled up to metal brackets that can be screwed to the side walls for an opening of 1, 2, 3, 4, or 5 cm (Figure 4.2).

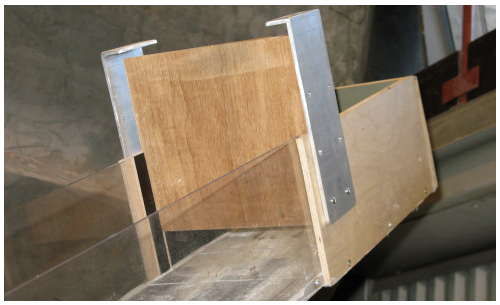

Figure 4.2: Container with metal brackets screwed to the side walls. Here, the wooden plate can be pulled up for an opening of 5 cm.

Surface

Snow avalanche motion may be viewed as the motion of a granular material along a rough surface. We considered surface materials with a roughness of one grain diameter. First, a frosted plastic film (Frostet innsynsvern 200x60 cm, bought at JULA) was tried. Trial experiments showed that the movement of the glass beads (which are electropositive) along the plastic (which is electronegative) generated an electrostatic charge. The more experiments were carried out, the more charge built up. Due to the increasing electrostatic attraction between the surface and the grains, the experiments were not repeatable. In order to prevent the generation of static electricity, the plastic film was sprayed with an antistatic aerosol (Vinylglans, bought at Biltema). The silicone oil contained in the spray, however, gradually changed the consistency of the gran-

ular material from that of fine, dry sand to that of moist sand. Again, experiments were not repeatable.

Instead, the surface of the upper and the middle section of the chute was covered with double-sided removable carpet tape (TESA Teppetape Avtagbar 25 m, ordered from BAUHAUS) which was covered with a thin layer of ballotini. By choosing the same material for the surface as for the snow, there would be no difference in electron affinity. Trial experiments confirmed that experiments now were repeatable. The lower section of the chute was left uncovered.

4.3.3 Filming equipment

The experiments were filmed from above and from the side with two GoPro Hero 4 Black cameras with a resolution of 1920x1080 (Full HD) and a frame rate of 60 fps. Figure 4.3 shows the positions of the cameras. The cameras were positioned precisely using the software GoPro Camera Control 2 (http://www.tequnique.com/gopro) to live-stream the current view of the camera to a PC screen. GoPro's remote control Smart Remote was used to start and stop the two cameras simultaneously.

Figure 4.3: Positions of the two cameras: one above the chute to the left in the photo, and one fixed to the side wall along the middle section of the chute to the right in the photo.

4.4 Parameters

In this thesis, we study the front velocity and the flow depth of the avalanche as it moves through the forest as a function of its incident front velocity, the stem diameter of the trees, and the forest

density. Further, we recorded the runout distance of each avalanche. The parameters and their range of values in prototype and model scale with a length scaling of $r = 1:100$ are summarized in Table 4.2.

Table 4.2: Parameters and range of values in prototype and model scale.

Parameter	Prototype	Model
Incident front velocity	10-30 ms^{-1}	1-3 ms^{-1}
Stem diameter	32 cm, 60 cm	3.2 mm, 6 mm
Forest density	10%, 25%, 50%, 90%	10%, 25%, 50%, 90%
Front velocity	10-30 ms^{-1}	1-3 ms^{-1}
Flow depth	0.5-2 m	5-20 mm
Runout distance	0-200 m	0-200 cm

4.4.1 Parameters to be varied

Incident front velocity

We used three different values for the incident front velocity of the avalanche. Three possible ways of varying the incident front velocity were considered: 1. varying the inclination of the middle and upper sections of the chute, 2. varying the initial flow depth of the avalanche, and 3. varying the mass of ballotini. The trial experiments described below were carried out without a forest.

Possibility 1 was considered impractical, and the inclination of the middle and upper sections of the chute was fixed at 35° (see Section 4.3.2).

Ideally, the avalanche should attain its terminal velocity before hitting the forest, and any acceleration or deceleration of the avalanche along the forest section should be due to the presence of the trees. For moderate angles of inclination, the flow on an inclined plane is steady and uniform if the flow depth h is greater than a threshold depth $h(\alpha)$, where α is the inclination of the plane. If the inclination is too large, the flow will accelerate along the plane (Pouliquen, 1999; G. D. R. MiDi, 2004). This is the basis of Possibility 2. For the fixed inclination of 35°, we carried out a number of trial experiments with initial flow depths of 1, 2, 3, 4, and 5 cm. The flow depth was varied by varying the opening of the container from which the avalanche is released. As an indicator of the velocity of the avalanche, the runout distance was measured (see Section

4.4.2). In accordance with Pouliquen (1999), it was found that the runout distance increased with increasing initial flow depth. For flow depths of 1 and 2 cm, however, the runout distance was considered too short (bearing in mind that the presence of a forest would further shorten the runout distance). From 3 to 4 cm, the increase in runout distance was about 15 cm, and from 4 to 5 cm it was about 10 cm. Bearing in mind a certain natural variability in the runout distances, this increase was considered very small.

For Possibility 3, the container was opened completely so that all ballotini were released at the same time. A number of trial experiments were carried out with different masses of ballotini. Again, the runout distance was measured as an indicator of the avalanche's velocity. We also measured the flow depth at the bottom of the starting section (see Section 4.4.2). For masses of 2, 4, and 6 kg, the corresponding flow depths were about 6, 9, and 12 mm. The runout distance increased by about 40 cm from 2 to 4 kg and by about 25 cm from 4 to 6 kg. This was considered sufficient, and Possibility 3 was chosen with the three masses 2, 4, and 6 kg. A scale with a precision of 1 g was used to weigh out the correct mass of ballotini before each experiment. A frame-by-frame video analysis (see Section 4.4.2) indicated that the avalanche did not accelerate along the forest section.

Stem diameter

For practical reasons, only two different stem diameters were used: a diameter of 3.2 mm and a diameter of 6 mm. For the value of 3.2 mm, the metal pins were used as trees by themselves. For the value of 6 mm, 50 mm long pieces of PVC tubes with an inner diameter of 4 mm and an outer diameter of 6 mm (ordered from VWR) were threaded onto the metal pins. The metal pins and pieces of PVC tube are shown in Figure 4.4.

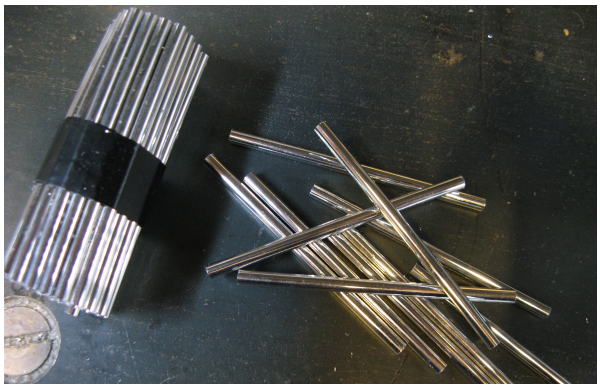

(a) Metal pins with a diameter of 3.2 mm.

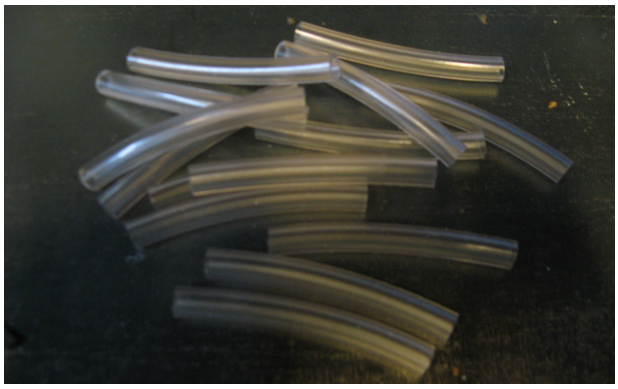

(b) Pieces of PVC tubes with an inner diameter of 4 mm and an outer diameter of 6 mm.

Figure 4.4: Varying the stem diameter.

Forest density

The forest density is the fraction of grid points where trees are growing. As we assume that an existing forest does not grow in a regular pattern, a MATLAB code was written to generate a random pattern of trees within a grid of 33 by 16 points for a given density (Appendix A.1). Three such patterns give one forest configuration. For each of the densities 10%, 25%, and 50%, two random forest configurations were generated. Metal pins were inserted into the aluminium plates according to the patterns for each configuration, creating holes in the surface cover of the forest section. When switching between configurations, redundant existing holes were plugged by pushing down the metal pin. Along the top and bottom rows and the leftmost and rightmost columns, the aluminium plates are screwed to the wooden frame so that redundant metal pins had to be taken out. The holes were sealed with a piece of double-sided Scotch tape covered with a layer of ballotini. For a density of 90%, metal pins were inserted into the existing holes from the forest configurations for 10%, 25%, 50%, and 90%. The seven configurations used are given in Appendix B.

4.4.2 Parameters to be measured

Front velocity

To compute the front velocity of the avalanche along the forest section of the chute, the videos with a front view of the chute were analysed frame-by-frame using the free software VirtualDub,

version 1.10.4. The bottom of the chute was marked with lines with a spacing of 1 cm normal to the flow direction (as well as with a spacing of 10 cm parallel to the flow direction in order to show the width of the avalanche), and the avalanche front's position was read off to the closest centimetre for each frame. As the avalanche generally does not have a well-defined front, the front position was taken to be the average of the two points furthest down the chute, one within 10 cm to the left and one within 10 cm to the right of the centre line. The front velocity was computed as the average of three consecutive frames.

Flow depth

For practical reasons, the flow depth in unforested terrain was measured at the bottom of the upper chute. A sheet of mm-paper was fixed to one of the side walls as shown in Figure 4.5a, and the maximal flow depth was read off manually as the avalanche flows past upon release from the container. The accuracy is about +/- 1 mm. In order to measure the flow depth in forested terrain, ten trees within the view of the side camera were marked with a scale as shown in Figure 4.5b. The red lines of the scale are 5 mm apart. The flow depth at each tree was read off frame-by-frame to the nearest 5 mm in an analysis of the videos with a side view of the chute.

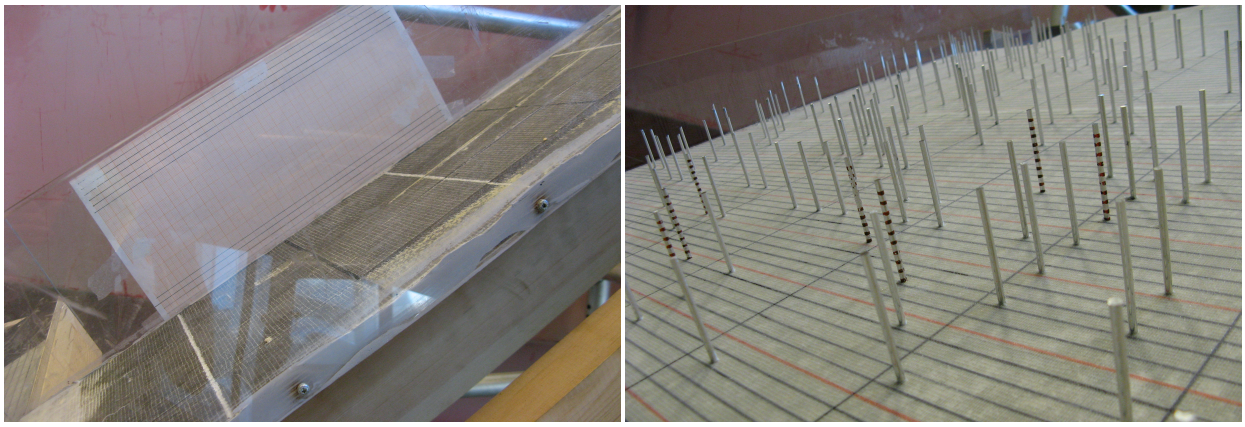

(a) Sheet of mm-paper from which the flow depth at the bottom of the upper chute is read off.

(b) Trees with a scale from which the flow depth in the forest section is read off.

Figure 4.5: Measuring the flow depth.

Runout distance

The runout distance as measured from the top of the runout section of the chute indicates the forest's braking effect without further analysis. The bottom of the chute was marked with lines with a spacing of 10 cm normal to the flow direction (as well as parallel to the flow direction in order to show the width of the runout), and a 30 cm plastic ruler was used to measure the distance from the closest line. The runout distance was recorded with a precision of 0.5 cm. Some runouts had a clearly defined front, while others had a two-part front with a very thin layer of ballotini in front of a markedly thicker layer (Figure 4.6). In the latter case, the runout distance of the thicker layer was recorded with the runout distance of the thin layer given in parentheses.

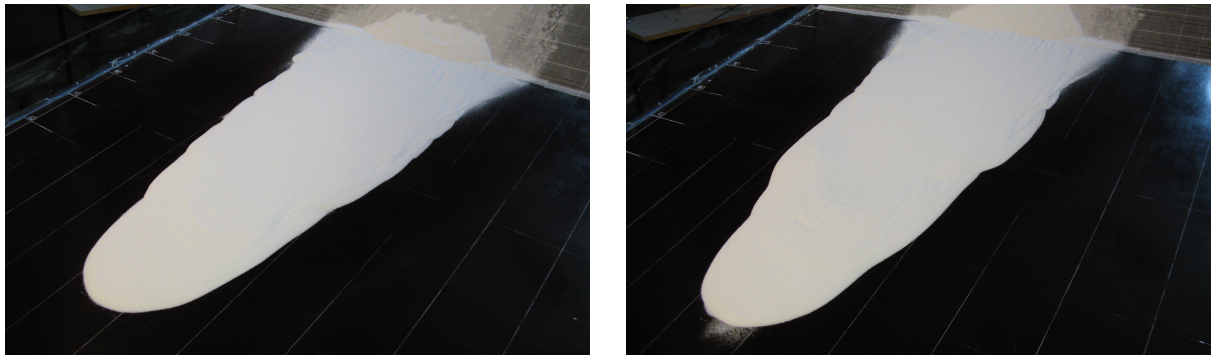

(a) Runout with a clearly defined front.

(b) Runout with a two-part front.

Figure 4.6: Runouts with different types of fronts.

4.5 Experimental program and procedure

In total, 54 experiments were carried out in sets of six experiments per day. On the first and last day (Days 1 and 9), we carried out reference experiments without a forest. On both days, two experiments each with 2, 4, and 6 kg of ballotini were carried out in random order. This enabled us to check for repeatability both within the same day and from the first day to the last day. The program for the reference experiments is given in Table 4.3.

Table 4.3: Program for the reference experiments.

Day		Mass of ballotini (kg)		
		2	4	6
1	1			x
	2		x	
	3	x		
	4	x		
	5			x
	6		x	
9	49		x	
	50	x		
	51			x
	52		x	
	53	x		
	54			x

The program for the experiments with a forest is given in Table 4.4. Each day, the six experiments for one forest configuration – one experiment each with 2, 4, and 6 kg of ballotini for each of the two stem diameters 3.2 and 6 mm – were carried out. For each forest configuration, the experiments were grouped into two subsets of three experiments, one with the three masses for the first stem diameter and one with the three masses for the second. Within each subset, the order of the masses was random. On the day with the second forest configuration for the same forest density, the order of the two subsets was switched. For time reasons, the experiments with a forest were not repeated.

Table 4.4: Program for the experiments with a forest.

Day		Mass of ballotini (kg)			Stem diameter (mm)		Forest density (%)			
		2	4	6	3.2	6	10	25	50	90
2	7	x			x			x		
	8		x		x			x		
	9			x	x			x		
	10	x				x		x		
	11		x			x		x		
	12			x		x		x		
3	13			x		x		x		
	14	x				x		x		
	15		x			x		x		
	16			x	x			x		
	17		x		x			x		
	18	x			x			x		
4	19		x		x				x	
	20			x	x				x	
	21	x			x				x	
	22		x			x			x	
	23			x		x			x	
	24	x				x			x	
5	25	x				x			x	
	26			x		x			x	
	27		x			x			x	
	28	x			x				x	
	29		x		x				x	
	30			x	x				x	
6	31	x			x		x			
	32		x		x		x			
	33			x	x		x			
	34	x				x	x			
	35		x			x	x			
	36			x		x	x			
7	37			x		x	x			
	38		x			x	x			
	39	x				x	x			
	40			x	x		x			
	41		x		x		x			
	42	x			x		x			
8	43		x			x				x
	44			x		x				x
	45	x				x				x
	46			x	x					x
	47	x			x					x
	48		x		x					x

Procedures for preventing the build-up of electrostatic charges

The experiments were carried out in NTNU's pile laboratory at the Department of Civil and Transport Engineering. A simple hygrometer from Clas Ohlson (http://www.clasohlson.com/no/Termometer-hygrometer/36-1264) was used to measure the temperature and relative humidity at the laboratory. The temperature was between 18 and 24°C every day, usually increasing by about 2°C from morning to evening. The accuracy of the hygrometer is, according to the product website, +/- 5% at room temperature for relative humidities between 25 and 95%. Most days, the relative humidity was below 25%. At low relative humidities, static electricity can have a particularly strong effect as it takes a long time until the electrostatic charge has been neutralized by the moisture in the air. To further prevent electrostatic charges from building up on the surfaces of the chute and on the ballotini, the ballotini were brushed off the upper and middle section of the chute after each experiment using a carbon fiber brush (hama Platebørste, bought at Clas Ohlson). Between the trees, a small paint brush was used. On the lower section, a plastic brush was used to brush off the bulk of the ballotini. Any remaining ballotini were wiped off using a microfiber cloth (Figure 4.7a). Before being weighed for the next experiment, the ballotini were sieved through an earthed metallic mesh to remove any electrostatic charge on the ballotini (Figure 4.7b). The ballotini were sieved into a metallic bowl, and a metallic cup was used to add or remove ballotini from the bowl (Figure 4.7c).

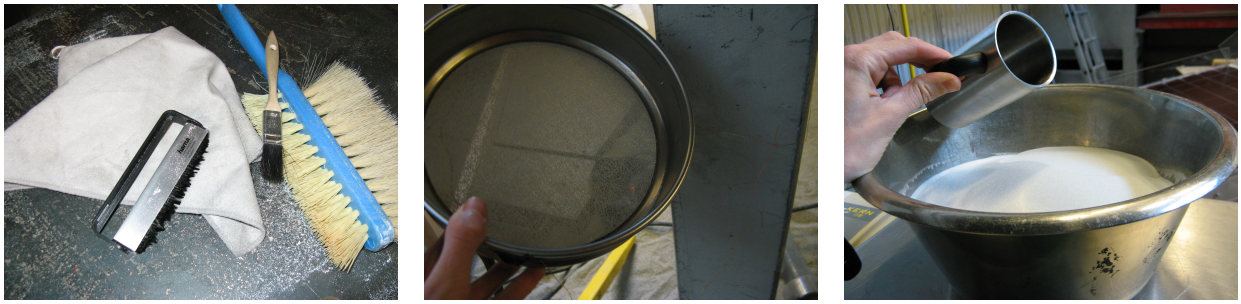

(a) Brushes. (b) Earthed metallic mesh. (c) Metallic bowl and cup.

Figure 4.7: Equipment used to prevent the build-up of electrostatic charges.

Chapter 5

Results

In this chapter, we present the results of the chute experiments described in Chapter 4. In Section 5.1, we describe the flow of the avalanche phenomenologically by example of selected experiments. Snapshot sequences of the corresponding videos are given in Appendix C, with the videos with a front view in Section C.1 and the videos with a side view in Section C.2. Photos of the corresponding runouts are given in Appendix D. We describe characteristic phenomena of the flow and look at how those phenomena are affected by different incident front velocities, stem diameters, and forest densities. The results of the measurements of the three parameters front velocity, flow depth, and runout distance are presented in Section 5.2. The raw data from the manual measurements of the flow depth at the bottom of the upper chute and the runout distance are given in Appendix E.

5.1 Phenomenological description of the flow of the avalanche

5.1.1 General description of flow characteristics

In this section, we give a detailed description of the flow of the avalanche from the top to the bottom of the middle section of the chute. The flow of the avalanche through unforested terrain is described by example of reference experiments carried out before and after the forest experiments with a mass of 4 kg (Experiments 2 and 49), and the flow of the avalanche through a forest is described by example of an experiment with a mass of 4 kg, a stem diameter of 3.2 mm and a

forest density of 50% (Experiment 19). We also describe the runout.

Reference experiments carried out before the forest experiments

First, we describe the flow of the avalanche without a forest for the reference experiments carried out before the forest experiments (Figures C.2 and C.13). Upon leaving the upper section of the chute, the avalanche begins to expand sideways (Figure C.2a). It appears that rather than expanding at the base, the avalanche expands by ballotini rolling off the top surface of the avalanche. The degree of expansion increases from the front towards the tail, with the width of the front remaining at 20 cm throughout its motion down the middle section of the chute. This gives the avalanche an oval shape (Figures C.2b and C.2c). From measuring the flow depth at the bottom of the upper section of the chute, we know that the flow depth of the avalanche increases from the front, attains a maximum, and decreases again towards the tail. The greater the flow depth, the more ballotini will have to roll off until the angle between the top surface of the avalanche and the ground no longer is greater than the angle of repose. The flow depth of the avalanche remains largest in the central 20 cm, which becomes apparent as all ballotini have left the upper chute and the flow depth gradually decreases (Figure C.2f). Figure C.2f also shows the maximum lateral expansion of the avalanche. We see that the degree of expansion increases linearly from the top to the bottom of the middle section of the chute, with a width of about 40 cm at the bottom of the first aluminium plate and a width of about 55 cm at the bottom of the third aluminium plate.

The lateral expansion of the avalanche is also visible from the side (Figures C.13b-C.13e). As the avalanche moves down the chute, streaks along the lateral edge of the avalanche come into view (Figure C.13c). Those streaks become more pronounced with time (Figure C.13d). New streaks appear closer and closer to the centre of the avalanche (Figure C.13f). The streaks may be created as ballotini roll off the moving avalanche and are layered on top of each other to the right and left of the central 20 cm, and all layers continue to move simultaneously.

Streaks in the direction of flow are also visible in a photo of the runout (Figure D.1). The streaks can be seen as a pattern of crests and troughs. Most clearly, however, one can see the contours of a layering normal to the direction of flow. The contours follow the shape of the front of the runout. The layering may be created as ballotini close to the surface of the avalanche

continue to move on top of ballotini that already have come to rest due to the frictional forces between the ballotini and the surface of the chute, depositing ballotini from behind on top of ballotini in front. The front of the avalanche comes to rest first before the rest of the avalanche is deposited in layers behind.

In the videos both from above and from the side, we see that the front of the avalanche is frayed. A reason for this may be that the strips of carpet tape on the upper section of the chute were not laid perfectly adjacent to each other but have some overlap and gaps. Another possible reason is that the front of the avalanche moves by saltation rather than gliding. According to Norem et al. (1987), there is a critical angle of inclination at which dispersive pressures become larger than the overburden pressure. At the front of the avalanche, the flow depth is very low so that the overburden pressure will be small. For glass beads, the critical angle is between 26° and 32°, which is less than the angle of inclination of the upper and middle sections of the chute. The lower chute has an angle of inclination less than the critical angle, and we see that the front of the runout is smooth.

Experiments with a forest

Figures C.5 and C.16 show the flow of the avalanche through a forest. The front of the avalanche appears to pass the first row of trees almost unhindered by simply flowing around the trees (Figure C.5a). Behind the trees, a grain-free region opens up. As more ballotini enter the middle section of the chute and hit the trees, the grain-free regions widen. Rather than flowing around the trees, the ballotini are thrown up and around the trees in a fan (Figure C.5b). The more ballotini that hit the trees, the larger the fans become.

The flow density of the avalanche may play a crucial role. If the front of the avalanche moves by saltation, the flow density near the front will be much lower than that of a dense-flowing core. The packing of the glass beads will be quite loose. This means that the mass of ballotini can be compressed into a denser packing to be able to flow in between the trees. As the flow depth of the avalanche increases from the front towards the tail, the overburden pressure increases. With an increasing flow density, the ballotini may approach their densest packing so that they no longer can be compressed further. When hitting a tree, the ballotini therefore have to climb up the tree before they can move around, creating a fan.

The front of the avalanche continues to flow around the trees in its path. Initially, no other fans are created. A reason for this may be that a large number of ballotini are slowed down in their motion and thrown into suspension by the fans in the first row of trees. As the avalanche continues its movement, however, large fans are created also behind some of the trees further down the chute (Figure C.5d). A possible reason is that the ballotini that were thrown up into suspension fall down again so that the amount of ballotini at the densest packing increases again. It appears that large fans are created primarily behind trees that have no immediate neighbours diagonally upstreams. A reason for this may be that the ballotini move towards those trees by gliding or saltation rather than being thrown at them from fans at neighbouring trees. The density of ballotini hitting those trees is therefore larger. The fans in the top row of trees, however, remain the largest.

While the fans in the centre point in the direction of flow, the fans on the lateral edges of the avalanche are asymmetric with the innermost wing of the fan pointing in the direction of flow and the outermost wing of the fan pointing away from the direction of flow at an angle of about 20-40°. This leads to a lateral spreading of the avalanche to a maximum width of about 45 cm at the bottom of the first aluminium plate and about 60 cm at the bottom of the second aluminium plate. The width remains at about 60 cm along the third aluminium plate (Figure C.5j). This means that more ballotini are spread sideways with a forest than without a forest, where the avalanche expands into a triangular shape. After all ballotini have left the upper chute and the avalanche thins, the fans narrow and decrease in height (Figures C.5j-C.5l).

The side view of the chute shows not only the lateral spreading of the avalanche, but also the flow height. In Figure C.16a, one can see that the front of the avalanche passes through the forest at a flow height similar to that in unforested terrain. Behind the front, however, clouds of ballotini are thrown up into the air to increasingly greater heights (Figures C.16b-C.16g). Along the lateral edge, one can observe the creation of fans at each tree. As the trees are hit by more ballotini, the height of the fans increases (Figures C.16e-C.16h). Towards the tail of the avalanche, the height of the fans decreases again (Figures C.16i-C.16o). Figure C.16p shows that a little wedge of ballotini remains behind each tree after the avalanche has passed through the forest.

Figure D.5 shows the runout of Experiment 19. As for the reference experiment, the front of the avalanche stops first before the rest of the avalanche is layered behind. The contours of

the layers are visible in the figure. In addition, one can see grooves in the runout that appear to follow the direction of the fans: in the direction of flow towards the centre of the runout, and slightly away from the direction of flow towards the lateral edges. The distance between two grooves appears to be about 3 cm, the minimum distance between two adjacent trees. The runout is only slightly wider than the runout for the reference experiment, but much shorter. The edges of the runout are jagged, while the edges of the runout for the reference experiment are almost smooth.

Reference experiments carried out after the forest experiments

Finally, we give a description of the flow of the avalanche without a forest for the reference experiments carried out after the forest experiments as compared to the reference experiments carried out before the forest experiments (Figures C.11 and C.22). As in Experiment 2, the avalanche expands into an oval shape. The degree of lateral expansion is the same for both experiments. However, both the front and the lateral edges of the avalanche are more frayed than for Experiment 2. At the centre of the chute, we see a fan being created (Figure C.11b). In both the front and the side view, we can see streaks in the flow direction (Figures C.11c and C.22b). It appears that those streaks are small fans that are created as the ballotini hit a piece of tape, a metal pin that has not been pushed far enough into its hole, or the edges of a hole where a metal pin has been pushed down too far (Figure C.22g). After the avalanche has passed, we can see parallel streaks along the columns of trees (Figures C.11f and C.22h). This is a further indication of the avalanche flow being disturbed by the holes in the carpet tape.

Also the edges of the runout are more frayed than for Experiment 2 (Figure D.11). In addition, we can see parallel grooves in the direction of flow that appear to be created downstreams of each column of trees. Again, this indicates that the holes in the carpet tape disturb the flow of the avalanche.

5.1.2 Description of flow characteristics for different incident front velocities

In this section, we look at how the phenomena described in Section 5.1.1 are affected by the three different incident front velocities resulting from releasing 2, 4, and 6 kg of ballotini. The characteristics of the flow are described by example of three reference experiments (Experiments 1, 2, and 3), and three forest experiments with a stem diameter of 3.2 mm and a forest density of 50% (Experiments 19, 20, and 21).

Reference experiments

Figures C.1, C.2, and C.3 and C.12, C.13, and C.14 show the flow of the avalanche for the three masses respectively from above and from the side for the reference experiments. We see that for all three masses, the avalanche expands into an oval shape (Figures C.1c, C.2c, and C.3c). The degree of expansion, however, depends on the mass of ballotini. At the bottom of the first and the third aluminium plate, the avalanche expands to a maximum width of about 35 and 50 cm for 2 kg, about 40 and 55 cm for 4 kg, and about 45 and 60 cm for 6 kg (Figures C.1f, C.2f, and C.3f).

From the side, we see some streaks in the direction of flow for all three masses (Figures C.12b, C.13b, and C.14c). Those streaks become much clearer in Figures C.12e, C.13e, and C.14e, which show the avalanche as it has reached its maximum lateral expansion. For 2 kg, there appear to be streaks across the entire width of the avalanche, for 4 kg, there appear to be no streaks at the centre of the avalanche, and for 6 kg, there are streaks only at the very edge of the avalanche. The formation of streaks may be related to shear stresses between the individual layers of moving ballotini. In analogy to fluid dynamics, the bottom layer of ballotini may be stopped in its motion by the bed friction ("no-slip condition"), inducing a shear stress between the bottom layer and the layer above. The individual layers of ballotini will be slowed down in their motion successively as the shear stress is transferred from layer to layer. As the shear stresses become smaller towards the top surface of the avalanche, it is possible that streaks only form up to a certain flow depth. From measurements at the bottom of the upper section of the chute, we know that the flow depth of the avalanche is smallest for 2 kg and largest for 6 kg. As the avalanche

thins towards the tail, the amount of streaks close to the centre of the avalanche increases for both 4 kg and 6 kg (Figures C.12f and C.13f).

The runouts for the three masses are shown in Figures D.1, D.2, and D.3. (As no photo was taken of the runout for Experiment 1, a photo of the runout of Experiment 5 is shown instead.) We see that while the runouts differ in width and length, with the runout for 6 kg being the widest and longest followed by the runouts for 4 kg and 2 kg, the shape of the runouts is the same. All three runouts have an elongated shape with a smooth curved front and fairly smooth straight edges that show the layering of the runout from the side. The layering can also be seen from above from contours in the shape of the front of the runout. In addition, all three runouts have streaks in the direction of flow.

Experiments with a forest

For the forest experiments, the flow of the avalanche for the three masses is shown from above in Figures C.5, C.6, and C.7 and from the side in Figures C.16, C.17, and C.18. The flow pattern appears to be the same for all three masses: the front of the avalanche passes unhindered through the forest by flowing around the trees, while further behind, the ballotini are thrown around the trees in fans that point in the direction of flow at the centre and away from the direction of flow at an angle of about 20-40° close to the edges of the avalanche (Figures C.5f, C.6f, and C.7f). Although the size of the fans for the different masses depends on the mass of ballotini, with the fans for 6 kg being largest followed by the fans for 4 kg and 2 kg, the relative sizes of the fans for each mass are the same: the largest fans are created in the top row of trees, and the largest of the remaining fans are created behind trees without immediate neighbours diagonally upstreams. In Figures C.5h, C.6h, and C.7h, we see the fans at their largest. The figures also show the degree of lateral spreading of the avalanche for the three masses. The avalanche with a mass of 6 kg spreads the most, followed by the avalanches with masses of 4 kg and 2 kg. The maximum spreading is shown in Figures C.5l, C.6l, and C.7l: about 50 cm for 2 kg, about 60 cm for 4 kg, and about 70 cm for 6 kg. For 2 kg, this is the same as for the reference experiment. For 4 kg and 6 kg, this is an increase by respectively 9.1% and 16.7% as compared to the reference experiments.

The degree of lateral spreading of the avalanche for the three different masses can also be seen from the side. As the avalanche spreads sideways, small fans are created along the lateral

edge of the avalanche for both 4 kg and 6 kg (Figures C.16g and C.17g), with the height of the fans being largest for 6 kg. The reason for this is that the flow depth along the edge becomes larger for 6 kg than for 4 kg. For 2 kg, the flow depth is too low for any fans to be created. From the red markings on some of the trees, we see that clouds of ballotini are thrown up to heights that increase from the front towards the tail of the avalanche for all three masses. At all times, the height of the clouds is greatest for a mass of 6 kg, followed by 4 kg and 2 kg. Figures C.16g, C.17g, and C.18f show the clouds at their maximum height.

Figures D.5, D.6, and D.7 show the runouts for the three experiments. The three runouts have almost the same shape. The edges are more jagged than for the reference experiments, and the jags are located in the same places for the three masses. The jags have, however, different sizes. The runout for 6 kg has the largest jags and the runout for 2 kg the smallest. Also, the overall size of the runouts is different. The runout for 6 kg is widest, longest, and appears highest, followed by the runouts for 4 kg and 2 kg. On top of each runout, we see grooves that appear to follow the direction of the fans. The grooves appear to have the same depth and the same relative length for the three masses.

5.1.3 Description of flow characteristics for different stem diameters

In this section, we describe how the two stem diameters 3.2 and 6 mm affect the flow of the avalanche through the forest. As examples, we use experiments with a mass of 4 kg and a forest density of 50% (Experiments 19 (Figures C.5 and C.16) and 22 (C.8 and C.19)).

We see that for both stem diameters, large fans are created behind the first row of trees (Figures C.5b and C.8b). Those fans appear to be both higher and wider for 6 mm than for 3.2 mm. A reason for this may be that due to the larger stem diameters, there is less room for ballotini to flow in between the trees. In order for all ballotini to pass the trees, a larger amount of ballotini will need to climb up the trees for 6 mm than for 3.2 mm. The front of the avalanche appears to flow unhindered through the forest for both stem diameters. Narrow grain-free regions with a width of about one tree diameter open up behind the trees. Although the fans behind the first row of trees remain the largest, large fans are created downstreams of the first row for both stem diameters some time after the front of the avalanche has passed (Figures C.5e and C.8e). Those fans are created behind the same trees and appear to be of similar size for the two stem diame-

ters. A reason for this may be that due to the fans in the first row being larger, more ballotini are slowed down in their motion as they enter the forest for 6 mm than for 3.2 mm. The density of ballotini at a given point further down the chute will therefore be less for 6 mm than for 3.2 mm, and the ballotini can be compressed more until the densest packing is reached. As a result, the fans do not become as large as they would have done had the density been the same as for 3.2 mm. However, the fans for 6 mm are wider so that the ballotini are spread sideways at a larger angle for 6 mm than for 3.2 mm. Nevertheless, the degree of lateral spreading appears to be the same for both stem diameters (Figures C.5l and C.8l).

From the side, we see the height that the clouds of ballotini are thrown up to. At all times, the height of the clouds is somewhat greater for 6 mm than for 3.2 mm. The maximum height, however, occurs later for 6 mm than for 3.2 mm (Figures C.16g and C.19h). This indicates that the flow density for 6 mm is less than for 3.2 mm: at a given time, more ballotini have moved a given distance for 3.2 mm than for 6 mm. In Figures C.16p and C.19p, we can see the wedges of ballotini that are deposited behind the trees after the avalanche has passed through the forest. The wedges appear to have about the same height, but the width is the same as the stem diameter so that the total volume of the wedges is larger for 6 mm than for 3.2 mm.

Figures D.5 and D.8 show the runouts for the two experiments. The width of the runouts is the same, but the runout for 6 mm is about 20 cm shorter than for 3.2 mm. The lateral edges of the runouts have similar shapes with jags in the same places, but the front of the runout is more jagged for 6 mm than for 3.2 mm. On the surface of both runouts, we see grooves that follow the directions of the fans – in the direction of flow towards the centre of the runout and at an angle to the direction of flow towards the edges. Further, the contours of a layering normal to the direction of flow can be seen. While the grooves appear to have about the same width and depth for the two stem diameters, the contours are much more pronounced for 6 mm than for 3.2 mm. The reason for this appears to be that the individual layers are much thicker for 6 mm than for 3.2 mm.

5.1.4 Description of flow characteristics for different forest densities

Finally, we look at the flow characteristics of the avalanche for four different forest densities: 10, 25, 50, and 90%. This is done by example of experiments with a mass of 4 kg and a stem diameter

of 3.2 mm (Experiments 8, 19, 32, and 48, with the corresponding figures C.4 and C.15, C.5 and C.16, C.9 and C.20, and C.10 and C.21).

For all four densities, large fans are created as the avalanche passes the first row of trees (Figures C.4b, C.5b, C.9b, and C.10b). The width of the grain-free region that opens up behind the trees appears to depend on the distance between adjacent trees in the first row. For 10%, the distance is so large that neighbouring fans do not interfere. For this density, we see the largest grain-free regions. For the other three densities, the distance between adjacent trees is so small that each fan is compressed by the wings of the neighbouring fan. If there are trees in two adjacent holes, the width of the grain-free region is hardly wider than the diameter of the tree. As there are trees in almost all holes for 90%, all fans are very narrow. For all four densities, fans are created downstreams of the first row with some delay after the front of the avalanche has passed. This delay is smallest for 10%, where fans are created immediately after the front has passed. A reason for this may be that the fraction of ballotini that flow between the trees is much larger than the fraction of ballotini that are thrown up into suspension by the fans in the first row. Except at the very front, the flow density will therefore be so large that the ballotini cannot be packed any more densely. We see that the delay increases with the density of the forest (Figures C.4e, C.5e, C.9e, and C.10e). It is reasonable to assume that ballotini that fall down again after having been thrown into suspension continue to move by saltation rather than gliding. The higher the forest density, the more ballotini are thrown into suspension by the first row of trees, and the more ballotini will therefore move by saltation. This means that the flow density will decrease with increasing forest density. While the relative sizes of the fans are the same for all four densities, with the fans in the first row being largest and the largest of the remaining fans being created behind trees with no immediate neighbours diagonally upstreams, the absolute size of the fans decreases with increasing forest density. The larger the fans, the larger the amount of ballotini that are spread sideways. The avalanche spreads to a maximum width of about 70 cm for 10%, 65 cm for 25%, 60 cm for 50%, and only 45 cm for 90% – 10 cm less than for the corresponding reference experiment.

From the side, we see that the flow height of the avalanche increases rapidly to its maximum for 10%, while the increase is more gradual for the other three forest densities. This would be expected as fans are created immediately after the front of the avalanche has passed for 10%, and

with some delay for the other three densities. The maximum height of the clouds of ballotini is largest for 10% and smallest for 90% (Figures C.20e and C.21g). For 25% and 50%, the maximum heights of the clouds are quite similar (Figures C.15h and C.16g).

The runouts of the four experiments are shown in Figures D.4, D.5, D.9, and D.10. In agreement with the degree of lateral spreading of the avalanche observed in the videos, the width of the runout is greatest for 10%, followed by 25%, 50%, and 90%. The runout is about 10 cm longer for 10% than for 50%, but about 10 cm shorter than for 25%. The length of the runout for 90% is about the same as for 50%. The shapes of the runouts are very different: the edges of the runouts for 10% and 50% are jagged, while the edges for 25% and 90% are much smoother. The shape of the runout, however, depends strongly on the random pattern of the forest.

5.1.5 Summary of observed phenomena

In summary, we have observed the following characteristic phenomena as the avalanche flows through a forest (Figure 5.1): (1) The front of the avalanche appears to flow unhindered through the forest; (2) The creation of fans. The largest fans are created in the first row of trees (or, more precisely, behind the first tree in each column). Smaller fans are created downstreams of the first row some time after the front of the avalanche has passed. The largest of those are created behind trees that have no immediate neighbours diagonally upstreams; (3) The ballotini are thrown up into suspension by the fans; (4) The lateral spreading of the avalanche by the fans, in particular fans along the lateral edges of the avalanche whose outermost wing points away from the direction of flow.

(a) Phenomena (1) and (2)

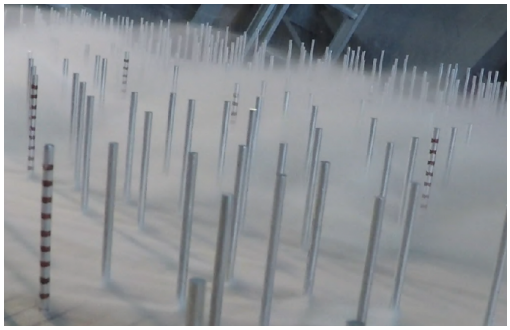

(b) Phenomenon (3)

(c) Phenomenon (4)

Figure 5.1: Four characteristic phenomena observed as the avalanche flows through a forest.

Varying the incident flow velocity of the avalanche affects the degree of lateral spreading. The relative size of the fans is the same for all three flow velocities, but the larger the incident flow velocity, the larger the absolute size of the fans. Varying the stem diameter affects the amount of ballotini that are thrown into suspension at the first row of trees. For a stem diameter of 6 mm, the fans created in the first row of trees are larger than for 3.2 mm. Finally, varying the forest density affects both the amount of ballotini that are thrown into suspension by fans behind the first row of trees and further downstreams and the degree of lateral spreading. The braking effect of the forest appears to be a combination of ballotini being slowed down in their motion by interfering fans, in particular in the first row of trees, and a lateral spreading of the avalanche.

5.2 Data analysis

5.2.1 Front velocity

Reference experiments

Figure 5.2 shows profiles of the front velocity of the avalanche along the middle section of the chute for the refererence experiments carried out before and after the forest experiments (Experiments 1-6 and 49-54). There does not appear to be a trend in the measured front velocity along the chute. For each mass, the front velocity appears to vary randomly about an average value. In Table 5.1, we have given the average front velocity for each experiment. For each mass, the values are within one standard deviation of each other. For the reference experiments carried out after the forest experiments (Experiments 1-6), however, the values appear to be somewhat higher than for the reference experiments carried out before the forest experiments (Experiments 49-54). From Section 5.1, we know that the flow of the avalanche in Experiments 49-54 is disturbed by pieces of carpet tape and metal pins. In the following, we therefore use the average values for Experiments 1-6: 1.46 ms^{-1} for 2 kg, 1.79 ms^{-1} for 4 kg, and 1.95 ms^{-1} for 6 kg.

Table 5.1: Average front velocities for the reference experiments.

Mass (kg)		Average front velocity (ms^{-1})		Average front velocity (ms^{-1})
2	3	1.46 ± 0.08	50	1.52 ± 0.07
	4	1.45 ± 0.08	53	1.52 ± 0.07
4	2	1.76 ± 0.16	49	1.82 ± 0.09
	6	1.82 ± 0.12	52	1.79 ± 0.12
6	1	1.93 ± 0.06	51	2.03 ± 0.11
	5	1.97 ± 0.09	54	2.03 ± 0.12

In Figure 5.3, we have plotted the average front velocity against the maximum flow depth measured for each mass. We have used the following values for the flow depth: 5.5 mm for 2 kg, 9 mm for 4 kg, and 12 mm for 6 kg. According to the Voellmy-Salm model (see Section 3.1), the terminal velocity u_∞ is proportional to $\sqrt{h}$, the square root of the flow depth. The plot shows the best fit: $u_\infty = 0.59\sqrt{h}$. Although a model cannot be reliably fitted with only three data points,

the plot indicates that the Voellmy-Salm model fits our data well.

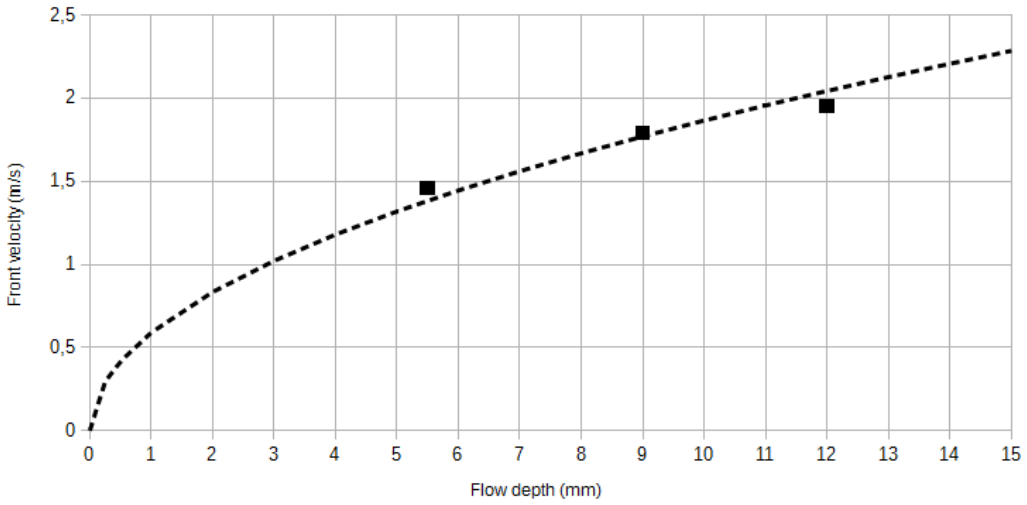

Figure 5.3: A plot of the average front velocity against the flow depth. The curve $u_\infty = 0.59\sqrt{h}$ has been fitted to the data by eye.

The Froude number of the flow is computed to be 6.94 for 2 kg, 6.65 for 4 kg, and 6.28 for 6 kg. This is within the typical range of values for a dense snow avalanche (see Section 3.3).

Experiments with a forest

In Figure 5.4, we have plotted profiles of the front velocity for the forest experiments together with profiles of the front velocity for a reference experiment carried out before the forest experiments and a reference experiment carried out after the forest experiments. The profiles indicate that the front velocity for the forest experiments does not differ significantly from the front velocity for the reference experiments. This is in agreement with the observation that the front of the avalanche appears to move through the forest unhindered by the trees in its path (see Section 5.1). We have plotted the corresponding energy lines in Figure 5.5. As the front velocity does not differ significantly from a constant average value, the energy lines are parallel to the surface of the chute.

5.2.2 Flow depth

The method for measuring the flow depth of the avalanche in forested terrain described in Section 4.4 was designed for the dense-flowing core of an avalanche. As described in Section 5.1, however, a large amount of ballotini moves in suspension or by saltation rather than gliding. We have therefore measured the flow depth as the height of the lowest red marking on a tree that is visible through the clouds of ballotini around. Even though this may not always give the correct height of the avalanche at the position of the marked tree, the measured heights allow us to compare the flow depths for different combinations of parameters qualitatively. As examples, we have used the same experiments as in Section 5.1. In Figure 5.6, we have plotted the flow depth for Experiments 19, 20, and 21 to compare the flow depths of avalanches with different incident front velocities, or masses. In Figure 5.7, we have plotted the flow depth for Experiments 19 and 22 to compare the flow depths of avalanches that move through forests with different stem diameters. Finally, we have plotted the flow depth for Experiments 8, 19, 32, and 48 in Figure 5.8 to compare the flow depths of avalanches that move through forests with different densities. The plots correspond to the snapshots of the videos with a side view given in Appendix C.2.

For different masses, we see that in general, the flow depth is greatest for 6 kg, followed by 4 kg and 2 kg. This is in agreement with the observations in Section 5.1. For the reference experiments, a smooth increase in flow depth was observed from the front to a maximum. The flow depth remained at this maximum for some time before decreasing again towards the tail of the avalanche (see Section 5.1). For the forest experiments, we see a similar increase, maximum, and decrease, but rather at each tree individually than for the avalanche as a whole. The flow depth at each tree may fluctuate. This appears natural as the ballotini are thrown through the air rather than glide along the surface. For different stem diameters, we see that the flow depth is generally greater for 6 mm than for 3.2 mm. This agrees with what we observed in Section 5.1. For different forest densities, we see that the flow depth increases most rapidly for 10%. Between about 0.3 s and 1.0 s, the flow depth for 10% is largest, followed by 25% and 50%, which are similar. The flow depth for 90% is much smaller. From about 1.0 s, the flow depths for all densities decrease, with the flow depth for 10% decreasing most rapidly and the flow depth for 90% decreasing most slowly. By about 1.4 s, the flow depths for 25% and 50% have become

largest, while the flow depth for 10% has become as small as the flow depth for 90%. This is in agreement with our observations in Section 5.1.

5.2.3 Runout distance

In Figure 5.9, we have plotted the runout distance against the forest density for all experiments. For each mass and stem diameter, we have fitted the corresponding individual data points with a quadratic trendline. We observe the following: (1) the runout distance decreases as the forest density increases from 0 to 50%. The more open the forest, the greater the decrease in runout distance as more trees are added. As the forest density increases to 90%, the runout distance increases again; (2) the runout distance is less for a stem diameter of 6 mm than for a stem diameter of 3.2 mm. The difference is greatest for 6 kg and smallest for 2 kg, and is larger at 25% and 50% than at 10% and 90%; (3) the gradient of the trendline is greater for a stem diameter of 6 mm than a stem diameter of 3.2 mm. This means that at any forest density, the effect on the runout distance of adding or removing trees is greater for 6 mm than for 3.2 mm. For each stem diameter, the gradients of the trendlines for the three masses 2 kg, 4 kg, and 6 kg are about the same; (4) the difference in runout distance for two forest configurations with the same density can be substantial. In particular, we see this for the two lowest forest densities 10% and 25%. At each density, the difference is largest for 6 kg, followed by 4 kg and 2 kg.

As we observed in Section 5.1, the braking effect of the forest on the avalanche appears to be a combination of two phenomena: the slow down of a large amount of ballotini by large fans in the first row of trees and the lateral spreading of ballotini by smaller fans further down the chute. At a density of 10%, there are so few trees high up on the chute that most ballotini continue to move down the chute unhindered by the forest. The fans further down the chute are almost as large as the fans in the first row of trees so that the degree of lateral spreading is greatest at 10%. At a density of 90%, most ballotini are slowed down by the many fans in the first row of trees. The fans further down the chute are very small so that the degree of lateral spreading is lowest at 90%. As the forest density increases from 0% to 100%, the amount of ballotini that are slowed down upon entering the forest increases, while the degree of lateral spreading decreases. It appears that the optimal combination of the two phenomena occurs around a forest density of 50%. In Section 5.1, we observed that the fans in the first row of trees are larger and wider for

a stem diameter of 6 mm than for 3.2 mm, while the fans further down the chute are of about the same size. The amount of ballotini slowed down upon entering the forest is therefore larger for 6 mm than for 3.2 mm, while the degree of lateral spreading is the same. Therefore, a forest with large stem diameters has a greater braking effect than a forest with small stem diameters.

It would be natural for the forest configuration to have the least effect on the runout distance at large and at very small forest densities. At small forest densities, the distance between the trees is so large that the braking effect of the forest can be expected to equal the sum of the braking effects of the individual trees. The position of each tree along the chute and relative to other trees is not as important as for intermediate forest densities, where the fans behind neighbouring trees interact. For the two configurations for a forest density of 25%, we see that there are no trees at all in the avalanche path in the first seven rows of the forest for Configuration 1, while there are a few trees in this area for Configuration 2. Therefore, ballotini will be slowed down and spread sideways earlier with Configuration 1 than with Configuration 2. The larger the forest density, the more trees will grow at the minimum distance to their neighbours, and the less probable it becomes for large areas of the forest to be without trees.

In summary, a forest appears to have a maximum braking effect for densities around 50% where trees grow quite densely high up in the avalanche path, slowing down the bulk of the snow, and more openly further down the chute so that the snow can be spread sideways. Further, the braking effect is greatest for mature forests where the trees have larger stem diameters than in younger forests. The larger the avalanche, the greater the braking effect of the forest.

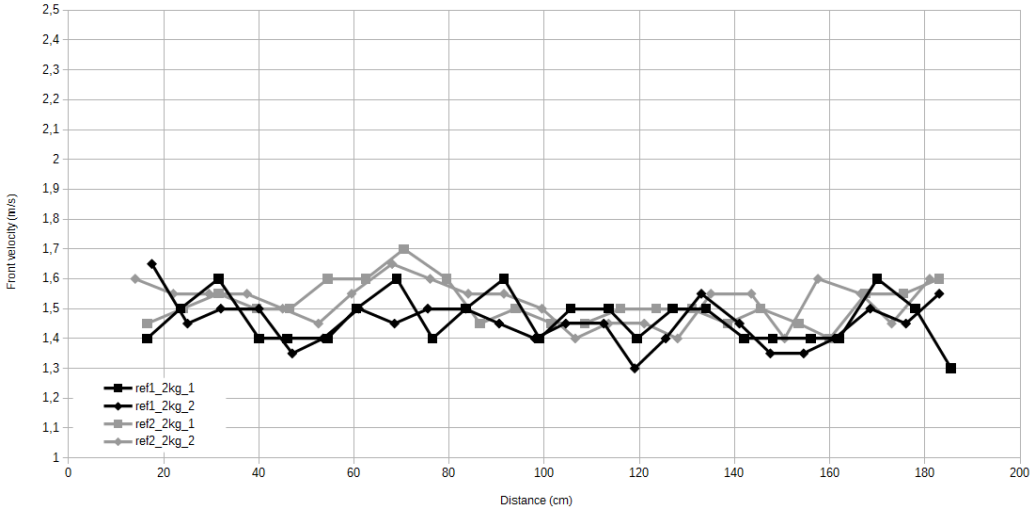

(a) Mass: 2 kg

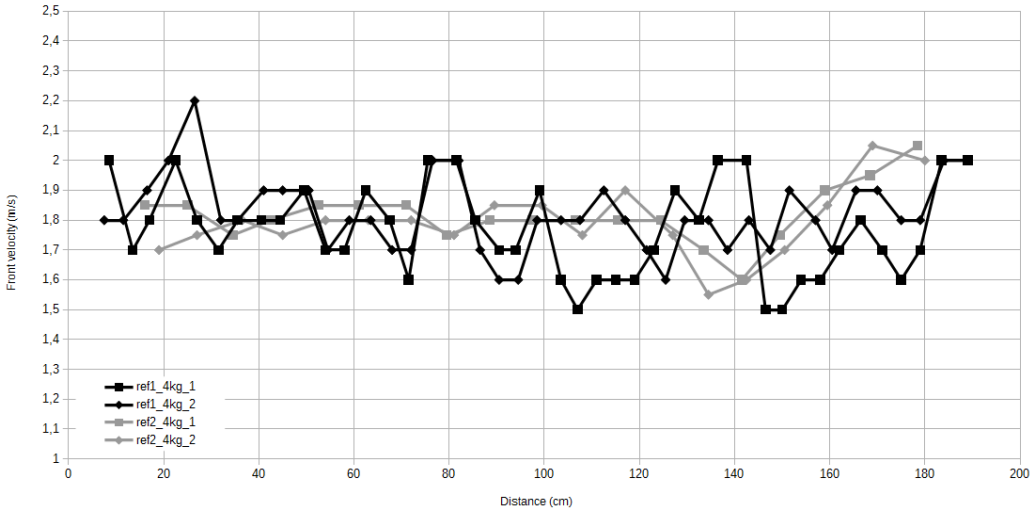

(b) Mass: 4 kg

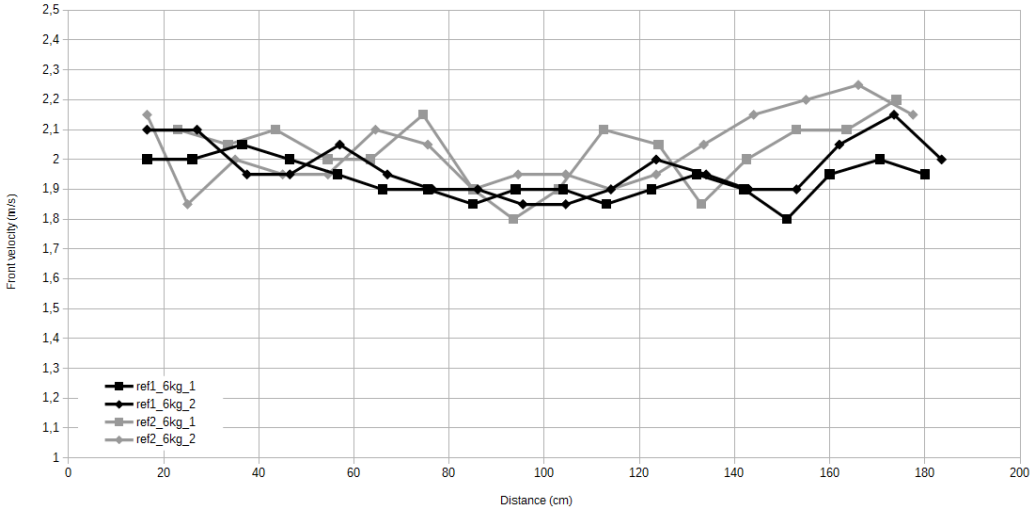

(c) Mass: 6 kg

Figure 5.2: Plots of the front velocity for the reference experiments.

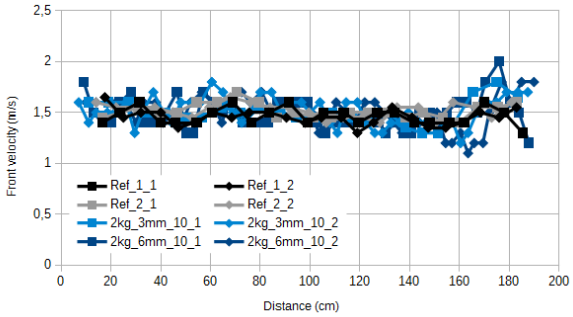

(a) Mass: 2 kg, forest density: 10%

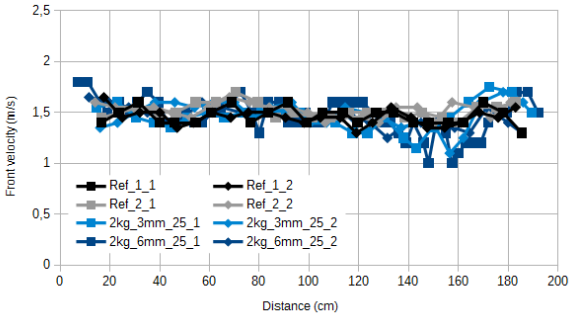

(b) Mass: 2 kg, forest density: 25%

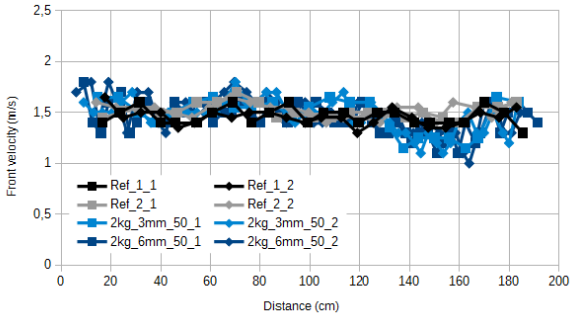

(c) Mass: 2 kg, forest density: 50%

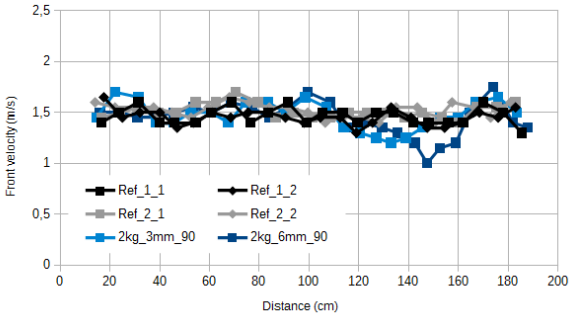

(d) Mass: 2 kg, forest density: 90%

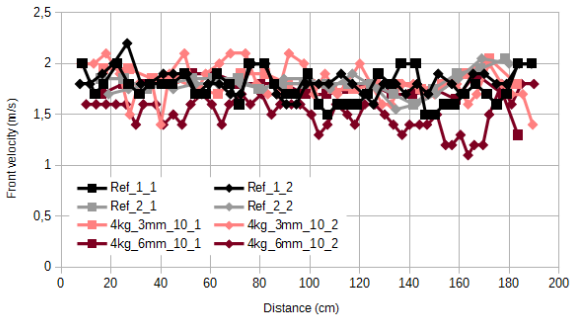

(e) Mass: 4 kg, forest density: 10%

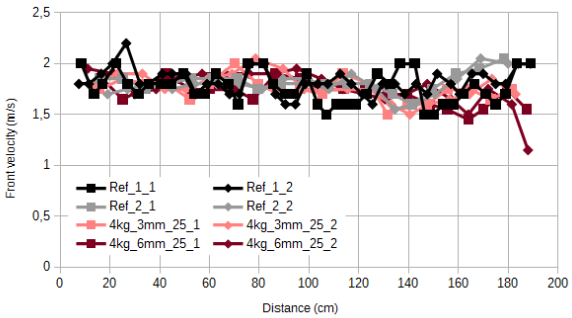

(f) Mass: 4 kg, forest density: 25%

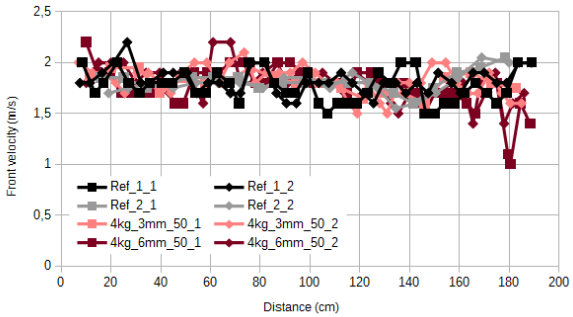

(g) Mass: 4 kg, forest density: 50%

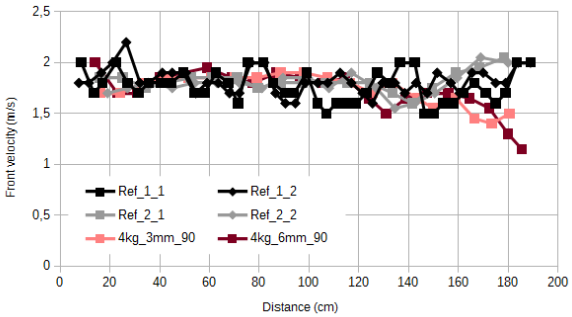

(h) Mass: 4 kg, forest density: 90%

Figure 5.4: Plots of the front velocity for the forest experiments.

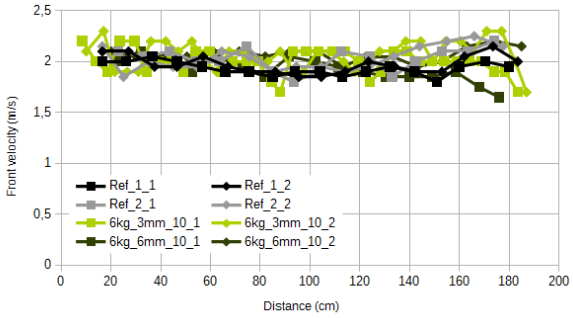

(i) Mass: 6 kg, forest density: 10%

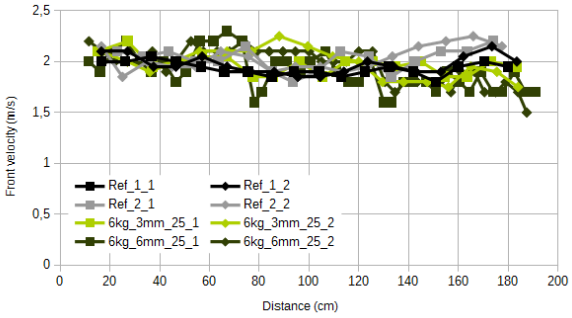

(j) Mass: 6 kg, forest density: 25%

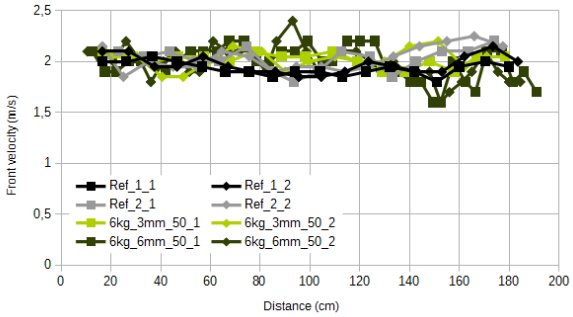

(k) Mass: 6 kg, forest density: 50%

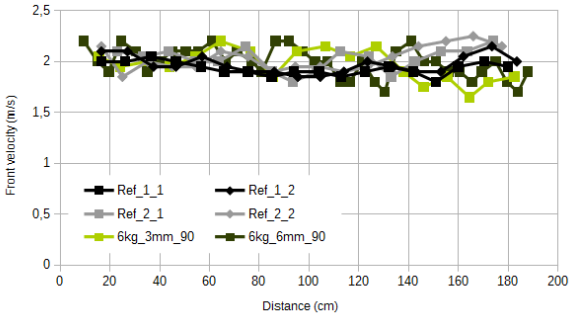

(l) Mass: 6 kg, forest density: 90%

Figure 5.4: Continued: Plots of the front velocity for the forest experiments.

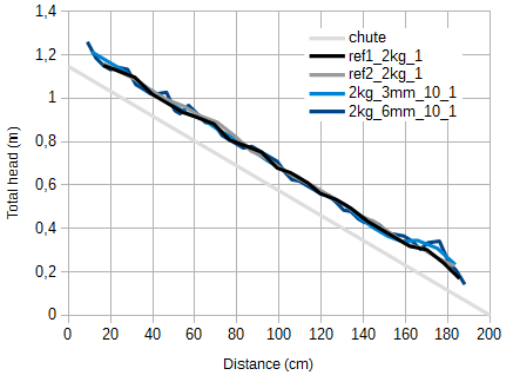

(a) Mass: 2 kg, forest density: 10%

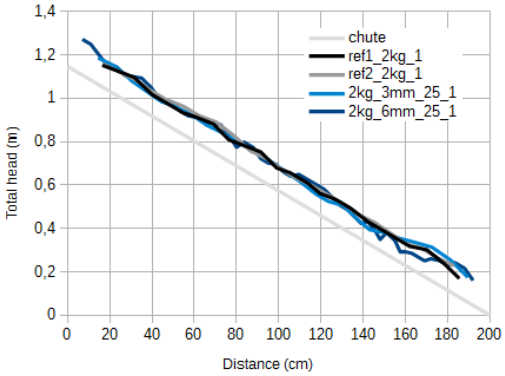

(b) Mass: 2 kg, forest density: 25%

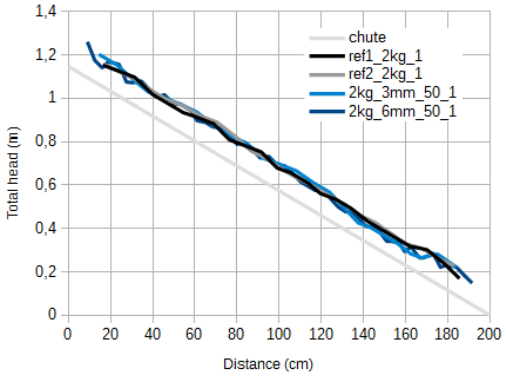

(c) Mass: 2 kg, forest density: 50%

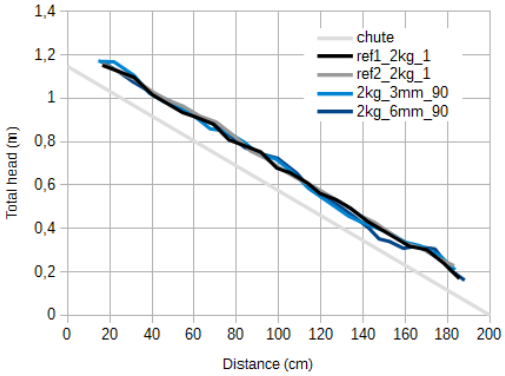

(d) Mass: 2 kg, forest density: 90%

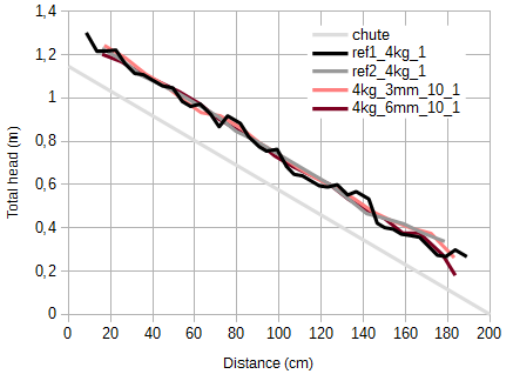

(e) Mass: 4 kg, forest density: 10%

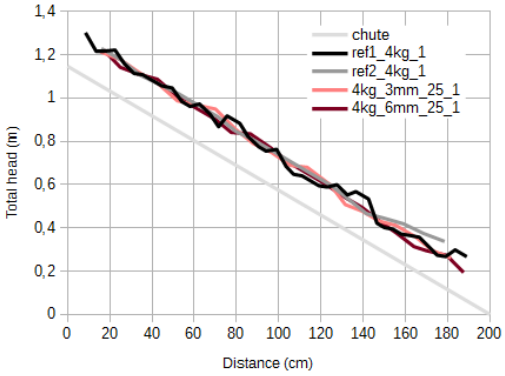

(f) Mass: 4 kg, forest density: 25%

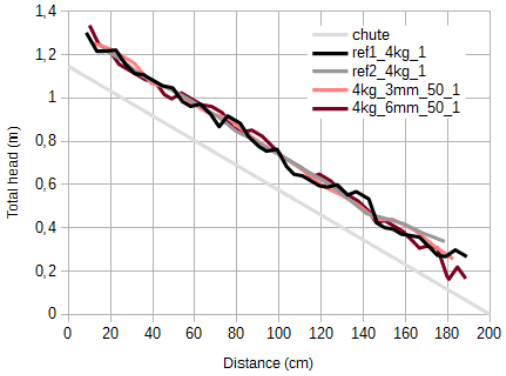

(g) Mass: 4 kg, forest density: 50%

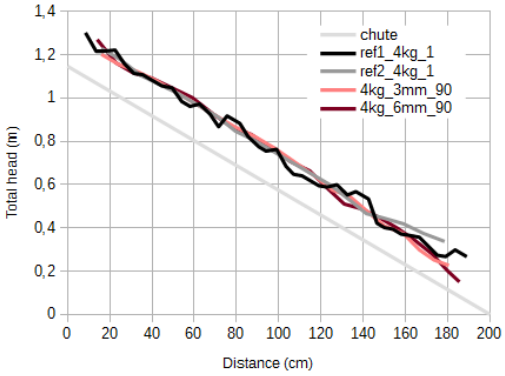

(h) Mass: 4 kg, forest density: 90%

Figure 5.5: Plots of the energy line.

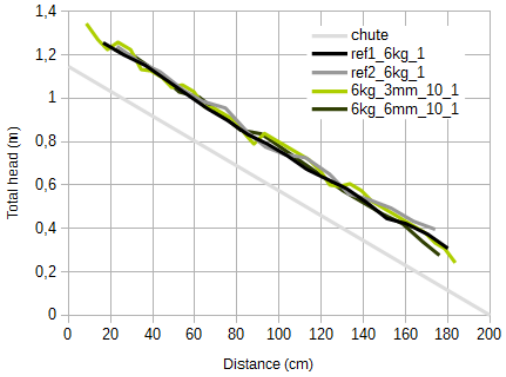

(i) Mass: 6 kg, forest density: 10%

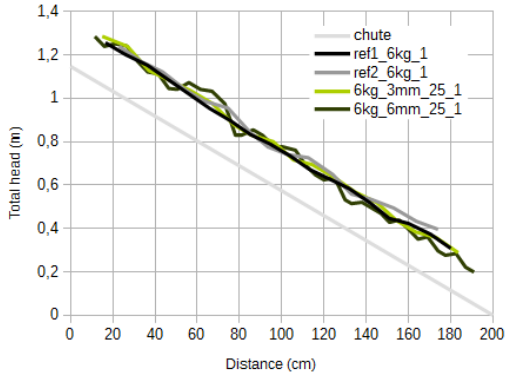

(j) Mass: 6 kg, forest density: 25%

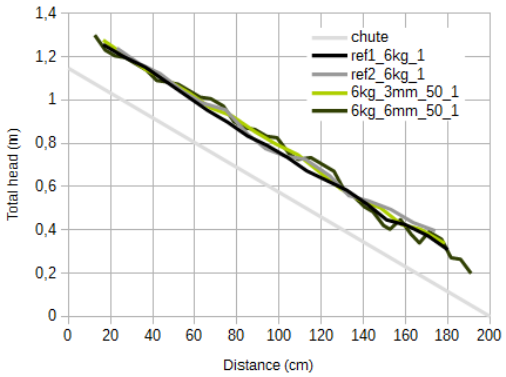

(k) Mass: 6 kg, forest density: 50%

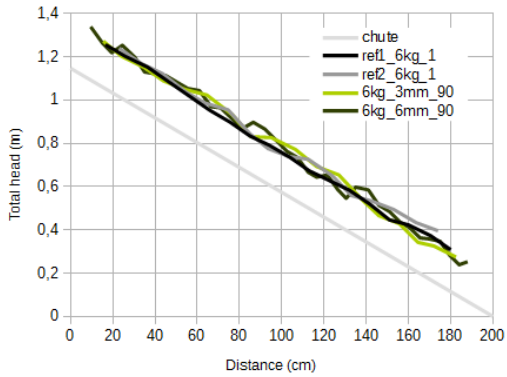

(l) Mass: 6 kg, forest density: 90%

Figure 5.5: Continued: Plots of the energy line.

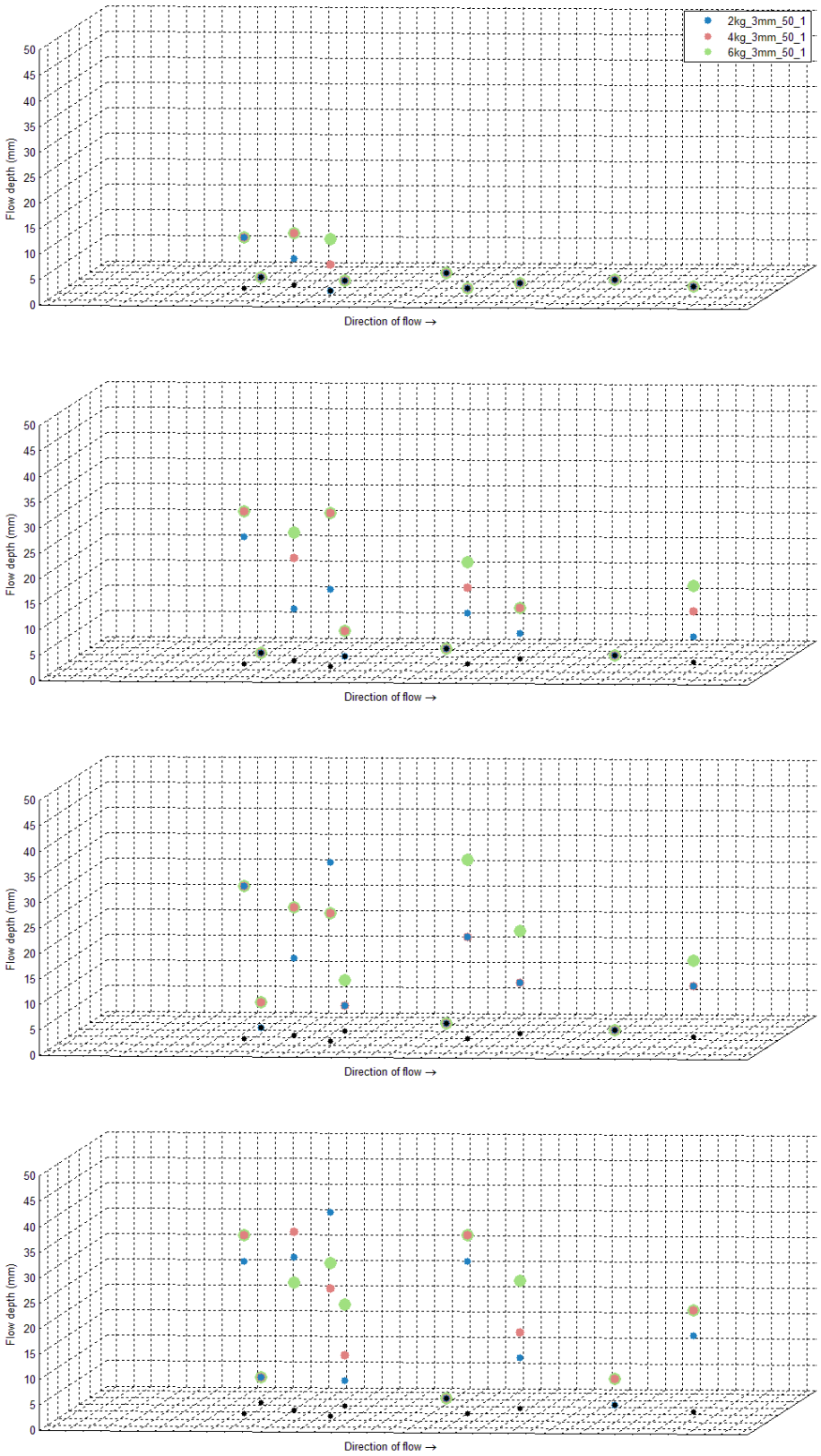

(a) t = 0

(b) t = 0.1 s

(c) t = 0.2 s

(d) t = 0.3 s

Figure 5.6: Plots of the flow depth for the three masses 2 kg, 4 kg, and 6 kg. Experiments 19, 20, and 21 are used as examples (stem diameter: 3.2 mm, forest density: 50%).

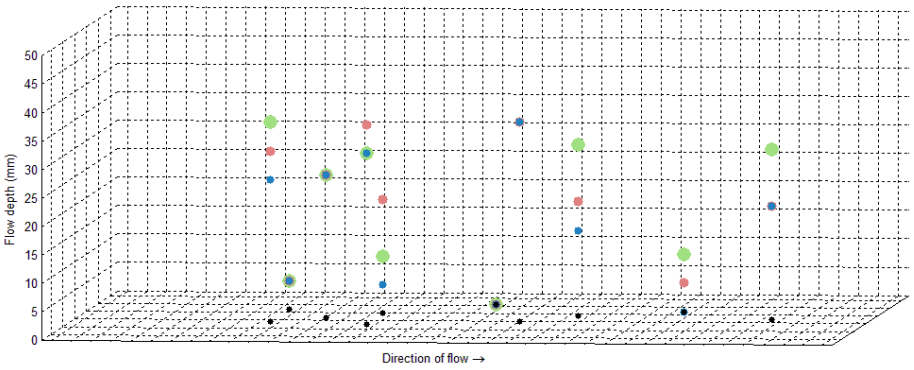

(e) t = 0.4 s

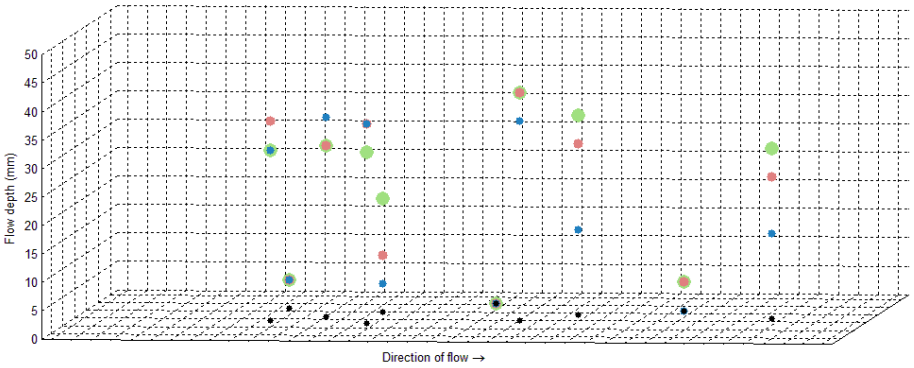

(f) t = 0.5 s

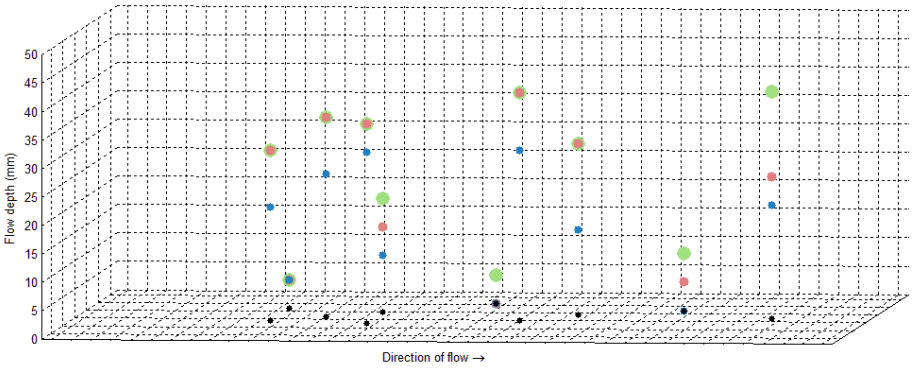

(g) t = 0.6

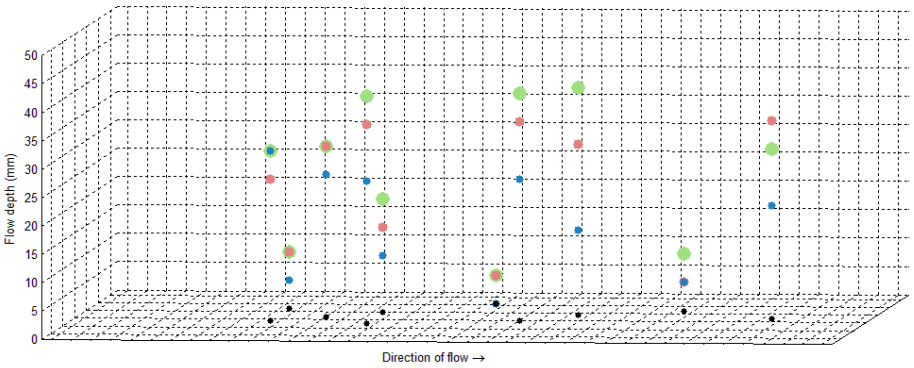

(h) t = 0.8 s

Figure 5.6: Continued: Plots of the flow depth for the three masses 2 kg, 4 kg, and 6 kg. Experiments 19, 20, and 21 are used as examples (stem diameter: 3.2 mm, forest density: 50%).

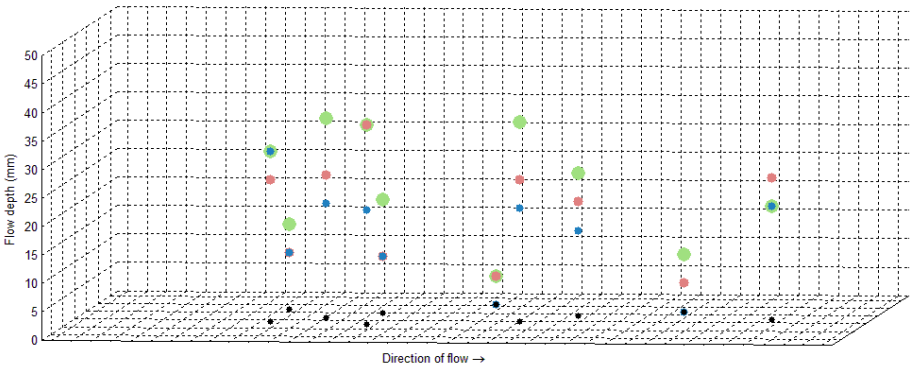

(i) t = 1.0 s

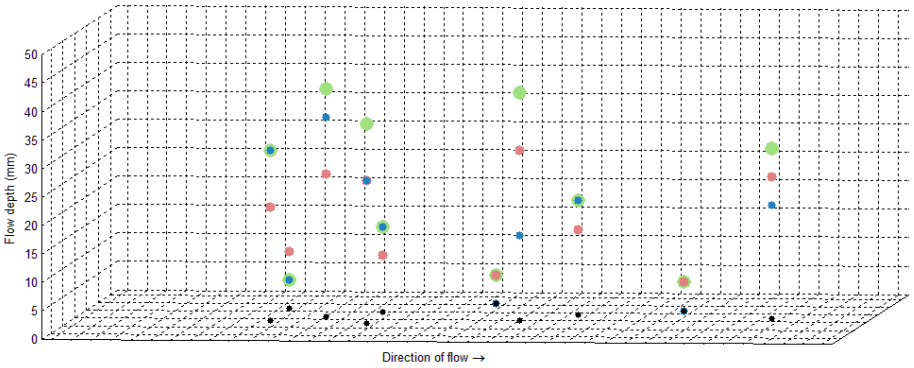

(j) t = 1.2 s

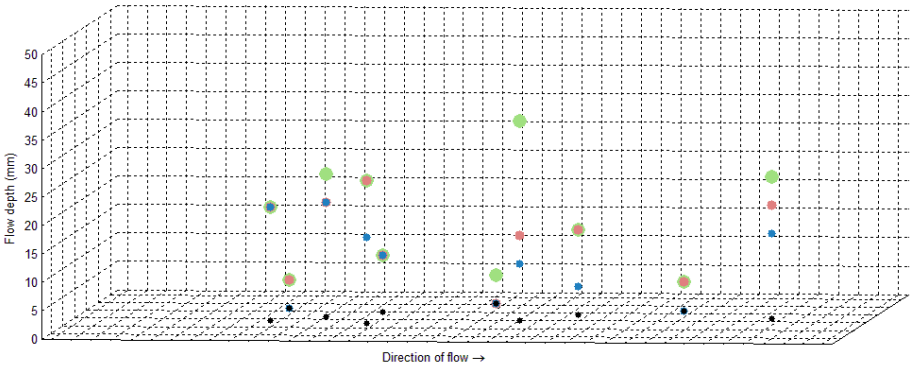

(k) t = 1.4 s

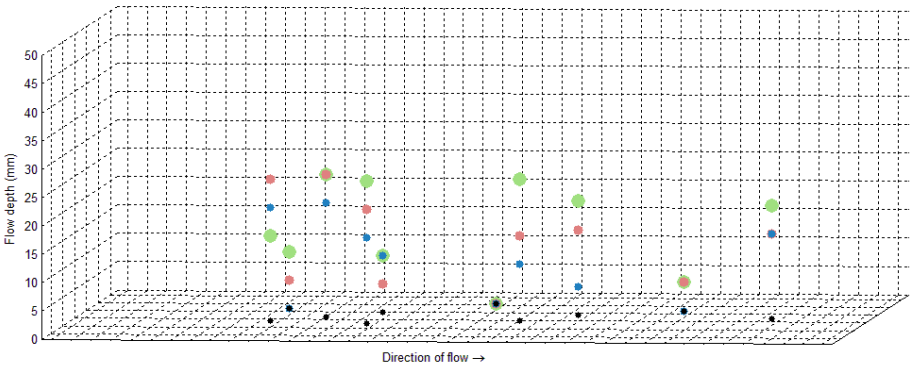

(l) t = 1.6 s

Figure 5.6: Continued: Plots of the flow depth for the three masses 2 kg, 4 kg, and 6 kg. Experiments 19, 20, and 21 are used as examples (stem diameter: 3.2 mm, forest density: 50%).

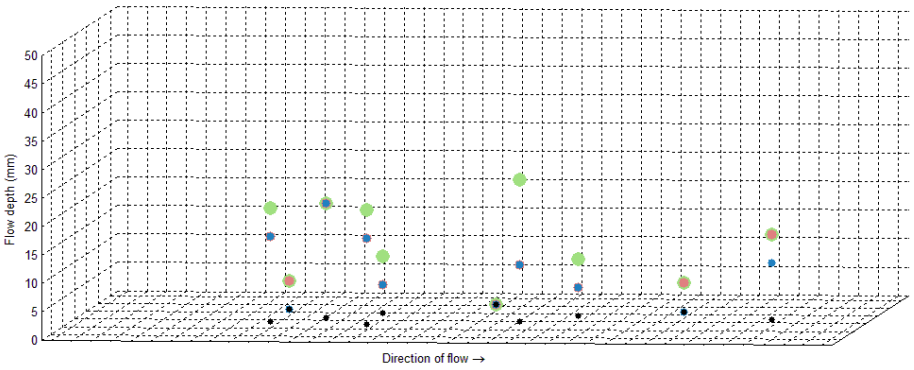

(m) t = 1.8 s

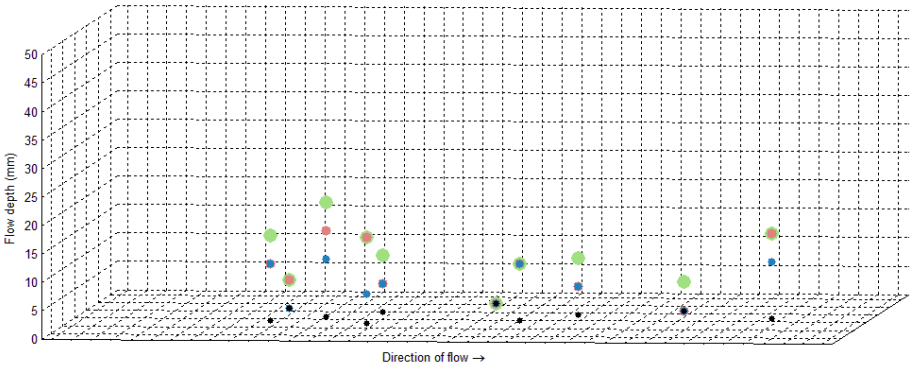

(n) t = 2.0 s

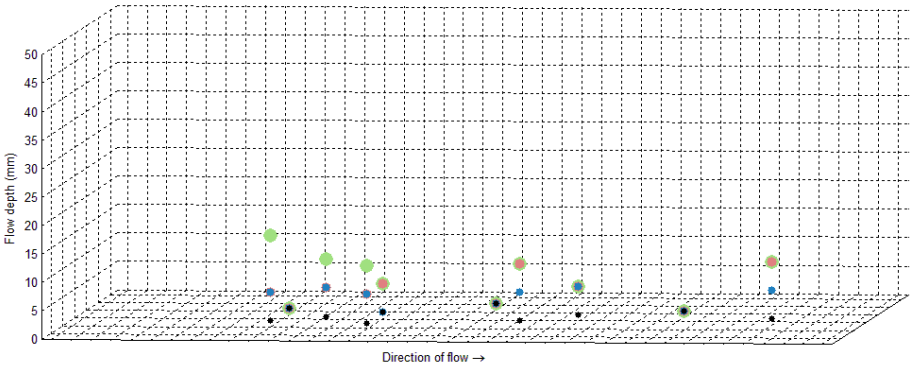

(o) t = 2.5 s

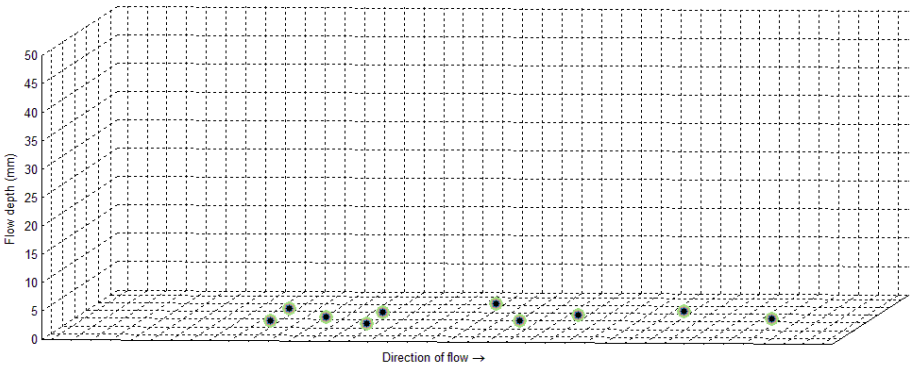

(p) t = 4.0 s

Figure 5.6: Continued: Plots of the flow depth for the three masses 2 kg, 4 kg, and 6 kg. Experiments 19, 20, and 21 are used as examples (stem diameter: 3.2 mm, forest density: 50%).

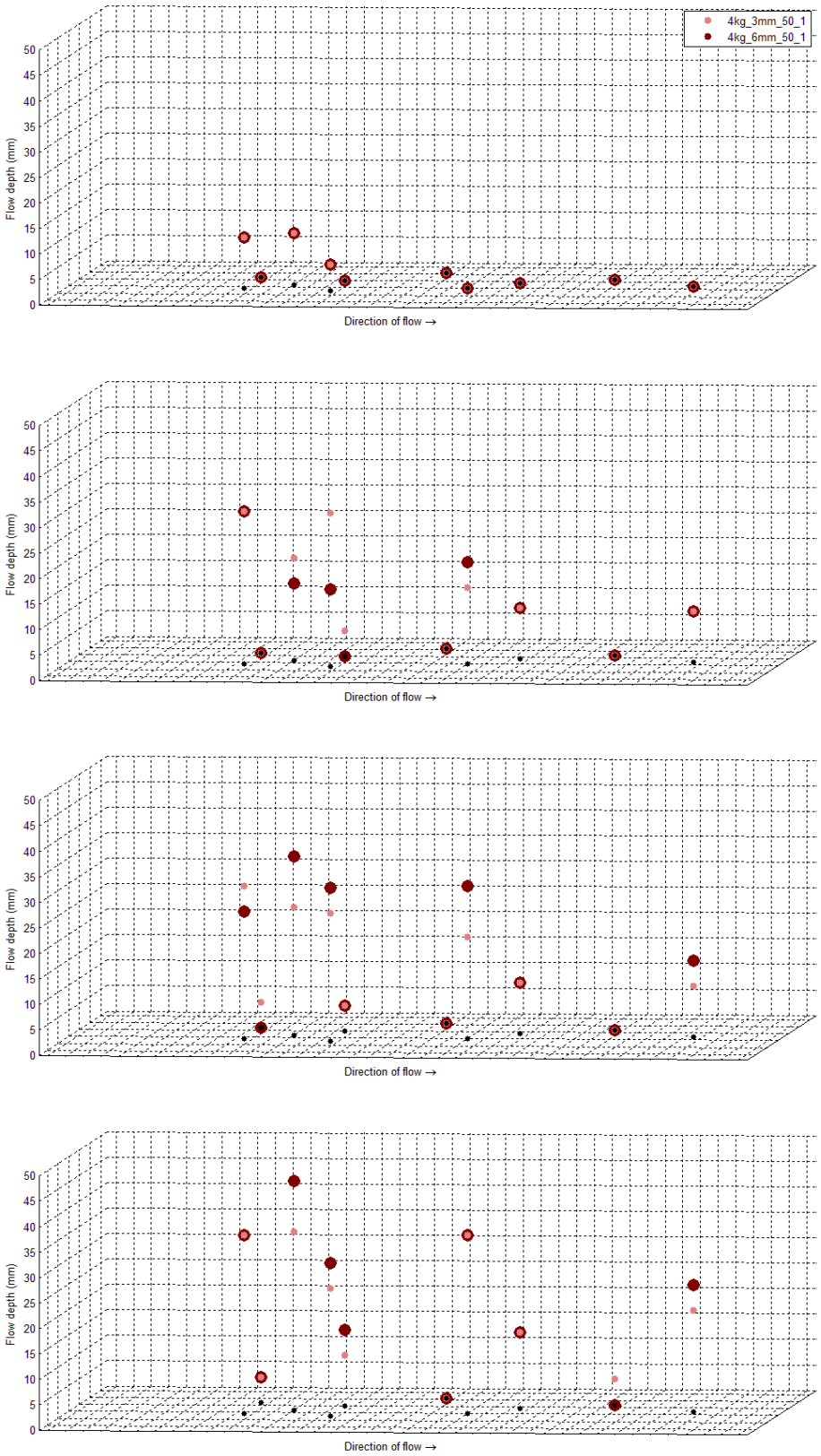

(a) t = 0

(b) t = 0.1 s

(c) t = 0.2 s

(d) t = 0.3 s

Figure 5.7: Plots of the flow depth for the two stem diameters 3.2 mm and 6 mm. Experiments 19 and 22 are used as examples (mass: 4 kg, forest density: 50%).

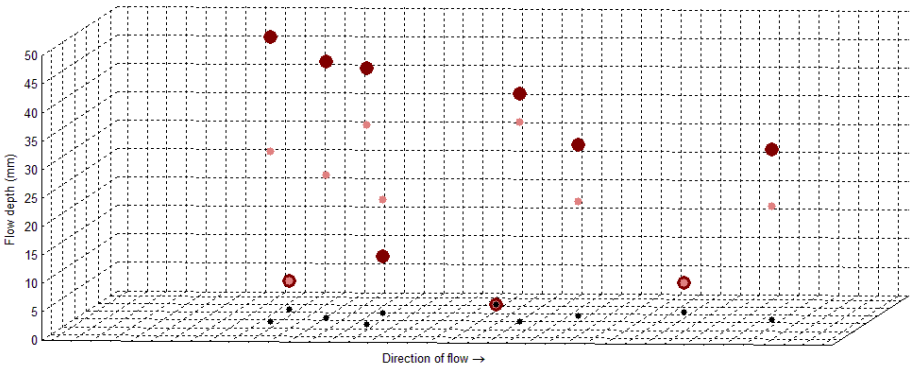

(e) t = 0.4 s

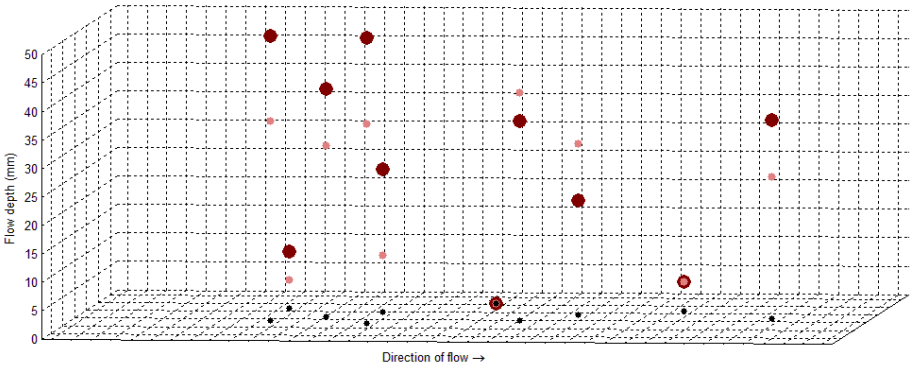

(f) t = 0.5 s

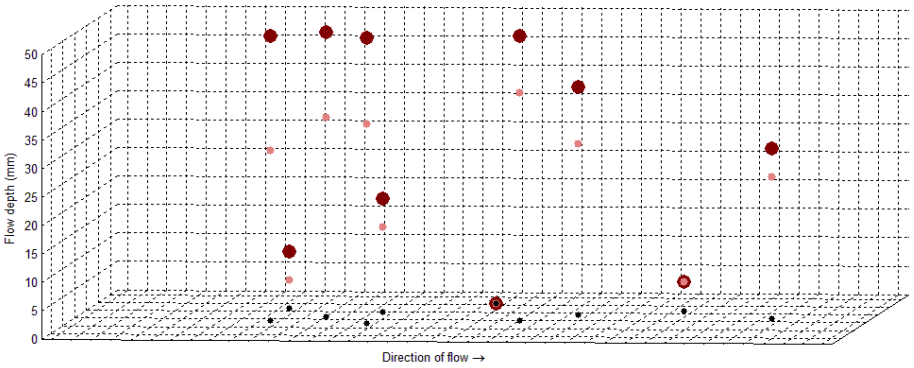

(g) t = 0.6

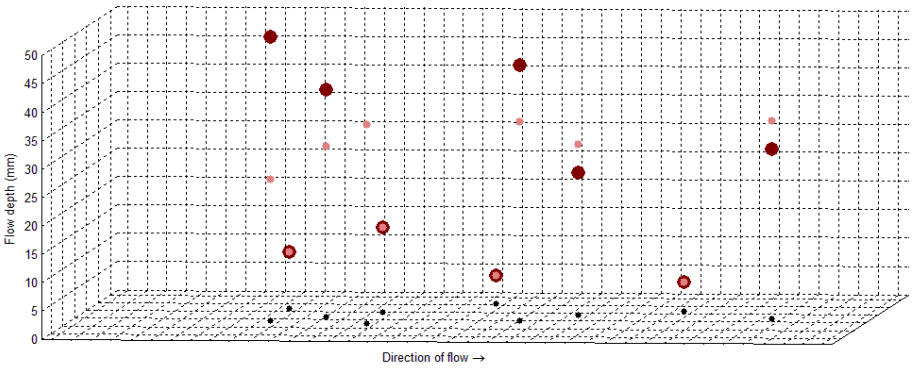

(h) t = 0.8 s

Figure 5.7: Continued: Plots of the flow depth for the two stem diameters 3.2 mm and 6 mm. Experiments 19 and 22 are used as examples (mass: 4 kg, forest density: 50%).

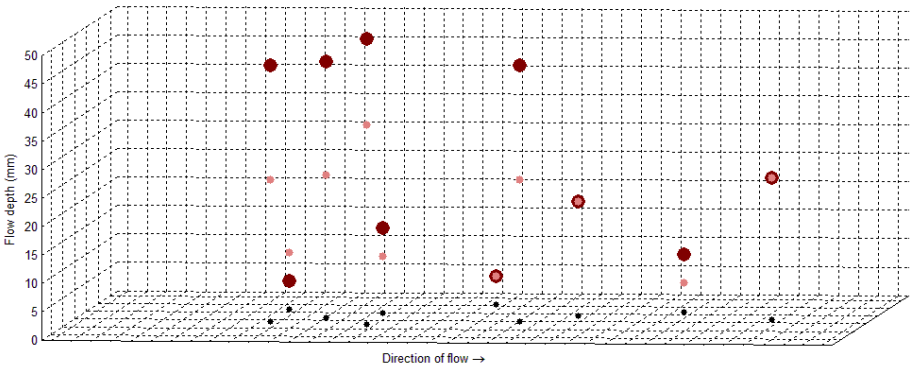

(i) t = 1.0 s

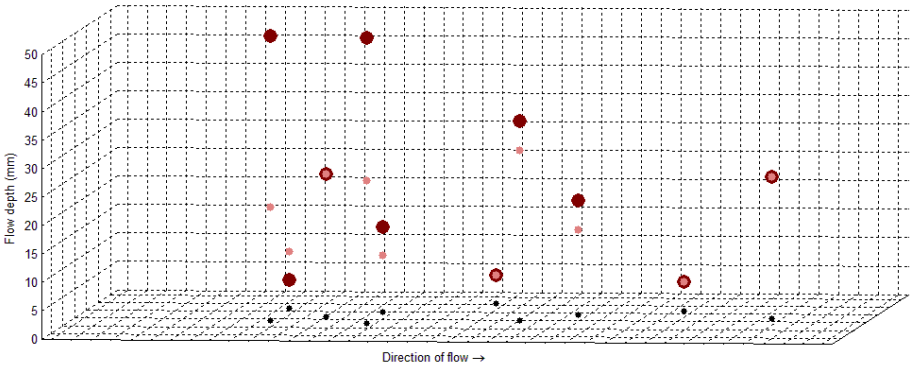

(j) t = 1.2 s

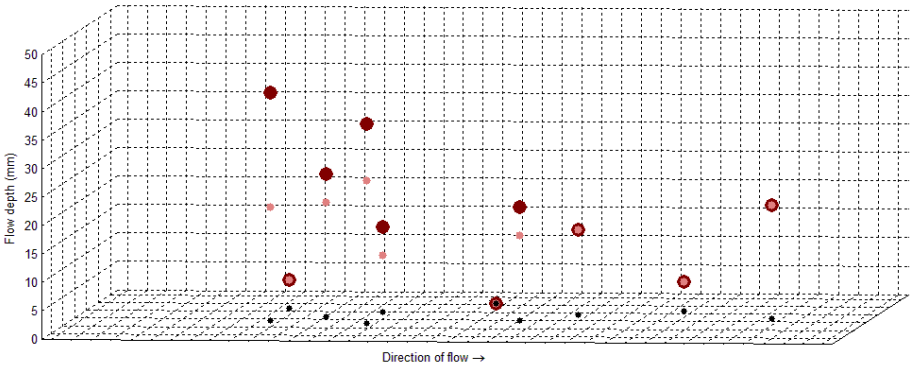

(k) t = 1.4 s

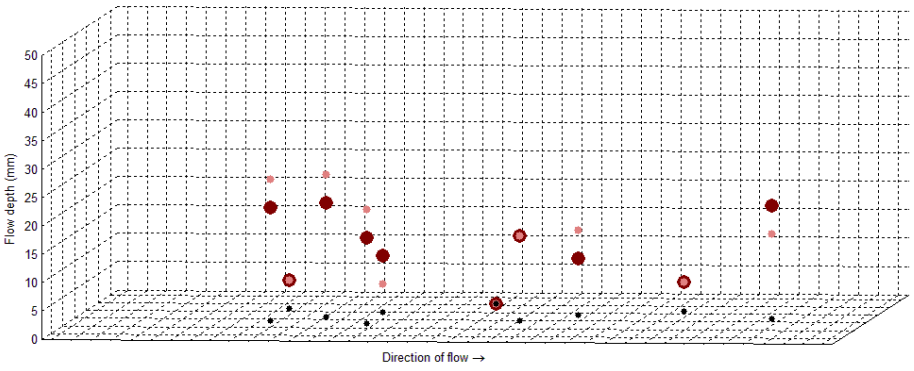

(l) t = 1.6 s

Figure 5.7: Continued: Plots of the flow depth for the two stem diameters 3.2 mm and 6 mm. Experiments 19 and 22 are used as examples (mass: 4 kg, forest density: 50%).

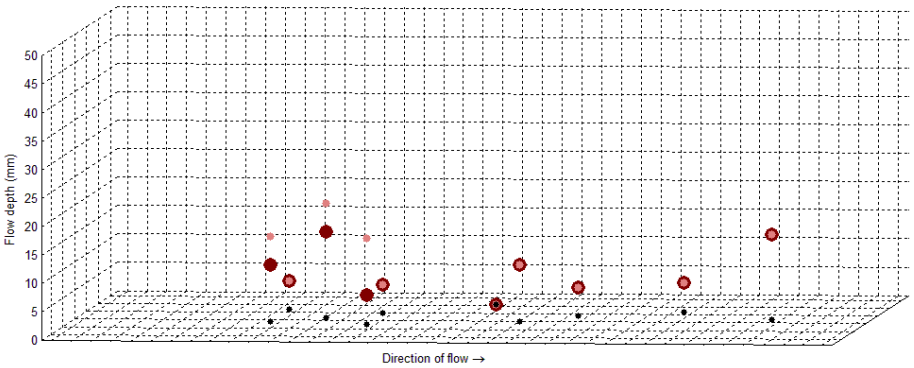

(m) t = 1.8 s

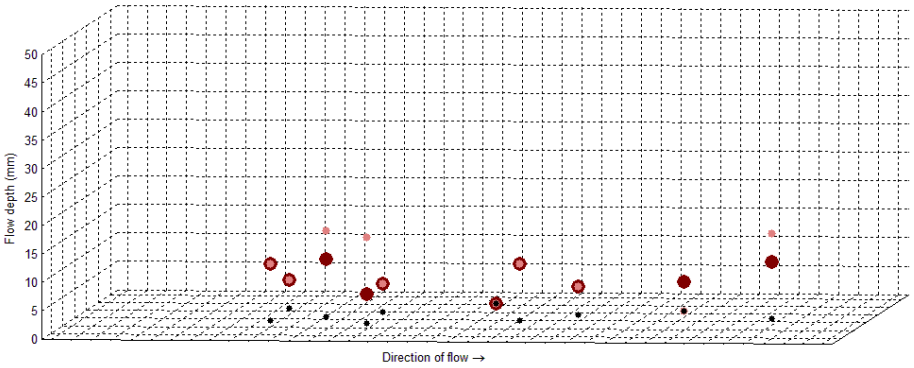

(n) t = 2.0 s

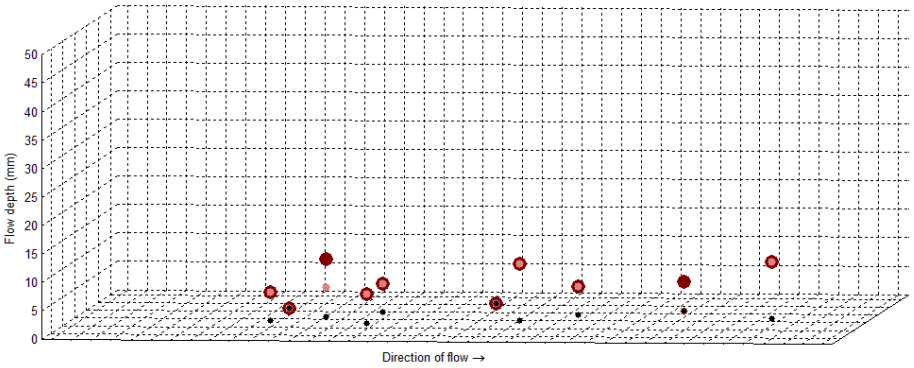

(o) t = 2.5 s

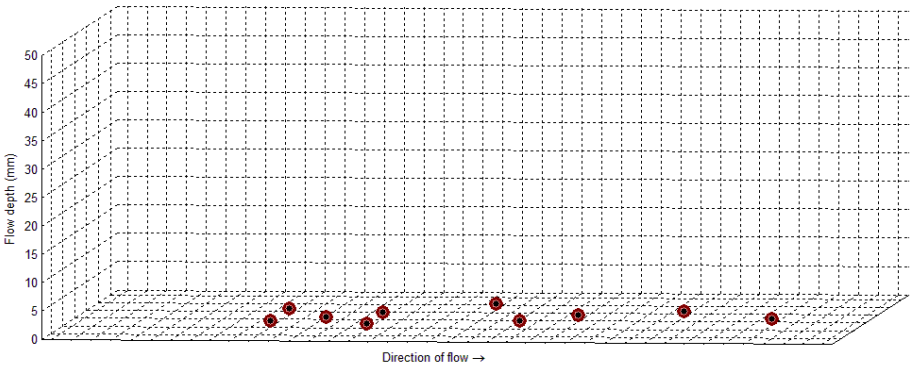

(p) t = 4.0 s

Figure 5.7: Continued: Plots of the flow depth for the two stem diameters 3.2 mm and 6 mm. Experiments 19 and 22 are used as examples (mass: 4 kg, forest density: 50%).

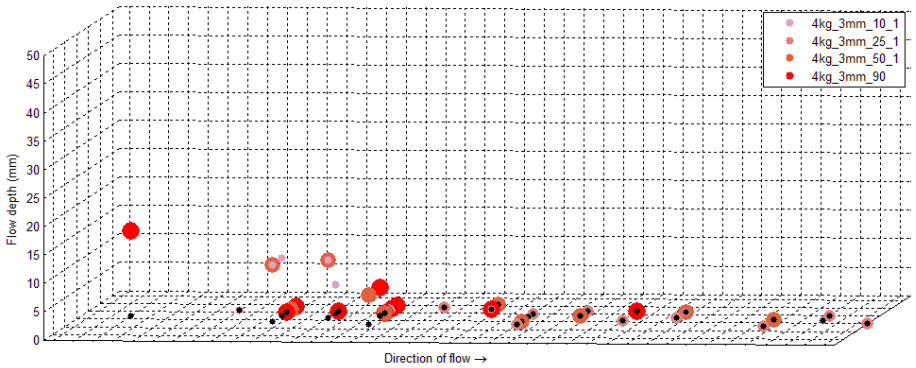

(a) t = 0

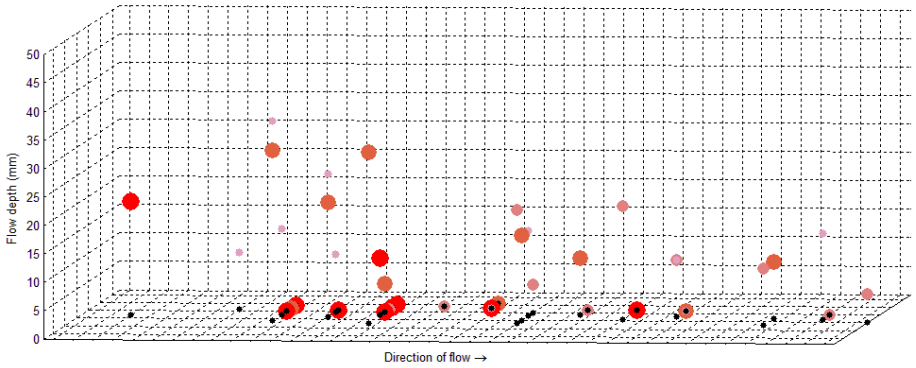

(b) t = 0.1 s

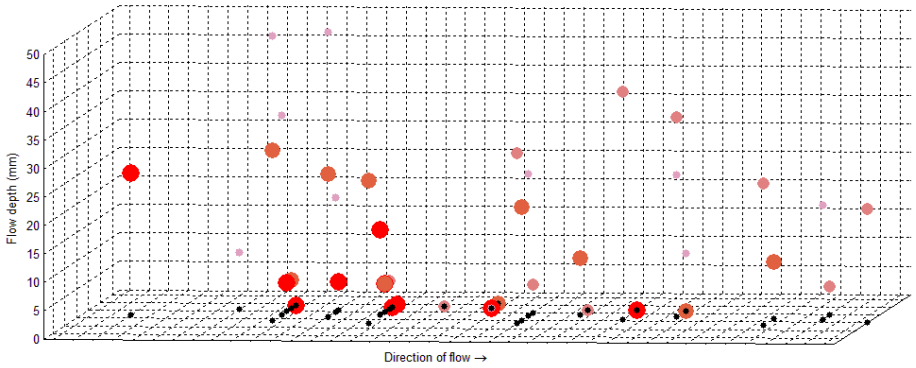

(c) t = 0.2 s

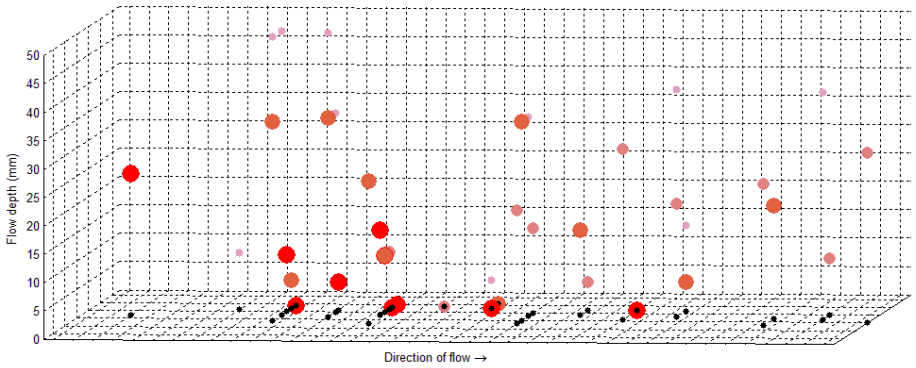

(d) t = 0.3 s

Figure 5.8: Plots of the flow depth for the four forest densities 10%, 25%, 50%, and 90%. Experiments 8, 19, 32, and 48 are used as examples (mass: 4 kg, stem diameter: 3.2 mm).

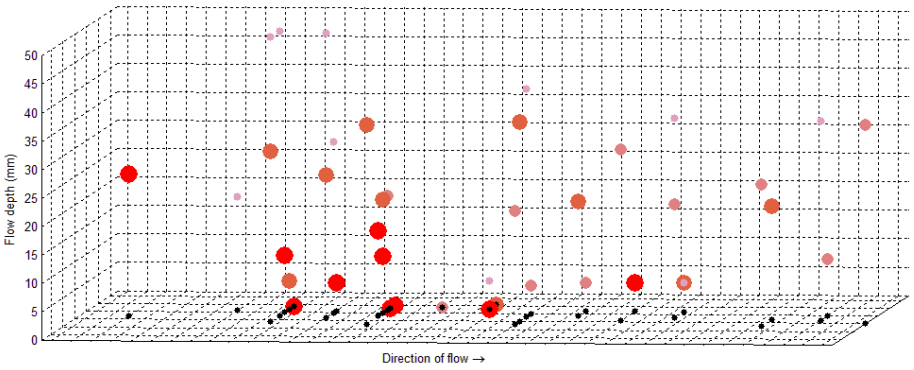

(e) t = 0.4 s

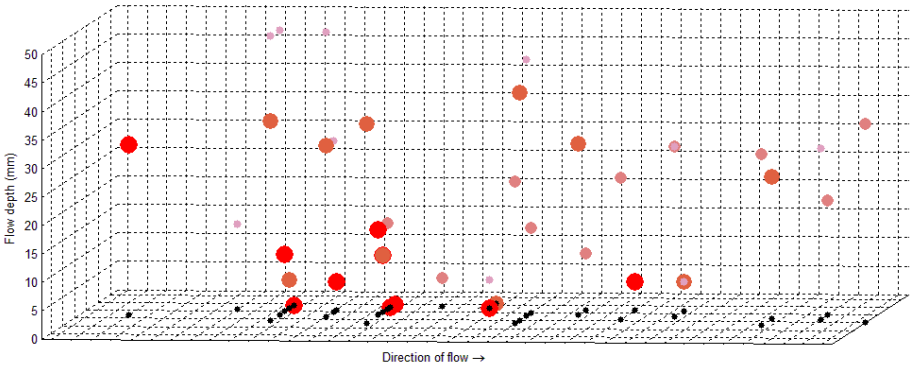

(f) t = 0.5 s

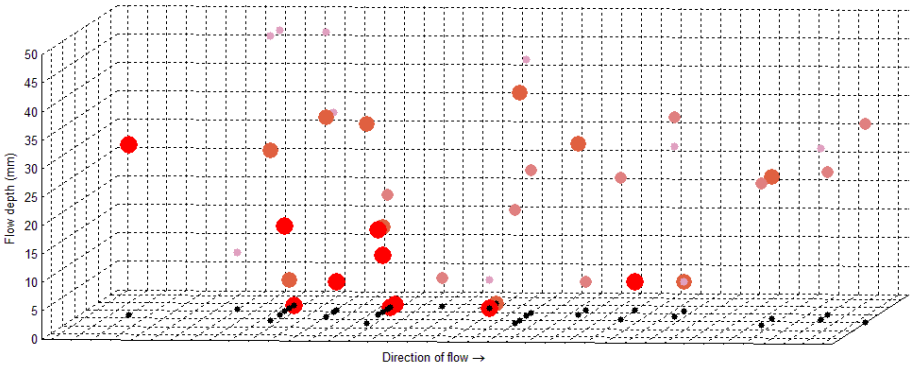

(g) t = 0.6

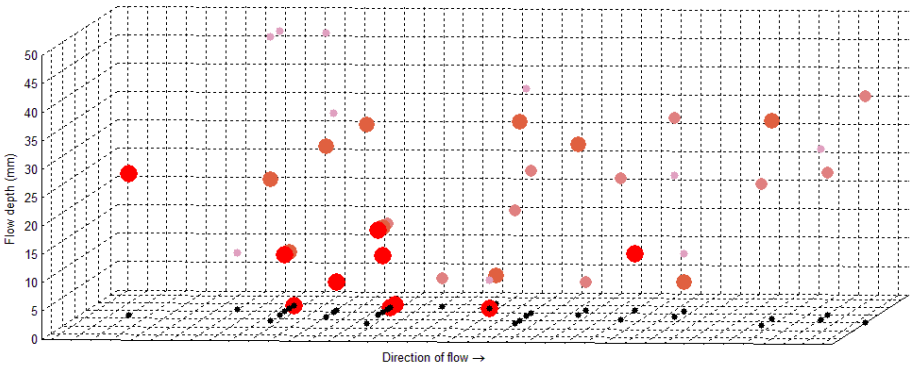

(h) t = 0.8 s

Figure 5.8: Continued: Plots of the flow depth for the four forest densities 10%, 25%, 50%, and 90%. Experiments 8, 19, 32, and 48 are used as examples (mass: 4 kg, stem diameter: 3.2 mm).

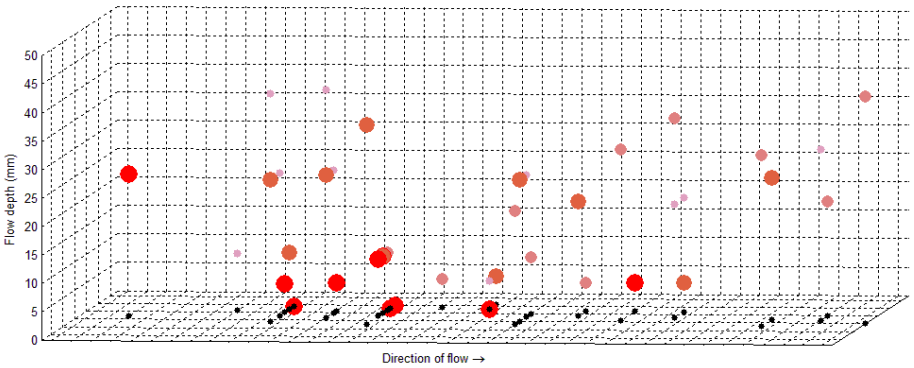

(i) t = 1.0 s

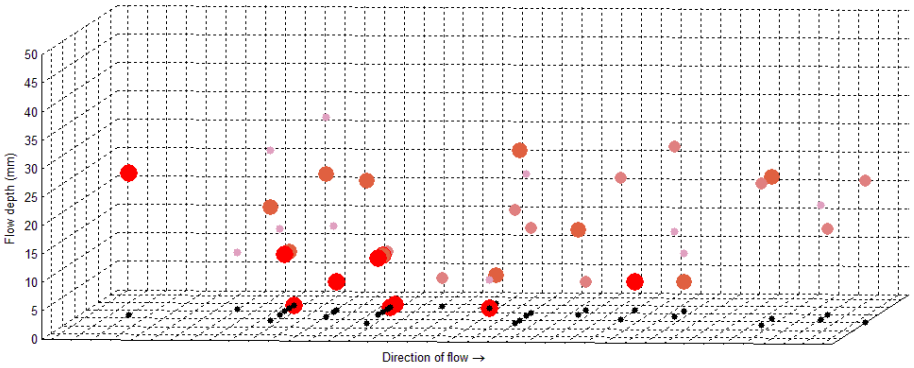

(j) t = 1.2 s

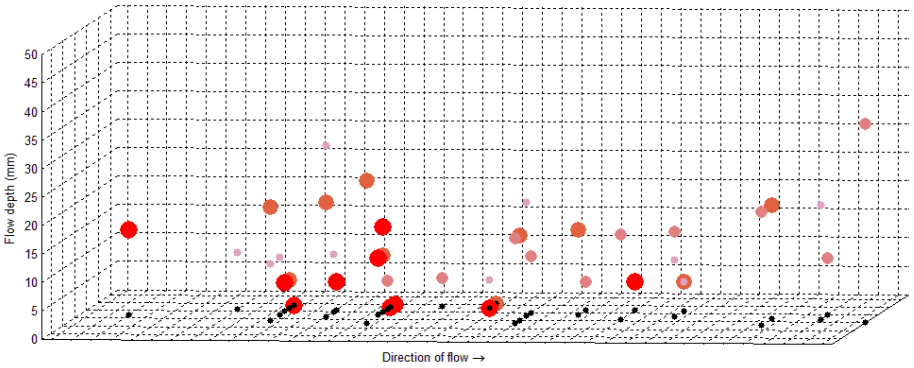

(k) t = 1.4 s

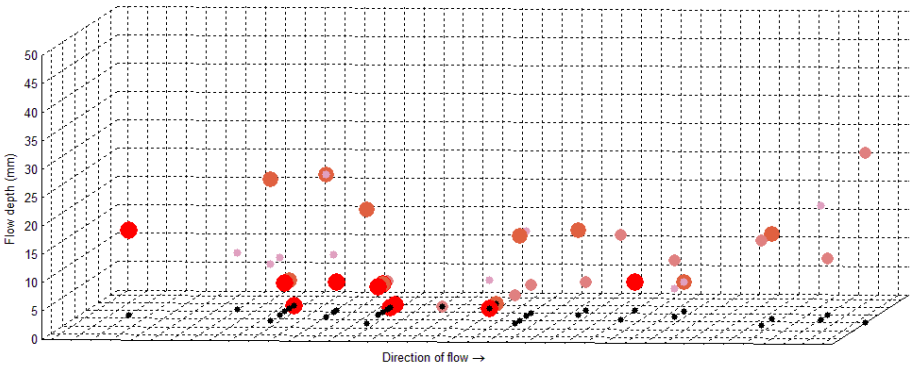

(l) t = 1.6 s

Figure 5.8: Continued: Plots of the flow depth for the four forest densities 10%, 25%, 50%, and 90%. Experiments 8, 19, 32, and 48 are used as examples (mass: 4 kg, stem diameter: 3.2 mm).

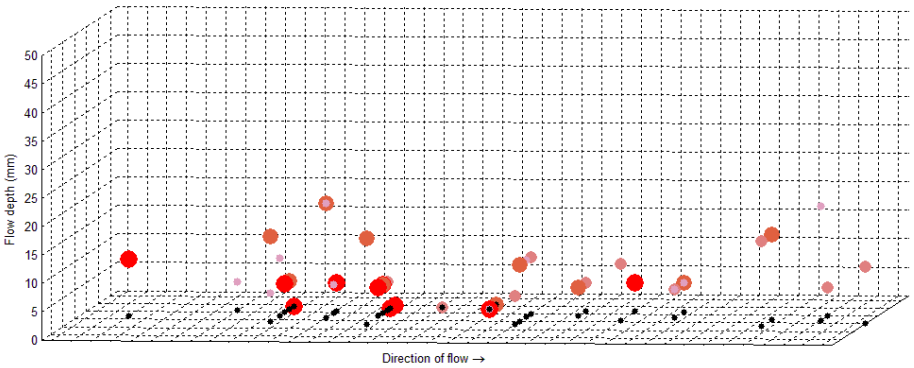

(m) t = 1.8 s

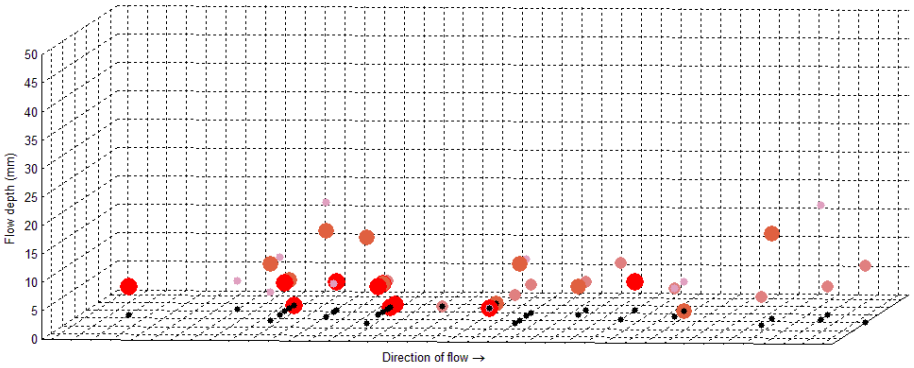

(n) t = 2.0 s

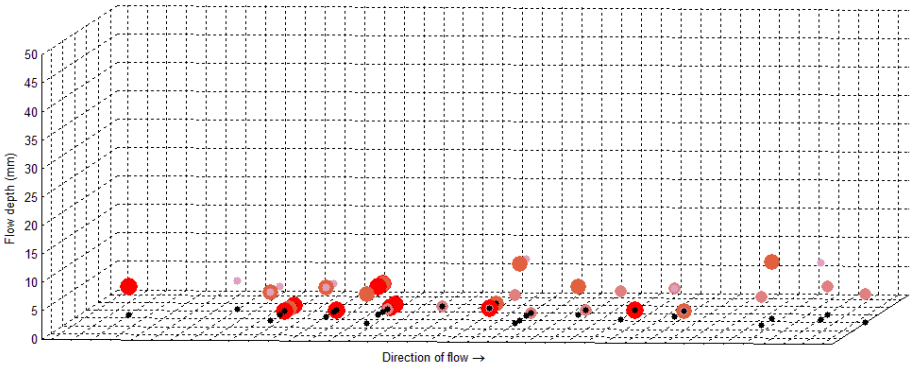

(o) t = 2.5 s

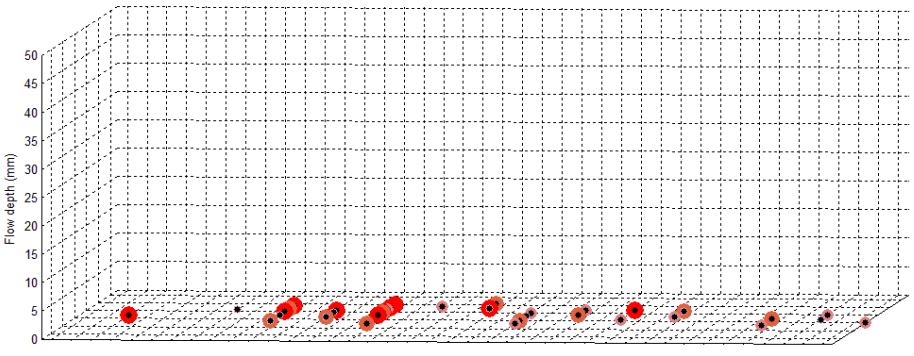

(p) t = 4.0 s

Figure 5.8: Continued: Plots of the flow depth for the four forest densities 10%, 25%, 50%, and 90%. Experiments 8, 19, 32, and 48 are used as examples (mass: 4 kg, stem diameter: 3.2 mm).

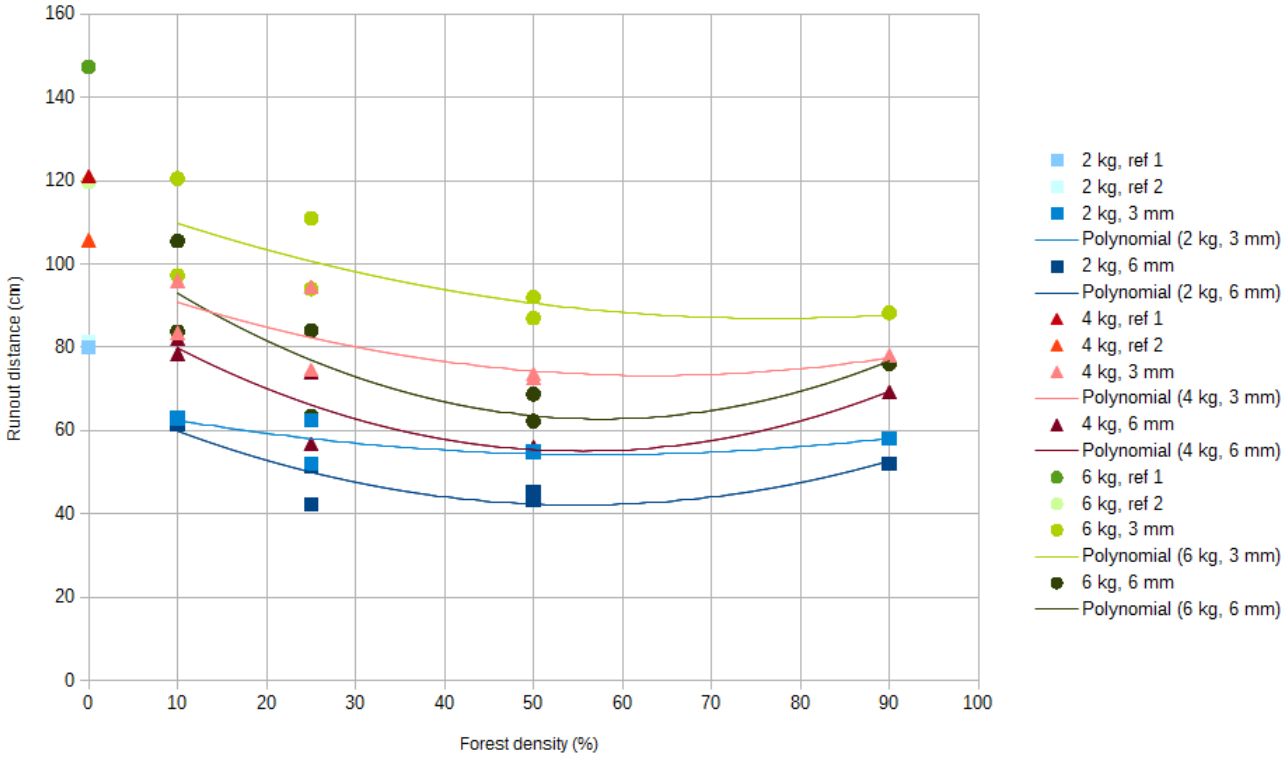

Figure 5.9: Plot of the runout distance against the forest density fitted with quadratic trendlines.

Chapter 6

Summary and recommendations for further work

6.1 Summary and conclusions

In this thesis, we have carried out a series of small-scale chute experiments to study the braking effect of trees on small to medium snow avalanches. We assume that the avalanche releases above the forest and that the trees are not broken or bent upon impact of the avalanche.

In Chapter 2, we have given an overview of snow avalanche terminology, types of snow avalanches, avalanche formation, and avalanche-prone terrain. The theoretical background for the experimental study has been given in Chapter 3. The large-scale behaviour of a snow avalanche is commonly approximated by the flow of a continuous homogeneous fluid. We have described the Voellmy-Salm model, a dynamical model that assumes that a snow avalanche behaves like fluid flow in an open channel. As the avalanche moves down the avalanche path and into the runout zone, it loses energy in friction and in collision with obstacles. The loss of energy may be visualised by energy lines. In our study, the trees act like rigid cylindrical obstacles to the flow. We have therefore described possible flow regimes for fluid flow around one cylinder and groups of cylinders.

In Chapter 4, we have described the setup of the chute, the materials, and the filming equipment. The chute consists of three straight sections: an upper or "acceleration" section 0.2 m wide and 1.5 m long, a middle or "forest" section 1.0 m wide and 2.0 m long consisting of three

aluminium plates with a rectangular grid of pre-drilled holes, and a lower or "runout" zone 1.0 m wide and 2.0 m long. The inclination of both the upper and the middle section is 35°, while the lower section is inclined at 10°. The avalanche is released from a container at the top of the upper section. The snow is modelled by glass beads (ballotini) with a diameter of 0.1 mm. The trees are modelled by metal pins that are inserted into the aluminium plates in computer-generated random patterns. The experiments were filmed from above and from the side with a frame rate of 60 fps.

Further, the program for the experiments has been described. A total of 54 experiments have been carried out: twelve reference experiments without a forest, of which six were carried out at the beginning and six at the end of the study, and 42 experiments with a forest. We have varied the following three parameters: the velocity at which the avalanche hits the forest (incident front velocity), the stem diameter of the trees, and the forest density. The incident front velocity was varied by varying the mass of the avalanche. Three different masses of ballotini were used: 2 kg, 4 kg, and 6 kg. We used two different stem diameters. The metal pins with a diameter of 3.2 mm were used as the thinner trees. For the thicker trees, plastic tubes with an outer diameter of 6 mm were threaded onto the metal pins. The forest density was varied by varying the number of metal pins inserted into the aluminium plates. The forest density is 100% if there is a metal pin inserted into every pre-drilled hole. Four different densities were used: 10%, 25%, 50%, and 90%. We have measured the front velocity and the flow depth of the avalanche along the forest section of the chute by analyzing the films manually frame-by-frame. Further, the runout distance was measured with a ruler straight after each experiment. This meets Objective 1.

In Section 5.1, we have given a detailed phenomenological description of the flow of the avalanche through the forest, meeting Objective 2. We have observed two main phenomena that have a braking effect on the avalanche: (1) the creation of large fans in the first row of trees that slow down a large amount of the ballotini and (2) the creation of smaller fans further down the chute that spread the ballotini sideways. The larger the mass of ballotini, the larger the fans. The relative effect of each phenomenon depends on the density of the forest. As the forest density increases from 0% to 100%, the amount of ballotini that are slowed down upon entering the forest increases, while the degree of lateral spreading decreases. The optimal combination of the two phenomena occurs around a forest density of 50%. For a stem diameter of 6 mm,

the fans in the first row are larger than for 3.2 mm, while the fans further down the chute are of about the same size as for 3.2 mm. Therefore, the amount of ballotini that are slowed down upon entering the forest is greater for 6 mm than for 3.2 mm, while the degree of lateral spreading is the same for both stem diameters.

For the reference experiments, the front velocity is proportional to the square root of the flow depth as predicted by the Voellmy-Salm model (Section 5.2). We have plotted profiles of the front velocity of the avalanche for both the reference experiments and the forest experiments. The front velocity does not differ significantly between the reference experiments and the forest experiments. The corresponding energy lines have been plotted. Further, we have plotted profiles of the flow depth of the avalanche and compared the flow depth for the different masses, the different stem diameters, and the different forest densities. The flow depth is greatest for a mass of 6 kg, followed by 4 kg and 2 kg, and is greater for a stem diameter of 6 mm than for 3.2 mm. The flow depth increases from the front of the avalanche, attains a maximum, and decreases again towards the tail. For a density of 10%, the flow depth both increases and decreases most rapidly. The flow depth is greatest for 10% at first, but after some time, the flow depths for 25% and 50% become greater. For 90%, the flow depth is smallest at all times. We have plotted the runout distance for each experiment as a function of the forest density and fitted quadratic trendlines for each mass and each stem diameter. The runout distance decreases from 0% through to 50%, but increases again slightly for 90%. This meets Objective 3.

In summary, a forest has a maximum braking effect for forest densities around 50% where trees grow quite densely high up in the avalanche path, slowing down the bulk of the snow, and more openly further down the chute so that the snow can be spread sideways. The braking effect is greatest for mature forests where the trees have larger stem diameters than in younger forests. The larger the avalanche, the greater the braking effect of the forest.

6.2 Discussion

Repeatability

The reference experiments were used to check the repeatability within one day as well as the day-to-day repeatability. From the data given in Table E.1, we see that the repeatability within

one day was very good, in particular for the reference experiments carried out before the forest experiments (Day 1) where the runout distances measured were within 0.5 cm of each other for each of the three masses of ballotini. However, we see that the runout distances measured during the reference experiments carried out after the forest experiments (Day 9) are about 15 cm (about 12%) shorter for 4 kg and about 27.5 cm (about 19%) shorter for 6 cm, and about the same only for 2 kg. Below, we discuss possible sources of error. The repeatability of the forest experiments was not checked.

Sources of error

Environmental errors There were both daily and day-to-day variations in the relative humidity and the air temperature at the laboratory. In particular, the air was very dry, increasing the build-up of electrostatic charges. The following precautions were introduced (see Section 4.5): using a thin layer of ballotini to cover the surface of the chute so that the electron affinity of the surface and the mass of ballotini was the same, using a carbonfibre brush and a microfiber cloth to wipe the ballotini off the surface of the chute, sieving the ballotini through an earthed metallic mesh after each experiment, and using a metallic bowl and a metallic cup. After that, the repeatability within one day was very good, indicating that electrostatic charges did not increase during the day. Day-to-day variations in the relative humidity and air temperature may, however, be one of the reasons for the bad day-to-day repeatability. However, we would expect the error to vary randomly from day to day so that the braking effect of the forest would not be systematically over- or underestimated. As the experiments were carried out in a pile laboratory, there was a lot of dust and sand. Precautions included storing the ballotini in sealed plastic bags and covering the bowl that was used to weigh and pour the ballotini into the container at the top of the chute with a piece of cardboard. As the ballotini were sieved after each experiment, all particles larger than 250 microns were eliminated from the mass of ballotini. As the same ballotini were used throughout the experimental study, the amount of smaller particles in the mass of ballotini is likely to have increased from Day 1 to Day 9.

Equipment errors Bits of carpet tape and metal sticking up from holes that trees had been

pushed down into disturbed the flow considerably (see Section 5.1). The later a forest configuration was used, the more holes there would be from earlier configurations, increasing the error. This is probably the main reason for the poor day-to-day repeatability. We can expect, however, that the higher the forest density, the smaller the error would be as the number of holes would be small relative to the number of trees. The highest error can be expected for the forest configurations with a density of 10%, which were not used until Days 6 and 7 so that the number of holes was high relative to the number of trees. For those configurations, it is possible that we have overestimated the braking effect of the forest considerably.

Human errors All measurements were based on manually reading a scale. When reading off the flow depth at the bottom of the upper chute, there may have been a parallax as the author may have looked at the scale from slightly above or below so that the flow depth may have been over- or underestimated. It was difficult to read off the position of the front of the avalanche from the scale on the bottom of the chute as the colour of the ballotini and the surface of the chute was the same. The very front of the avalanche was almost invisible. Further, the front of the avalanche was jagged and not well-defined. When reading off the flow depth in the forest section from the scale on some of the trees, there were clouds of suspended ballotini between the camera and the trees so that the height of the avalanche at the trees was not visible. Due to the ballotini moving in both suspension, saltation, and gliding, the flow depth was not well-defined. However, as all measurements were carried out by the author of this thesis, there should be no error due to different people defining the front position or the height of the avalanche in different ways.

Model vs. nature

The goal of the thesis was to model the dense core of a small-to-medium dry snow avalanche. The Froude number of the model avalanche was between 6 and 7, which is within the typical range of Froude numbers for dense snow avalanches. With a length scaling of 1:100, the front velocity of the avalanche becomes about 15-20 m/s and the flow height about 0.5-1.3 m. Those are realistic values for the dense core of a small dry snow avalanche.

A natural mountain forest will grow in a random pattern. Although we randomized the pattern in which the trees were inserted in the aluminium plates in the forest section of the chute, the underlying pattern of holes was regular. The higher the forest density, the more regular the pattern of trees became. Even with a forest density of 90%, there were 32 corridors without any trees. With a stem diameter of 3.2 and 6 mm, the total width of the corridors was respectively 89% and 80% of the width of the forest. Further, natural trees have a crown. Assuming that the branches of the trees are not broken upon impact of the avalanche, the crown will intercept snow balls in suspension. Rather than being spread sideways out of the avalanche path or falling back to the ground and continuing to move down the avalanche path, snow balls may be slowed down or stopped upon impact.

Ballotini are uniformly graded and cohesionless. Dry snow is commonly considered a cohesionless material. However, while the collisions between ballotini and between ballotini and metal pins may be considered elastic, grains of snow and snow balls may deform as they collide with each other and with trees. Upon impact, some of the kinetic energy may be transformed into heat so that snow balls melt in motion and refreeze together as the motion stops. This will give avalanche snow a much higher cohesion.

Rheology of the avalanche

Although the goal of the thesis was to model the dense core of a snow avalanche, it appears that the model avalanche is partly fluidized. In both forested and unforested terrain, the density of the avalanche near the front appears to be very low. In unforested terrain, the density of the rest of the avalanche appears to be that of a dense flowing core. In forested terrain, however, the ballotini are thrown up into the air upon hitting trees. Although there is no powder cloud, a large amount of ballotini are suspended in clouds of very low density at any time. After the ballotini have fallen back to the ground, it is reasonable to assume that they will behave as a saltation layer rather than a dense flowing core. The analogy with the flow of a continuous homogeneous fluid that the theory in Chapter 3 is based on may not be valid for the model avalanche in this study. In contrast to an incompressible liquid, large parts of the avalanche may be compressed into a denser packing. The less dense the avalanche, the more compressible it becomes. For an incompressible fluid, one would expect the permeability of a group of cylinders to decrease

with an increasing number of cylinders in the flow path. This analogy may not be valid as the density of the avalanche decreases with increasing forest density as more ballotini are thrown into suspension by the first row of trees. Further, the theory on fluid flow around cylinders and groups of cylinders assumes that the cylinders are immersed in the fluid before the fluid is set in motion. There is no fluid front that hits the cylinders. This may be the reason why we have observed the creation of fans rather than a flow regime with the creation of a laminar vortex street.

Comparison with other studies

To the author's knowledge, no experimental studies have been published on the flow of a granular material around a group of slender cylindrical obstacles. In Chapter 1, we gave an overview over five experimental studies on the flow of a granular material around respectively a pyramid-shaped obstacle (Gray et al., 2003), braking mounds and a dam (Hákonardóttir et al., 2001), a dam (Faug et al., 2003), braking mounds, collecting dams, and diverting dams (Brateng, 2005), and a single slender cylinder or rectangular block (Hauksson et al., 2007). The behaviour of the avalanche upon hitting the obstacle depends on the geometry of the obstacle. The metal pins we used to model the tree stems may be considered as slender cylindrical obstacles. Like Hauksson et al. (2007), we observed the creation of fans. However, the size of the fans depends on the position of the metal pin on the chute and the pin's position relative to other pins. While fans near the centre of the chute are symmetrical, fans furthest to the side have one wing pointing in the direction of flow and one wing pointing away from the direction of flow. The slender obstacles in Hauksson et al. (2007) are located at the centre of the chute and therefore symmetrical. Although Hákonardóttir et al. (2001), Faug et al. (2003), and Brateng (2005) observe a different type of flow behaviour, with the granular material being thrown up into a jet from the top of the obstacles, the conclusions on the braking effect of the obstacles may be compared with the conclusions from our study. Brateng (2005) concludes that placing the mounds in a row gives the highest degree of spreading, that the degree of spreading is highest if the row of mounds is placed high up on the chute, that more than one row of mounds increases the total braking effect, and that increasing the density of mounds per row increases the braking effect up to a density of 0.7-0.8. For higher densities, the braking effect decreases again. In our study, we have

not compared the degree of lateral spreading for forest configurations with different positions of the first row, and we have not compared the degree of lateral spreading for a row of trees and single trees in different rows. However, for a forest density of 25%, Configuration 2 with the first row of trees high up on the chute had a greater braking effect than Configuration 1, where the first row of trees was located further down the chute. This agrees with the findings in Brateng (2005). We found, however, that the degree of lateral spreading was greatest for a forest density of 10%, with fewer trees per row than for higher forest densities. This is in disagreement with Brateng (2005). In agreement with Brateng (2005), we expect the braking effect of a forest with a single row of trees to be lower than that of a forest with multiple rows of trees as trees further down the chute increase the degree of lateral spreading. However, we expect there to be an upper bound for how many rows there should be and how closely the rows should be located to each other. Like Brateng (2005), we found that increasing the forest density from 0% to 50% increases the braking effect of the forest, while further increasing the density to 90% slightly decreases the braking effect. This is in disagreement with Hákonardóttir et al. (2001), who conclude that the density of mounds in the avalanche path should be as high as possible. Hákonardóttir et al. (2001), however, place the mounds in one row and do not test multiple rows of mounds. Faug et al. (2003) conclude that the braking effect of a dam is a combination of two effects: storage of the granular material upstreams of the dam and local energy dissipation at the dam, where the local dissipation of energy is the most important. In our study, we found that the amount of granular material stored behind the trees was negligible. This is to be expected as a dam has a much larger cross-sectional area normal to the direction of flow than a tree. As we computed energy lines based on the front velocity of the avalanche, which was virtually the same in the experiments in unforested and forested terrain, we have not been able to compute the loss of energy per tree. The slow-down and lateral spreading of the bulk of the granular material upon impact with the trees, which we found to be the most important braking effects of the forest, however, indicates a considerable dissipation of energy at each tree.

6.3 Recommendations for further work

Several approaches have been used to account for the braking effect of trees on snow avalanches in theoretical models for snow avalanche flow. Two approaches were briefly presented in Chapter 1: the "friction approach", where the loss of energy in breaking and overturning trees and entraining woody debris is computed and the friction parameters μ and ξ in the Voellmy-Salm model are adjusted accordingly (Bartelt and Stöckli, 2001), and the "detrainment approach" by Feistl et al. (2014), where the authors compute the loss of momentum due to snow mass being deposited behind tree stems. A third approach would be to adjust μ and ξ by back-calculating model avalanches. As the Voellmy-Salm model applies to the dense-flowing core of a snow avalanche, it is important that the model avalanche not be fluidized. According to Norem et al. (1987), the critical angle above which a model avalanche of glass beads becomes fluidized is between 26° and 32°. We recommend to extend the experimental study of this thesis as follows:

- The inclination of the forest section of the chute should be reduced to 25°. The upper section of the chute might have to be inclined more. As the internal friction angle of the ballotini is about 25°, the avalanche might not start moving at an inclination of 25°.

- As metal bits and pieces of carpet tape sticking up from holes in the carpet tape disturbed the flow of the avalanche considerably, the experiments should be carried out in order of increasing forest density. We recommend to start by generating one random pattern of trees per aluminium plate for the lowest forest density. The plates can be swapped and rotated by 180° to generate a total of 48 possible configurations. Patterns for higher forest densities should be generated by randomly adding trees to the existing three patterns, not by generating completely new patterns. To make the swapping and rotating of the plates more practicable, we recommend using plywood plates rather than aluminium plates.

- We recommend drilling the holes in the plates with a spacing of 10 mm rather than 30 mm. With a minimum spacing of the trees of 30 mm, this will allow for forest configurations where the rows of trees are shifted relative to each other. At high forest densities in particular, this will make the patterns of trees less regular and reduce the total width of corridors without any trees to 68% of the width of the forest for a stem diameter of 3.2 mm

and 41% for a stem diameter of 6 mm.

– To improve the visibility of the front of the avalanche in the forest section of the chute, we recommend using dark plates. The visibility of the front of the avalanche was much better in the highest and lowest parts of the forest section that were made of dark plywood than on the light aluminium plates.

– We recommend to measure the flow depth of the avalanche using a laser. This will allow measurements with a precision of +/- 1 mm, and a profile of the avalanche from front to tail can be measured.

– We recommend to measure the surface velocity of the avalanche at different positions along the avalanche as the front velocity was a poor indicator of the braking effect of the forest. This can be done by adding coloured glass beads of a larger size to the mass of ballotini and tracking the position of each bead along the chute. One should check that the flow of the avalanche is not disturbed by the beads, neither in unforested nor in forested terrain.

Appendix A

MATLAB code

A.1 Generation of a random forest pattern

Below, the code of the MATLAB function `forest_generator` used for generating a random forest pattern within a grid of 33 by 16 points is given. The function is called with the parameter `density`, the forest density given as a fraction of the total number of grid points.

```
function forest_generator(density)

rows = 16;
cols = 33;
f = zeros(rows,cols);
no_trees = floor(density*rows*cols);
r = randperm(rows*cols,no_trees);

for i=1:no_trees
    f(r(i)) = 1;
end
print_matrix(f);

end
```

The function `print_matrix` given below prints a given matrix to the computer screen. Here, `print_matrix` is called by the function `forest_generator` to print the forest pattern generated.

```
function print_matrix(matrix)

[rows cols] = size(matrix);
for i=1:rows
    for j=1:cols
        fprintf('%i ',matrix(i,j));
    end
    fprintf('\n');
end

end
```

Appendix B

Forest configurations

- `.` – grid point without a tree
- `*` – tree
- `*` – tree marked with a scale
- • – grid point with a broken metal pin pushed down into the hole

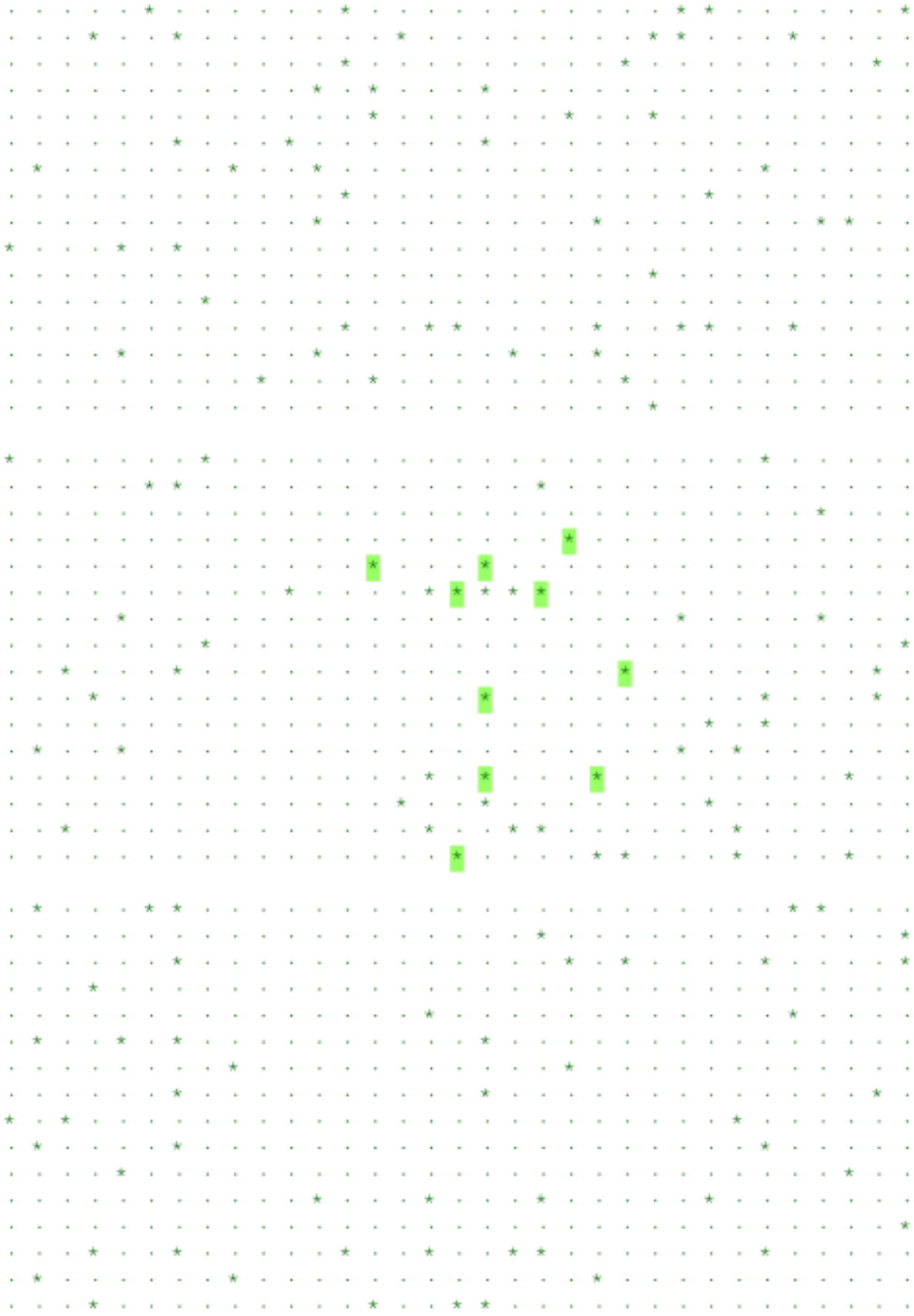

Figure B.1: Forest density 10%, Configuration 1

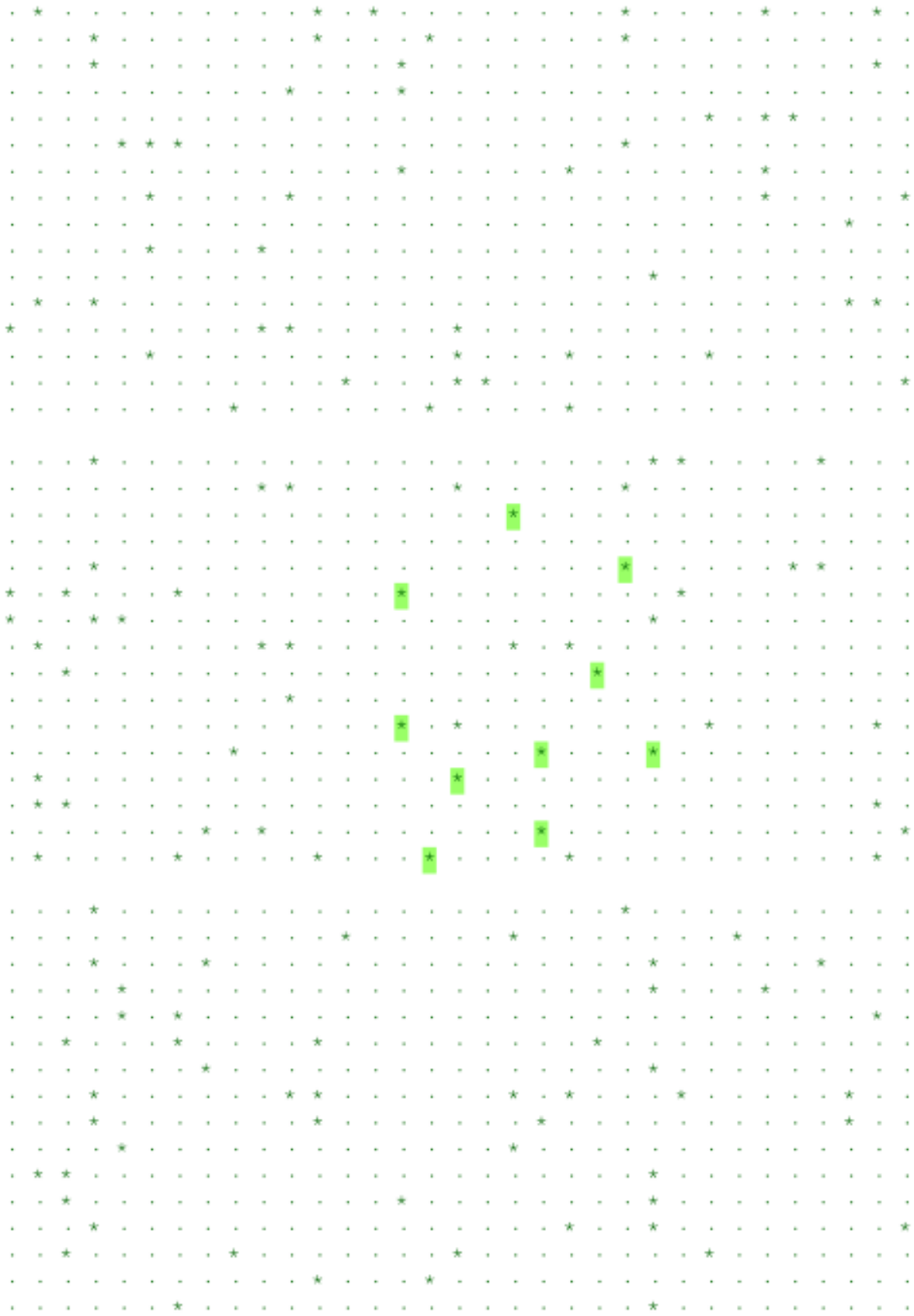

Figure B.2: Forest density 10%, Configuration 2

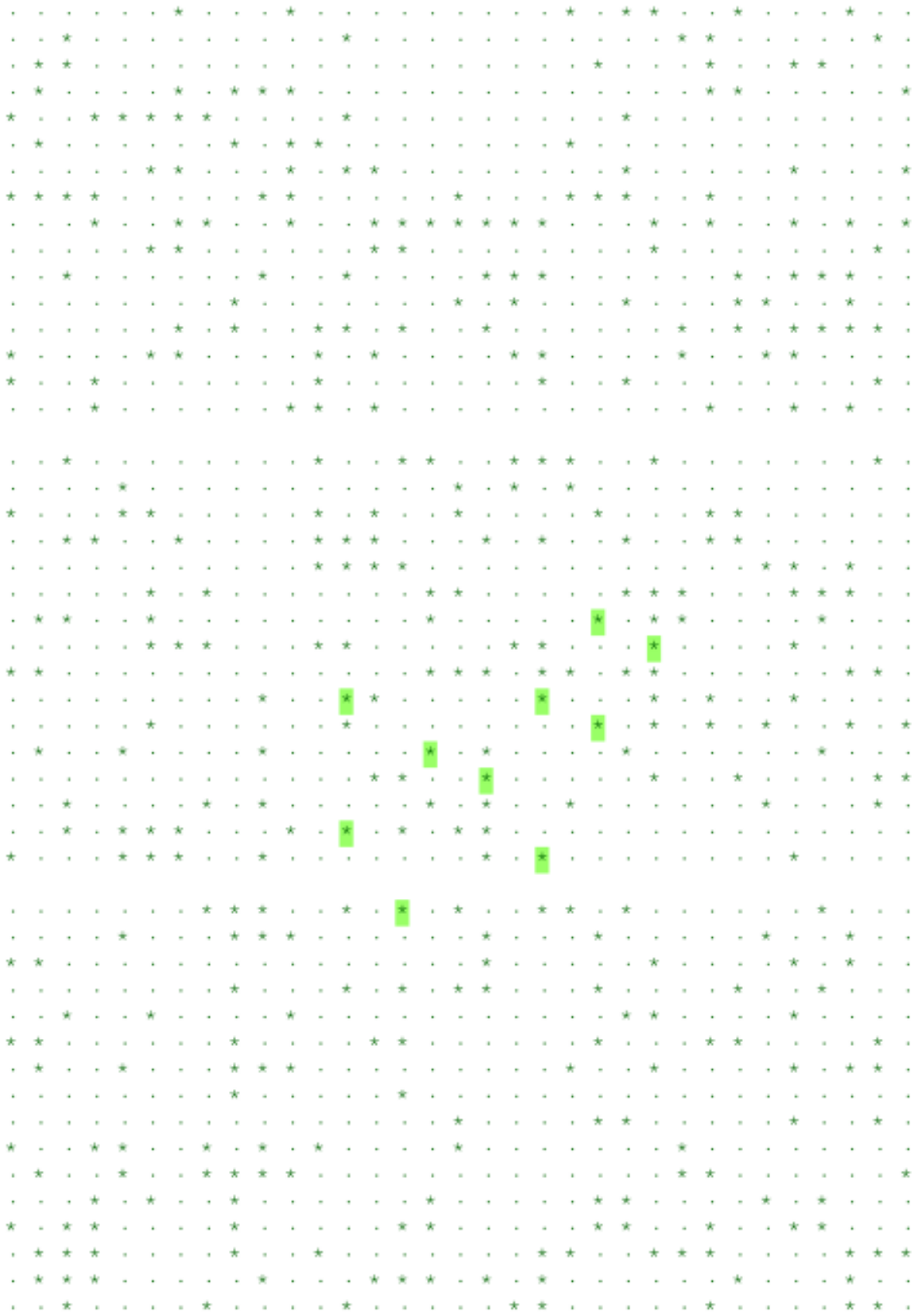

Figure B.3: Forest density 25%, Configuration 1

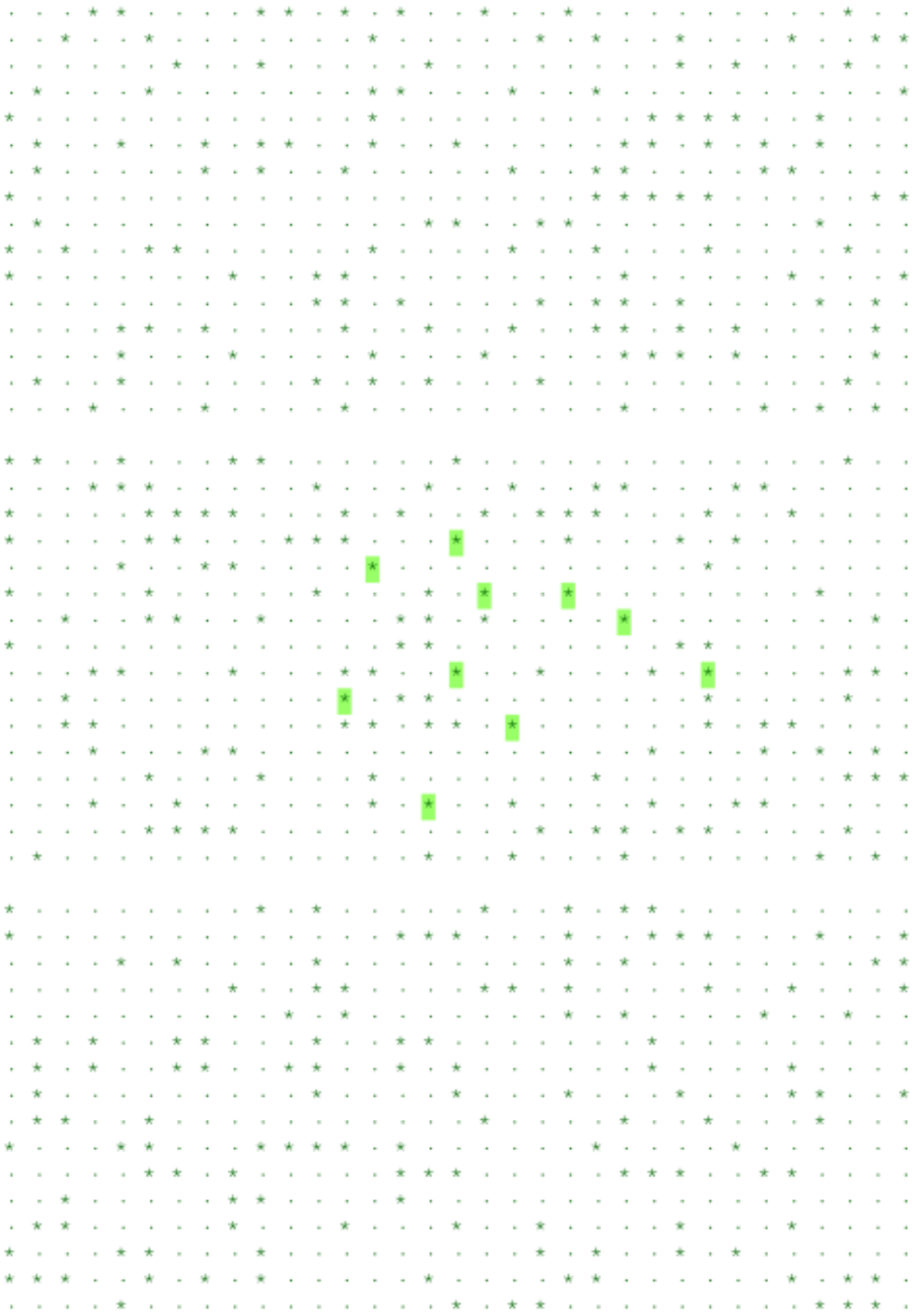

Figure B.4: Forest density 25%, Configuration 2

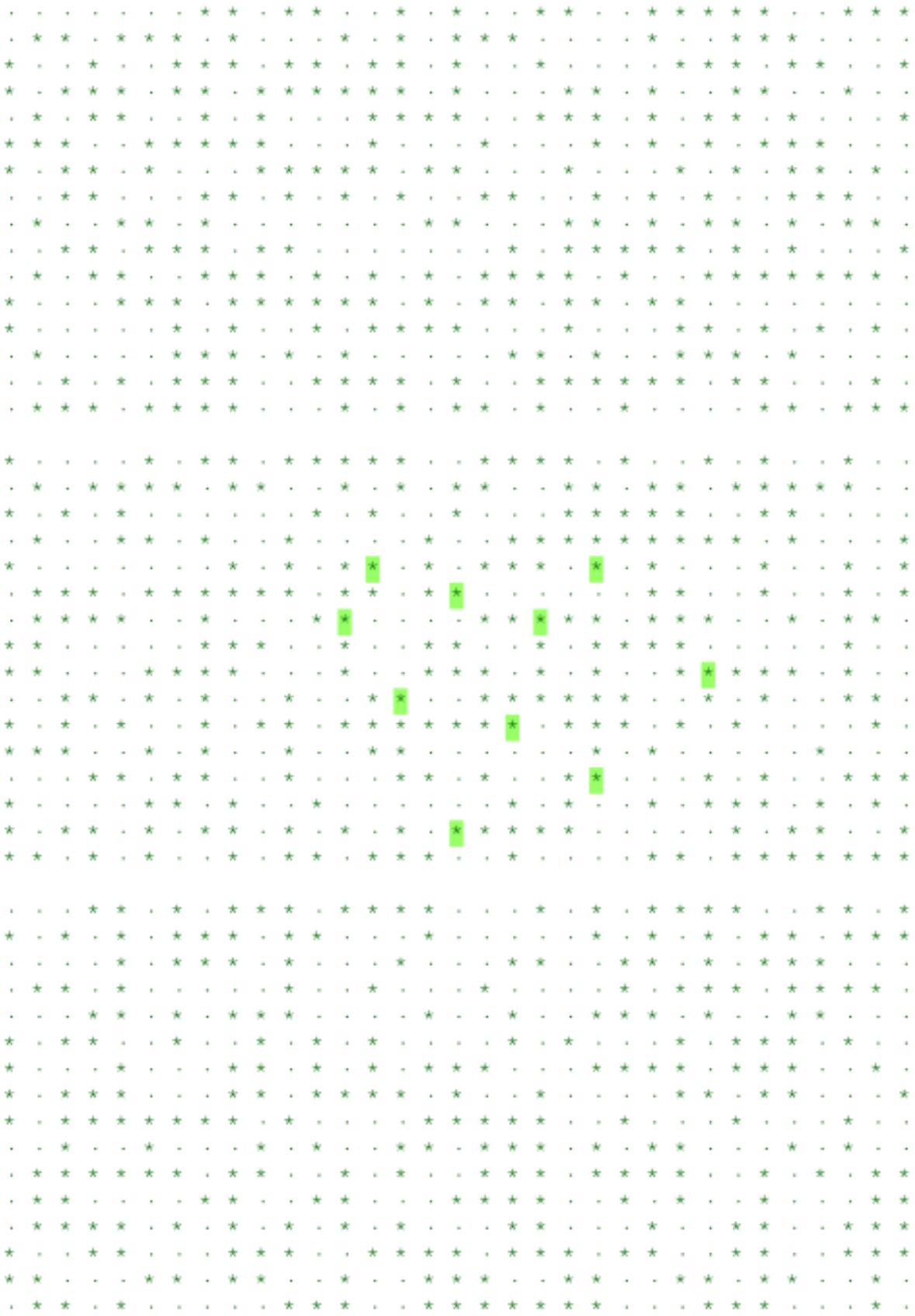

Figure B.5: Forest density 50%, Configuration 1

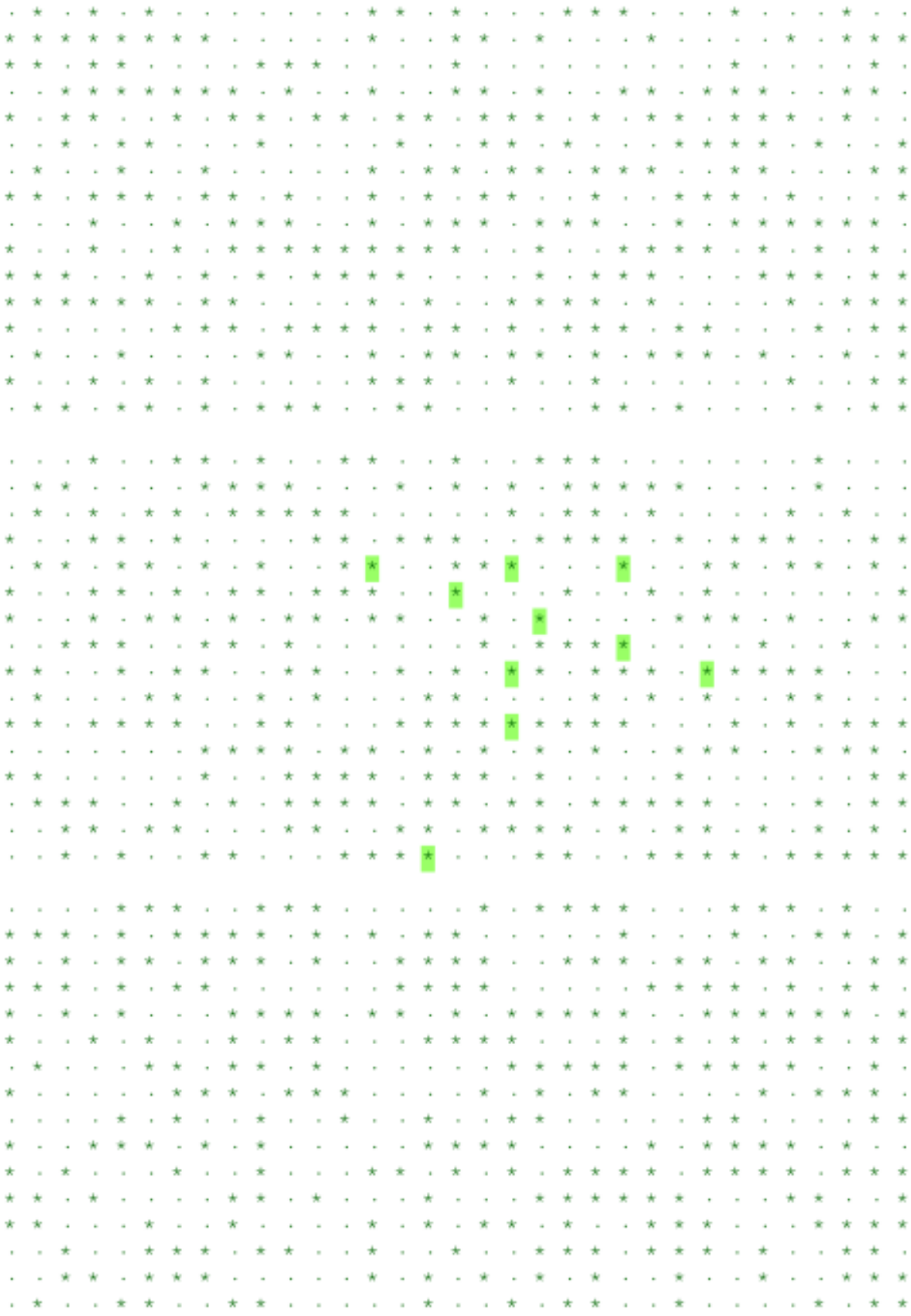

Figure B.6: Forest density 50%, Configuration 2

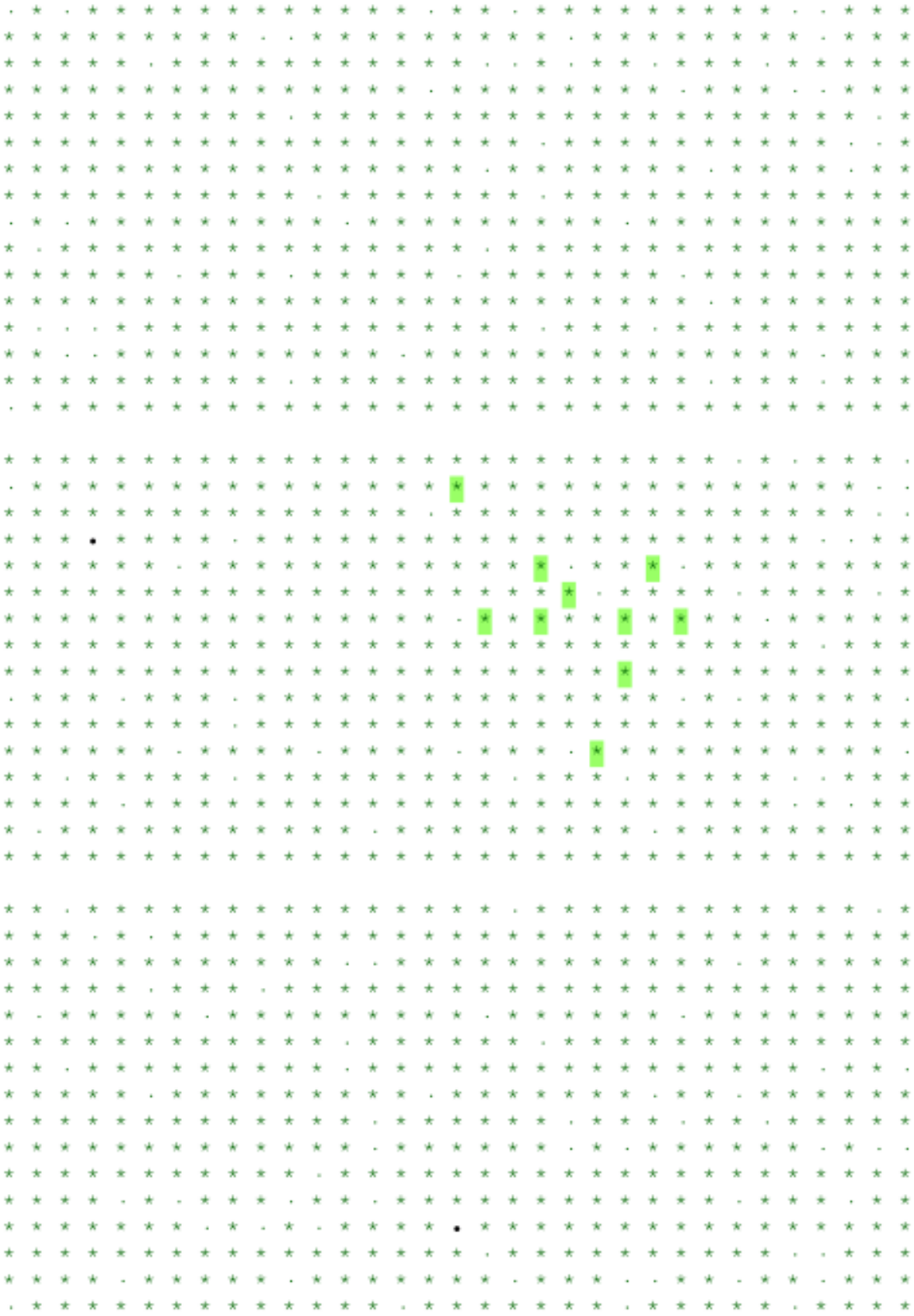

Figure B.7: Forest density 90%

Appendix C

Snapshot sequences from selected videos

C.1 Front view

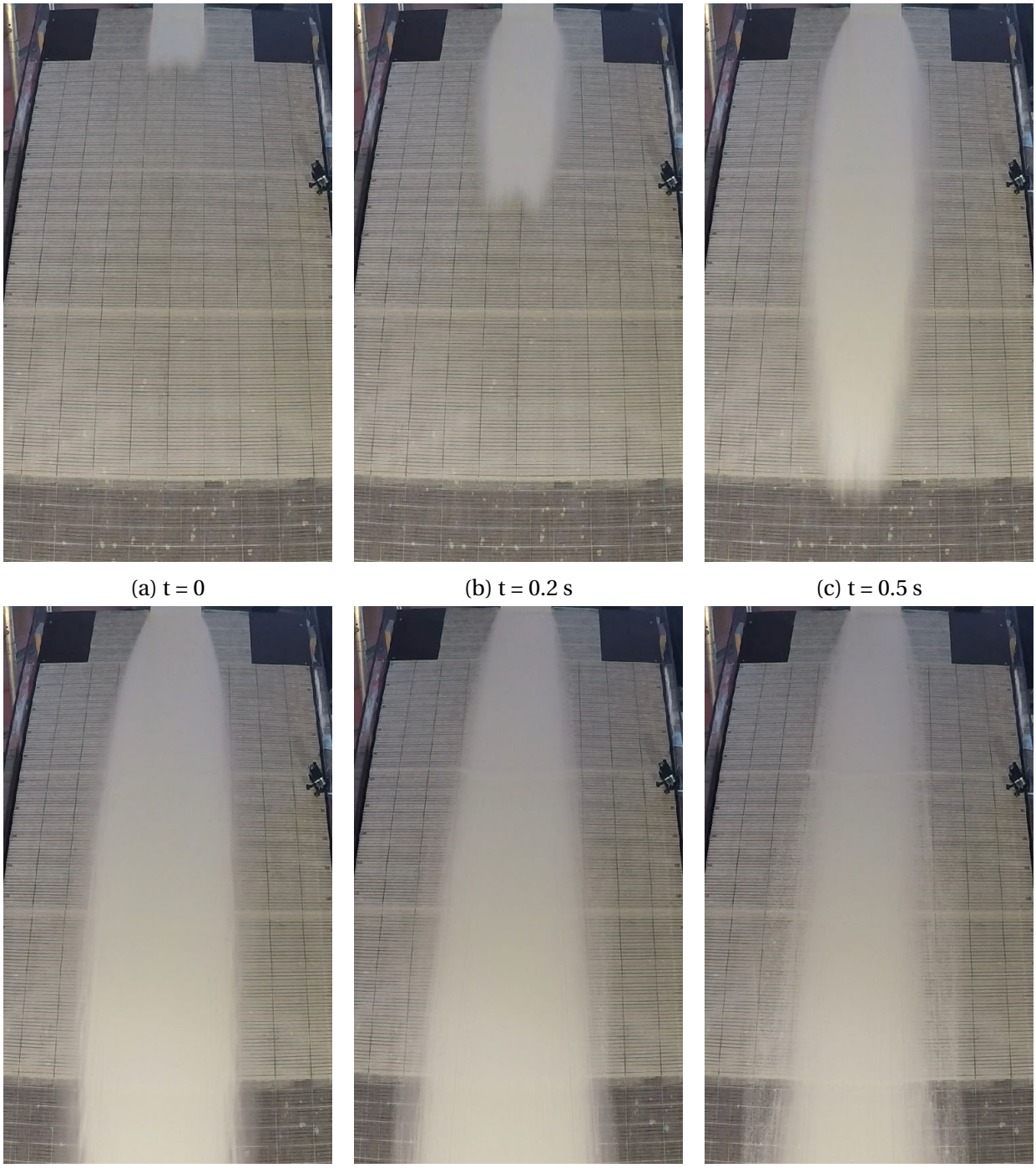

(a) t = 0 (b) t = 0.2 s (c) t = 0.5 s

(d) t = 1.0 s (e) t = 2.0 s (f) t = 3.0 s

Figure C.1: Experiment 1 (mass: 6 kg)

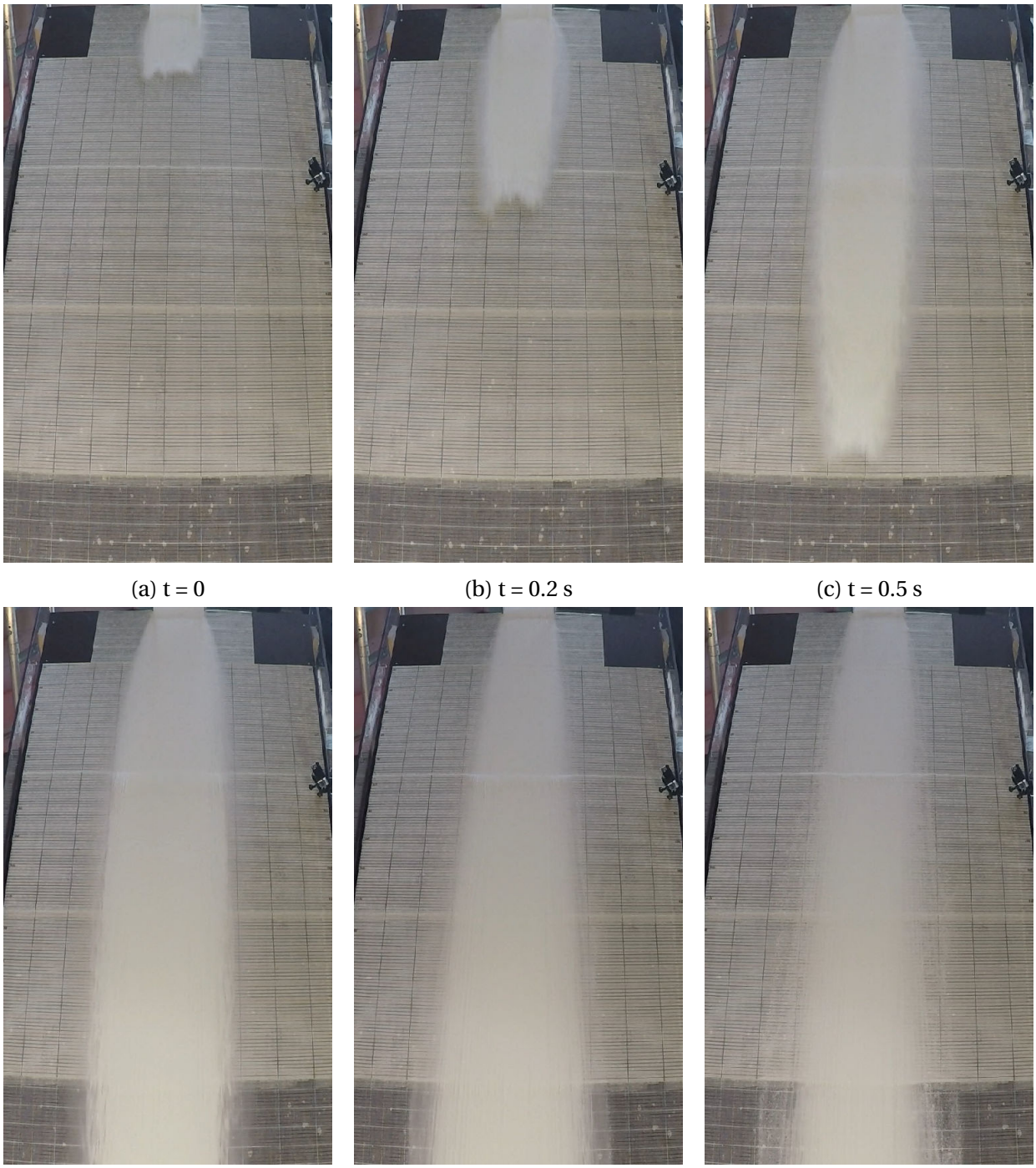

(a) t = 0 (b) t = 0.2 s (c) t = 0.5 s

(d) t = 1.0 s (e) t = 2.0 s (f) t = 3.0 s

Figure C.2: Experiment 2 (mass: 4 kg)

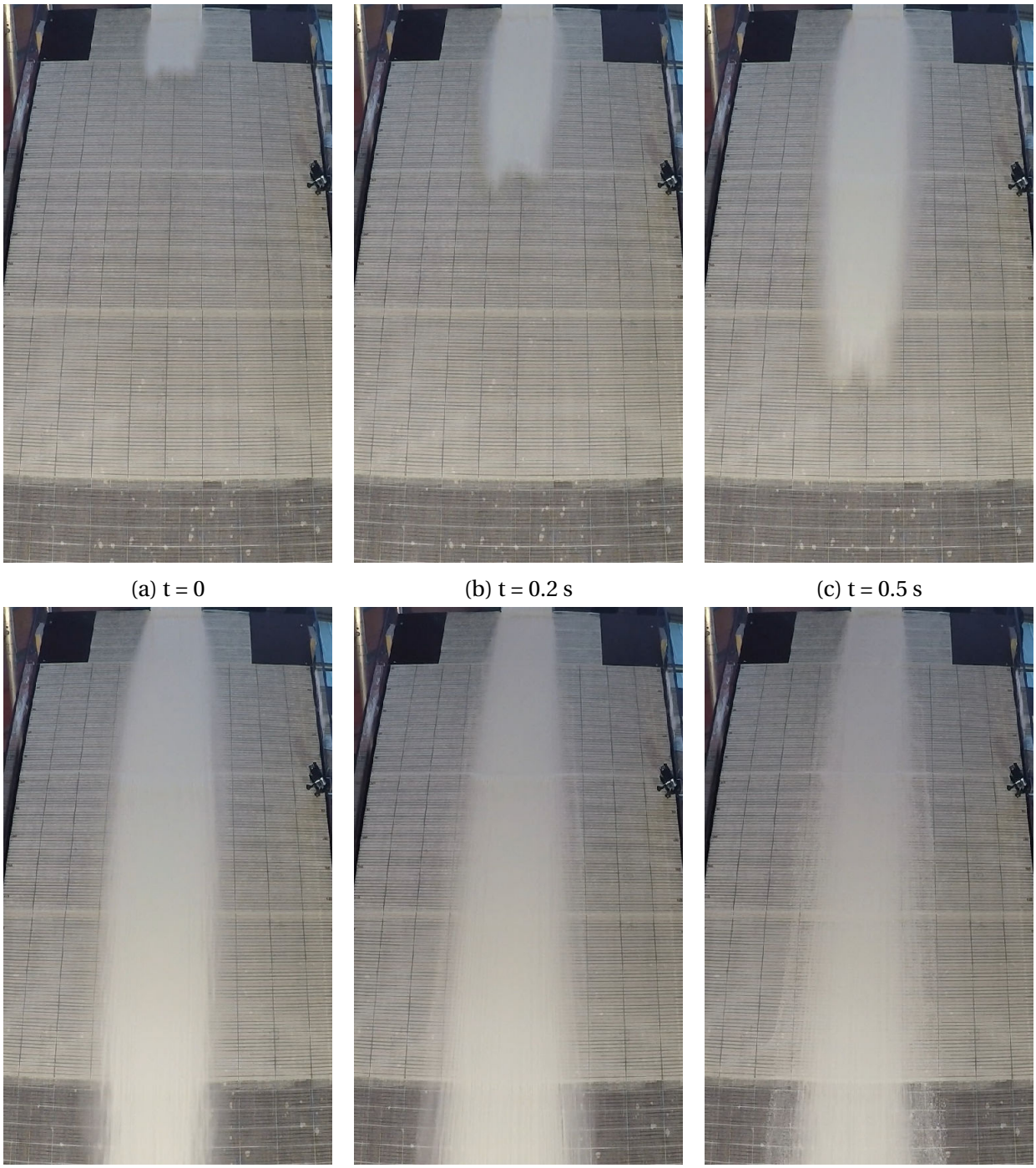

(a) t = 0 (b) t = 0.2 s (c) t = 0.5 s

(d) t = 1.0 s (e) t = 2.0 s (f) t = 3.0 s

Figure C.3: Experiment 3 (mass: 2 kg)

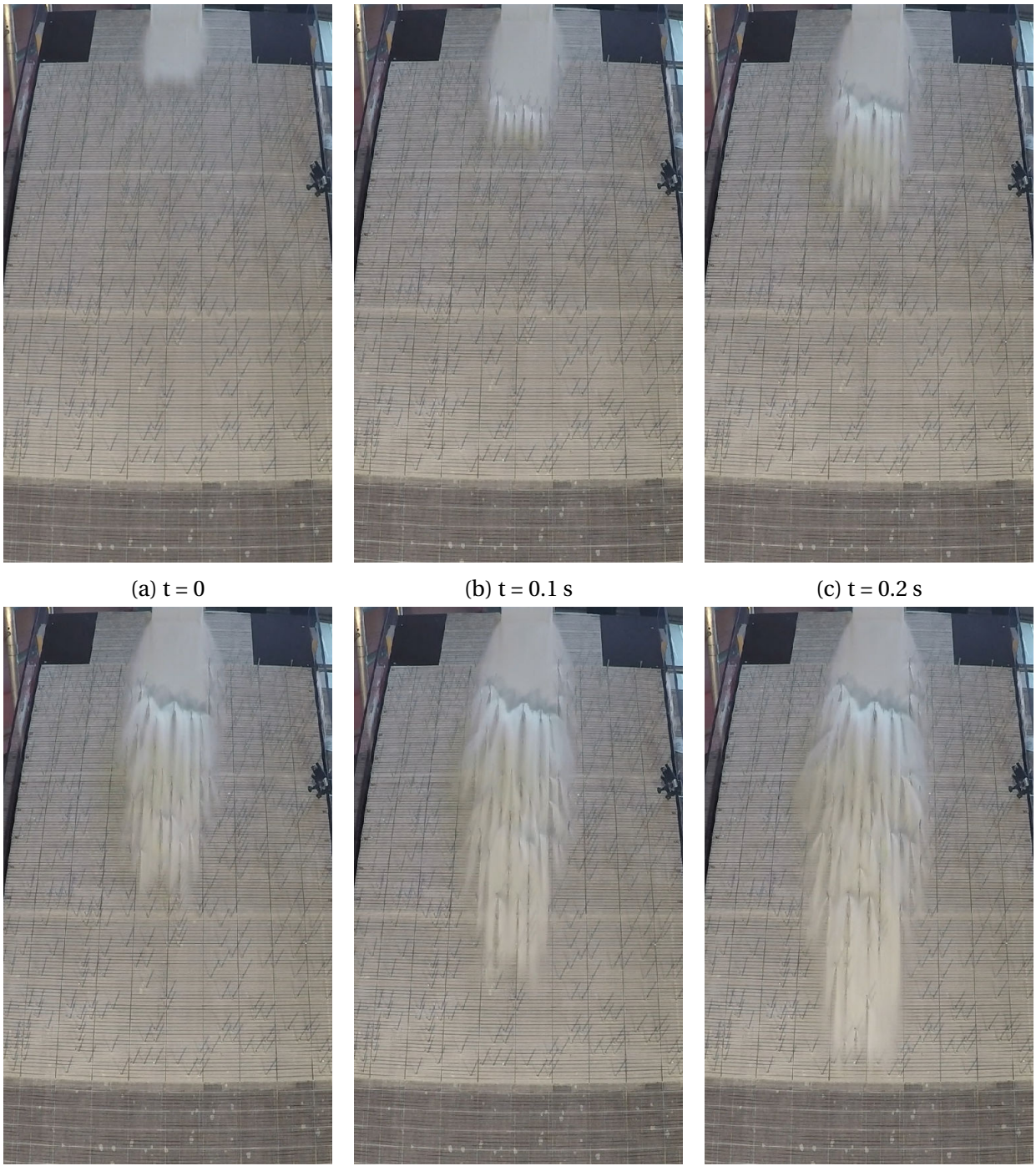

(a) t = 0 (b) t = 0.1 s (c) t = 0.2 s

(d) t = 0.3 s (e) t = 0.4 s (f) t = 0.5 s

Figure C.4: Experiment 8 (mass: 4 kg, stem diameter: 3.2 mm, forest density: 25%)

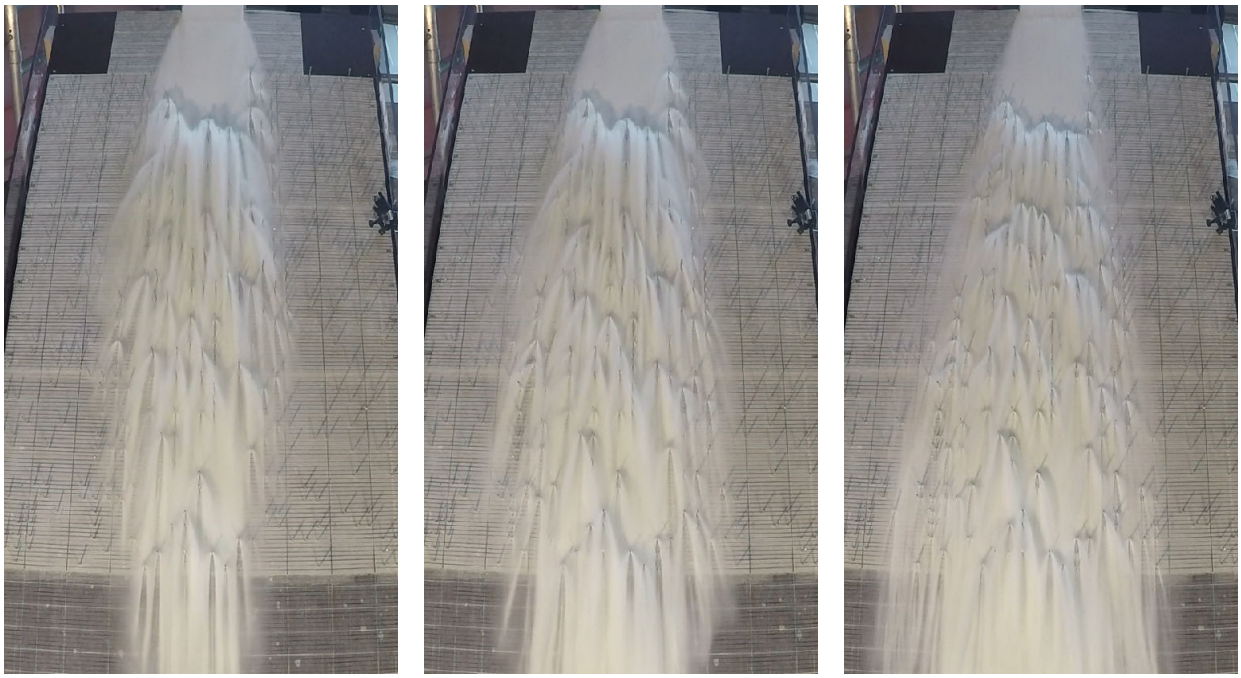

(g) t = 0.7 s (h) t = 1.0 s (i) t = 1.5 s

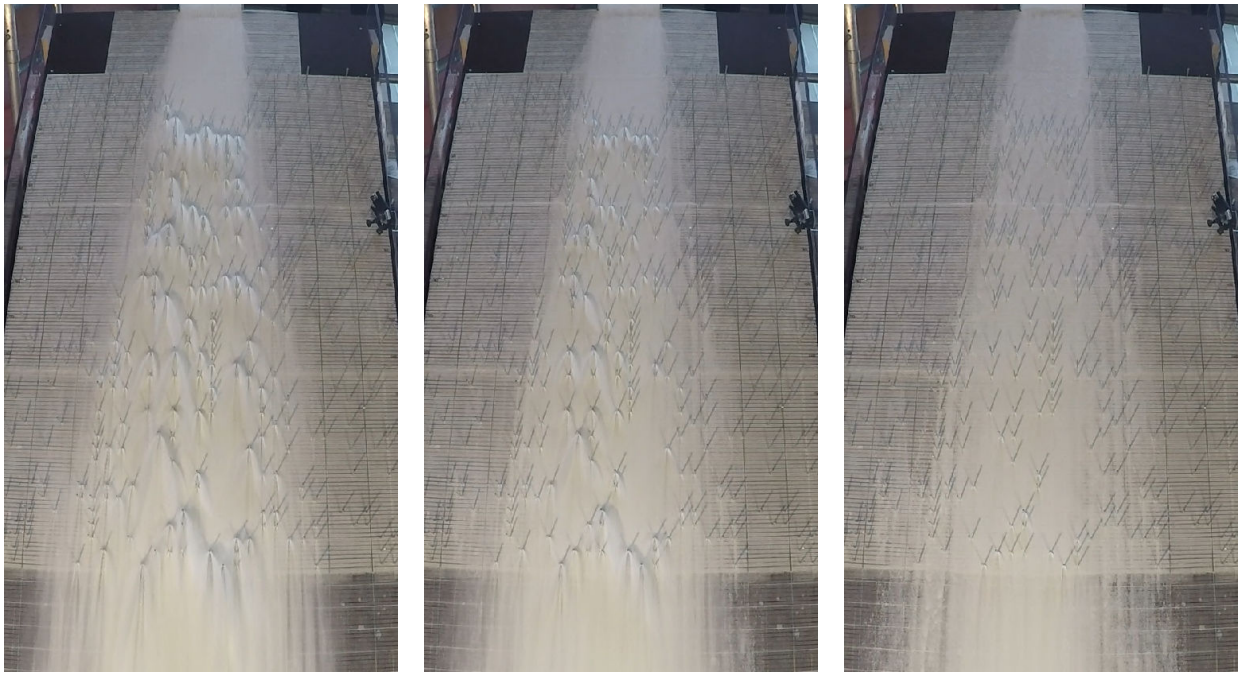

(j) t = 2.0 s (k) t = 2.5 s (l) t = 3.5 s

Figure C.4: Continued: Experiment 8 (mass: 4 kg, stem diameter: 3.2 mm, forest density: 25%)

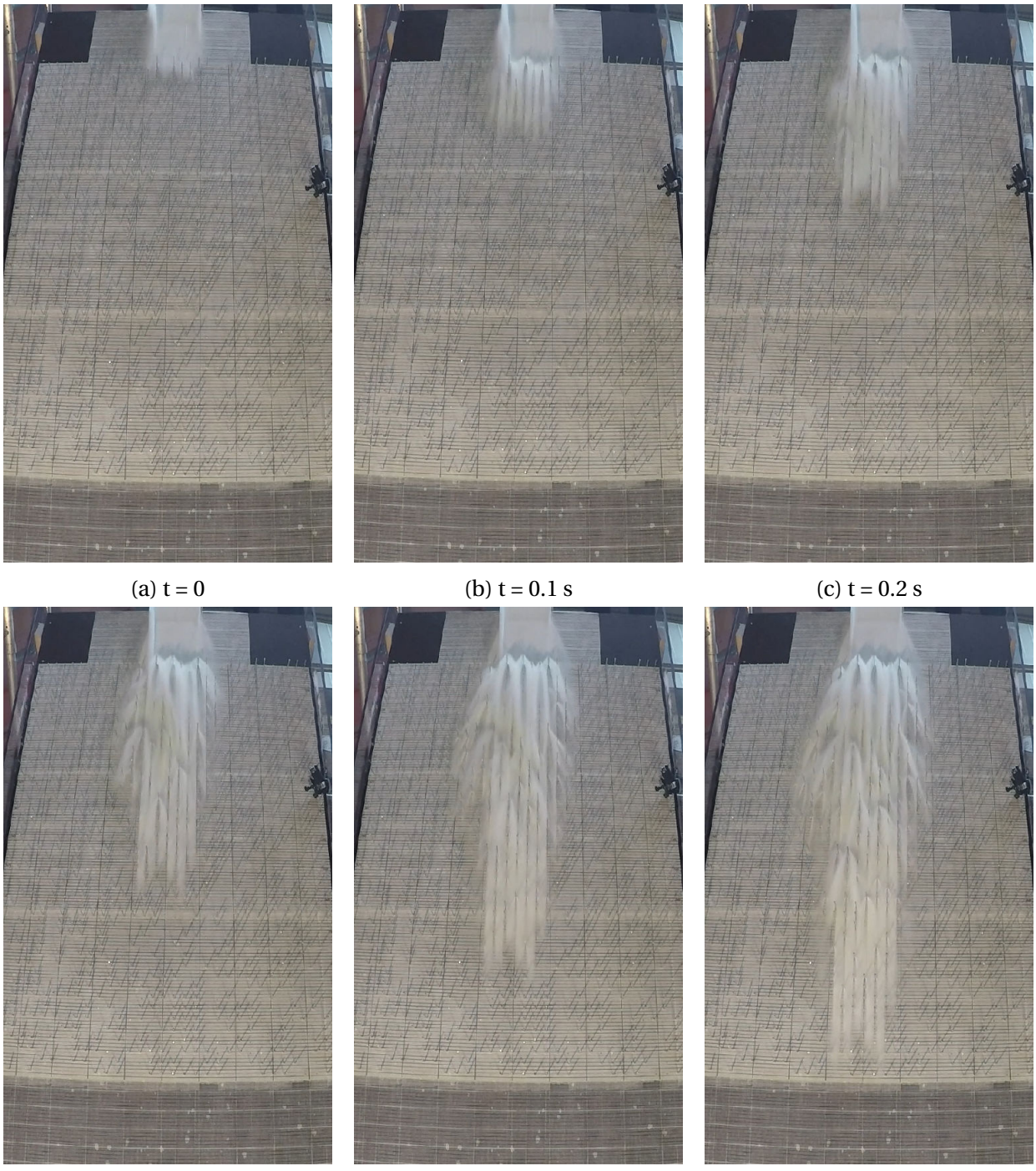

(a) t = 0 (b) t = 0.1 s (c) t = 0.2 s

(d) t = 0.3 s (e) t = 0.4 s (f) t = 0.5 s

Figure C.5: Experiment 19 (mass: 4 kg, stem diameter: 3.2 mm, forest density: 50%)

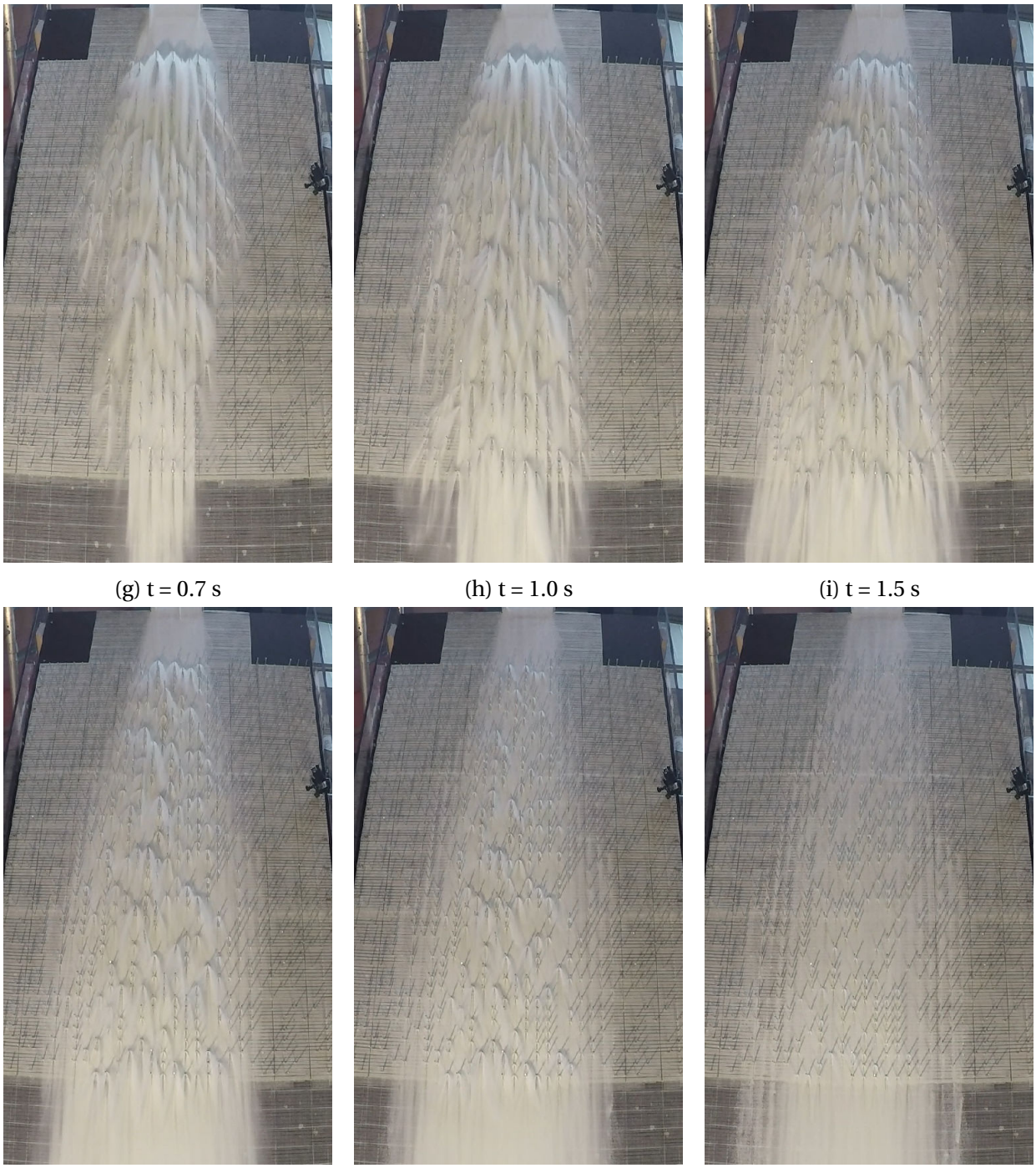

(g) t = 0.7 s (h) t = 1.0 s (i) t = 1.5 s

(j) t = 2.0 s (k) t = 2.5 s (l) t = 3.5 s

Figure C.5: Continued: Experiment 19 (mass: 4 kg, stem diameter: 3.2 mm, forest density: 50%)

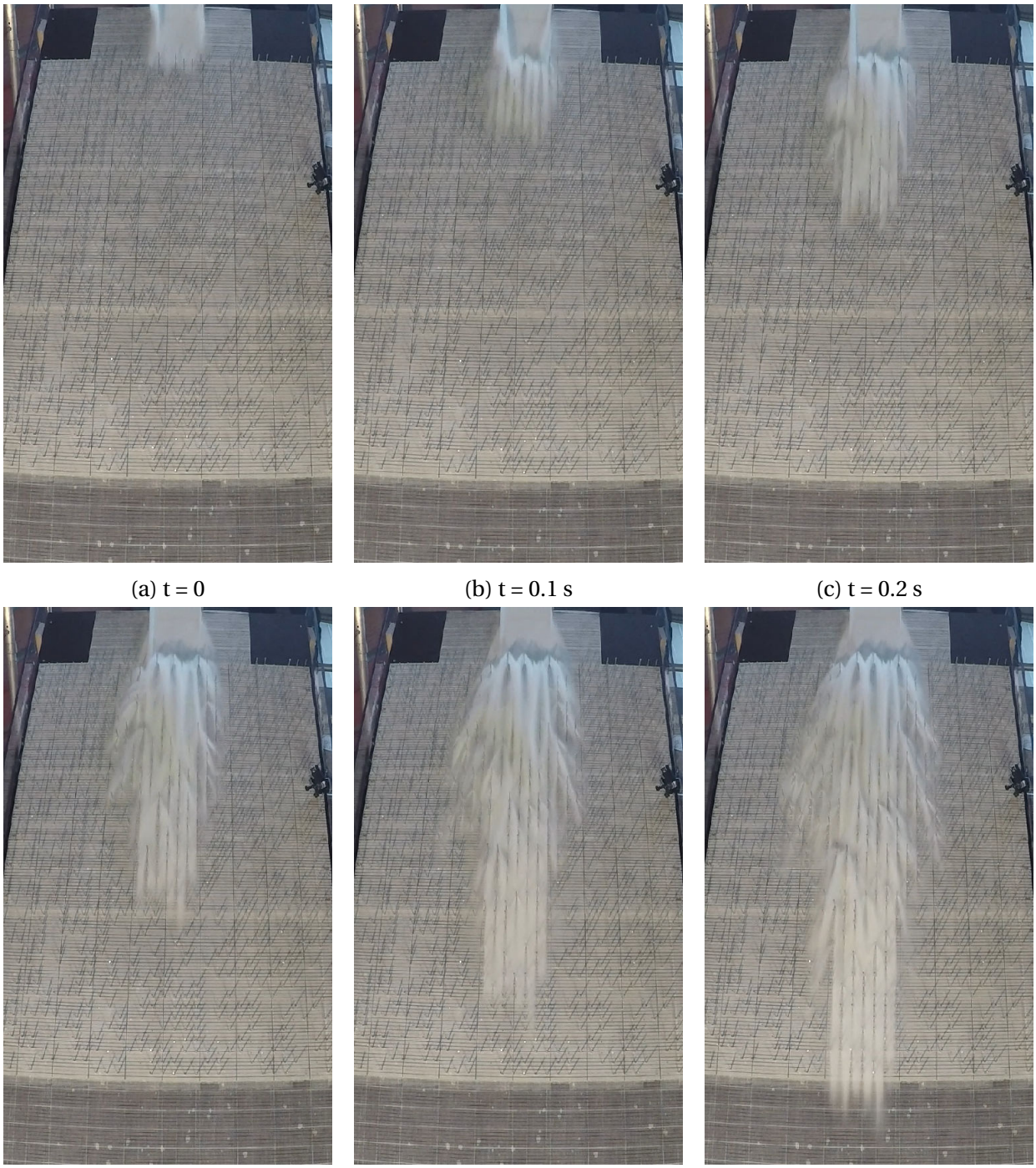

(a) t = 0 (b) t = 0.1 s (c) t = 0.2 s

(d) t = 0.3 s (e) t = 0.4 s (f) t = 0.5 s

Figure C.6: Experiment 20 (mass: 6 kg, stem diameter: 3.2 mm, forest density: 50%)

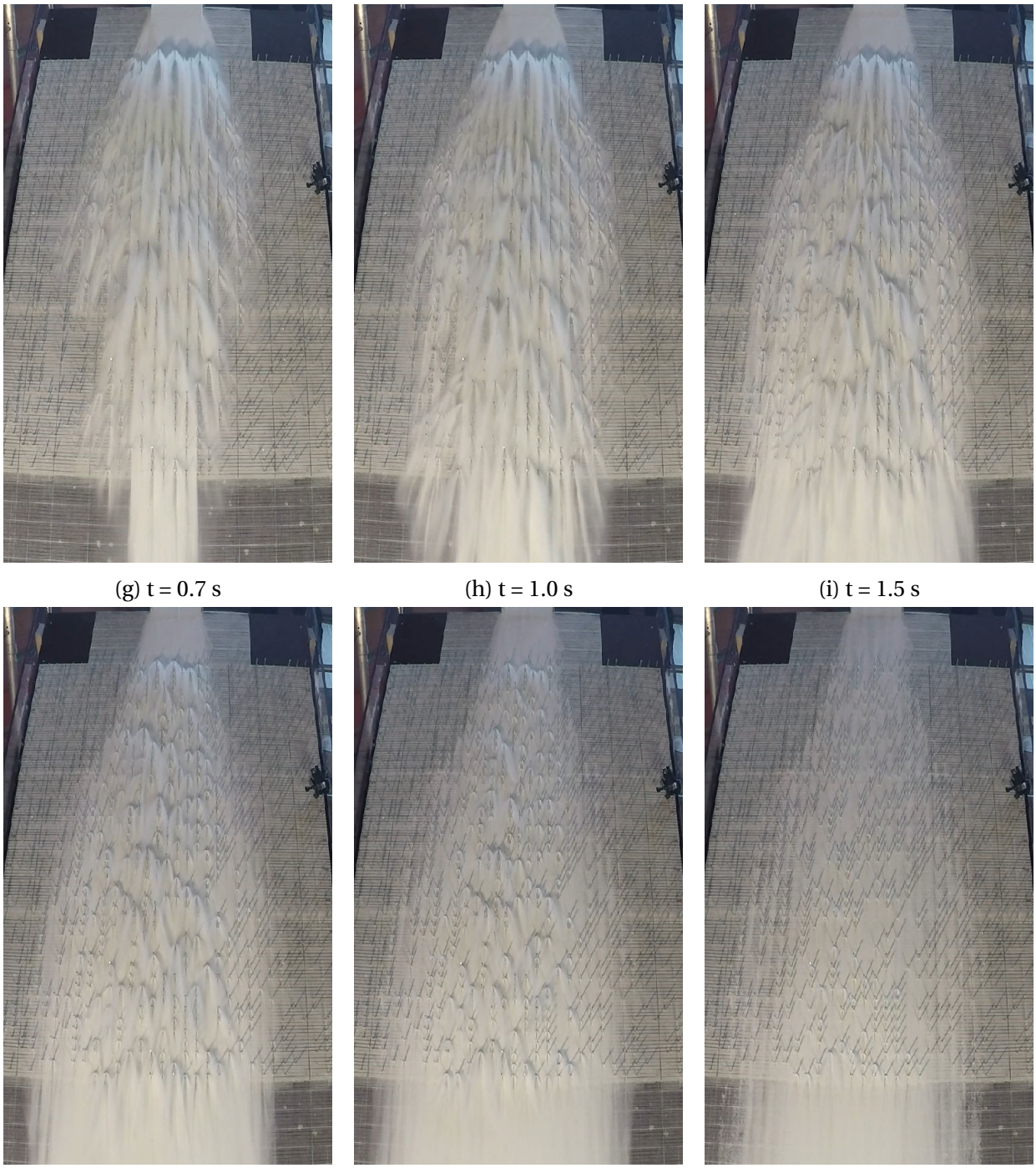

(g) t = 0.7 s (h) t = 1.0 s (i) t = 1.5 s

(j) t = 2.0 s (k) t = 2.5 s (l) t = 3.5 s

Figure C.6: Continued: Experiment 20 (mass: 6 kg, stem diameter: 3.2 mm, forest density: 50%)

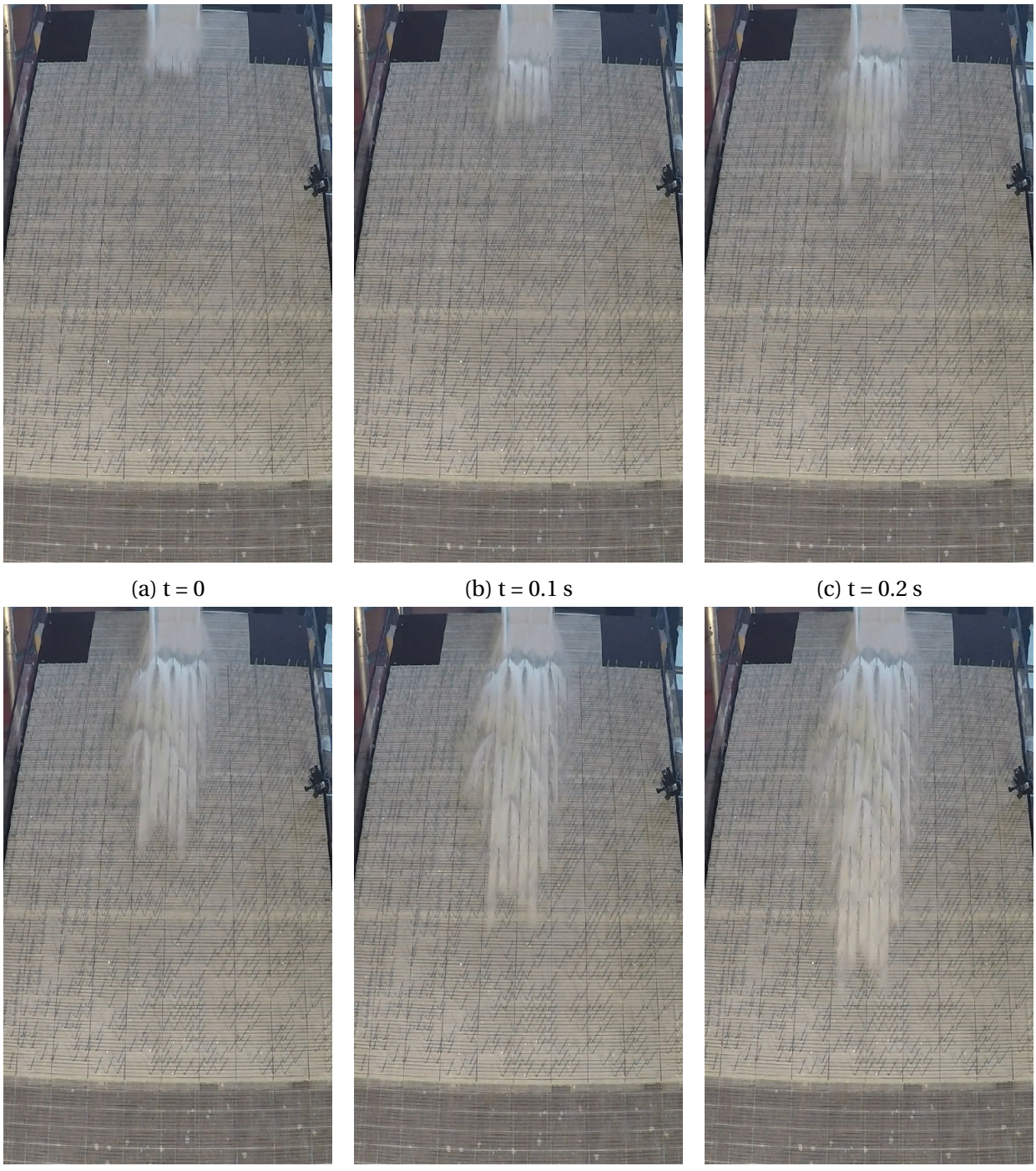

(a) t = 0 (b) t = 0.1 s (c) t = 0.2 s

(d) t = 0.3 s (e) t = 0.4 s (f) t = 0.5 s

Figure C.7: Experiment 21 (mass: 2 kg, stem diameter: 3.2 mm, forest density: 50%)

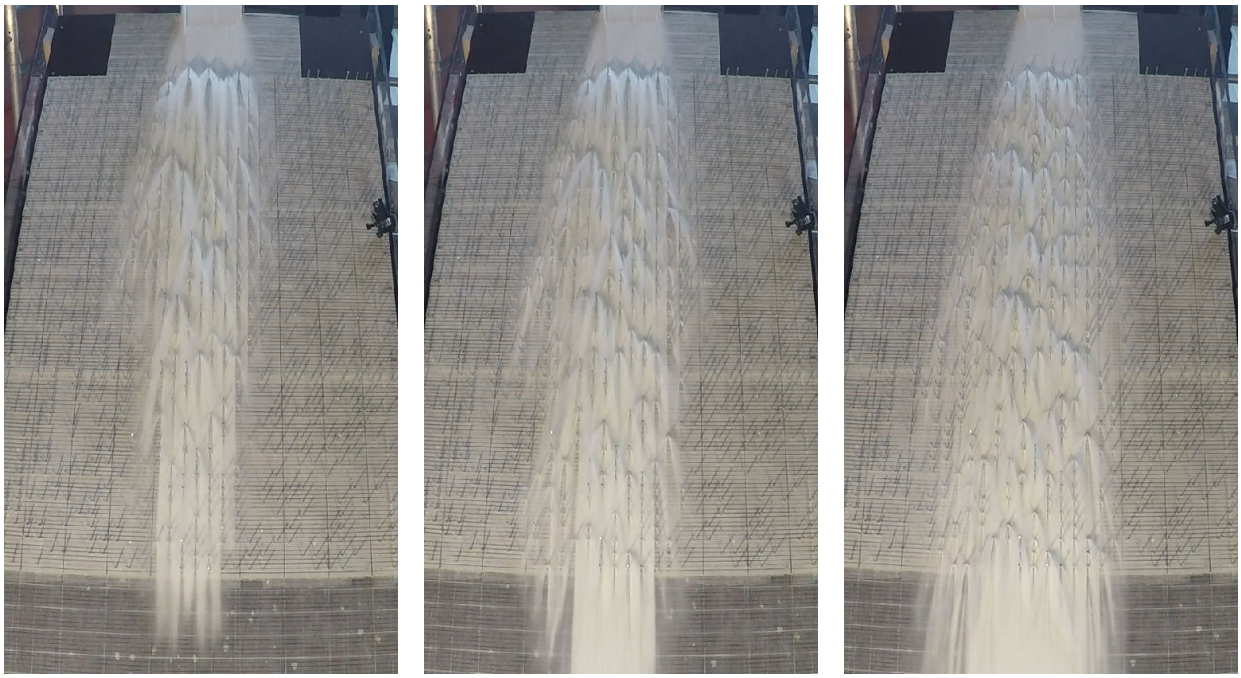

(g) t = 0.7 s (h) t = 1.0 s (i) t = 1.5 s

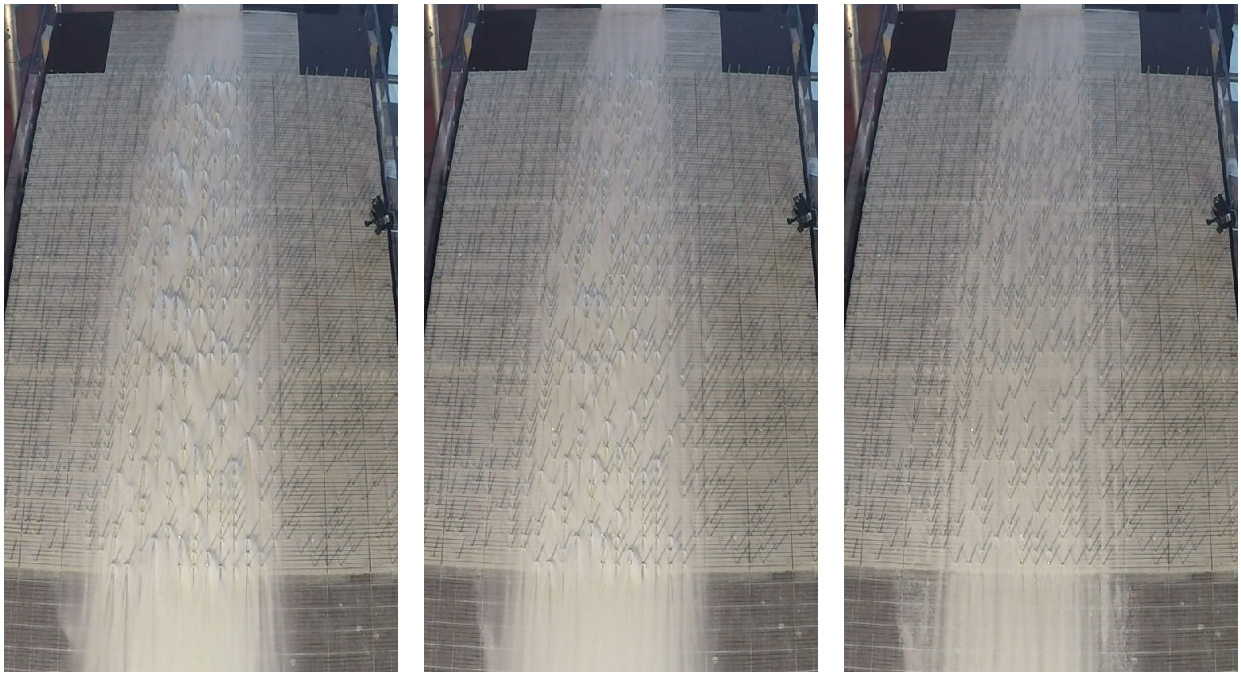

(j) t = 2.0 s (k) t = 2.5 s (l) t = 3.5 s

Figure C.7: Continued: Experiment 21 (mass: 2 kg, stem diameter: 3.2 mm, forest density: 50%)

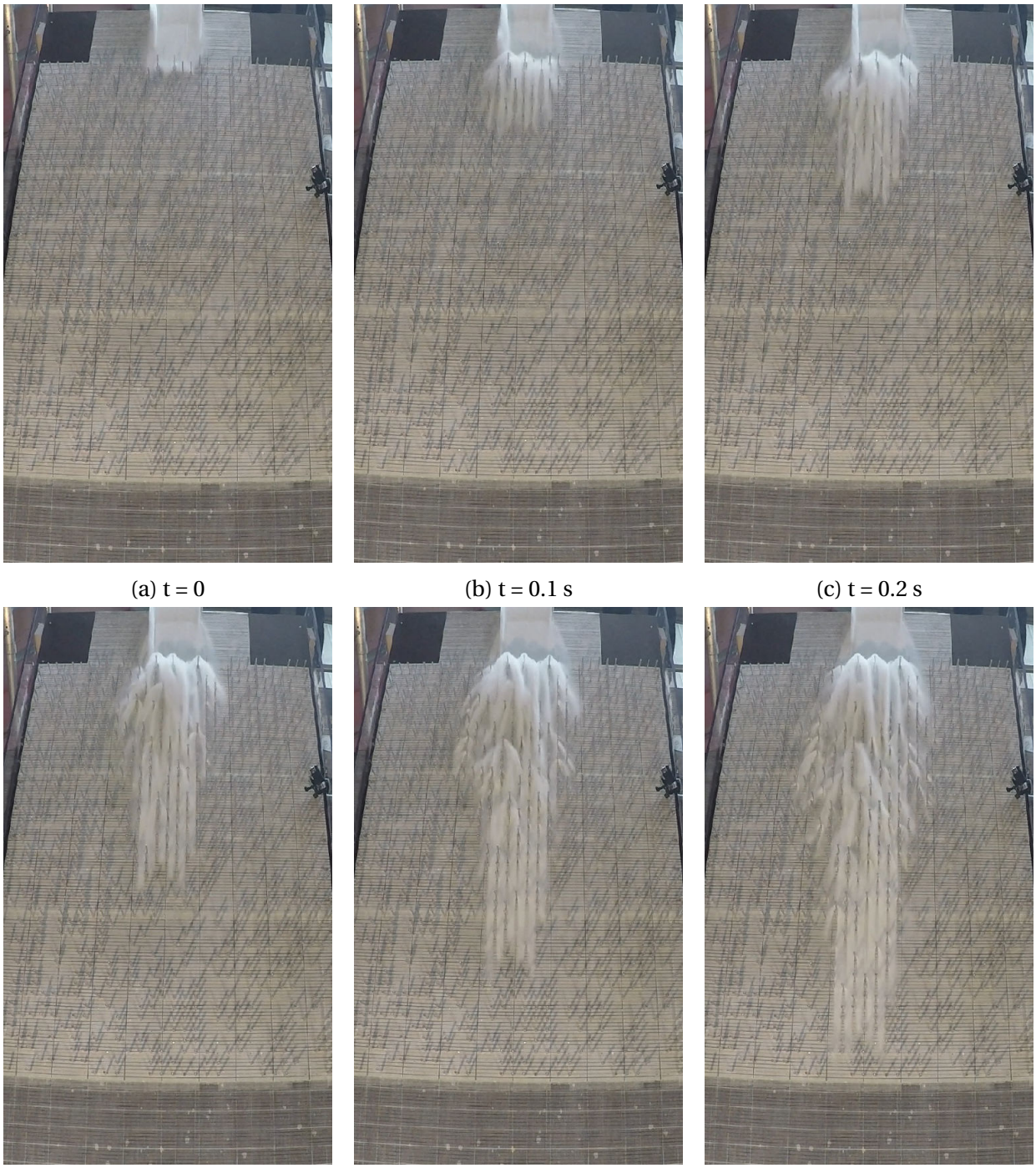

(a) t = 0 (b) t = 0.1 s (c) t = 0.2 s

(d) t = 0.3 s (e) t = 0.4 s (f) t = 0.5 s

Figure C.8: Experiment 22 (mass: 4 kg, stem diameter: 6 mm, forest density: 50%)

(g) t = 0.7 s (h) t = 1.0 s (i) t = 1.5 s

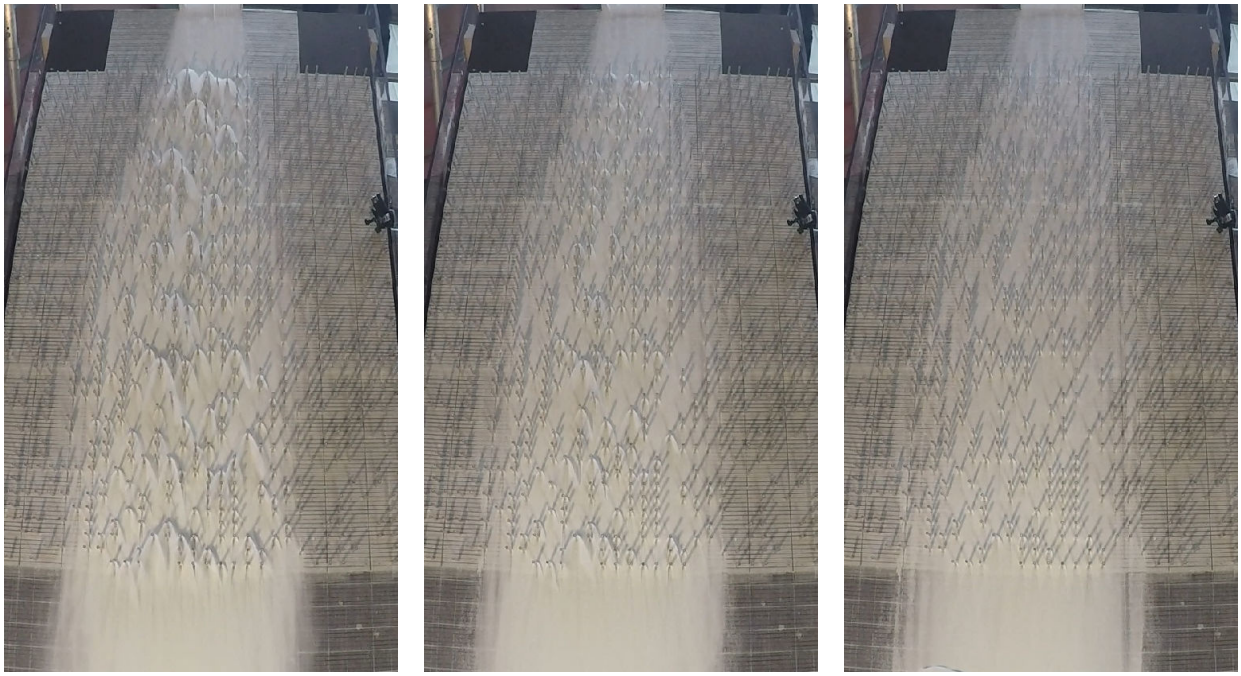

(j) t = 2.0 s (k) t = 2.5 s (l) t = 3.5 s

Figure C.8: Continued: Experiment 22 (mass: 4 kg, stem diameter: 6 mm, forest density: 50%)

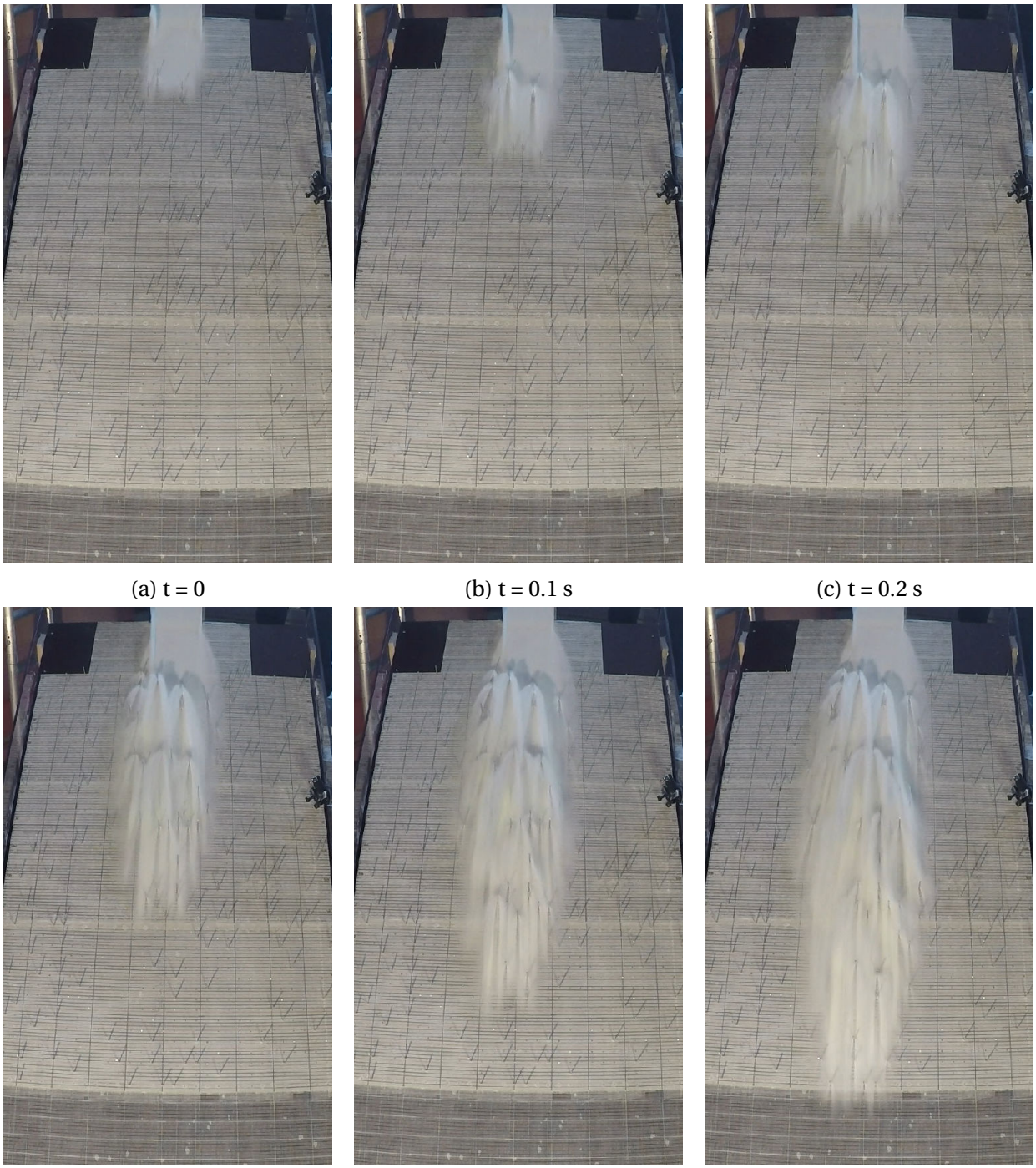

(a) t = 0 (b) t = 0.1 s (c) t = 0.2 s

(d) t = 0.3 s (e) t = 0.4 s (f) t = 0.5 s

Figure C.9: Experiment 32 (mass: 4 kg, stem diameter: 3.2 mm, forest density: 10%)

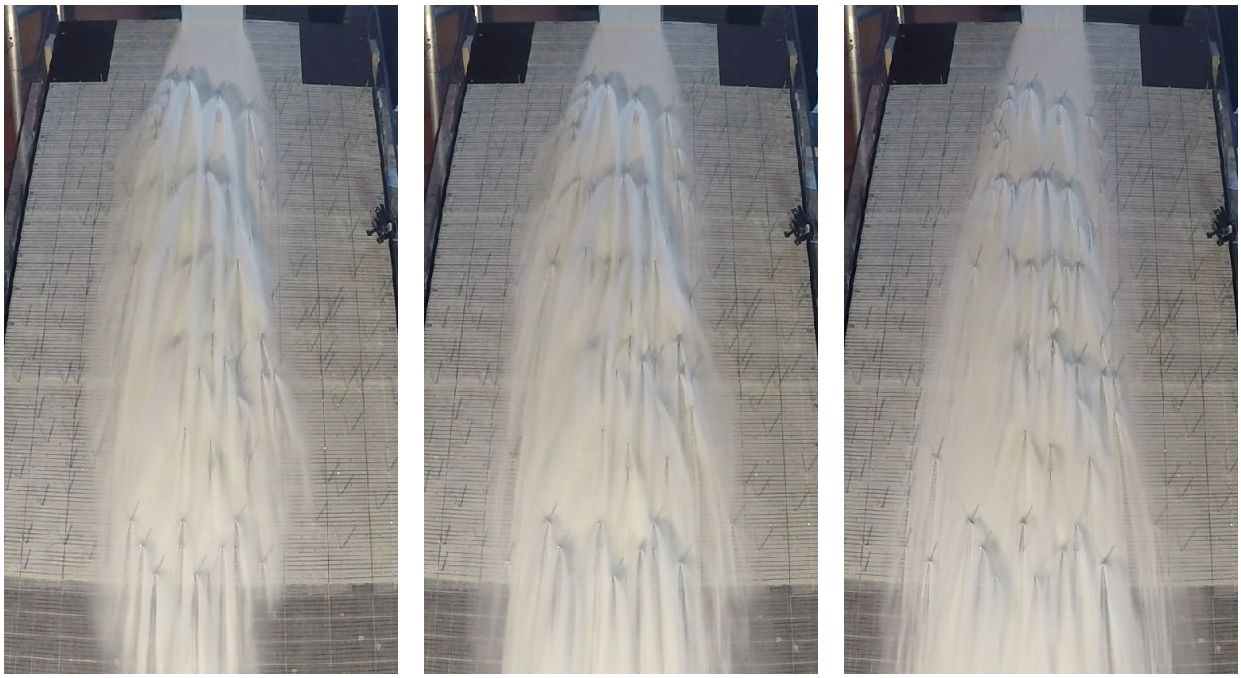

(g) t = 0.7 s (h) t = 1.0 s (i) t = 1.5 s

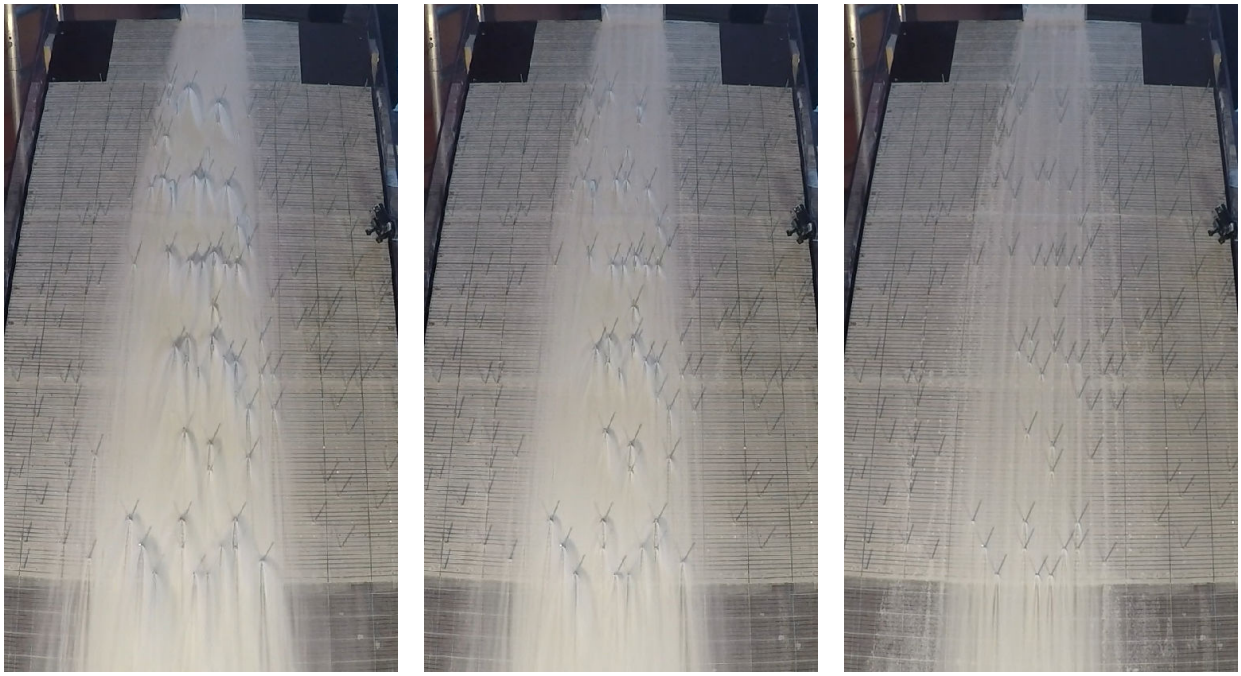

(j) t = 2.0 s (k) t = 2.5 s (l) t = 3.5 s

Figure C.9: Continued: Experiment 32 (mass: 4 kg, stem diameter: 3.2 mm, forest density: 10%)

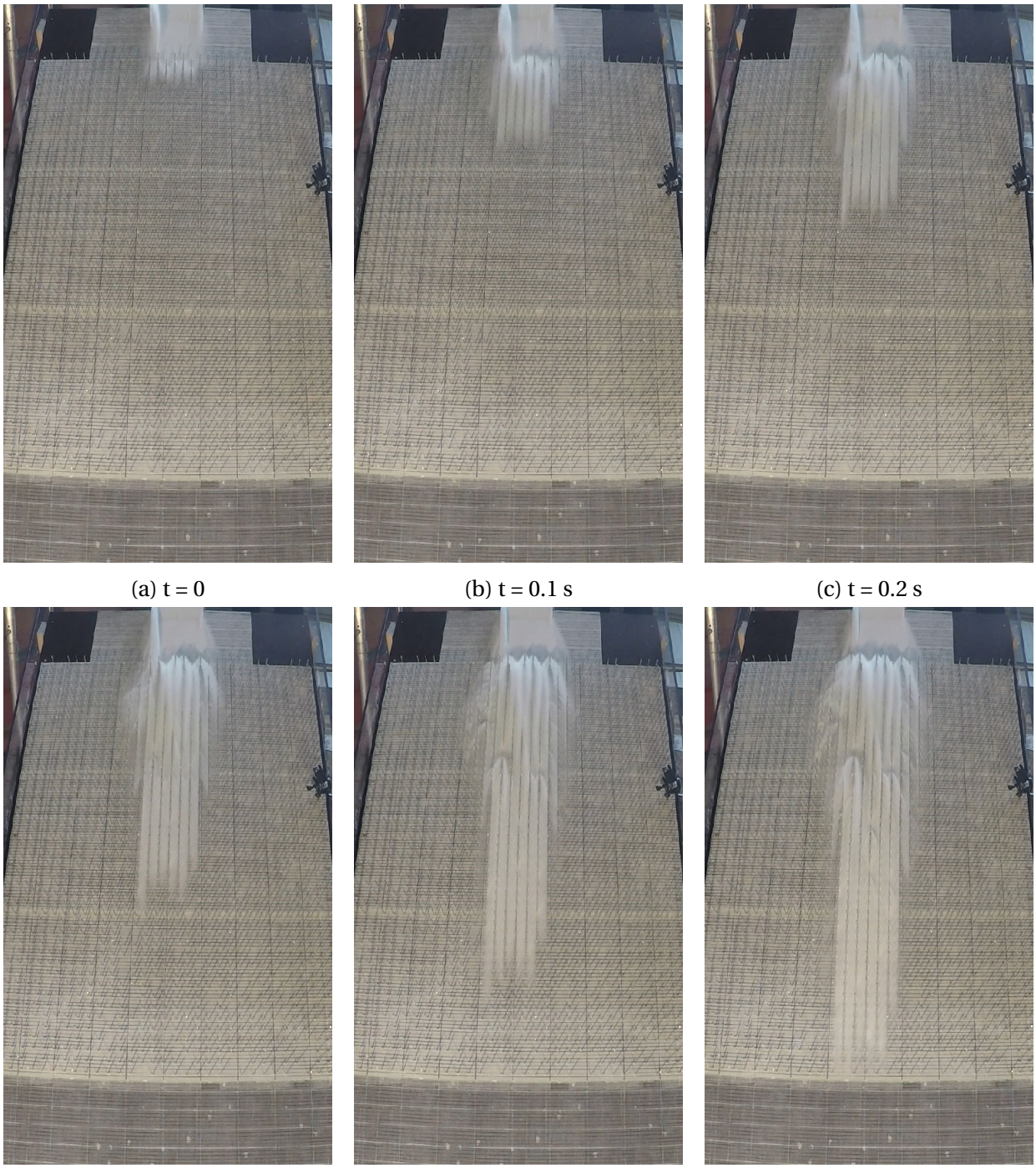

(a) t = 0 (b) t = 0.1 s (c) t = 0.2 s

(d) t = 0.3 s (e) t = 0.4 s (f) t = 0.5 s

Figure C.10: Experiment 48 (mass: 4 kg, stem diameter: 3.2 mm, forest density: 90%)

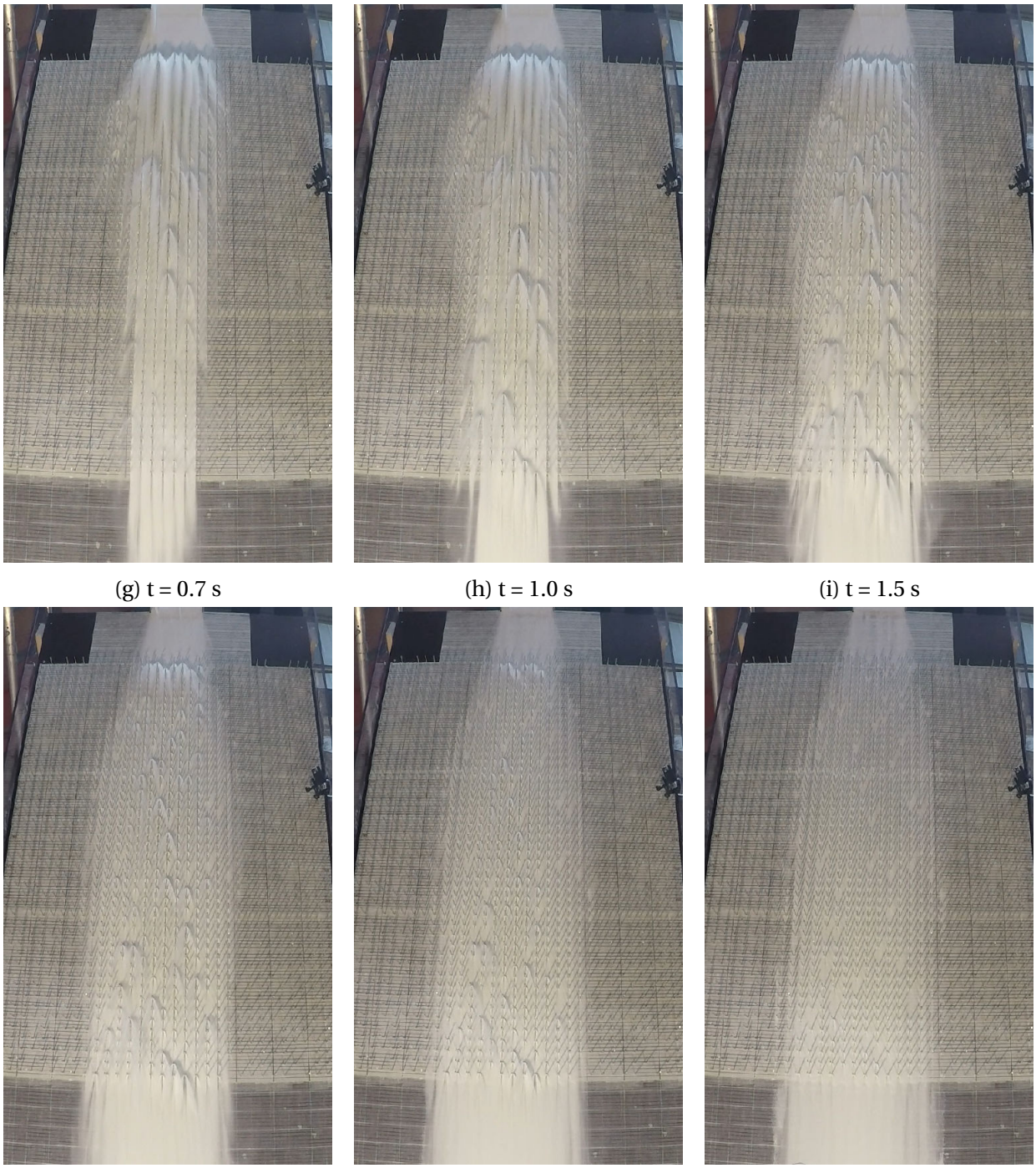

(g) t = 0.7 s (h) t = 1.0 s (i) t = 1.5 s

(j) t = 2.0 s (k) t = 2.5 s (l) t = 3.5 s

Figure C.10: Continued: Experiment 48 (mass: 4 kg, stem diameter: 3.2 mm, forest density: 90%)

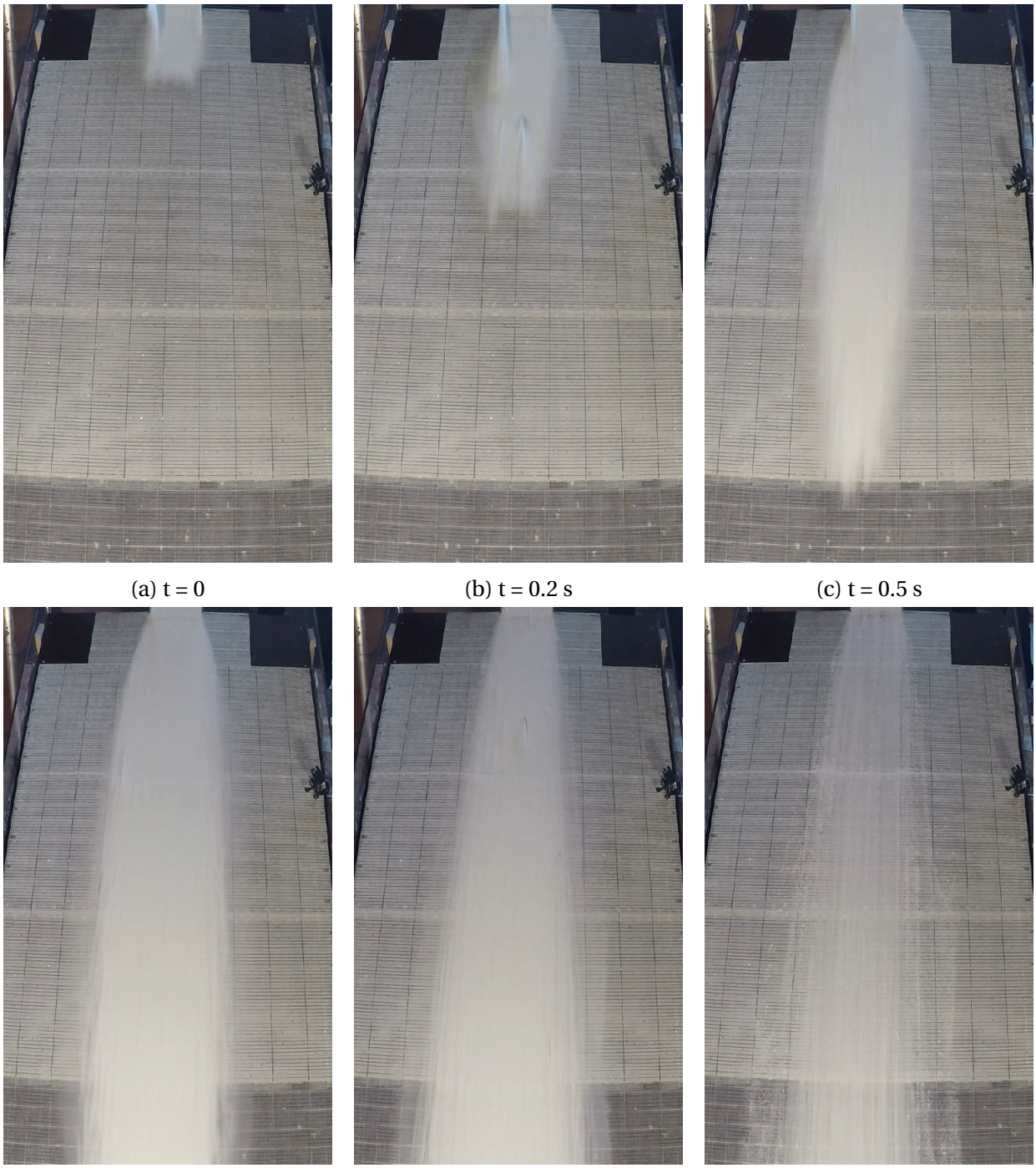

(a) t = 0 (b) t = 0.2 s (c) t = 0.5 s

(d) t = 1.0 s (e) t = 2.0 s (f) t = 3.5 s

Figure C.11: Experiment 49 (mass: 4 kg)

C.2 Side view

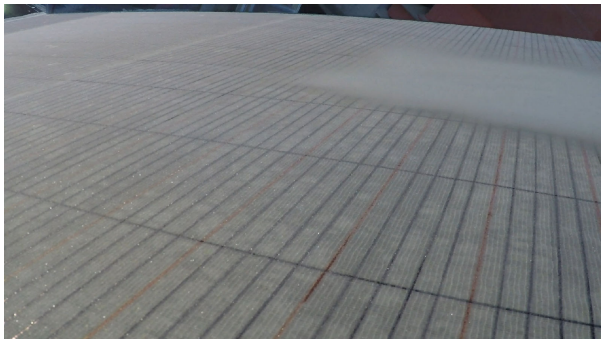

(a) t = 0

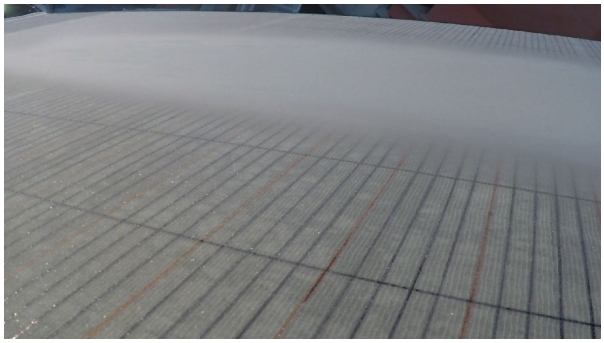

(b) t = 0.17 s

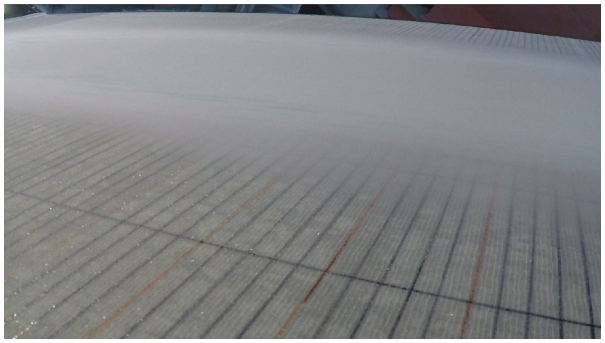

(c) t = 0.33 s

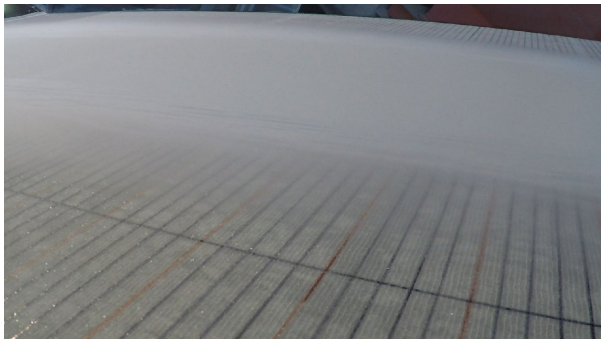

(d) t = 0.67 s

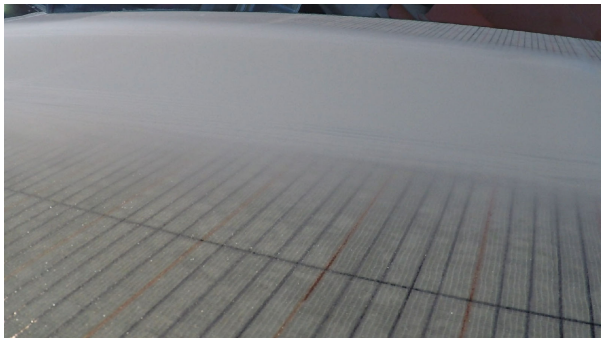

(e) t = 1.0 s

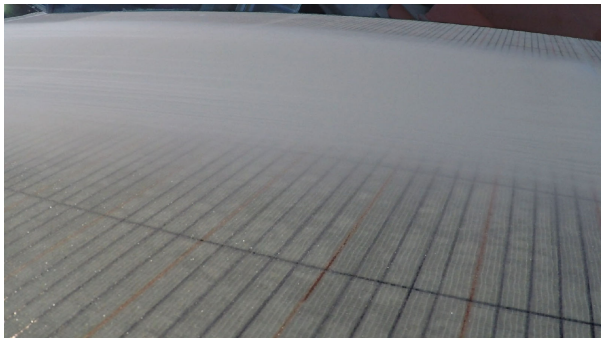

(f) t = 1.5 s

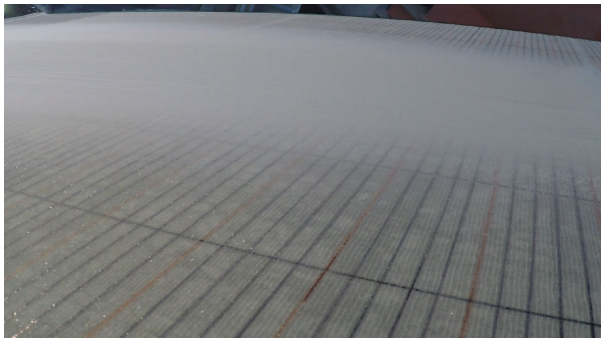

(g) t = 2.0 s

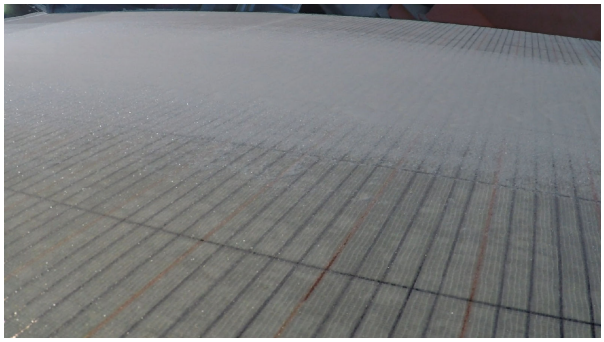

(h) t = 4.0 s

Figure C.12: Experiment 1 (mass: 6 kg)

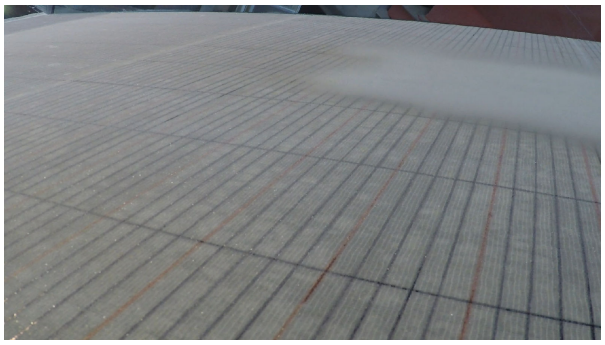

(a) t = 0

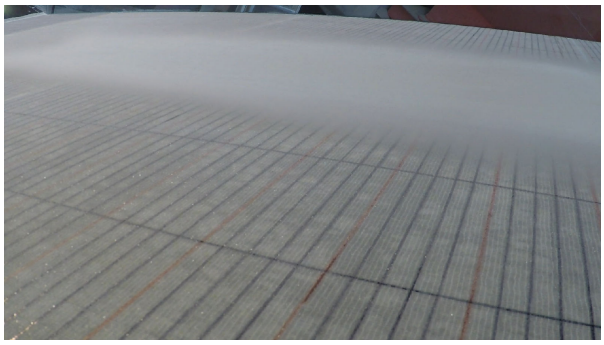

(b) t = 0.17 s

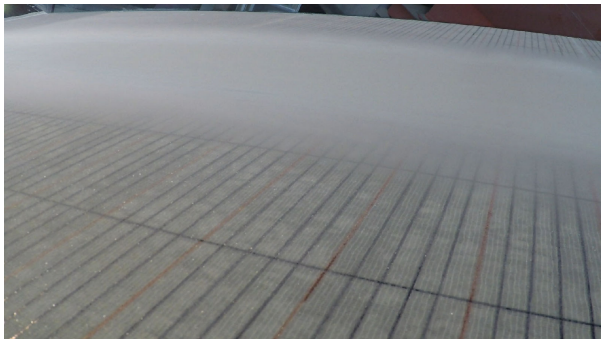

(c) t = 0.33 s

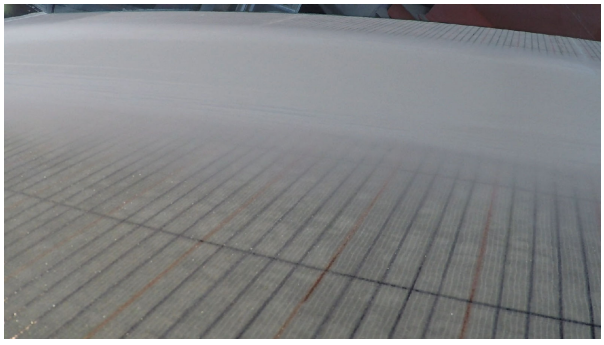

(d) t = 0.67 s

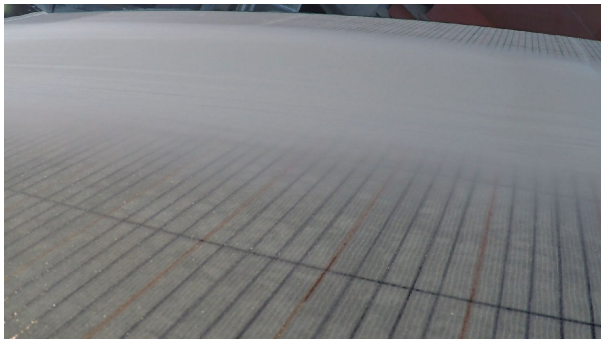

(e) t = 1.0 s

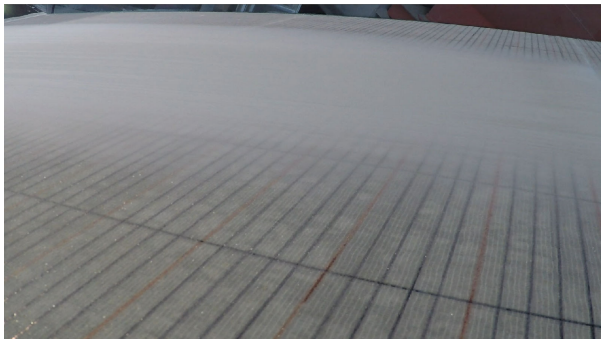

(f) t = 1.5 s

(g) t = 2.0 s

(h) t = 4.0 s

Figure C.13: Experiment 2 (mass: 4 kg)

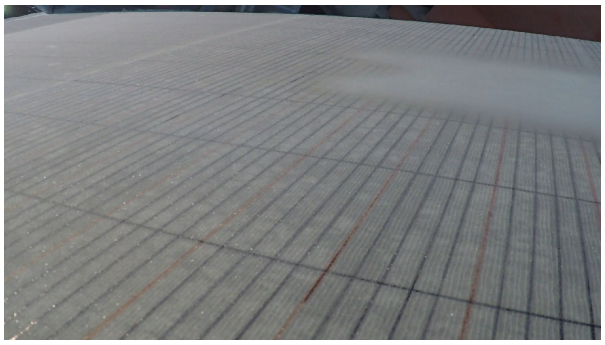

(a) t = 0

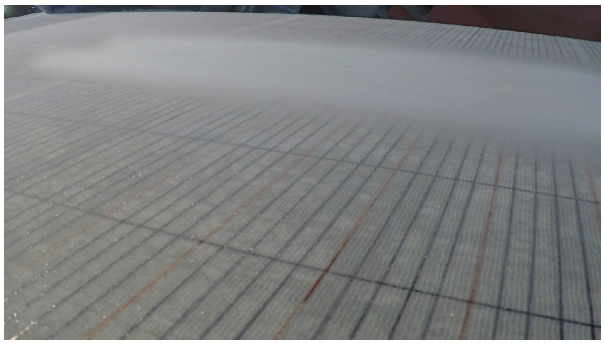

(b) t = 0.17 s

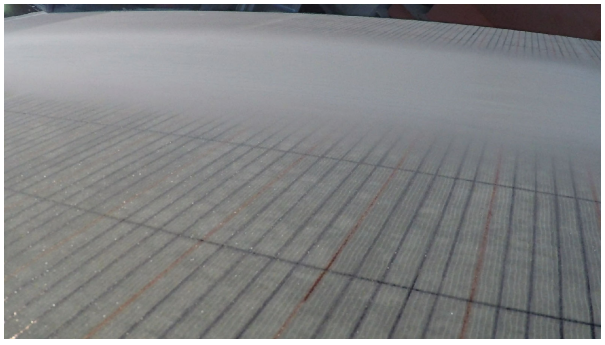

(c) t = 0.33 s

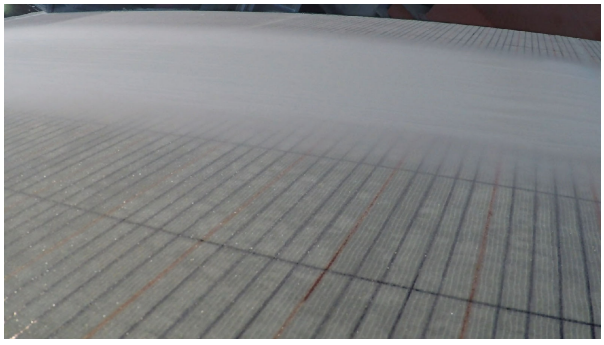

(d) t = 0.67 s

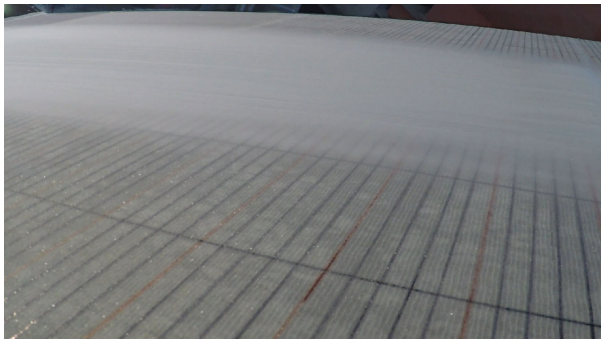

(e) t = 1.0 s

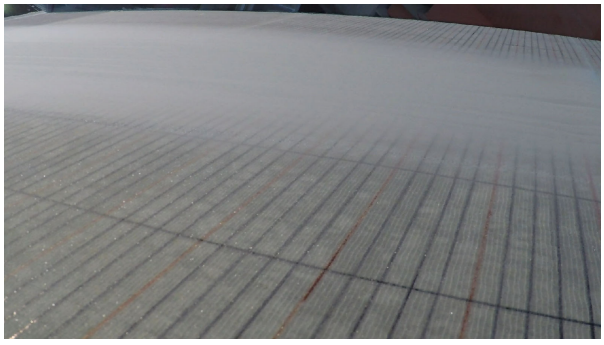

(f) t = 1.5 s

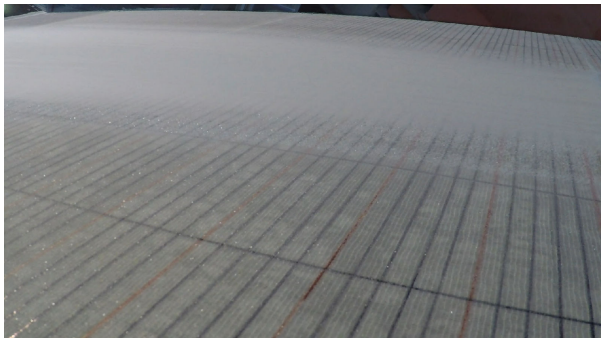

(g) t = 2.0 s

(h) t = 4.0 s

Figure C.14: Experiment 3 (mass: 2 kg)

(a) t = 0

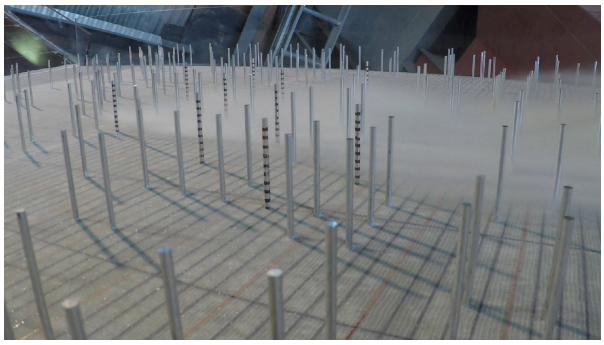

(b) t = 0.1 s

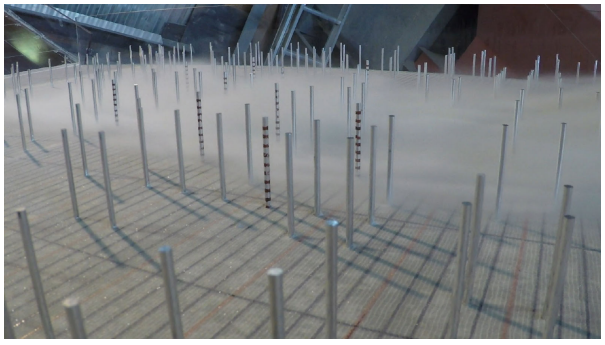

(c) t = 0.2 s

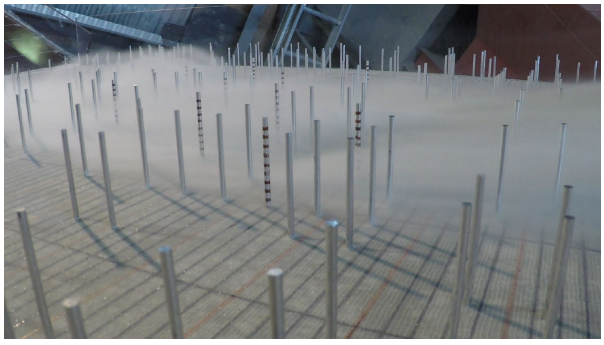

(d) t = 0.3 s

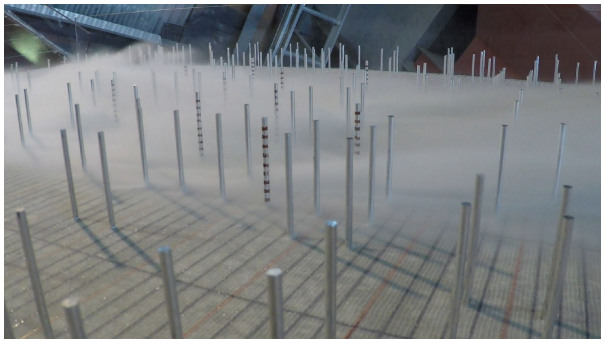

(e) t = 0.4 s

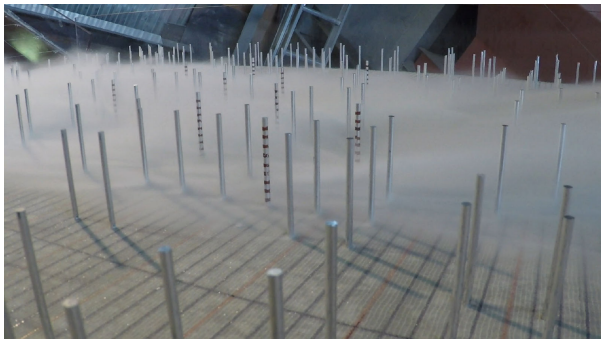

(f) t = 0.5 s

(g) t = 0.6 s

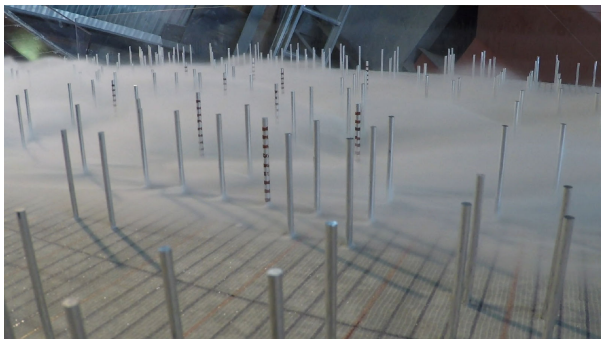

(h) t = 0.8 s

Figure C.15: Experiment 8 (mass: 4 kg, stem diameter: 3.2 mm, forest density: 25%)

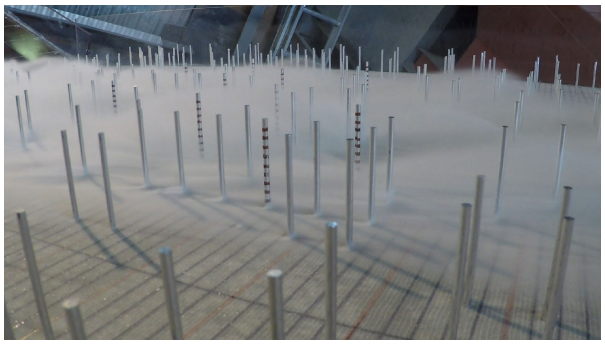

(i) t = 1.0 s

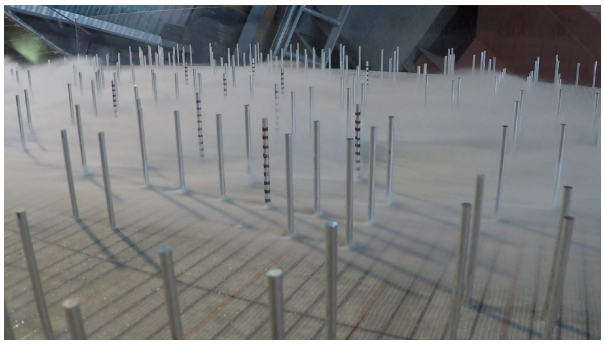

(j) t = 1.2 s

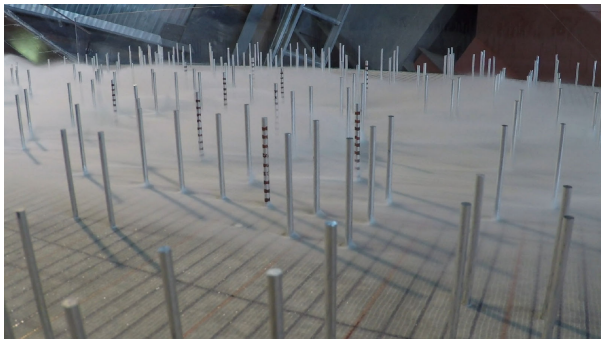

(k) t = 1.4 s

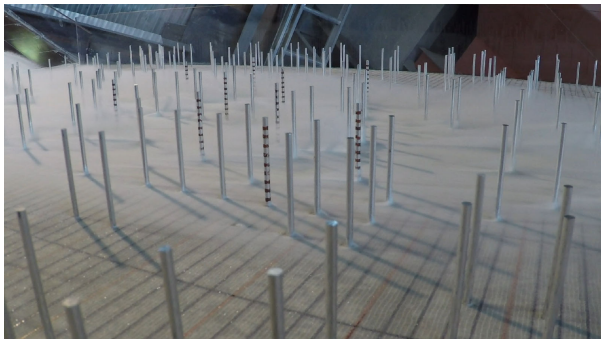

(l) t = 1.6 s

(m) t = 1.8 s

(n) t = 2.0 s

(o) t = 2.5 s

(p) t = 4.0 s

Figure C.15: Continued: Experiment 8 (mass: 4 kg, stem diameter: 3.2 mm, forest density: 25%)

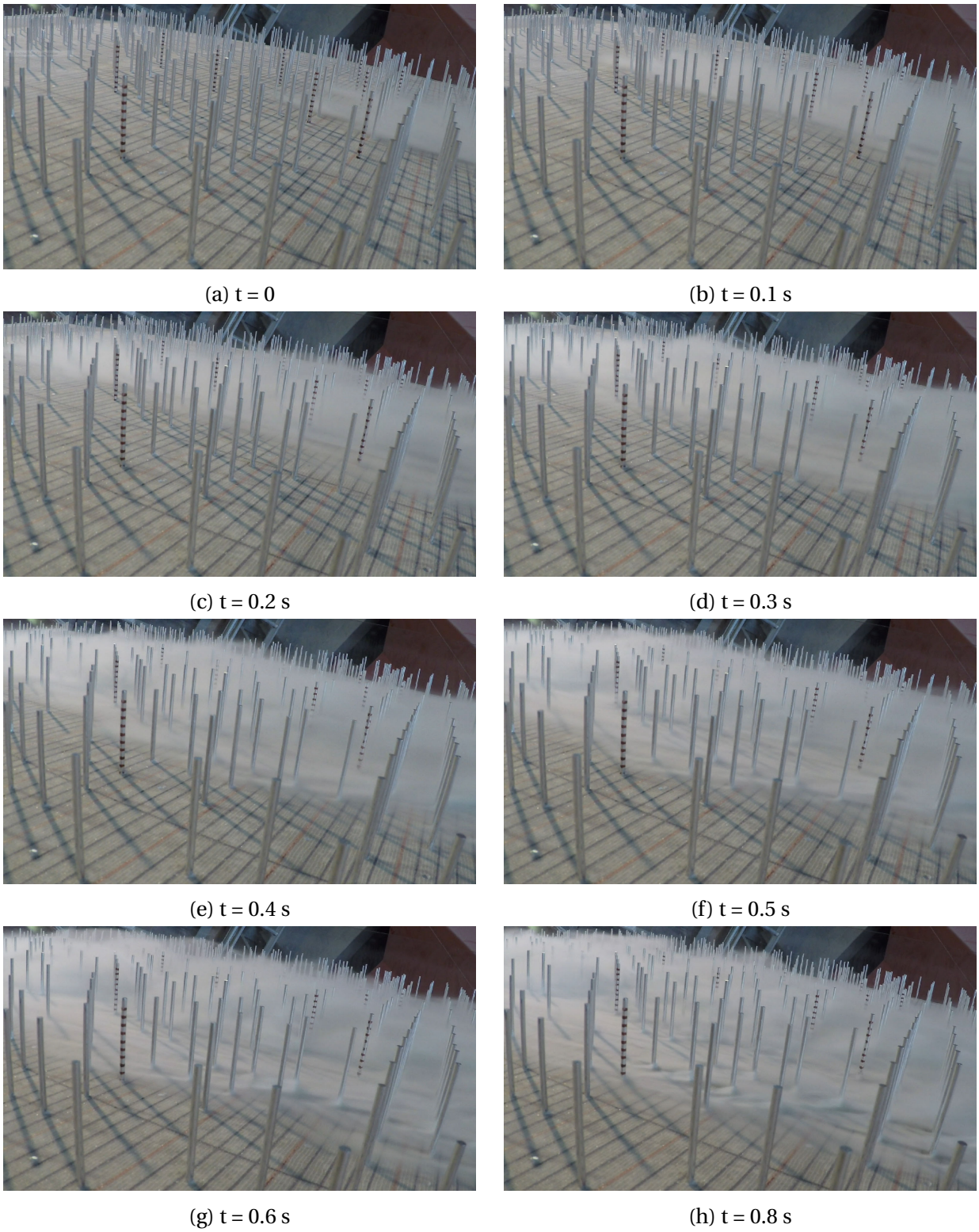

(a) t = 0 (b) t = 0.1 s

(c) t = 0.2 s (d) t = 0.3 s

(e) t = 0.4 s (f) t = 0.5 s

(g) t = 0.6 s (h) t = 0.8 s

Figure C.16: Experiment 19 (mass: 4 kg, stem diameter: 3.2 mm, forest density: 50%)

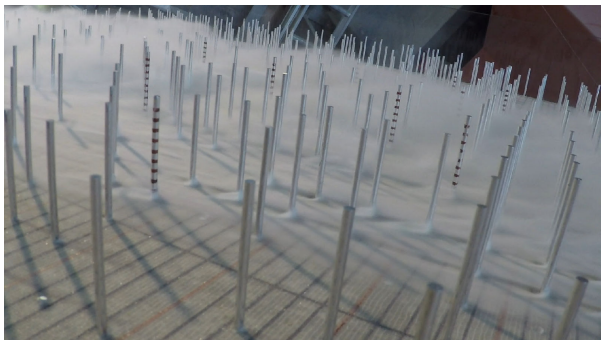

(i) t = 1.0 s

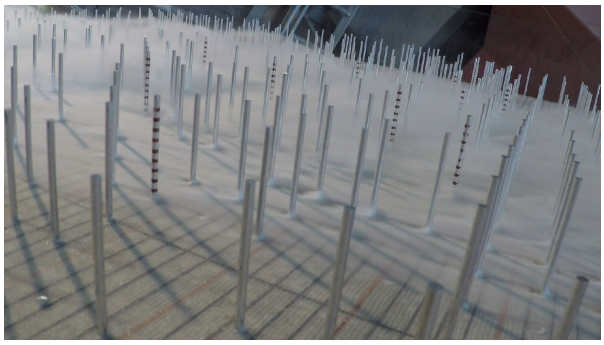

(j) t = 1.2 s

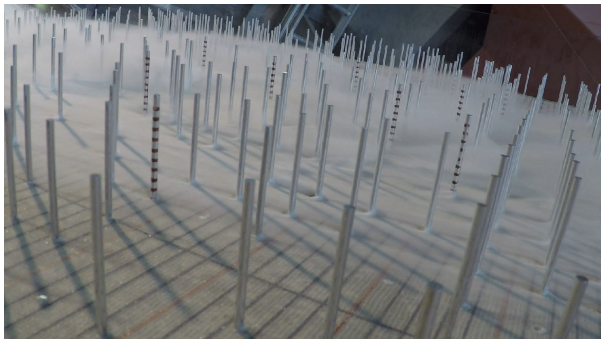

(k) t = 1.4 s

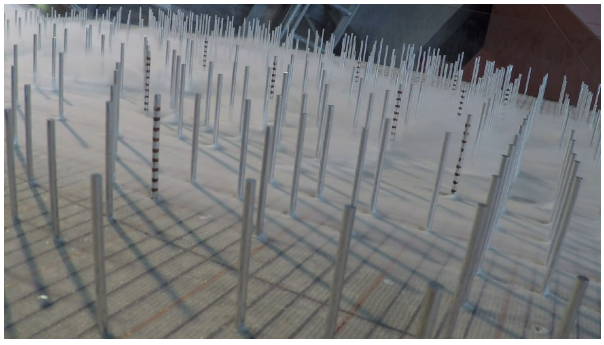

(l) t = 1.6 s

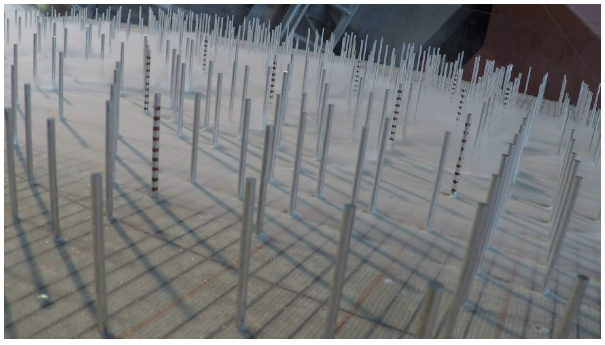

(m) t = 1.8 s

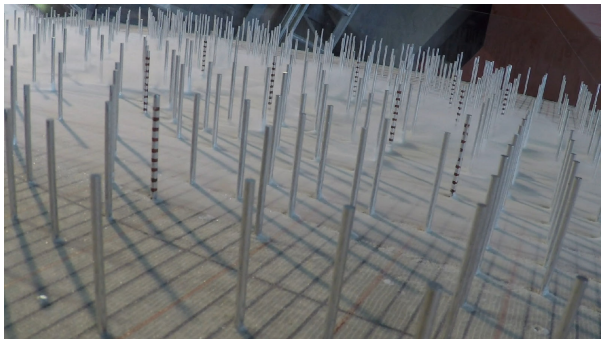

(n) t = 2.0 s

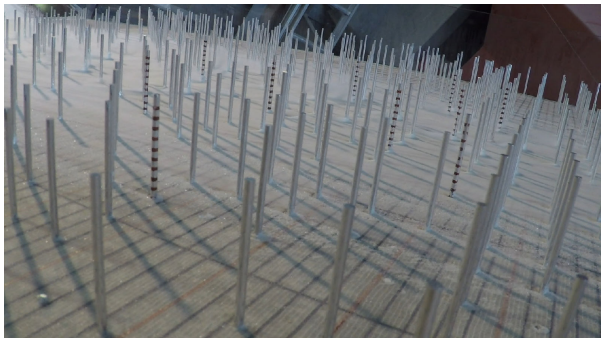

(o) t = 2.5 s

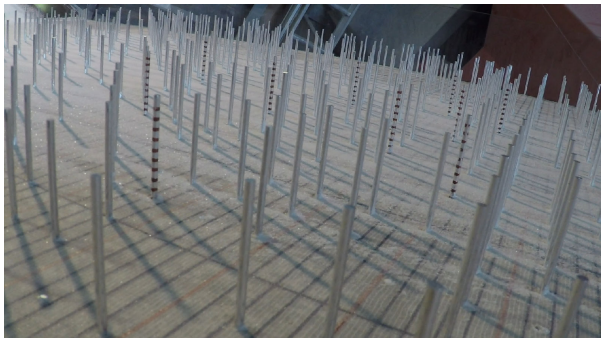

(p) t = 4.0 s

Figure C.16: Continued: Experiment 19 (mass: 4 kg, stem diameter: 3.2 mm, forest density: 50%)

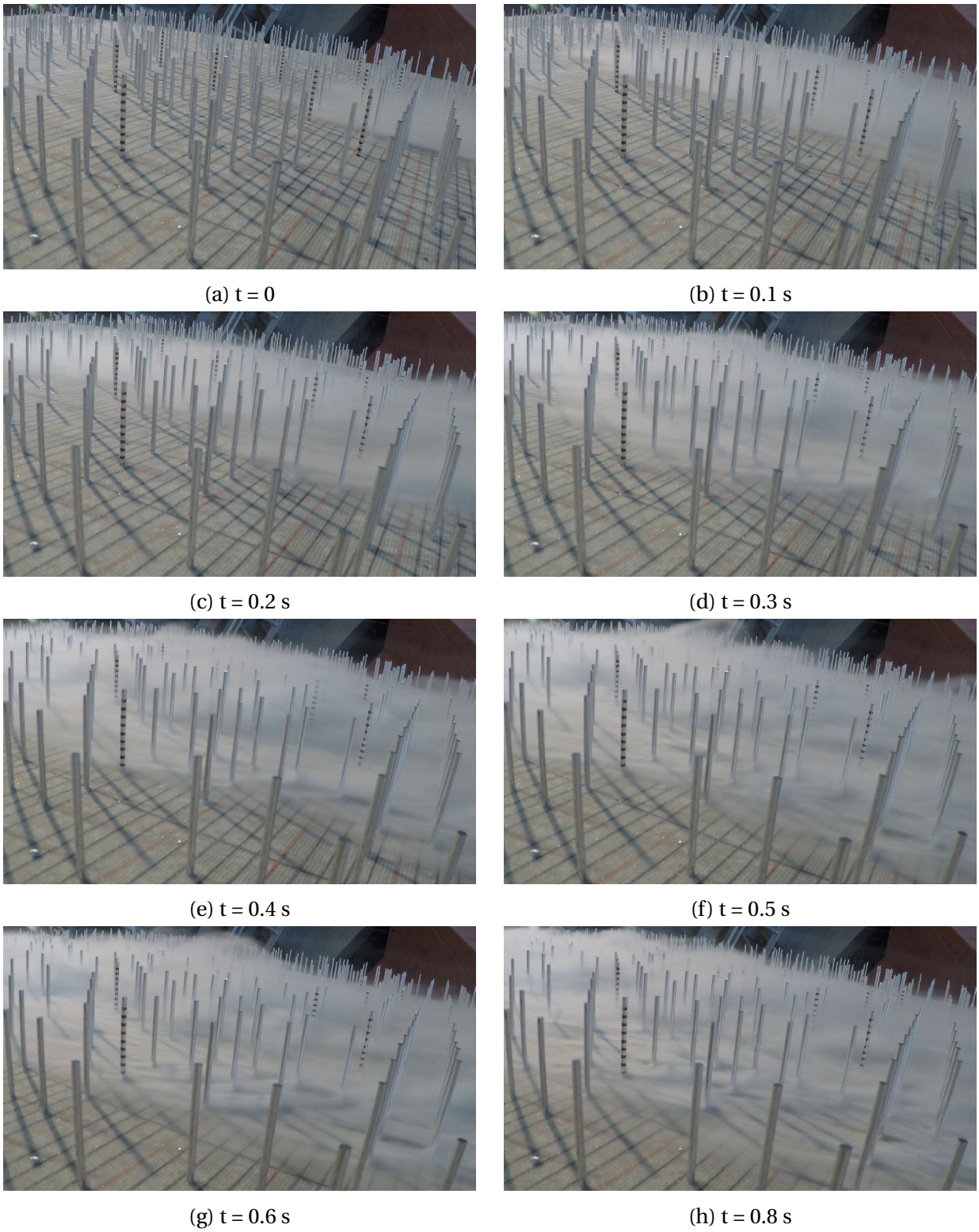

(a) t = 0 (b) t = 0.1 s

(c) t = 0.2 s (d) t = 0.3 s

(e) t = 0.4 s (f) t = 0.5 s

(g) t = 0.6 s (h) t = 0.8 s

Figure C.17: Experiment 20 (mass: 6 kg, stem diameter: 3.2 mm, forest density: 50%)

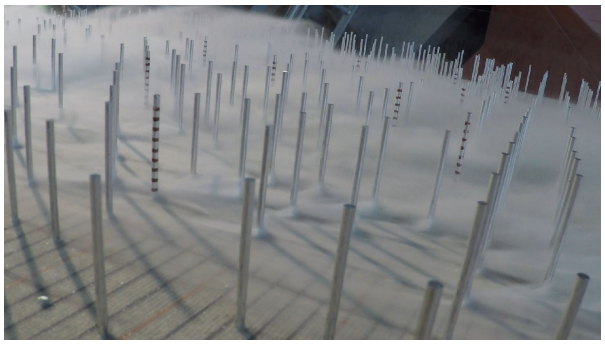

(i) t = 1.0 s

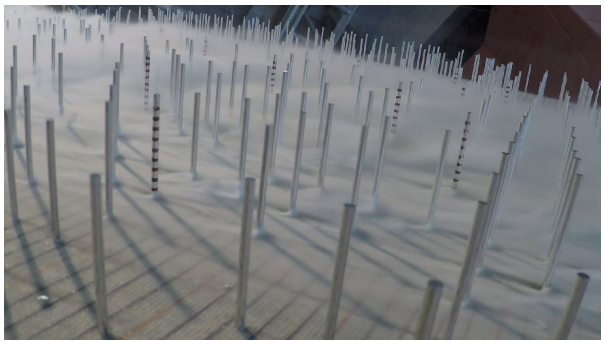

(j) t = 1.2 s

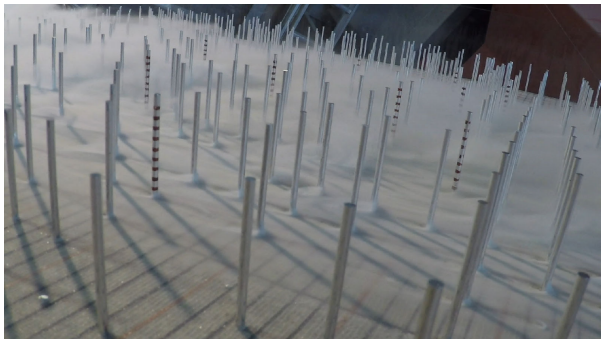

(k) t = 1.4 s

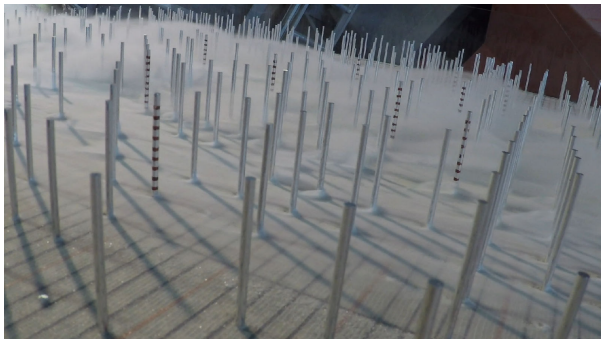

(l) t = 1.6 s

(m) t = 1.8 s

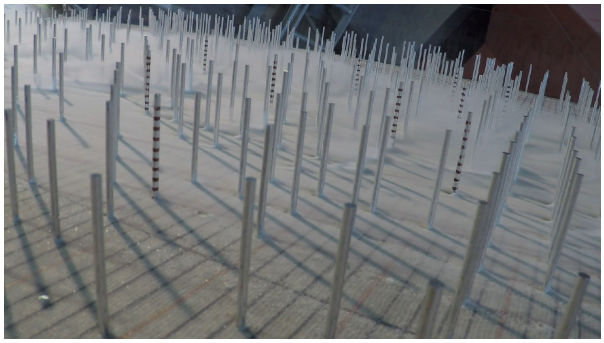

(n) t = 2.0 s

(o) t = 2.5 s

(p) t = 4.0 s

Figure C.17: Continued: Experiment 20 (mass: 6 kg, stem diameter: 3.2 mm, forest density: 50%)

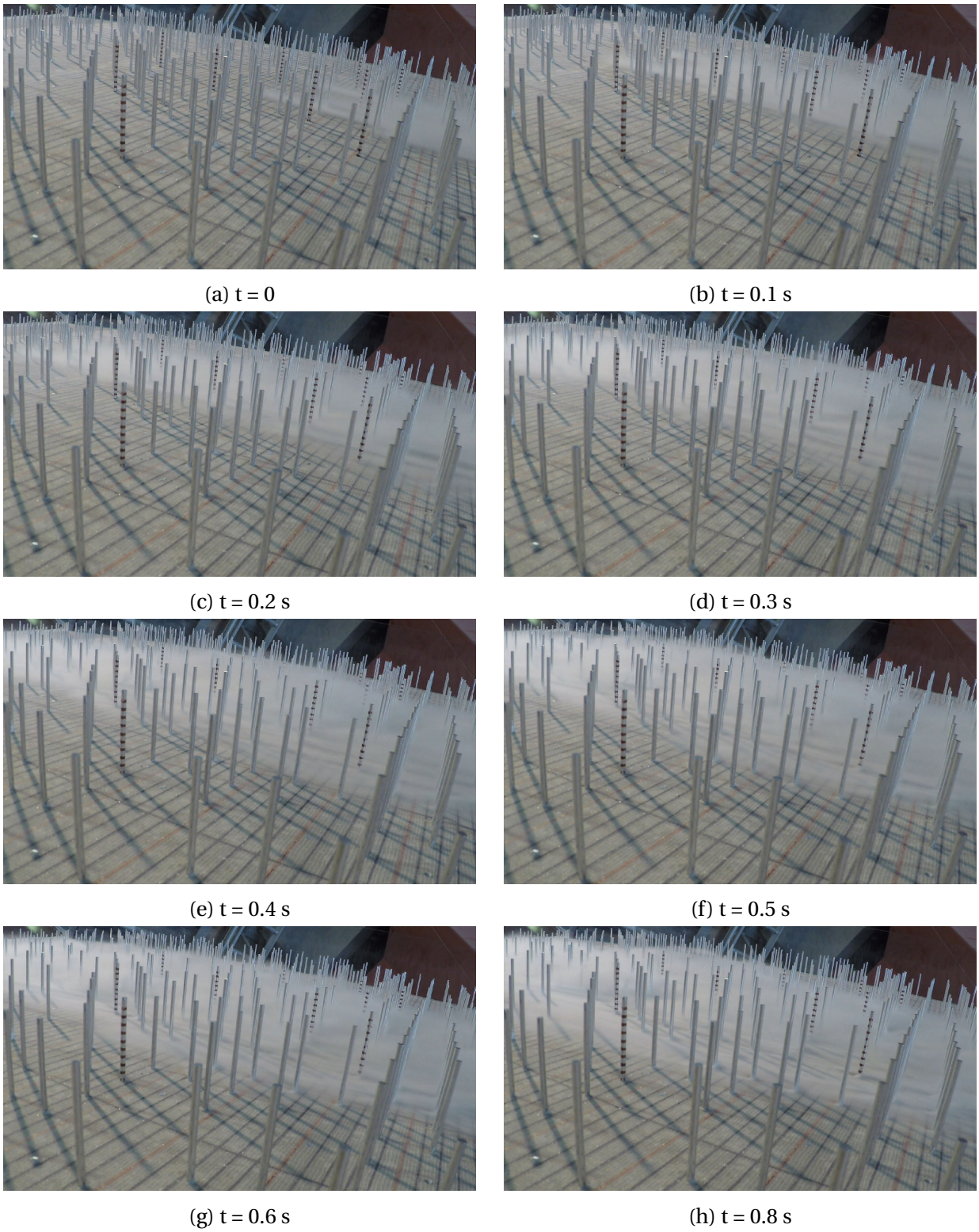

(a) t = 0 (b) t = 0.1 s

(c) t = 0.2 s (d) t = 0.3 s

(e) t = 0.4 s (f) t = 0.5 s

(g) t = 0.6 s (h) t = 0.8 s

Figure C.18: Experiment 21 (mass: 2 kg, stem diameter: 3.2 mm, forest density: 50%)

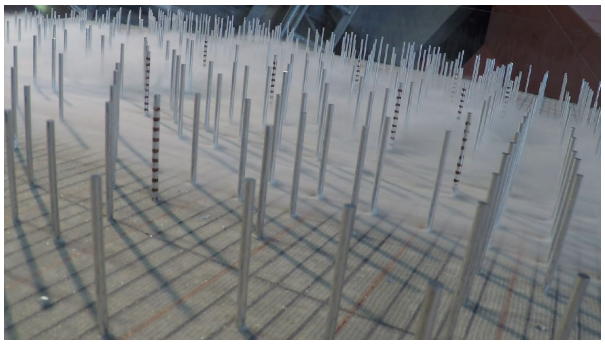

(i) t = 1.0 s

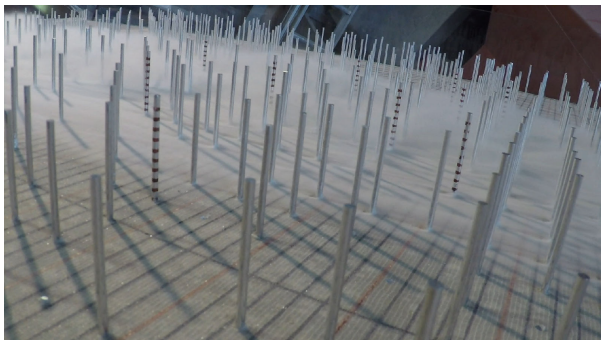

(j) t = 1.2 s

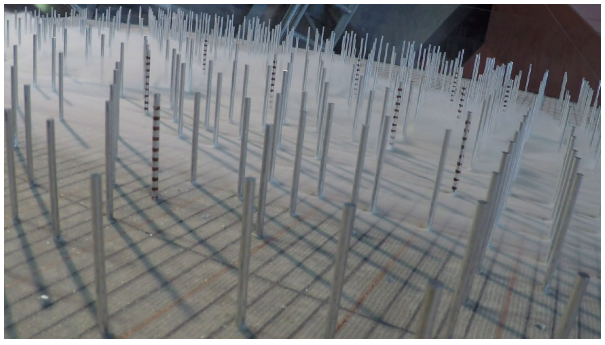

(k) t = 1.4 s

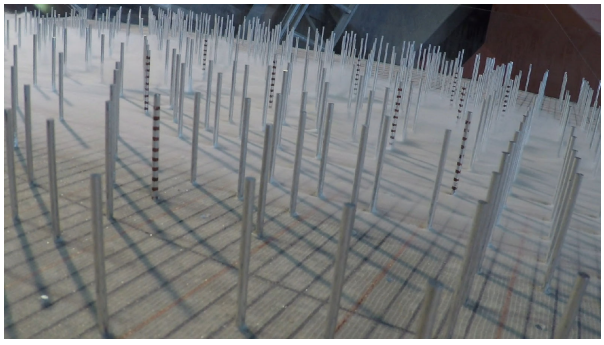

(l) t = 1.6 s

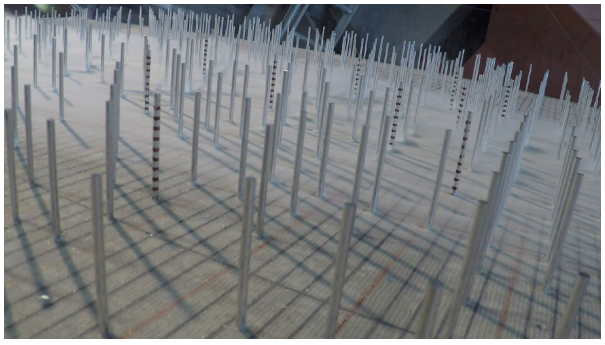

(m) t = 1.8 s

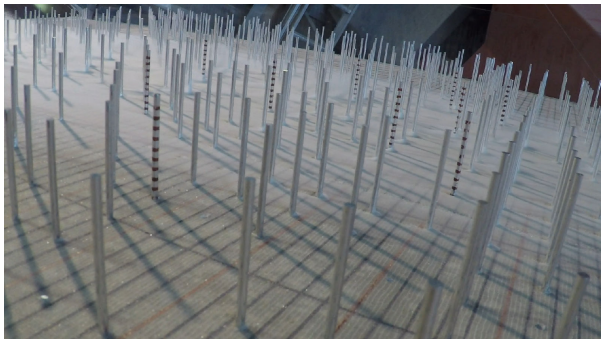

(n) t = 2.0 s

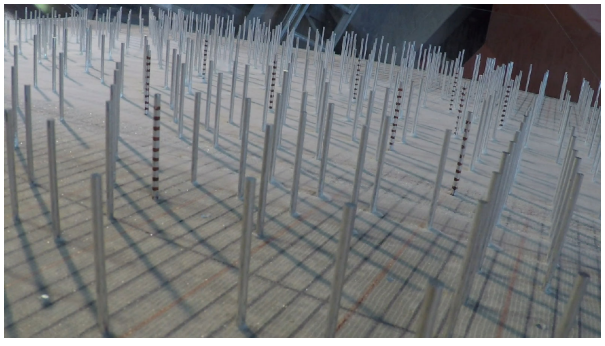

(o) t = 2.5 s

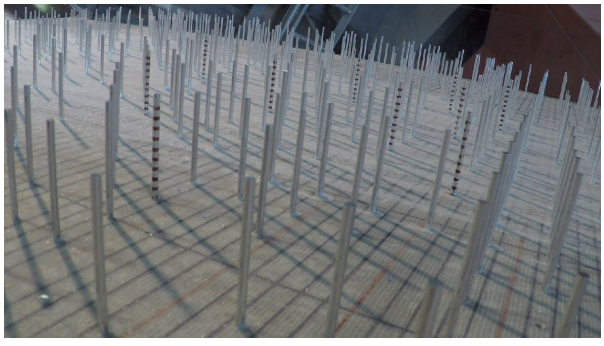

(p) t = 4.0 s

Figure C.18: Continued: Experiment 21 (mass: 2 kg, stem diameter: 3.2 mm, forest density: 50%)

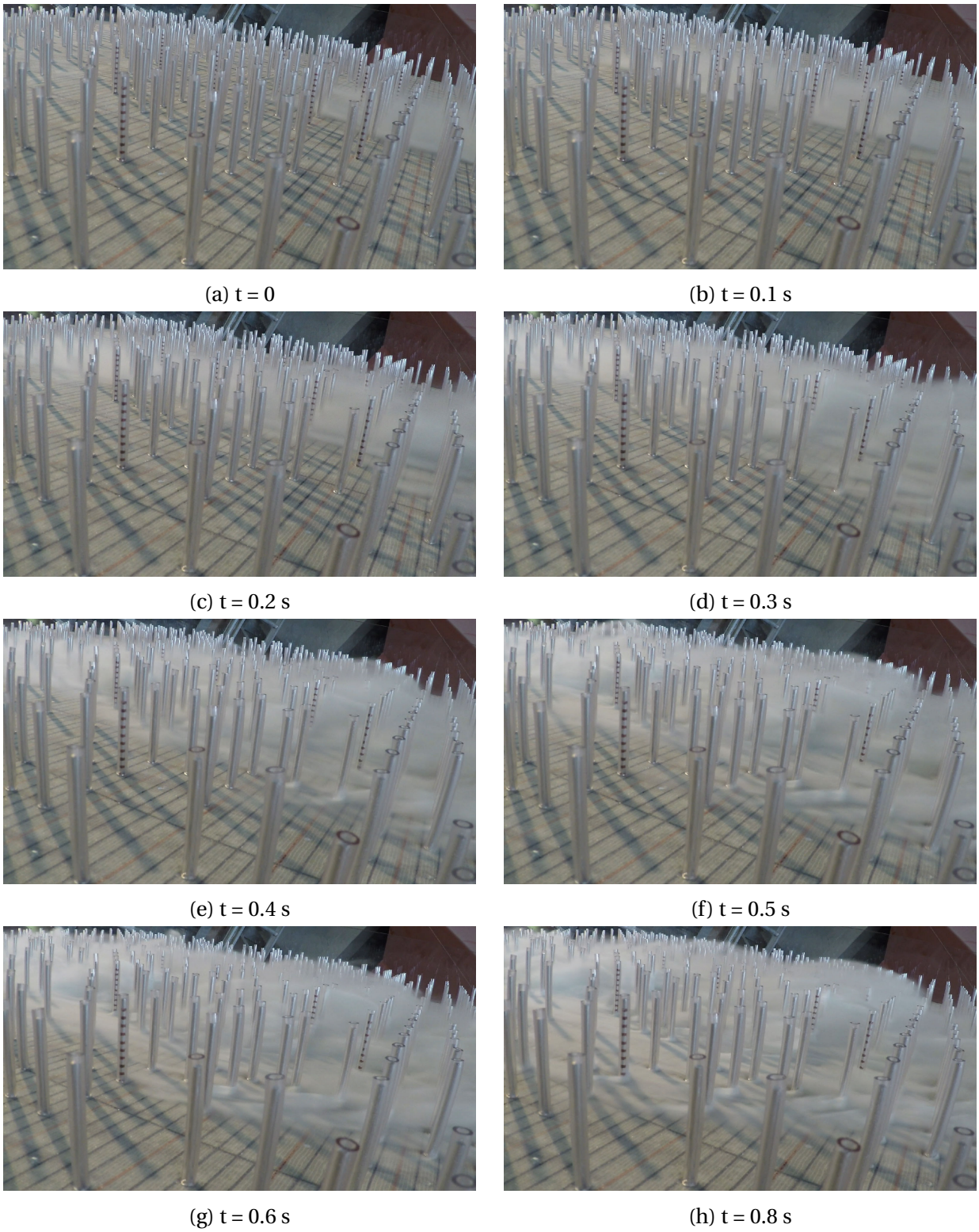

(a) t = 0 (b) t = 0.1 s

(c) t = 0.2 s (d) t = 0.3 s

(e) t = 0.4 s (f) t = 0.5 s

(g) t = 0.6 s (h) t = 0.8 s

Figure C.19: Experiment 22 (mass: 4 kg, stem diameter: 6 mm, forest density: 50%)

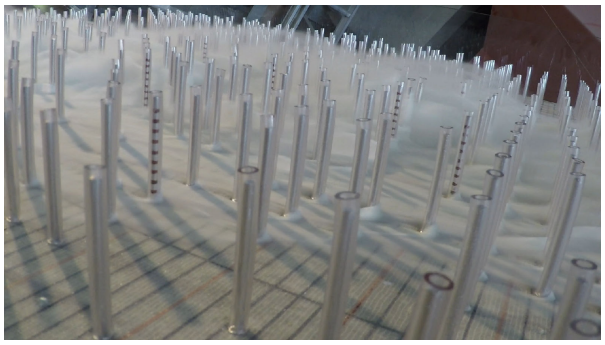

(i) t = 1.0 s

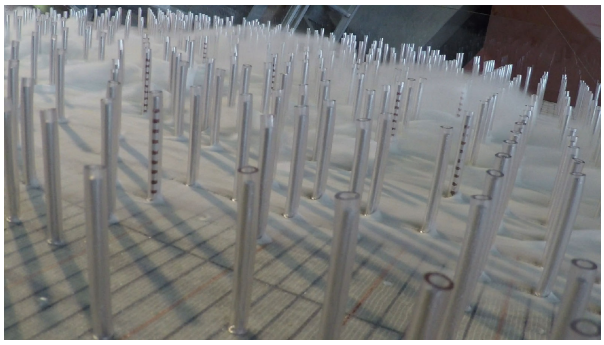

(j) t = 1.2 s

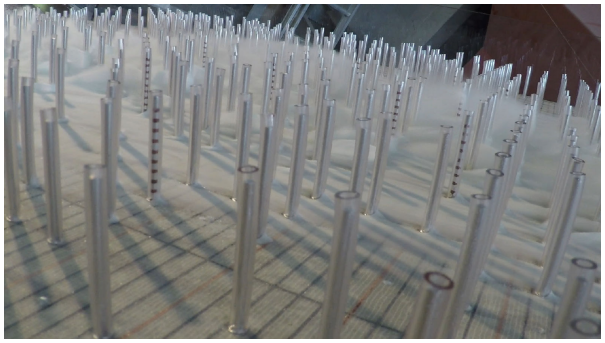

(k) t = 1.4 s

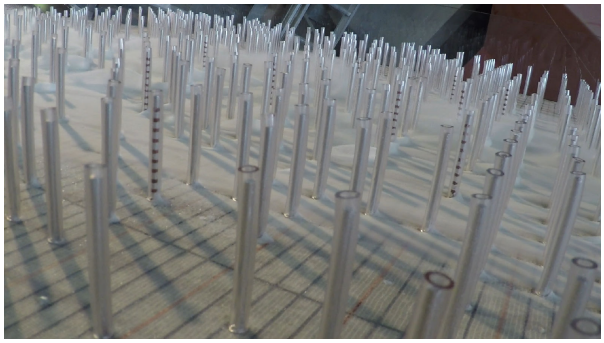

(l) t = 1.6 s

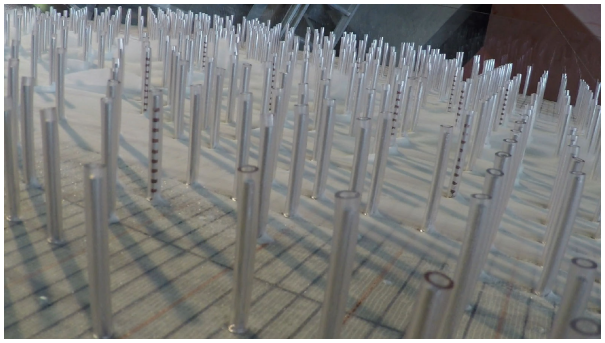

(m) t = 1.8 s

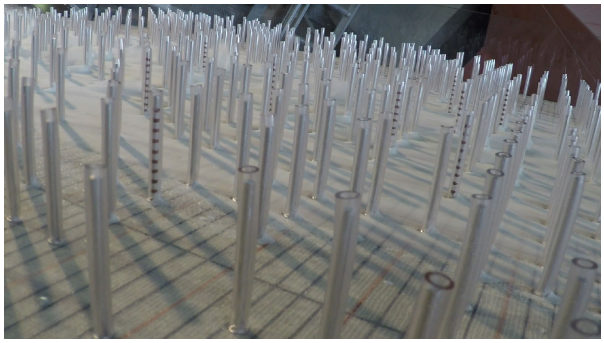

(n) t = 2.0 s

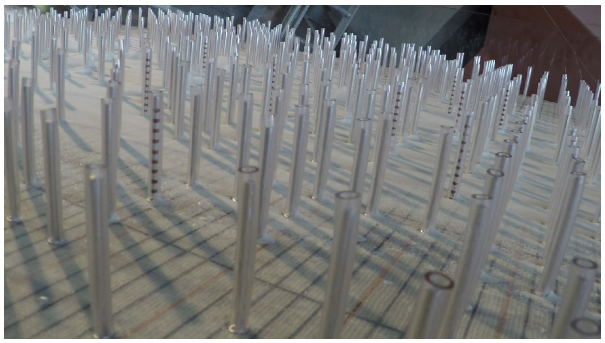

(o) t = 2.5 s

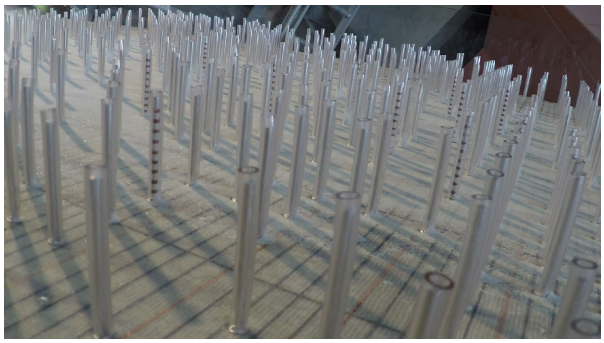

(p) t = 4.0 s

Figure C.19: Continued: Experiment 22 (mass: 4 kg, stem diameter: 6 mm, forest density: 50%)

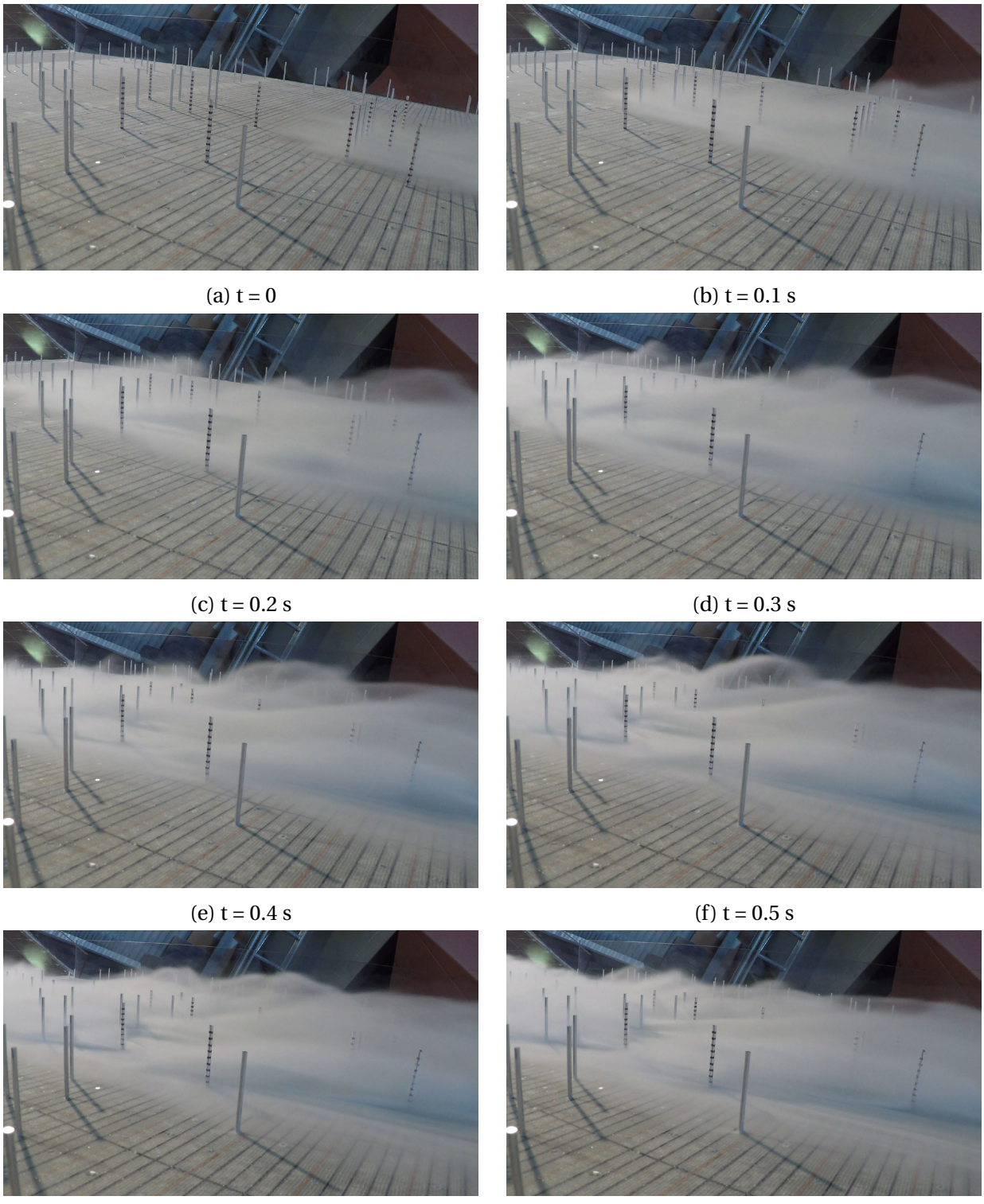

(a) t = 0 (b) t = 0.1 s

(c) t = 0.2 s (d) t = 0.3 s

(e) t = 0.4 s (f) t = 0.5 s

(g) t = 0.6 s (h) t = 0.8 s

Figure C.20: Experiment 32 (mass: 4 kg, stem diameter: 3.2 mm, forest density: 10%)

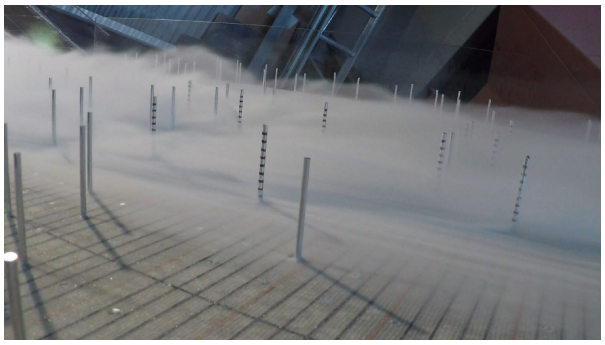

(i) t = 1.0 s

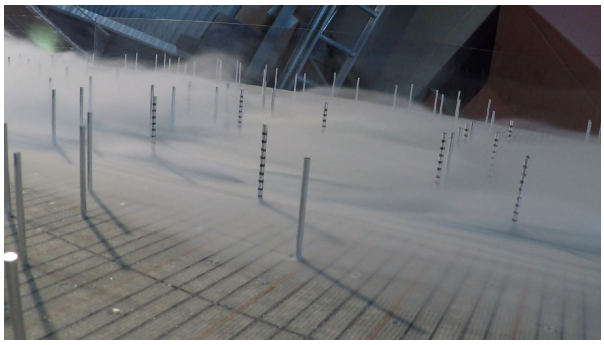

(j) t = 1.2 s

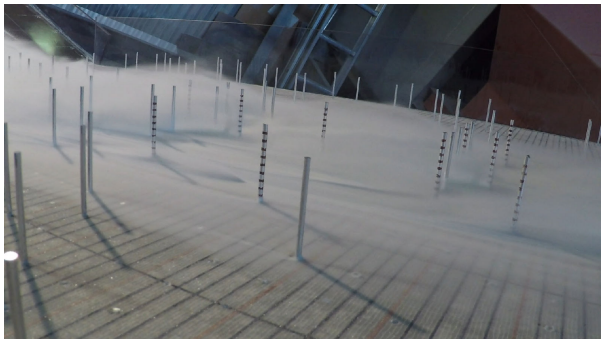

(k) t = 1.4 s

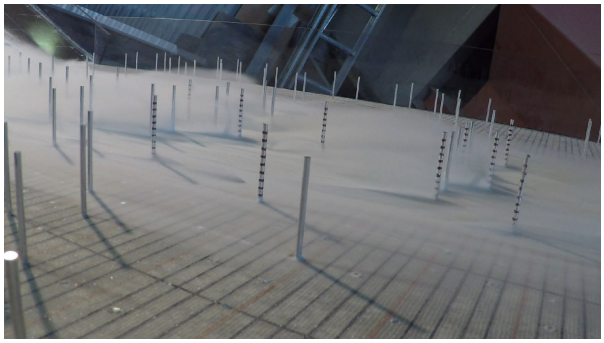

(l) t = 1.6 s

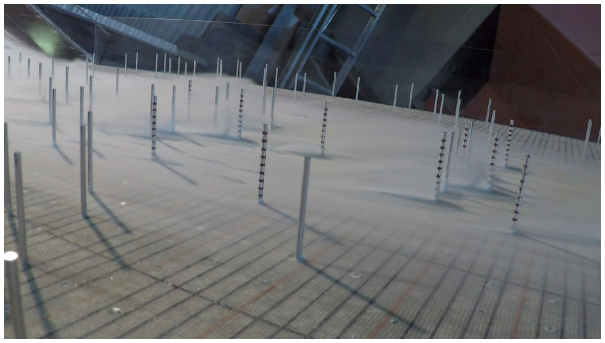

(m) t = 1.8 s

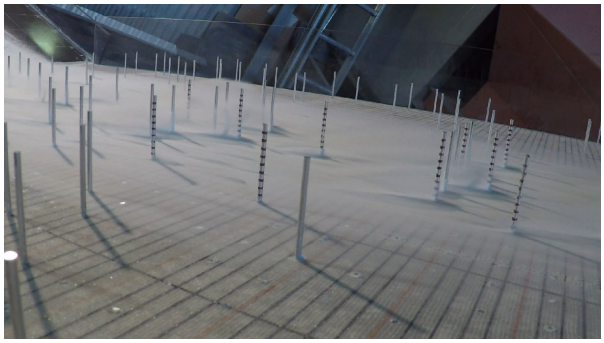

(n) t = 2.0 s

(o) t = 2.5 s

(p) t = 4.0 s

Figure C.20: Continued: Experiment 32 (mass: 4 kg, stem diameter: 3.2 mm, forest density: 10%)

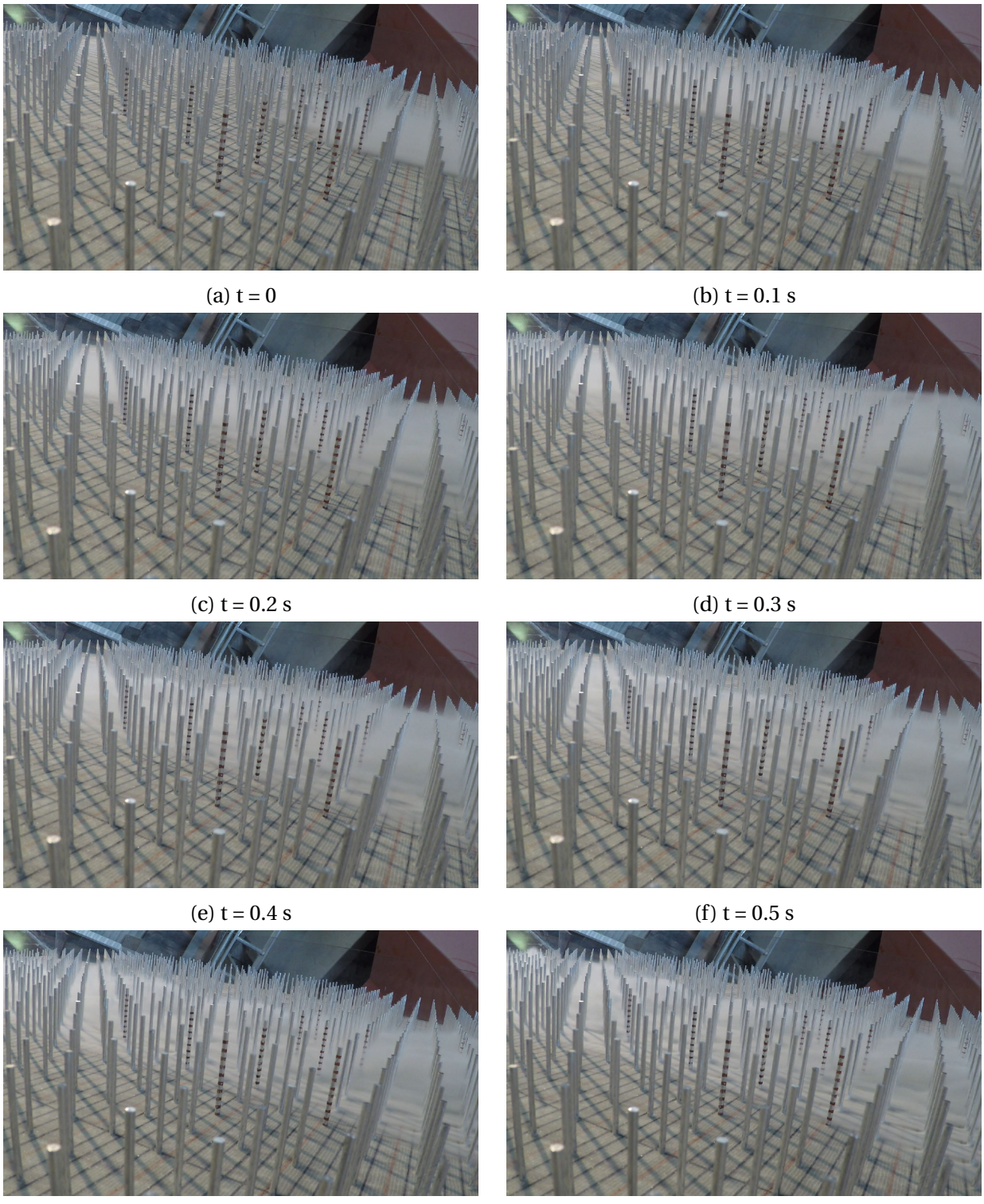

(a) t = 0

(b) t = 0.1 s

(c) t = 0.2 s

(d) t = 0.3 s

(e) t = 0.4 s

(f) t = 0.5 s

(g) t = 0.6 s

(h) t = 0.8 s

Figure C.21: Experiment 48 (mass: 4 kg, stem diameter: 3.2 mm, forest density: 90%)

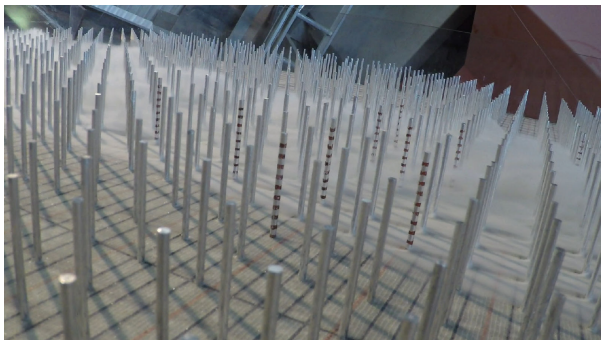

(i) t = 1.0 s

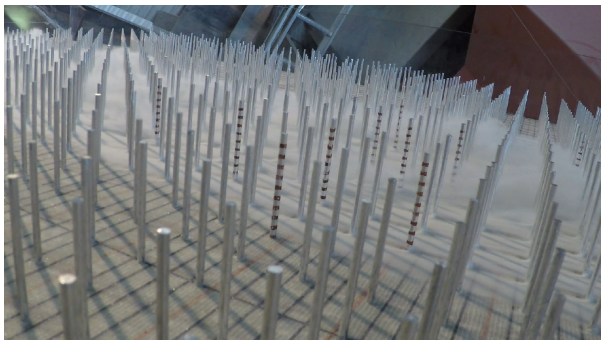

(j) t = 1.2 s

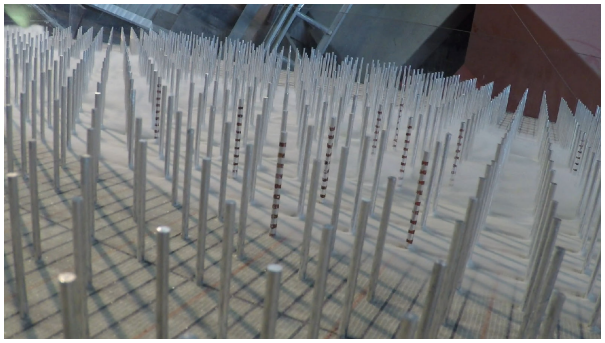

(k) t = 1.4 s

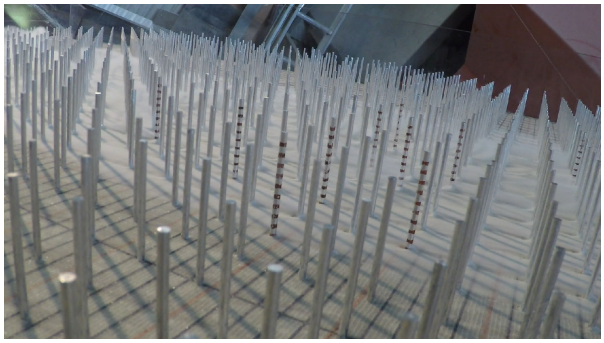

(l) t = 1.6 s

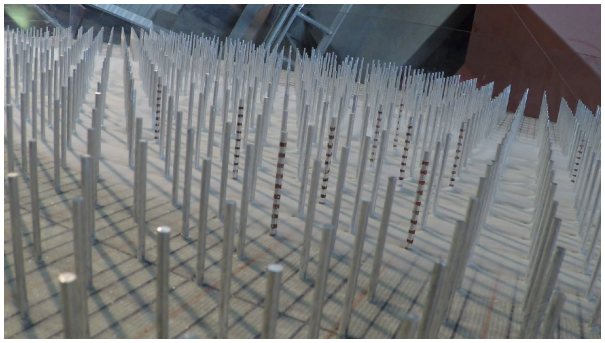

(m) t = 1.8 s

(n) t = 2.0 s

(o) t = 2.5 s

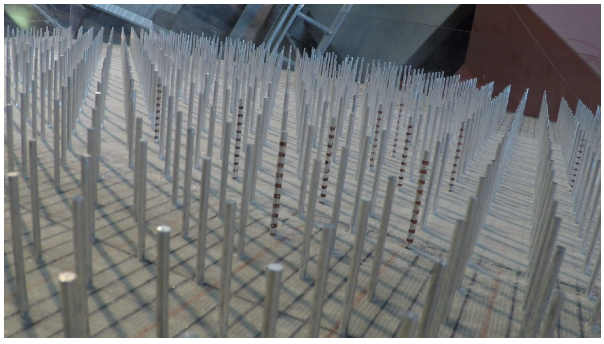

(p) t = 4.0 s

Figure C.21: Continued: Experiment 48 (mass: 4 kg, stem diameter: 3.2 mm, forest density: 90%)

(a) t = 0

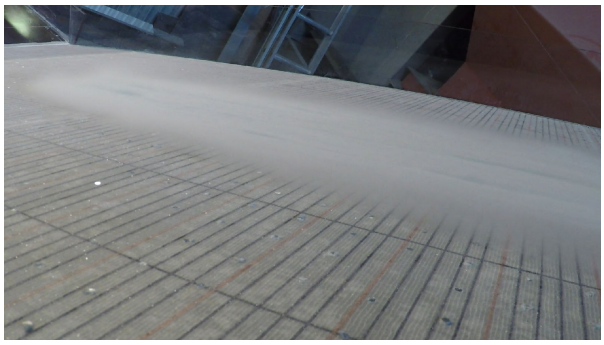

(b) t = 0.17 s

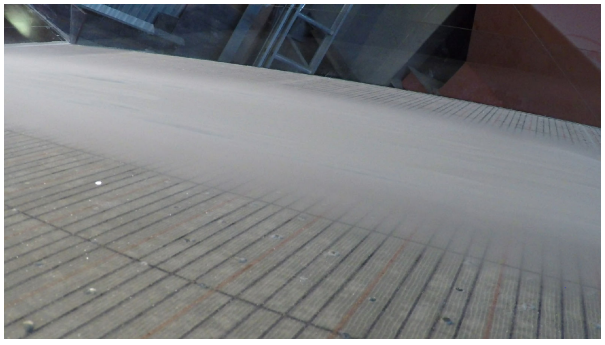

(c) t = 0.33 s

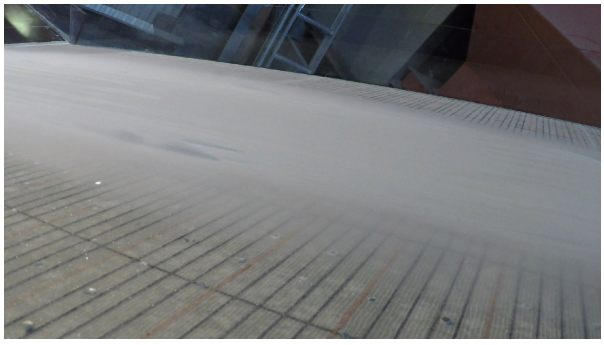

(d) t = 0.67 s

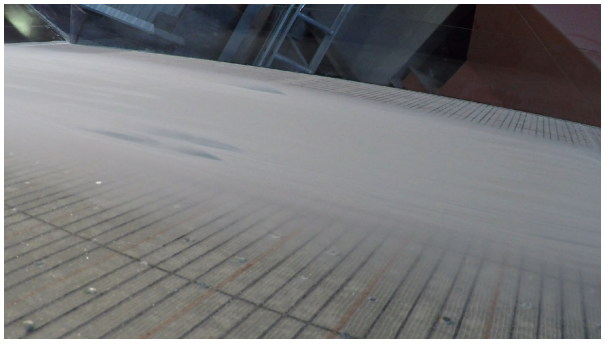

(e) t = 1.0 s

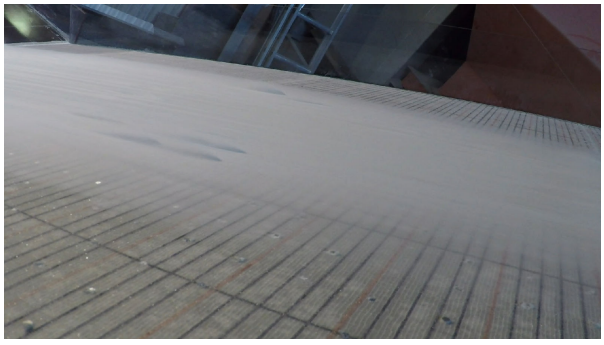

(f) t = 1.5 s

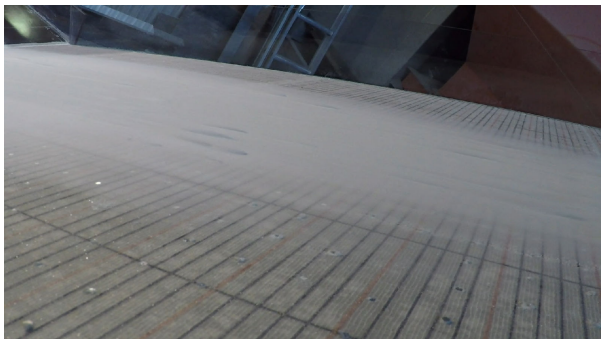

(g) t = 2.0 s

(h) t = 4.5 s

Figure C.22: Experiment 49 (mass: 4 kg)

Appendix D

Selected photos of the runout

Figure D.1: Experiment 2

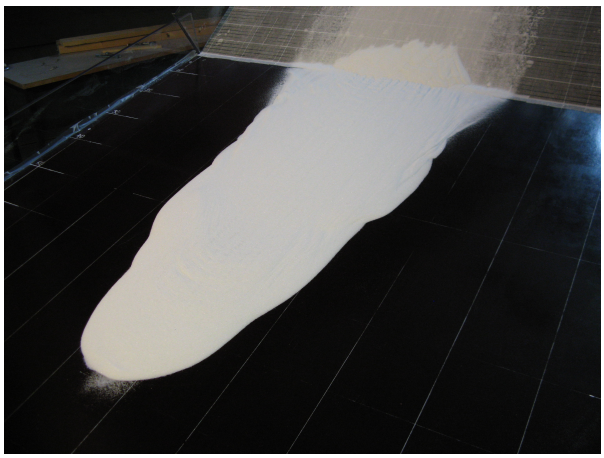

Figure D.2: Experiment 3

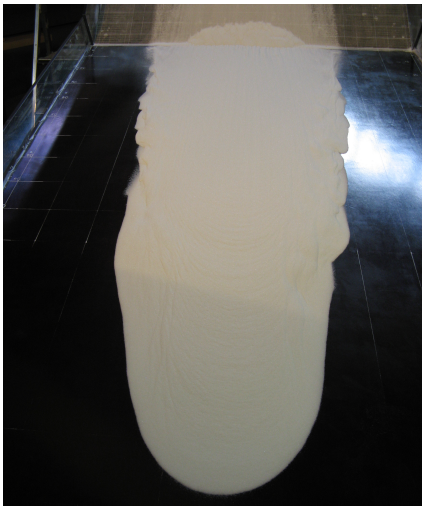

Figure D.3: Experiment 5

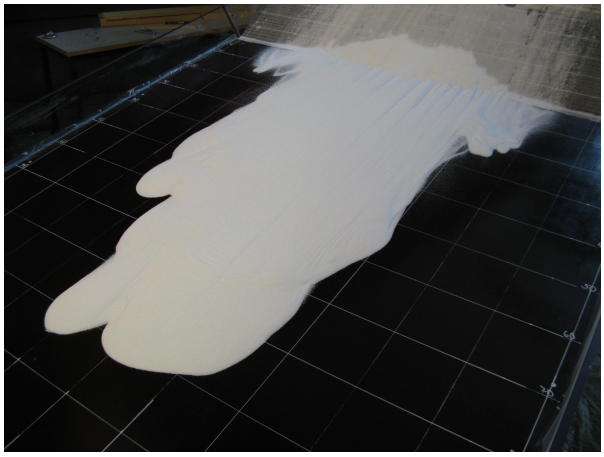

Figure D.4: Experiment 8

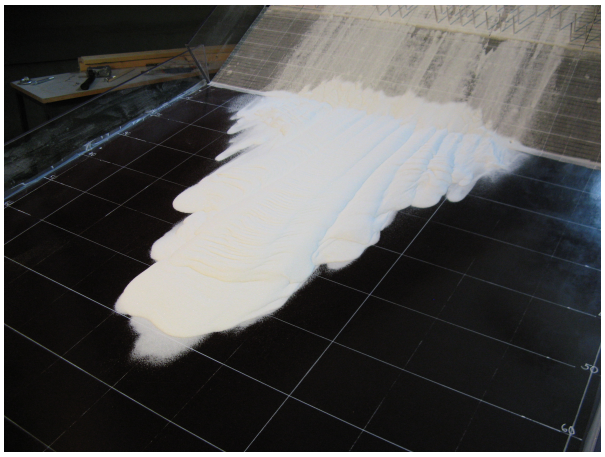

Figure D.5: Experiment 19

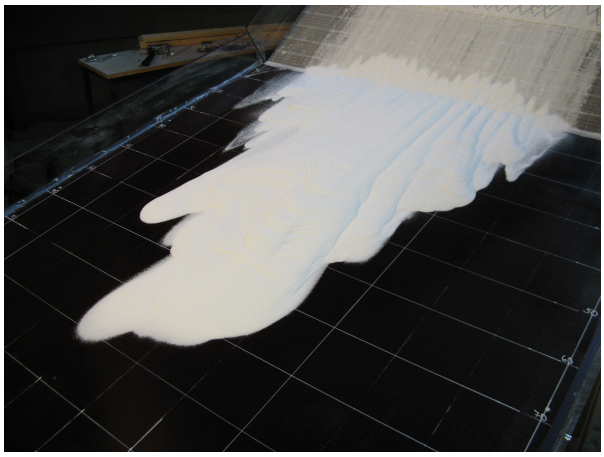

Figure D.6: Experiment 20

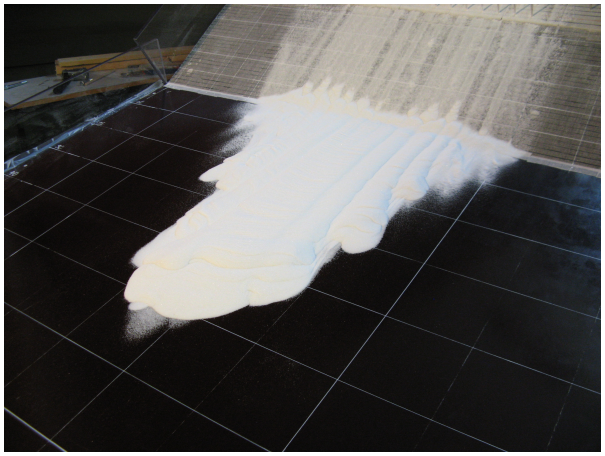

Figure D.7: Experiment 21

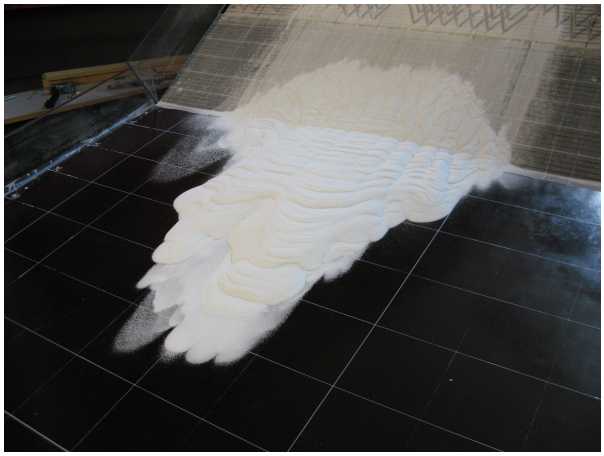

Figure D.8: Experiment 22

Figure D.9: Experiment 32

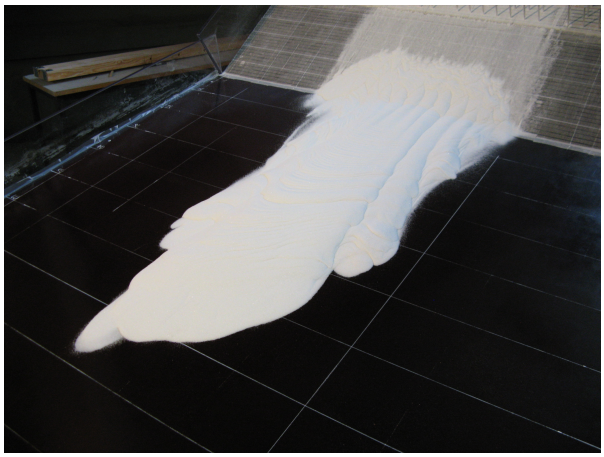

Figure D.10: Experiment 48

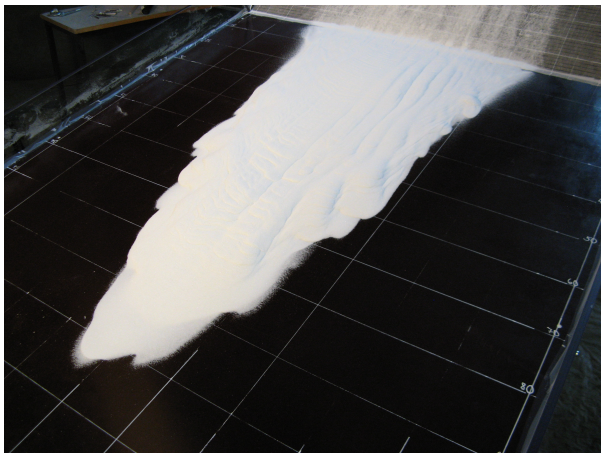

Figure D.11: Experiment 49

Appendix E

Raw data

Table E.1: Manual measurement data for the reference experiments.

	Flow depth (mm)	Runout distance (cm)		Flow depth (mm)	Runout distance (cm)
1	12	147.0	49	9	103.5 (105.5)
2	8	121.0	50	4-5	77.0 (84.5)
3	6	79.0 (81.0)	51	12-13	116.0 (122.0)
4	5-6	80.0	52	9	106.5 (107.5)
5	12-13	147.5	53	5-6	81.5 (83.5)
6	9	121.0	54	12	120.5

Table E.2: Manual measurement data for the experiments with a forest.

	Runout distance (cm)		Runout distance (cm)		Runout distance (cm)		Runout distance (cm)
7	62.5	19	70.0 (75.0)	31	62.0 (63.5)	43	66.5 (72.0)
8	94.5	20	92.0	32	80.5 (86.5)	44	76.0
9	111.0	21	53.0 (56.5)	33	91.0 (103.5)	45	52.0
10	51.5	22	54.5 (57.5)	34	61.5	46	85.5 (91.0)
11	74.0	23	55.5 (70.0)	35	78.5	47	58.0
12	84.0	24	41.0 (45.5)	36	78.0 (89.5)	48	78.0
13	63.5	25	41.0 (49.5)	37	103.5 (107.5)		
14	39.5 (45.0)	26	66.5 (71.0)	38	80.5 (83.5)		
15	56.0 (57.5)	27	54.0 (57.5)	39	61.5		
16	94.0	28	53.0 (57.0)	40	119.5 (121.5)		
17	74.5	29	73.5	41	96.0		
18	50.0 (54.0)	30	87.0	42	63.0		

Bibliography

Anderson, G. and McClung, D. (2012). Snow avalanche penetration into mature forest from timber-harvested terrain. *Canadian Geotechnical Journal*, 49(4):477–484.

Bakkehøi, S., Domaas, U., and Lied, K. (1983). Calculation of snow avalanche runout distance. *Annals of Glaciology*, 4:24–29.

Bartelt, P. and Stöckli, V. (2001). The influence of tree and branch fracture, overturning and debris entrainment on snow avalanche flow. *Annals of Glaciology*, 32(1):209–216.

Berger, F., Dorren, L., Kleemayr, K., Maier, B., Planinsek, S., Bigot, C., Bourrier, F., Jancke, O., Toe, D., and Cerbu, G. (2013). *Eco-Engineering and Protection Forests Against Rockfalls and Snow Avalanches*, chapter 12, pages 191–210. InTech.

Bozhinskiy, A. and Sukhanov, L. (1998). Physical modelling of avalanches using an aerosol cloud of powder materials. *Annals of Glaciology*, 26:242–246.

Brang, P., Schönenberger, W., Ott, E., and Gardner, B. (2001). Forests as protection from natural hazards. In Evans, J., editor, *The Forests Handbook*, volume 2, chapter 3, pages 53–81. Blackwell Science Ltd.

Brateng, L. E. (2005). Laboratorieforsøk for utforming av terrengtiltak mot snøskred. Master's thesis, NTNU.

Breien, H. and Høydal, Ø. A. (2014). Snøskred i bjørkeskog - testforsøk i Abisko. Technical Report 20130918-01-R, NGI.

Buser, O. and Frutiger, H. (1980). Observed maximum run-out distance of snow avalanches and the determination of the friction coefficients μ and ξ. *Journal of Glaciology*, 26:121–130.

Christen, M., Bartelt, P., and Gruber, U. (2002). Aval-1D: An avalanche dynamics program for the practice. In *International Congress Interpraevent*, volume 2, pages 715–725, Matsumoto, Japan.

Christen, M., Kowalski, J., and Bartelt, P. (2010). RAMMS: Numerical simulation of dense snow avalanches in three-dimensional terrain. *Cold Regions Science and Technology*, 63(1):1–14.

Faug, T., Naaim, M., Bertrand, D., Lachamp, P., and Naaim-Bouvet, F. (2003). Varying dam height to shorten the run-out of dense avalanche flows: Developing a scaling law from laboratory experiments. *Surveys in Geophysics*, 24(5-6):555–568.

Feistl, T., Bebi, P., Christen, M., Margreth, S., Diefenbach, L., and Bartelt, P. (2015). Forest damage and snow avalanche flow regime. *Natural Hazards and Earth System Sciences Discussions*, 3(1):535–574.

Feistl, T., Bebi, P., Teich, M., Bühler, Y., Christen, M., Thuro, K., and Bartelt, P. (2014). Observations and modeling of the braking effect of forests on small and medium avalanches. *Journal of Glaciology*, 60(219):124–138.

G. D. R. MiDi (2004). On dense granular flows. *The European Physical Journal E*, 14(4):341–365.

Gray, J., Tai, Y.-C., and Noelle, S. (2003). Shock waves, dead zones and particle-free regions in rapid granular free-surface flows. *Journal of Fluid Mechanics*, 491:161–181.

Greve, R. and Hutter, K. (1993). Motion of a granular avalanche in a convex and concave curved chute: experiments and theoretical predictions. *Philosophical Transactions of the Royal Society of London A: Mathematical, Physical and Engineering Sciences*, 342(1666):573–600.

Hákonardóttir, K. M., Jóhannesson, T., Tiefenbacher, F., and Kern, M. (2001). A laboratory study of the retarding effect of breaking mounds in 3, 6 and 9 m long chutes. Technical Report 01007, Veðurstofa Íslands, Reykjavík.

Hauksson, S., Pagliardi, M., Barbolini, M., and Jóhannesson, T. (2007). Laboratory measurements of impact forces of supercritical granular flow against mast-like obstacles. *Cold Regions Science and Technology*, 49(1):54–63.

Holzinger, G. and Hübl, J. (2004). Belastung eines Murbrechers: Abgeleitet aus Laborversuchen (Impact forces on a debris flow breaker derived from laboratory experiments). In Mikos, M. and Gutknecht, D., editors, *10th Congress INTERPRAEVENT 2004*, pages 131–139. Internationale Forschungsgesellschaft INTERPRAEVENT, Klagenfurt, Austria.

Høydal, Ø. A., Breien, H., and Sandersen, F. (2013). Forslag til kriterier for vernskog mot skred - del 1. Technical Report 20120078-01-R, NGI.

Hutter, K. and Koch, T. (1991). Motion of a granular avalanche in an exponentially curved chute: Experiments and theoretical predictions. *Philosophical Transactions of the Royal Society of London A: Mathematical, Physical and Engineering Sciences*, 334(1633):93–138.

Hutter, K., Koch, T., Plüss, C., and Savage, S. (1995). The dynamics of avalanches of granular materials from initiation to runout. Part II. Experiments. *Acta Mechanica*, 109(1-4):127–165.

Issler, D. (2004). Méthodologie d'expertise: les calculs des avalanches. Lecture Notes, Université européenne d'été, Sept. 2004, Courmayeur, Italy. Available from http://snf.ngi.no/reports/uee_2004.mod8.040725.pdf.

Iverson, R. M., Logan, M., and Denlinger, R. P. (2004). Granular avalanches across irregular three-dimensional terrain: 2. Experimental tests. *Journal of Geophysical Research: Earth Surface*, 109(F1). F01015.

Kahrs, K. (2015). The braking effect of trees on snow avalanches: Design of an experimental study. Project thesis, NTNU.

Lam, K., Gong, W., and So, R. (2008). Numerical simulation of cross-flow around four cylinders in an in-line square configuration. *Journal of Fluids and Structures*, 24(1):34–57.

Lam, K., Li, J., Chan, K., and So, R. (2003a). Flow pattern and velocity field distribution of cross-flow around four cylinders in a square configuration at a low reynolds number. *Journal of Fluids and Structures*, 17(5):665–679.

Lam, K., Li, J., and So, R. (2003b). Force coefficients and strouhal numbers of four cylinders in cross flow. *Journal of Fluids and Structures*, 18(3):305–324.

Lam, K. and Zou, L. (2007). Experimental and numerical study for the cross-flow around four cylinders in an in-line square configuration. *Journal of Mechanical Science and Technology*, 21(9):1338–1343.

Lied, K. and Kristensen, K. (2003). *Snøskred: håndbok om snøskred*. Vett & Viten.

Lienhard, J. H. (1966). *Synopsis of lift, drag, and vortex frequency data for rigid circular cylinders*. Technical Extension Service, Washington State University.

McClung, D. and Schaerer, P. (2006). *The avalanche handbook*. Mountaineers Books, Seattle, Washington, 3rd edition.

Moe, G. (2014). Forces on slender structures. In *Kompendium, TBA4265 Arctic and Marine Civil Engineering*, pages 235–258. Department of Civil and Transport Engineering, NTNU.

NGI. Snøskred. http://www.ngi.no/no/snoskred/Ulykker/. Accessed: 2016-04-12.

Nicolle, A. and Eames, I. (2011). Numerical study of flow through and around a circular array of cylinders. *Journal of Fluid Mechanics*, 679:1–31.

Norem, H. (2014). *Veger og snøskred*. Statens vegvesen.

Norem, H., Brateng, L. E., and Hustad, A. (2006). Ideas on the design of earth mounds and dams to protect highways against snow avalanches. PIARC XII International Winter Roads Congress, Torino, 2006. Available from http://brage.bibsys.no/xmlui/bitstream/id/201130/Norem2.pdf.

Norem, H., Irgens, F., and Schieldrop, B. (1987). A continuum model for calculating snow avalanche velocities. In *Avalanche Formation, Movement and Effects (Proceedings of the Davos Symposium, September 1986)*, pages 363–379.

Olsen, N. R. B. (2015). Kompendium del 2 og 4, TVM4116 Hydromekanikk. Department of Hydraulic and Environmental Engineering, NTNU.

Pouliquen, O. (1999). Scaling laws in granular flows down rough inclined planes. *Physics of Fluids*, 11(3):542–548.

Pouliquen, O. and Forterre, Y. (2002). Friction law for dense granular flows: application to the motion of a mass down a rough inclined plane. *Journal of Fluid Mechanics*, 453:133–151.

Protocol for the implementation of the Alpine Convention in the field of mountain forests (1996). http://www.ecolex.org/ecolex/ledge/view/RecordDetails?id=TRE-001240&index=treaties. Accessed: 2015-10-12.

Salm, B., Gubler, H. U., and Burkard, A. (1990). *Berechnung von Fliesslawinen: eine Anleitung für Praktiker mit Beispielen*. Mitteilung 47, Eidgenössisches Institut für Schnee-und Lawinenforschung, Weissfluhjoch/Davos.

Sovilla, B. (2004). *Field experiments and numerical modelling of mass entrainment and deposition processes in snow avalanches*. PhD thesis, Swiss Federal Institute of Technology (ETH), Zurich, Switzerland.

Sumner, D. (2010). Two circular cylinders in cross-flow: A review. *Journal of Fluids and Structures*, 26(6):849–899.

Takeuchi, Y., Torita, H., Nishimura, K., and Hirashima, H. (2011). Study of a large-scale dry slab avalanche and the extent of damage to a cedar forest in the Makunosawa valley, Myoko, Japan. *Annals of Glaciology*, 52(58):119–128.

Tatsuno, M., Amamoto, H., and Ishi-i, K. (1998). Effects of interference among three equidistantly arranged cylinders in a uniform flow. *Fluid dynamics research*, 22(5):297–315.

Teich, M., Fischer, J., Feistl, T., Bebi, P., Christen, M., and Grêt-Regamey, A. (2013). Computational snow avalanche simulation in forested terrain. *Natural Hazards and Earth System Sciences Discussions*, 1(5):5561–5601.

Voellmy, A. (1955). Über die Zerstörungskraft von Lawinen. *Schweiz. Bauzeitung*, 73(12, 15, 17, 19):159–165, 212–217, 246–249, 280–285. (English as: On the destructive force of avalanches. 63p. Alta Avalanche Study Center, Translation 2, 1964).

Wieland, M., Gray, J., and Hutter, K. (1999). Channelized free-surface flow of cohesionless granular avalanches in a chute with shallow lateral curvature. *Journal of Fluid Mechanics*, 392:73–100.